Probing galaxy evolution with quasar absorption lines

by

Trystyn Andrew Munro Berg
B.Sc., University of Victoria, 2012
M.Sc., University of Victoria, 2014

A Thesis Submitted in Partial Fulfillment of the
Requirements for the Degree of

DOCTOR OF PHILOSOPHY

in the Department of Physics and Astronomy

Probing galaxy evolution with quasar absorption lines

by

Trystyn Andrew Munro Berg
B.Sc., University of Victoria, 2012
M.Sc., University of Victoria, 2014

Supervisory Committee

Dr. Sara Ellison, Supervisor
(Department of Physics & Astronomy)

Dr. Luc Simard, Departmental Member
(Department of Physics & Astronomy)

Dr. Matthew Moffitt, Outside Member
(Department of Chemistry)

ABSTRACT

When we look throughout the Universe, we can see the stages of galaxy evolution across cosmic time; however there are still many unanswered questions about the details of galaxy evolution. How did galaxies like our Milky Way assemble? Do the first galaxies look different than our own? What makes galaxies stop forming stars? Many of these questions can be addressed by studying the detailed chemistry of gas located in and around galaxies. Absorption lines imprinted on quasar spectra probe this hard-to-see gas within and surrounding galaxies, giving an luminosity-unbiased census of gas from $z \approx 0$ to the epoch of the most distant quasars. In this thesis, I present two samples of high resolution spectra of quasars obtained from both ground- and space-based observatories to study the evolution of galaxies through their gas-phase absorption lines.

The first of the two samples presented in this thesis consists of the 100 quasar sightlines from the XQ-100 legacy survey completed with the X-Shooter spectrograph on the Very Large Telescope in Chile. The XQ-100 survey provides a blind sample of over 350 H I absorption line systems associated with galaxies with column densities 18.8 $\leq$logN(H I)$\leq$ 21.5). Using this sample, I investigated the evolution of neutral gas reservoirs from $z \approx 4.5$ to $z \approx 2.0$. I demonstrate that the lower column density sub-damped Lyman alpha systems (with column densities 19.0 $\leq$logN(H I)$<$ 20.3) contribute $\approx 20\%$ of the H I observed in galaxy gas reservoirs compared to the rarer but high column density damped Lyman alpha systems (DLAs; logN(H I)$\geq$ 20.3). Furthermore, I show that using the presence of metal lines (particularly Mg II absorption) to identify and select absorbing systems can potentially bias the properties of the sample; absorbers selected to contain strong metal line absorbers tend to exclude low metallicity and low H I column density systems. I demonstrate that the systems missed by metal-selected searches can have a significant impact on the study of the cosmic evolution of neutral gas reservoirs.

In addition to the H I content, the metal abundances for 13 elements in the 41 DLAs of the XQ-100 sample are presented. In concert with my literature compilation of 280 DLA metal abundance measurements, I studied the dust-corrected [Zn/Fe]. This work emphasizes that near-IR coverage of X-Shooter provides unprecedented access to Mg II, Ca II and Ti II lines (at redshifts 3–4) to provide additional evidence for subsolar [Zn/Fe] ratio in DLAs, a chemical signature that DLAs can be high-redshift dwarf galaxy analogues. Furthermore, the XQ-100 DLA sample consists of several unique systems that probe the effects of environment on the chemical evolution of the Universe, as well as the chemical makeup of the first generations of stars. I demonstrate that DLAs close to their background quasar (within 5000 km s^{-1}) with logN(HI)$<$ 21.0 show lower [S/H] and [Fe/H] (relative to intervening systems with similar redshift and N(H I)), whilst higher [S/H] and [Si/H] are seen in these proximate systems with logN(HI)$>$ 21.0. Contrary to previous studies, DLAs within 10 000 km s^{-1} of another DLA show no difference in [α/Fe] relative to single DLAs matched in metallicity and redshift. In addition, I present follow-up high-resolution data of J0034+1639, a sightline containing three DLAs, including a metal-poor DLA with [Fe/H]$= -2.82$ (the third lowest [Fe/H] in DLAs identified to date) at $z_{abs}= 4.25$.

In the latter part of this thesis, I study the circumgalactic medium (CGM) of galaxies that host an active galactic nucleus (AGN). AGN are thought to play a critical role in shaping galaxies, but their effect on the gaseous reservoirs surrounding galaxies is not well studied. I present results from the COS-AGN survey: 19 quasar sightlines that probe the gas surrounding 20 optically-selected AGN host galaxies observed over 65 hours with the Hubble Space Telescope. Absorption lines from a variety of species are measured and compared to a stellar mass and impact parameter matched sample of sightlines through non-AGN galaxies. Amongst the observed species in the COS-AGN sample (Lyα, C II, Si II, Si III, C IV, Si IV, N V), only Lyα shows a high covering fraction whilst many of the metal ions are not detected in individual sightlines. A sightline-by-sightline comparison between COS-AGN and the control sample yields no significant difference in equivalent width distribution. However, stacked spectra of the COS-AGN and control samples show significant enhancements in the equivalent width of both Lyα and Si III at high impact parameters ($>$ 164 kpc) by a factor of $+0.45 \pm 0.05$ dex and $> +0.75$ dex respectively. The lack of detections of both high-ionization species near the AGN and strong kinematic offsets between the absorption systemic galaxy redshifts indicates that neither the AGN's ionization nor its outflows are the origin of these differences. Instead, I suggest the observed differences could result from either AGN hosts residing in haloes with intrinsically distinct gas properties, or that their CGM has been affected by a previous event, such as a starburst, which may also have fuelled the nuclear activity.

Contents

List of Tables

List of Figures

LIST OF ABBREVIATIONS

AD — Anderson-Darling

AGN — Active Galactic Nuclei

AODM — Apparent Optical Depth Method

BPT — Baldwin-Phillips-Terlevich

COS — Cosmic Origins Spectrograph

CGM — Circumgalactic Medium

DLA — Damped Lyman Alpha System

ESI — Echellette Spectrograph and Imager

EW — Rest-frame Equivalent Width

FS — Full Sample

FWHM — Full Width Half Maximum

GALEX — Galaxy Evolution Explorer

HIRES — High Resolution Echelle Spectrometer

HSLA — Hubble Spectroscopic Legacy Archive

HST — Hubble Space Telescope

ISM — Interstellar Medium

KS — Kolmogorov-Smirnov

LINER — Low-Ionization Nuclear Emission-line Region

LLS — Lyman Limit System

MCB — Monte Carlo Bootstrap

MDLA — Multiple Damped Lyman Alpha system

MPDLA — Metal-poor Damped Lyman Alpha system

MS — Metal-selected Sample

NIR — Near Infrared

OB — Observing Block

PDLA — Proximate Damped Lyman Alpha System

QAL — Quasar Absorption Line System

QSO — Quasar

SDSS — Sloan Digital Sky Survey

SFR — Star Formation Rate

sSFR — Specific Star Formation Rate

subDLA — Sub-Damped Lyman Alpha System

UV — Ultraviolet

UVES — Ultraviolet-Visual Echelle Spectrograph

VLT — Very Large Telescope

ACKNOWLEDGEMENTS

First and foremost, much of this thesis has greatly benefited from the input of all of my co-authors (in particular V. D'Odorico, S. Ellison, S. Lopez, B. Oppenheimer, J. X. Prochaska, R. Sánchez-Ramírez, J. Schaye, J. Tumlinson), as well as discussions with or data provided by S. Borthakur, H.W. Chen, R. Cooke, T. Heckman, C. Martin, S. Rao, and J. Werk.

I am indebted to S. Ellison for being an excellent supervisor through-out my graduate studies; particularly for providing me with the opportunities to grow my research interests and networks, a wealth of knowledge when I encountered problems, and support when research got messy. I am also grateful for the time invested by my supervisory committee and my external examiner (J. Werk) in helping me complete this degree, and to the graduate students who have been (and continue to be) a great reference for both science and programming queries.

During the research required for this thesis, over 10,000 kg of rocks were thrown at houses as significant source of relaxation; although I am sure some people would not believe it. Either of these feats would not have been possible without all of my teammates, as well as our opponents, that made (or missed) every shot in those 300+ games of curling.

I leave Sisyphus at the foot of the mountain. One always finds one's burden again. But Sisyphus teaches the higher fidelity that negates the gods and raises rocks. He too concludes that all is well. This universe henceforth without a master seems to him neither sterile nor futile. Each atom of that stone, each mineral flake of that night-filled mountain, in itself, forms a world. The struggle itself toward the heights is enough to fill a man's heart. One must imagine Sisyphus happy.

— Albert Camus, *Myth of Sisyphus*

For all those who have shaped this mountain.

Chapter 1

On the importance of gas in the Universe

When we look out into the *observable* Universe, we can see its primary contents; stars and gas[1]. Although the stars primarily define the visible structures of galaxies we observe, it is the processing of gas in galaxies that traces the many processes of the evolution of galaxies. Many of the details of galaxy evolution are still unknown. For example, what processes regulate the growth of a galaxy? How do the elements from the periodic table get produced? What did the first stars and galaxies look like? These questions can be (partially) answered through the observations of the chemistry and temperature of gas in and around galaxies.

1.1 The origin and distribution of gas in the Universe

Big Bang nucleosynthesis

The origin of the primordial gas in the Universe is a direct result of the Big Bang. The extreme temperature and density of the Universe in its infancy kept matter, antimatter, and photons in thermal equilibrium with each other (Hayashi, 1950). As the Universe expanded adiabatically, this material *froze-out* of its thermal equilibrium, leaving behind the baryonic material we see and interact with today.

[1]Note these components only make up $\approx 5\%$ of the total matter-energy budget of the Universe; the remaining unseen components are dark matter ($\approx 27\%$) and dark energy ($\approx 68\%$ Planck Collaboration et al., 2015).

Big Bang nucleosynthesis (Wagoner et al., 1967; Walker et al., 1991; Cyburt et al., 2008) is responsible for the production of the primordial ratio of hydrogen, helium, and trace amounts of lithium in gas. Surprisingly, the production of the elements during the Big Bang is highly dependent on very few quantities: the baryon-photon ratio (limiting how many nuclei that can form), the proton-neutron ratio (constraining the amount of neutrons available to form the heavier elements), and the expansion rate of the early Universe (setting the amount of time nucleosynthesis can occur). Constraining these three quantities uses a combination of measurements of the Cosmic Microwave Background (the relic radiation from the Big Bang; Penzias & Wilson, 1965; Planck Collaboration et al., 2015) and the amount of primordial material left over from the Big Bang (namely deuterium and ^{7}Li; Spite & Spite, 1982; Tytler et al., 1996; Asplund et al., 2006; Pettini et al., 2008; Cooke et al., 2018). The resulting product is gas that is approximately 75% hydrogen, 25% helium, and trace amounts of lithium.

The buildup of structure in the Universe

After the Big Bang, all matter in the Universe (both baryonic [$\approx$ 10% of matter], and the so-called dark matter [$\approx$ 90% of matter] whose origin is uncertain; Planck Collaboration et al., 2015) are uniformly distributed on large scales across the Universe. However, density perturbations on small scales lead to the growth of structure in the Universe as the attractive force of gravity brings the matter together into the so-called *cosmic web*, which is characterized by long filamentary structures connecting nodes of large matter buildup (see Figure 1 of Springel et al., 2005b). Gas residing outside of galaxies (known as the *inter-galactic medium*; Gunn & Peterson, 1965) funnels along the filamentary structures into the dark matter haloes that have formed at the nodes, leading to the formation of stars and galaxies (e.g. see Figure 1 of both Vogelsberger et al., 2014; Schaye et al., 2015). Furthermore, the gravitational attraction of neighbouring nodes brings smaller structures (such as dark matter haloes or stellar clusters) together, leading to the build up of more massive structures; a process known as *hierarchical assembly* (Searle & Zinn, 1978; White & Rees, 1978).

1.2 Star formation, evolution, and the synthesis of metals

As the gas cools within a dark matter halo or galaxy, the atomic hydrogen settles onto dust grains or, in dust-free environments such as the early Universe, free protons and electrons to form molecular hydrogen (e.g. Gould & Salpeter, 1963; Bromm & Larson, 2004). The molecular gas continue to cool into giant molecular clouds, which continues to contract until they reach high enough densities that the thermal pressure of the gas can no longer support it and the cloud fragments and collapses (Jeans, 1902). Each fragment continues to contract until the temperature of the core can begin fusion reactions, forming stars. The hottest, brightest stars formed emit enormous amounts of ultra-violet (UV) light, which heat up and ionize the remains of the giant molecular clouds, preventing stars from continuing to form until the gas cools again (McKee & Ostriker, 2007).

Stellar fusion

Fusion of nuclei in stars starts at a temperature of 5×10^6 K, converting four hydrogen nuclei into one helium nucleus through the proton-proton (pp) chain (Burbidge et al., 1957). At higher temperatures ($\sim 10^8$ K), a preferential mechanism known as the CNO cycle dominates over the burning of hydrogen into helium (Bethe, 1939). In brief, the pp-chain combines three hydrogen nuclei into ^{3}He, and ^{3}He nuclei into ^{4}He . The pp-chain is the only hydrogen burning cycle that does not require additional catalysts, whereas the CNO cycles requires the catalysts carbon, nitrogen, and/or oxygen for hydrogen fusion.

Upon the exhaustion of hydrogen within the stellar core, the star can no longer support its outer layer. Further collapse of the star increases the temperature of the core to 10^8 K, igniting helium in the *triple alpha* process to produce carbon ash. In summary, the triple alpha process converts three helium into carbon by first fusing two helium nuclei into ^{8}Be, and then adding a third ^{4}He (e.g. Burbidge et al., 1957). The difficulty that the stellar core faces during helium burning is that ^{8}Be is easily dissociated at these high temperatures. To overcome this problem, high densities and temperatures are needed to quickly merge ^{8}Be+^{4}He and overcome the small cross-section of this nuclear reaction (Salpeter, 1952).

For the more massive varieties of stars, further stages of burning occur in the core (and in shells beyond the core), as more massive stars can reach central (shell) temperatures for further fusion reactions using fuel such as carbon (temperature of $\sim 5 \times 10^8$ K), oxygen ($\sim 10^9$ K), neon ($\sim 1.5 \times 10^9$ K), and silicon ($\sim 3 \times 10^9$ K). These massive stars have complex shells of burning, leading to a stellar structure often denoted as the onion-skin model (see Figure 1.1). Once nickle and iron ash are produced in the core, nuclear fusion is no longer favourable and the star can no longer support itself from further collapse. This final collapse results in a supernova, releasing a portion of the newly processed elements back into the gaseous interstellar medium (ISM) of the galaxy whilst the remaining materials forms a remnant corpse of a neutron star or black hole.

Metal enrichment and chemical evolution

As stars live and die, the production of elements from the stellar nuclear reactions pollute the gas within the galaxy, resulting in future generations of stars with these new material in their atmosphere. The measure of the content of all the elements that are not hydrogen or helium in a gas cloud or on the surface of a star is known as the metallicity, as these elements are commonly referred to as *metals*. As this cycling of ISM gas leads to an increase in metallicity with time (e.g. Timmes et al., 1995), the gas-phase metallicity is a useful tracer of the star formation history of a galaxy. The effects of metal enrichment have been seen within the ISM of galaxies across cosmic time (since redshift[2] $z \sim 4.5$; e.g. Pettini et al., 1997; Prochaska et al., 2003a; Rafelski et al., 2012, 2014), finding a steady increase in metallicity with time.

Metallicity is measured as the ratio of the number of atoms of metals (or more typically using a standard element or ion M as a metal tracer, e.g. Fe or Zn) relative to the amount of hydrogen. For reference and simplicity, it is also generally scaled to the value of the Sun's abundance and measured in the log, namely [M/H]$= log(\frac{n_{\rm M}}{n_{\rm H}}) - log(\frac{n_{\rm M_\odot}}{n_{\rm H_\odot}})$, where $n_{\rm M}$ and $n_{\rm H}$ are the number densities of the metal M and hydrogen, while $n_{\rm M_\odot}$ and $n_{\rm H_\odot}$ are the number densities of M and hydrogen in the Sun (e.g. as compiled by Asplund et al., 2009).

In addition to the general increase in metallicity, the abundances of individual

[2]Redshift is a quantity typically used to define an epoch of the Universe in the past. Due to the expansion of the Universe, the observed light from objects further away appear redder due to the Doppler shifting of light. The redshift of an object is quantified as $z = \frac{\lambda{\rm obs} - \lambda_0}{\lambda_0}$, where $\lambda_{\rm obs}$ and λ_0 are the respective observed and rest-frame wavelengths of light; such that larger values of z refer to earlier epochs in the Universe.

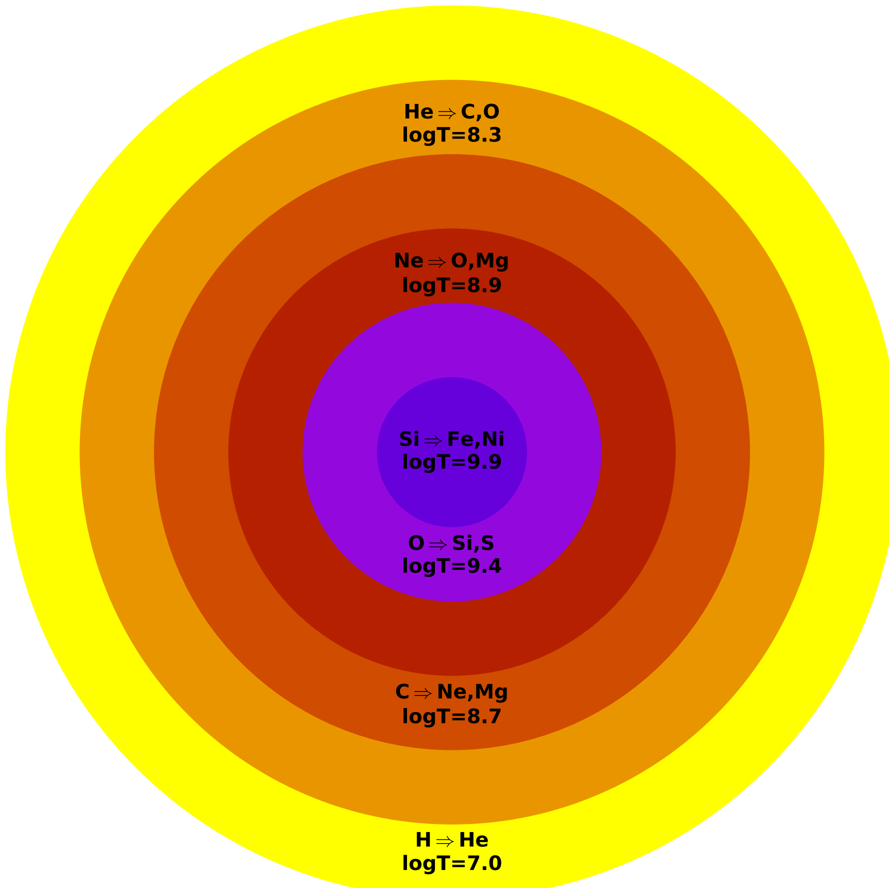

Figure 1.1 A schematic cross-section of a star undergoing multiple burning phases. Each concentric ring shows the fuel and main end products of the fusion reactions within the layer, along with the typical temperature (logT; in units of log(K)) of those reactions. Temperatures for each layer are adopted from Kippenhahn & Weigert (1994).

elements also change with time. However, the rates of these metal abundance changes depend on the types of stars within the stellar populations formed. Within a given molecular cloud, a population of stars with a range of stellar masses form at the same time. The most massive stars of this population evolve the fastest, contributing to the metal production first through Type II supernova explosions. These massive stars dominate the production of elements such as oxygen, magnesium, neon, silicon, and sulphur (i.e. the α-elements, for containing an integer number of α-particles in their atomic nucleus; note these are the bulk of fuel and products in the fusion layers of Figure 1.1). The long-lived, less massive stars will later nucleosynthetically contribute more to the production of iron (and other metals of similar atomic numbers) through Type Ia supernovae, thus diluting the ratio of α-elements to iron (the [α/Fe] ratio). Therefore, [α/Fe] is often used as an indicator of how fast the gas has evolved with time or metallicity (see Figure 1.2; Tinsley, 1979; McWilliam, 1997). As a result, the evolution of the [α/Fe] ratio with metallicity varies for different galaxies. Comparing the [α/Fe]-metallicity trend of the Milky Way (e.g. McWilliam, 1997; Venn et al., 2004) with local dwarf galaxies (Tolstoy et al., 2009) has revealed that the lower mass dwarf spheroidal galaxies (dSphs) have a drop in the [α/Fe] ratio at lower metallicities relative to the Milky Way (see Figure 1.2). This discrepancy results from dwarf galaxies having fewer massive stars, and are unable to enrich the global metallicity of the galaxy as quickly as the Milky Way (Tolstoy et al., 2009) before the contributions of lower mass stars to [α/Fe]. Similar effects can be seen in the lack of Zn in dwarf galaxies (Shetrone et al., 2003; Venn et al., 2012; Berg et al., 2015a; Skúladóttir et al., 2017), where the dearth of the most massive stars (the suggested dominant producer of Zn; Umeda & Nomoto, 2002) in dwarf galaxies leads to an under-abundance of [Zn/Fe] relative to the Milky Way.

1.3 The evolution and death of galaxies

Evolutionary states of galaxies

Upon the collection of gas into the dark matter haloes and the formation of stars, galaxies are born. Although this definition of a galaxy is simple, observational studies of galaxies show they are much more complex systems with a diverse range of properties such as mass and shape. Two of the simplest ways of classifying galaxies, which are inter-connected, are by morphology (Hubble, 1926; Willett et al., 2013) or colour

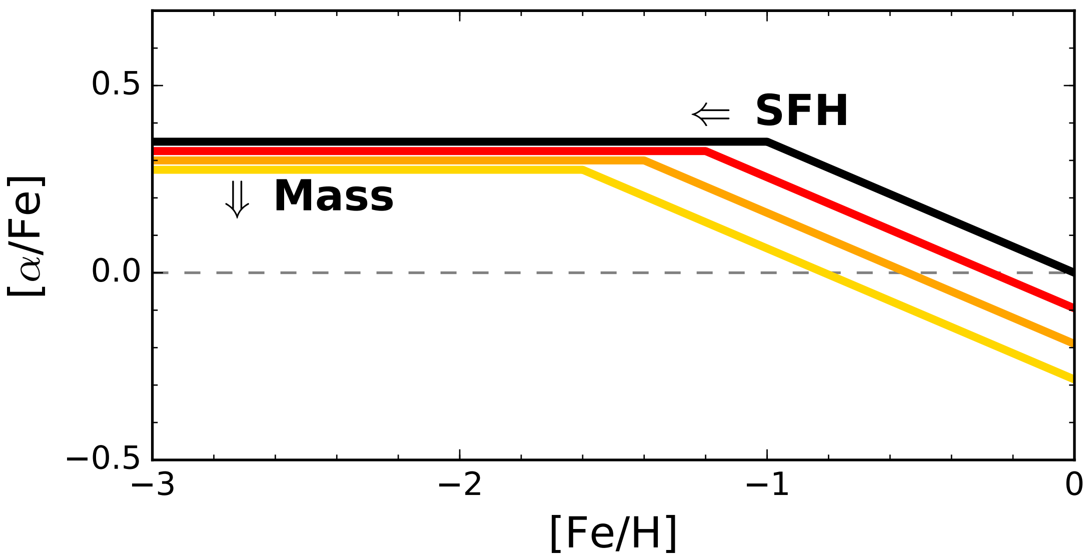

Figure 1.2 The schematic evolution of [α/Fe] with metallicity in the Milky Way (black line) and lower-mass dwarf galaxies (coloured lines). At low metallicities [α/Fe] does not evolve as the abundance ratio is set by the nucleosynthetic yields of massive stars. The metallicity at which [α/Fe] is no longer constant (i.e. the 'knee'; [Fe/H]≈ -1.0 in the Milky Way) is the time when lower-mass stars contribute to the production of Fe through Type Ia supernovae explosions. The height of the [α/Fe] plateau is effectively set by the mass of the galaxy, while the metallicity location of the knee is dependent on the star formation history (SFH).

(a reflection of the amount of star formation in a galaxy; Strateva et al., 2001; Baldry et al., 2004; Schawinski et al., 2014). Galaxies that are blue in colour tend to be less massive, actively forming stars, and disc-shaped, while redder galaxies are passive (i.e. minimal star formation rates) and tend to be spheroidal or elliptical in shape. How galaxies evolve from this blue, star-forming nature and become passive is poorly understood. The dearth of galaxies at an intermediate stage of star-formation (the so called 'green valley' galaxies) suggests that the evolutionary process(es) that truncate star formation are quick (Martin et al., 2007; Schiminovich et al., 2007; Gonçalves et al., 2012).

A notable feature from studying the environments in which star forming and passive galaxies are found, is that galaxies in denser environments (such as galaxy groups or clusters) tend to have higher mass but lower star formation rates (SFR) and gas content than galaxies in isolation (Dressler, 1980; Kauffmann et al., 2004; Baldry et al., 2006; Weinmann et al., 2006). A natural consequence of groups and clusters of galaxies due to the hierarchical assembly of the Universe are galaxy mergers. In terms of morphology, both simulations and observations have shown that the merging of two star-forming, disc galaxies results in a elliptical-like galaxy (e.g. Wright et al., 1990; Mihos & Hernquist, 1994). Studies of galaxies undergoing interactions have, relative to field galaxies of similar mass, increased SFRs (Lambas et al., 2003; Di Matteo et al., 2007; Patton et al., 2011; Knapen et al., 2015) with a dilution in metallicity, a likely result of gas funneling into the centres of galaxies (Kewley et al., 2006a; Ellison et al., 2008; Scudder et al., 2012; Torrey et al., 2012).

The regulation of galaxy growth

The large halt in star formation during galaxy evolution suggests a change in the amount of cold gas in the galaxy to form stars. One of the currently proposed mechanisms for removing gas from a galaxy is a process known as *feedback*. Although a galaxy can accrete material that flows down from filaments, galaxy feedback mechanisms stunt the growth of a galaxy by removing gas from within the galaxy and thus preventing future star formation. Energetic supernovae and stellar winds heat up and ionize the gas, pushing the material outside the galaxy (e.g. Shapiro & Field, 1976; Putman et al., 2012; Fox et al., 2016). Furthermore, feedback and other baryonic processes are required in galaxy evolution simulations in order to match the mass and frequency distribution of galaxies that is observed in large surveys (Scannapieco et al., 2012; Vogelsberger et al., 2014; Schaye et al., 2015).

Within the nucleus of many galaxies resides a super-massive black hole. The growth of this black hole is closely tied to the growth of the galaxy, leading to various scaling relations between the properties of the central nucleus and the galaxy (e.g. the black hole mass–velocity dispersion or black hole mass–bulge mass relations; Ferrarese & Merritt, 2000; Häring & Rix, 2004). For such tight relations to occur, the accretion of material onto the black hole is likely responsible for the regulation the growth of the host galaxy (or vice versa) with some sort of active galactic nuclei (AGN) feedback (for a review, see Fabian, 2012). The two main modes of AGN feedback reflect how the AGN interacts with the gas. In the 'quasar' (or 'radiative') mode, some of the accreted gas is blown out of the galaxy in the form of strong winds (e.g. Heckman et al., 2000; Veilleux et al., 2005), photoionizing the surrounding material. The 'radio' (or 'mechanical') mode uses the powerful AGN jets to mechanically heat the gas outside the galaxy, preventing the reservoirs of gas beyond the galaxy from returning to feed future star formation (McNamara & Nulsen, 2007).

1.4 Measuring the gas in and around galaxies

As described in the previous sections, the evolution of the Universe is heavily dependent on the interplay of gas, stars, and galaxies. However, one of the greatest challenges to constrain the interaction of gas with the rest of the Universe comes down to its detection. Gas excited by radiating sources do emit photons as electronic (atomic transitions) or rotational-vibrational (molecular transitions) states shift to lower energy states. Detecting this emitted light from the earliest epochs of the Universe becomes increasingly challenging as the detectable flux from the emitted light requires enormous telescopes and integration times. Furthermore, interpreting such a signal also requires an understanding of what the emitting source is, which is not known a priori. However molecular and atomic gas can be detected through the absorption of light at the corresponding transitions that excite the molecules or electrons (Kirchhoff, 1860). We are fortunate that the Universe has provided a natural, background light source in the form of quasars (further denoted QSOs) that can be seen to very early times ($z \approx 6$; Venemans et al., 2015). Furthermore, QSOs are bright across a large range of wavelengths, particularly in the rest-frame UV where many important atomic transitions occur, including the Lyman series lines of hydrogen. Thus, probing the evolution of the gas across cosmic time has usually been

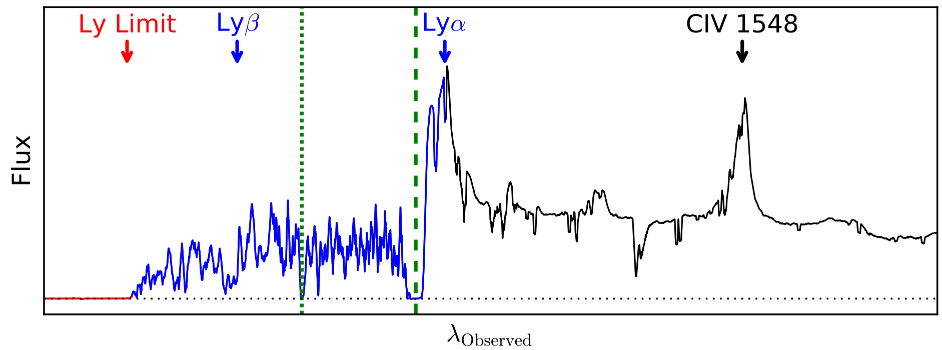

Figure 1.3 A mock QSO spectrum (at rest-frame UV wavelengths). Notable QSO emission lines are noted by the blue and black arrows at the top of the figure. The blue portion of the spectrum represents the Lyα forest, the region where the intergalactic medium absorbs high energy photons emitted by the QSO. The large decrement in flux at low wavelengths (the red-coloured spectrum) denotes the blanket absorption of all photons with energies greater than the ionizing potential of hydrogen (13.6 eV; i.e. the Lyman limit). The dotted and dashed green vertical lines denote two quasar absorption line systems identified by strong Lyα absorption, which are likely associated with two different galaxies.

done by using the imprinted absorption lines on top of a QSO spectrum (Figure 1.3). The corresponding collection of gas associated with the absorption lines are typically referred to *quasar absorption line systems* (QALs) or simply absorbers.

1.4.1 Quantifying the abundance of gas

The Voigt profile

The absorption lines imprinted on top of QSO spectra contain information about the number of atoms along the sightlines (typically referred to as the *column density*, and is measured in units of atoms cm^{-2}), and the temperature of the gas. Due to the finite lifetime of an electron occupying a given state (Δt), the Heisenberg uncertainty principle ($\Delta E \cdot \Delta t > \hbar/2$) dictates that the width of the absorption line (ΔE) is *naturally broadened.* The amount of natural broadening is dependent on the number of atoms present in the gas (and thus the column density), and is represented by a Lorentzian distribution. In addition, the random motions of the gas results in a distribution of particle velocities, further thermally broadening the absorption lines. This thermal, or Doppler, broadening is characterized by a Maxwellian or

Gaussian profile and is dependent on the gas temperature. The convolution of these two broadening mechanisms results in an absorption line from a single cloud of gas being describes as a Voigt profile. For an atomic absorption line at the rest-frame wavelength λ_0 (with oscillator strength f and natural damping parameter Γ; for a list of laboratory measurements or predictions see Morton, 2003; Cashman et al., 2017) , the absorption line profile in terms of optical depth (τ) at wavelength λ is given by:

$$\tau(\lambda) = \frac{\pi e_c^2 f}{mc} \frac{N}{\pi^{0.5} b} \int_{-\infty}^{\infty} \frac{e^{-y^2}}{(\frac{\Gamma \lambda_0}{4\pi b})^2 + (\frac{c}{b}(1 - \frac{\lambda}{\lambda_0}) - y)^2} dy, \tag{1.1}$$

where m and e_c are the mass and charge of the electron, c is the speed of light, N is the column density of gas, y is the velocity field of the gas, and b is the Doppler parameter. The Doppler parameter can be further refined in terms of the temperature of the gas T, namely $b = \sqrt{\frac{2kT}{m}}$; where k is the Boltzmann constant.

Equivalent widths and the curve of growth

In addition to the column density, a commonly-used metric for measuring the amount of absorption is the equivalent width. The equivalent width is defined as the width (in units of wavelength) of a rectangle with infinite optical depth such that the area of the rectangle is equal to the integral of the absorption line's profile (i.e. $\int e^{-\tau(\lambda)} d\lambda$; see left panel of Figure 1.4). The equivalent width is dependent on the column density, but the functional dependence varies with column density. The right panel of Figure 1.4 shows the nature of this dependence using a simulated Voigt profile of a Lyα line. When the line is unsaturated, the equivalent width is directly proportional to the column density. Upon saturation of the line, the equivalent width becomes mildly proportional to the column density, but is more dependent on the Doppler parameter (b). Once natural broadening is the dominant source of broadening (i.e. the Lorentzian component of the Voigt profile), the wings of the absorption profile are damped and are moderately sensitive to column density.

1.4.2 Classification of quasar absorption line systems

QALs are typically classified based on their column density of neutral hydrogen [i.e. logN(H I)]. The logN(H I) cuts used to separated classes of QALs are a combination of the level of saturation of the Lyman series (namely Ly α and the Lyman limit),

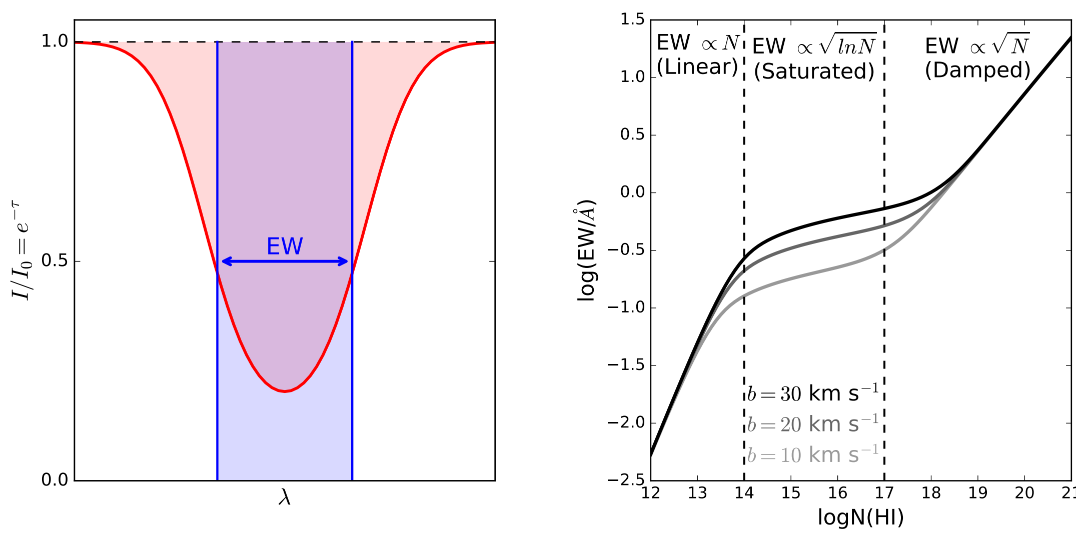

Figure 1.4 *Left panel:* A cartoon Voigt profile (red; in units of relative intensity). The equivalent width (EW; denoted by the blue arrow) of the absorption profile corresponds to the width of a rectangle (from I/I_0 of 0 to 1) whose area (blue shaded region) is the same as the area between the continuum ($I/I_0 = 1$; black dashed line) and the absorption line profile (red shaded region).
Right panel: The equivalent width as a function of column density (N) for a Lyα profile of a given Doppler parameter b (10, 20 and 30 km s^{-1}; lighter to darker curves respectively). The vertical dashed lines approximately separate the three regimes of the curve of growth; where the line profile is: unsaturated (left), saturated but not damped (middle), and saturated and damped (right).

the presence of damping wings, and whether the neutral gas is self-shielded[3] or of similar column density to the ISM of the Milky Way. The Lyα forest [14 $\lesssim$ logN(H I) $\leq$ 17] are clouds of gas that are optically thin ($\tau << 1$) at the Lyman limit, but are saturated in Lyα (thin blue absorption lines in Figure 1.3). The Lyα forest tends to probe the inter-galactic medium, and is often used to statistically measure the matter distribution in the Universe on large scales (Cen et al., 1994; Hernquist et al., 1996; Bi & Davidsen, 1997; McQuinn, 2016; Iršič et al., 2017a). The next step in logN(H I) column density corresponds to Lyman limit systems (LLS; logN(H I)$>$ 17), which refers to optically thick ($\tau \gtrsim 1$) Lyman limit absorption. LLS probe column densities of gas that are typically associated with galaxy structures, whether it is gas residing in the ISM or outskirts of galaxies (but still bound in its dark matter halo; Lanzetta et al., 1995a; Wakker & Savage, 2009; Prochaska et al., 2011; Lehner et al., 2013). LLS are often further classified into damped Lyα systems (DLAs; logN(H I)$\geq$ 20.3; Wolfe et al., 1986) and subDLAs (19.0 $\leq$logN(H I)$<$ 20.3), where these column densities limits denote the approximate column densities associated with strong damping wings (subDLAs; see Figure 1.4) and full self shielding[4] (DLAs; Wolfe et al., 1986, 2005). Historically, the logN(H I)$\geq$ 20.3 threshold for DLAs also corresponds to the approximate column density of the Milky Way's ISM, as DLAs were thought to be proto-Milky Way galaxies (Wolfe et al., 1986).

At optical wavelengths that are observable from the ground, the Lyα transition can only be observed for redshifts 1.5 $\lesssim z_{\rm abs} \lesssim$ 4.8. Identifying lower redshift systems without the need for space-based observations of the observed-frame UV transition requires the used of another absorption line associated with neutral gas. This wavelength limitation has led astronomers to use the strong Mg II doublet at rest-frame wavelengths of $\lambda\lambda$ 2796 Å and 2803 Å to identify absorbers, which can probe absorbers within the redshift range 0.2 $\lesssim z_{\rm abs} \lesssim$ 1.5 (Bergeron, 1986; Bergeron & Boissé, 1991; Bouché et al., 2006; Nielsen et al., 2013; Huang et al., 2016; Lan & Fukugita, 2017). The nature of these absorbers are unclear, as they span a large range in H I column densities (e.g. Rao & Turnshek, 2000; Rao et al., 2006)

[3]Self-shielding refers to the effect that, when the density of gas is large enough, the lifetime of the gas ionized from the external source is less than the time required to ionize all the gas. This resonance of absorption and re-emission of light keeps a large portion of the gas in a neutral state.

[4]Note that self-shielding effects can be observed down to column densities close to logN(H I)$\gtrsim$ 19.2 (Zheng & Miralda-Escudé, 2002).

DLAs

DLAs are of particular interest to understanding both the cosmic evolution of neutral gas reservoirs and metal enrichment. Although DLAs are relatively rare compared to their lower column-density counterparts, they contain the bulk of H I gas in the Universe (Lanzetta et al., 1995b; Prochaska et al., 2005; Noterdaeme et al., 2012), making them ideal tracers of the evolution of neutral gas. Furthermore, their self-shielding effects makes determining their metal abundances relatively straightforward as the bulk of metals remain in a single ionization state, so no ionization corrections are usually deemed necessary to obtain the total number of metals. DLAs thus provide a complementary study of chemical evolution, as their column densities provide an average measure of the metal abundance of many galactic systems, whereas stellar abundances are measured for many stars in few galactic systems. DLA abundances are typically more accurately measured than stellar abundances, as stellar abundances suffer from relying on a model stellar atmosphere to back out the measured equivalent widths into atomic number densities.

What are the absorbers?

The trade-off of measuring accurate column densities in QALs is that they are very difficult to image due to the bright background quasar blinding one from seeing the fainter galaxy along the line of sight. Although intials observations of DLAs suggested that these high H I column densities probed high-redshift, Milky Way analogues (Wolfe et al., 1986; Prochaska & Wolfe, 1997), the kinematics and chemical signatures are also consistent with lower mass, dwarf-like galaxies (Haehnelt et al., 1998; Cooke et al., 2015; Berg et al., 2015a). To better understand the morphological nature of DLA absorbers, clever techniques to remove the background quasar light have been used to image the absorbing galaxy. These techniques include:

- Angular differential imaging (Johnson-Groh et al., 2016). A technique pioneered for direct imaging of exo-solar planets (Marois et al., 2006). In summary, the telescope rotator is turned off while observing the background point source (QSO) and many short exposures are taken over a long period of time. Using the multiple exposures to accurately model the point spread function of the point source, the QSO light can be removed from the image to identify any projected nearby galaxies.

- Multiple, close DLAs along the same sightline (Fumagalli et al., 2015). This so-called double-DLA technique requires a pair of DLAs identified along the same QSO sightline, such that the absorption from the higher-redshift DLA partially obscures the QSO light, allowing for the detection of the foreground DLA.

- 2D spectral imaging (Péroux et al., 2011; Fynbo et al., 2013; Krogager et al., 2013; Jorgenson & Wolfe, 2014). With the advent of integral field spectroscopy, which can provide spectra for multiple position in a field of view, DLA absorbers can be positionally identified (Péroux et al., 2011; Jorgenson & Wolfe, 2014). Similarly, multiple emission spectra can be taken of the QSO with different position angles of the slit orientation on the sky to build up a 2D spectrum of the QSO (Fynbo et al., 2013; Krogager et al., 2013). Using these emission lines, one can obtain a model of the point spread function with wavelength and fit Lyα emission seen in 2D spectra.

- Cold, molecular gas imaging (Neeleman et al., 2016b, 2017). At rest-frame wavelengths where the molecular gas is emitting (i.e. sub-millimetre wavelengths), the contrast between the galaxy and QSO is heavily reduced. Until the recently commissioned Atacama Large Millimetre Array, this imaging technique was limited by the poor spatial resolution of sub-millimetre telescopes.

- Gamma ray bursts (Ellison et al., 2006). Rather than using a QSO as the background light source, intervening absorbers are fortuitously observed along sightlines towards gamma ray bursts. After the gamma ray burst fades, follow-up observations image the absorbing galaxy.

These imaging technique have typically shown that DLAs probe a variety of different morphologies (Fumagalli et al., 2015; Fynbo et al., 2013; Kashikawa et al., 2014), consistent with the kinematic and chemical signatures of dwarf and Milky Way-like galaxies.

1.5 Thesis Overview

This thesis concerns the study of galaxy evolution using quasar absorption line systems to probe the gas within and surrounding galaxies. Although DLAs dominate the H I content of the Universe, comparatively little attention has been paid to the slightly lower column density subDLA systems (e.g Péroux et al., 2005; O'Meara et al., 2007; Quiret et al., 2016). Chapter 2 takes advantage of a large, homogeneous, and absorber-blind dataset of QAL spectra to pinpoint the contribution of subDLAs to the overall H I budget of the Universe, and quantify the effects of selection biases of subDLAs and DLAs on this H I budget.

As described above, chemical evolution can be a useful tool to understand the evolution of stellar population of galaxies. Given the limitations of observing the galaxies responsible for the neutral gas absorption directly, Chapter 3 takes advantage of the detailed chemical abundances measured in DLAs to refine our understanding of the physical nature of DLA absorbers.

Feedback processes are an extremely important regulator of gas accretion and consumption in galaxies. AGN feedback in particular is thought to be one of the primary culprits in transforming star-forming galaxies into a passive state (e.g. Springel et al., 2005a; Schawinski et al., 2007; Fabian, 2012; Bluck et al., 2014, 2016), and should have a direct impact on the neutral gas reservoirs that surround galaxies (Tumlinson et al., 2017). Chapter 4 uses QALs to probe these gaseous surrounding AGN host galaxies to better define the connection between feedback and the gas reservoirs of galaxies.

The thesis concludes in Chapter 5 with a brief highlight of the main results from this work. These findings are used to motivate future work with both currently available and future telescope facilities.

Chapter 2

The cosmic evolution of HI

One of the best ways to characterize the evolutionary history of galaxies is through understanding the star formation history of the galaxies in question. Stars within galaxies compose key physical and chemical signatures which astronomers use to understand how galaxies evolve. To form stars however, galaxies need vast amounts of cold gas; thus observing the gas reservoirs of galaxies is key to studying how galaxies grow.

The bulk of neutral gas in the Universe is in the form of neutral hydrogen (H I), which typically only emits light at the 21 cm hyperfine transition. Due to the fainteness of the 21 cm emission, studies of H I gas have for the most part been limited to the current epoch ($z \approx 0$; Giovanelli et al., 2005; Zwaan et al., 2005) and thus is unable to provide a picture of gas evolution over a large portion of cosmic time. However, as QSOs are ubiquitous in the high redshift Universe, QALs provide an excellent tracer of the evolution of H I gas reservoirs over cosmic time.

In this chapter, I present the sample of DLAs and subDLAs selected from the XQ-100 legacy survey of 100 QSO sightlines. Using this sample of absorbing systems, I investigate the contribution of H I gas from subDLAs to the cosmic H I reservoirs that are more traditionally traced by DLAs. In addition, I introduce work on understanding the effects of using metal absorption lines to pre-select both subDLA and DLA systems, and discuss the potential biases in the evolution of H I introduced by these metal selection techniques. The identification of DLAs in the XQ-100 legacy survey was originally presented in Sánchez-Ramírez et al. (2016, on which I am a co-author), but I perform my own identification of DLAs in this chapter using a consistent method to homogenize the full absorber sample. The work on Mg II selection of DLAs was published in Berg et al. (2017), and relies on XQ-100 data previously published in Berg et al. (2016, see Chapter 3 for more details). The work on subDLAs will appear in a future publication (Berg et al., in prep.). To be consistent with the previous work on the evolution of H I reservoirs, in this chapter I assumed a flat ΛCDM Universe with $H_0 = 70$ km s^{-1} Mpc^{-1} and $\Omega_M = 0.3$.

2.1 Quantifying the HI content of quasar absorbers

To quantify the contribution of quasar absorption line systems to the H I content of the Universe, one needs to assess the number of absorption line systems of a given H I column density [N(H I)] and absorption redshift ($z_{\rm abs}$). This quantity, known as the column density distribution function ($f(N,X)$), is defined as

$$f(N,X)dNdX = \frac{m_{\rm abs}}{\Delta N \times \sum_i^{n_{\rm QSO}} \Delta X_i} dNdX, \tag{2.1}$$

where $m_{\rm abs}$ is the total number of absorbers with column densities between $N - \Delta N/2$ and $N + \Delta N/2$ along the observed absorption distance ΔX_i of the i^{th} QSO sightline, and $n_{\rm QSO}$ is the number of QSO sightlines observed. The absorption distance ΔX_i is the total redshift path covered by the sightline, and is computed on a sightline-by-sightline basis using

$$\Delta X(z) = \int_{z_{min}}^{z_{max}} (1+z)^2[\Omega_M(1+z)^3 + \Omega_\Lambda]^{-0.5} dz, \tag{2.2}$$

where z_{min} and z_{max} are the minimum and maximum redshift observed along the QSO path, while Ω_M and Ω_Λ are the matter and dark energy densities of the Universe observed at the current epoch. z_{max} is typically set by the emission redshift of the QSO ($z_{\rm em}$).

Although $f(N,X)$ contains all the necessary information to understand how the number of H I absorbers evolve with time, the more commonly-used metric to assess the contribution of H I contained in QSO absorption systems is the comoving mass density of neutral gas ($\Omega_{\rm HI}$), and is defined as

$$\Omega_{\rm HI}(X) = \frac{H_0 m_H}{c\rho_0} \int_{N_{min}}^{N_{max}} N f(N,X) dN = \frac{H_0 m_H}{c\rho_0} \frac{\sum_j^{m_{\rm abs}} N_i}{\sum_j^{n_{\rm QSO}} \Delta X_i} \tag{2.3}$$

where H_0 is the Hubble constant at the current epoch, c is the speed of light, m_H is the atomic mass of hydrogen, and ρ_0 is the critical density of the Universe ($\rho_0 = \frac{3H_0^2}{8\pi G}$

for a flat Universe; where G is the gravitational constant).

The cosmic evolution of DLAs

Of the many classes of QALs, DLAs are the highest H I column density absorbers, defined as having log N(H I)$\geq$ 20.3 (Wolfe et al., 1986, 2005). Although fewer in number compared to lower N(H I) counterparts (such as subDLAs; 19.0 $<$logN(H I)$<$ 20.3), DLAs dominate the H I column density distribution from $z_{abs}\sim$ 5 to the present epoch and are used to trace the cosmological gas density of H I (Ω_{HI}), eventually fueling future generations of star formation (Lanzetta et al., 1995b; Rao & Turnshek, 2000; Storrie-Lombardi & Wolfe, 2000; Péroux et al., 2003b; Prochaska et al., 2005; Rao et al., 2006; Prochaska & Wolfe, 2009; Noterdaeme et al., 2012; Zafar et al., 2013a; Crighton et al., 2015; Neeleman et al., 2016a; Sánchez-Ramírez et al., 2016). At absorption redshifts where the H I is observed in optical bands (1.5 $\lesssim z_{abs}\lesssim$ 4.7), Ω_{HI} remains relatively constant with redshift (for the most recent results at these redshifts, see Crighton et al., 2015; Sánchez-Ramírez et al., 2016). At $z\sim 0$, Ω_{HI} is currently best measured from 21 cm emission line surveys of galaxies (Zwaan et al., 2005; Martin et al., 2010). Between these $z\sim 0$ measurements and Ω_{HI} measured in DLAs at $z\sim 1.5$, the gas content of galaxies has only evolved by a factor of ~ 2 (Zwaan et al., 2005; Sánchez-Ramírez et al., 2016, see grey shaded region and solid circles in Figure 2.1). This shallow evolution in Ω_{HI} (which, upon cooling into molecular gas, is thought to be the fuel for star formation) is in stark contrast with the rapid, order of magnitude decline in the cosmic star-formation rate density over the same epoch (Madau & Dickinson, 2014). To explain the discrepancy between the two quantities, it has been been suggested that H I reservoirs in galaxies are being replenished by the intergalactic medium to maintain the density in a steady state (Lanzetta et al., 1995b; Prochaska et al., 2005; Noterdaeme et al., 2012; Zafar et al., 2013a; Sánchez-Ramírez et al., 2016).

Despite well constrained estimates of Ω_{HI} at $z\sim 0$ and at $z>2$, studying the nature of the Ω_{HI} evolution between 0.3 $\lesssim z_{abs}\lesssim$ 1.5 is challenging, as the Lyα transition shifts into the UV, requiring expensive space-based observations; and 21 cm emission becomes extremely difficult to detect at intermediate redshifts (Rhee et al., 2016). In an effort to improve the efficiency of space telescope observations, it has become common practice to pre-select candidate DLAs based on the rest-frame equivalent widths of the associated Mg II $\lambda\lambda$ 2796, 2803 Å absorption observed in the optical

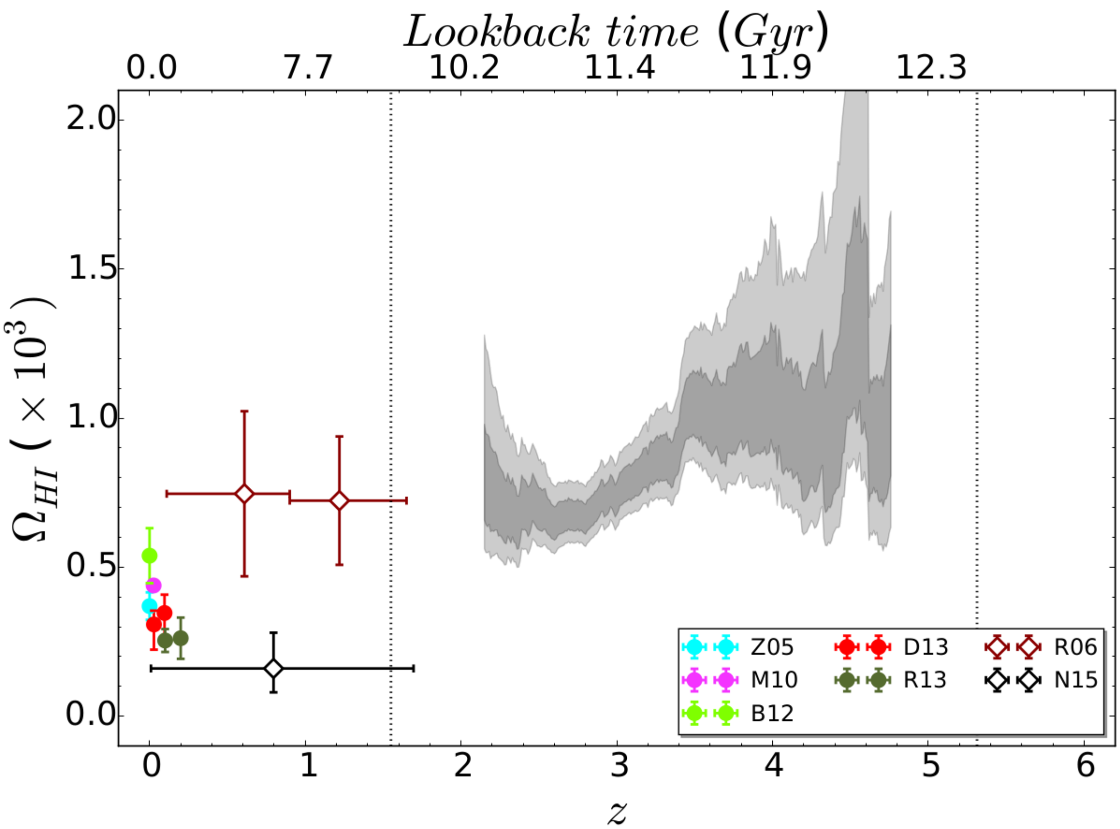

Figure 2.1 The cosmic evolution of $\Omega_{\rm HI}$ as probed by DLAs. The grey shaded region denotes the high redshift DLA sample from Sánchez-Ramírez et al. (2016), while the black and red diamonds denote intermediate redshift DLA measurements from Neeleman et al. (2016a) and Rao et al. (2006), respectively. The $z \approx 0$ measurements from various radio surveys are denoted by the filled coloured circles. Figure taken with permission from Sánchez-Ramírez et al. (2016).

(Rao & Turnshek, 2000; Rao et al., 2006). $\Omega_{\rm HI}$ derived from $z_{\rm abs}\sim 1$ DLA samples pre-selected from Mg II ($\Omega_{\rm HI}\sim 7.5\times10^{-3}$) is consistent with the $z_{\rm abs}\gtrsim 2$ value, implying strong evolution at the lowest redshifts (Rao et al., 2006, red diamonds in Figure 2.1). However, a recent 'blind' archival survey of DLAs at $z\sim 1$ derived a value of $\Omega_{\rm HI}$ a factor of 3 lower than Rao et al. (2006, $\sim 2.5\times10^{-3}$), and is consistent with 21 cm results at $z\sim 0$ (Neeleman et al., 2016a, black diamond in Figure 2.1). This tension in $\Omega_{\rm HI}$ has led to suggestions that Mg II DLA pre-selection may be biased, possibly leading to high $\Omega_{\rm HI}$ (Péroux et al., 2004; Dessauges-Zavadsky et al., 2009; Neeleman et al., 2016a).

The cosmic evolution of subDLAs

Although DLAs dominate $f(N,X)$ over a large range of redshifts (Wolfe et al., 2005; Prochaska et al., 2005; Noterdaeme et al., 2012), subDLAs (19.0 $\leq$logN(H I)$<$ 20.3) are also thought to host a modest contribution of the H I gas of in the Universe. The trouble with using subDLAs to probe the neutral gas reservoirs of the Universe is that these systems are often not completely self-shielded from the cosmic UV background, and thus do not completely trace neutral gas reservoirs (e.g. Zheng & Miralda-Escudé, 2002; O'Meara et al., 2007). Nevertheless, there has been a substantial body of working calculation the contribution of H I from subDLAs to f(N,X) and $\Omega_{\rm HI}$ (Péroux et al., 2003b,a, 2005; O'Meara et al., 2007; Guimarães et al., 2009; Zafar et al., 2013a), as well as understanding whether subDLAs probe different types of gaseous systems than DLAs (Péroux et al., 2003a; Kulkarni et al., 2007; Dessauges-Zavadsky et al., 2009; Quiret et al., 2016). Early work had suggested a distinct evolution in $f(N,X)$, where more subDLAs were present at higher redshifts (Péroux et al., 2003b,a; Zafar et al., 2013a), although other studies have only detected this evolution at $\leq 2\sigma$ confidence (O'Meara et al., 2007; Guimarães et al., 2009). If such a redshift evolution exists in $f(N,X)$ for subDLAs, this would imply that subDLAs become more important at high redshifts ($z_{\rm abs}> 3.5$) and contribute more than $\approx 10-20\%$ of $\Omega_{\rm HI}$ traced solely by DLAs (Péroux et al., 2005; Guimarães et al., 2009; Zafar et al., 2013a).

2.2 The XQ-100 survey and its intervening absorbers

2.2.1 Survey design and data reduction

The XQ-100 Legacy Survey (PI S. López) observed 100 QSO sightlines at redshift $z_{em}\sim 3.5$–4.5. with the X-Shooter Spectrograph Vernet et al. (2011) on the Very Large Telescope (VLT) in Chile. The XQ-100 survey was designed to cover many science cases, including: measuring the Lyα forest with moderately high resolution at large redshifts (Iršič et al., 2017a,b), observing the proximity effect of gas near to QSOs (Perrotta et al., 2016), and studying the properties of the QSOs themselves. As a bonus to addressing these science cases, the QSOs were purposefully chosen to be blind to any intervening absorption line systems; thus providing a nearly random sample of sub-DLAs and DLAs to study the cosmological implications of these intervening absorbers (Sánchez-Ramírez et al., 2016; Berg et al., 2016, 2017; Christensen et al., 2017). For more details about the science cases and survey design, see López et al. (2016).

The X-Shooter spectrograph is built with three pick-off arms (i.e. a blue [UVB], visible [VIS], and near-infrared [NIR] arm) to provide simultaneous wavelength coverage from the near UV (3150 Å) to the NIR (25000 Å) at a full width at half maximum (FWHM) resolution R$\sim$5000–9000. For each QSO in the XQ-100 survey, the per-arm exposures were either $\sim$ 0.5 or $\sim$ 1 hour in length (depending whether the QSO was classified as 'bright' or 'faint'; respectively), providing signal-noise ratios of $\sim$ 20 pixel^{-1} (median $\sim$ 30 pixel^{-1}). The spectra for each arm were reduced using an internal IDL package by G. Cupani and G. Becker. For more details on the data reduction, see López et al. (2016).

Continuum fitting

From the extracted, 1-dimensional X-Shooter spectra, I created by-hand fits to the continuum using a cubic spline[1]. In brief, the input spline points were selected by-hand as regions where the QSO emission flux appeared to be free of any absorption lines. The typical spline points are separated by $\sim 20-40$ Å, although regions close to QSO emission lines or large variations in the continuum level contain a higher

[1] Code available at `https://github.com/trystynb/ContFit`.

density of points to capture the change in the continuum's slope. As the Lyα forest and intervening gas clouds along every sightline partially absorb all QSO photons below the Lyman limit, the QSO's flux is systematically absorbed for all wavelengths below the corresponding observed Lyman Limit at the redshift of the QSO ($\lambda_{LL} = (1 + z_{\rm em}) \times 911.7633$ Å), making accurate continuum placement difficult. For this reason, the continuum was artificially set to a constant high value for wavelengths below λ_{LL}; this wavelength regime is consequently not used for the work presented in this chapter. Both the science and error spectra were then normalized by the resulting spline-fitted continua.

2.2.2 Identification of intervening absorbers

Using my by-hand continuum-normalized XQ-100 spectra, I visually identified candidate subDLAs and DLAs. This identification was done by carefully scrolling through the XQ-100 spectra from the Lyα emission of the QSO to λ_{LL} and searching for saturated absorption broad enough to fit a simulated Lyα Voigt profiles of column density logN(H I)$\geq$ 18.8 (assuming a typical Doppler parameter of $b = 10$ km s^{-1}; e.g. Dessauges-Zavadsky et al., 2003). Simultaneously, a simulated second order Lyman series line profile (i.e. Lyβ) was checked at the corresponding wavelength. For each of these saturated regions identified, one or more Voigt profiles were fitted by adjusting logN(H I) and $\rm z_{abs}$ until the modelled Lyα and Lyβ Voigt profiles matched the continuum-normalized spectra. If required, the original continuum fits were simultaneously adjusted to best fit the data. These continuum adjustments were common for large column density absorption systems on top or near QSO emmission lines. In many of these adjustments, the best-fit column logN(H I) was constrained by the corresponding Lyβ profile. Errors on the logN(H I) column density were estimated as the minimum and maximum possible logN(H I) that would also be a reasonable fit. Given the signal-noise of the spectra, the typical error on logN(H I) is about $\pm$0.2 dex. For cases where the continuum was uncertain, the assigned logN(H I) error was increased to match this uncertainty in the continuum placement.

To ensure higher redshift Ly series lines were not confused with lower redshift Lyα absorption, a full model spectrum was generated to keep track of all absorption along each sightline. Upon identifying a new absorber, the associated Voigt profiles for several key Lyman series lines (Lyα, Lyβ, Lyγ, and Lyδ) were added to the full model spectrum. The identification of systems was terminated when the observed-frame wavelength of additional Lyα absorbers was shorter than λ_{LL}.

Given the modest resolution of the XQ-100 spectra, it is difficult to disentangle regions of extended saturated absorption without the constraining characteristic of Voigt profile wings on either side of the profile. In these cases, it is possible that one or more subDLAs could fit these regions, but was also degenerate with several smaller LLS clouds. Unless a higher-order Ly series line could disentangle this degeneracy, no candidate absorbers were fitted to the data in these degenerate regions.

Once this identification process was complete, the list of obtained absorption line systems was cleaned by adjusting or removing any absorbing systems whose Ly series lines (down to Lyδ) did not fit the continuum normalized spectra. The final cleaned sample of identified candidate absorbers consists of 131 18.8 $\leq$logN(H I)$<$ 19.0 LLS, 194 sub-DLAs and 33 DLAs. Table A.1 contains the full list of 358 candidate absorbers, including their $z_{\rm abs}$ and logN(H I), while Figures A.1 – A.15 show the Lyα absorption line profiles and best-fitting H I Voigt profiles for all the candidate absorbers.

Comparison to Sánchez-Ramírez et al. (2016)

In Sánchez-Ramírez et al. (2016), Rubén Sánchez-Ramírez previously identified 41 DLAs in the XQ-100 sample using a similar absorber identification method, but using different continuum fits over a slightly longer redshift path. Note that the redshift path in Sánchez-Ramírez et al. (2016) was not truncated at λ_{LL} but extended to lower wavelengths until the QSO emission flux was completely wiped out by Lyman limit absorption; as a result their search includes eight more DLAs. As previously unidentified subDLAs were fitted also, it was important that I used the same continuum fits for both the DLA and subDLA identification. All of the Sánchez-Ramírez et al. (2016) DLAs within the same redshift range were recovered, and their column densities are consistent (within the H I column density errors) with those that I derived. The largest discrepancies occurred in regions where the continuum is difficult to constrain, such as systems that are nearby the background QSO as part of the Lyα emission line is absorbed. Unless stated otherwise, I continue to use the logN(H I) measurements presented in this chapter for the XQ-100 DLAs.

Recovery test

To assess the completeness of the visual identification process and ensure that the modest XQ-100 spectral resolution did not affect the determination of column densities, an absorption line recovery test was necessary. To ensure the Lyα forest statistics and X-Shooter instrumental effects are reproduced while maintaining the same continuum fits used in the original identification process, artificial absorption systems were randomly inserted into the XQ-100 spectra.

Prior to insertion, a list of artificial systems was first generated to ensure that an approximately uniform distribution of column densities was used. In bins of column density from logN(H I)= 18.0 to 20.3[2] (in steps of 0.1 dex), 15 ± 3 systems of that column density were generated. A random number of systems (~ 350) was generated to prevent subconscious counting during the recovery process. For each of these fake systems, a model Ly series (down to Lyδ) spectrum was generated, and randomly inserted into one of the XQ-100 QSO spectra at a random redshift. To simulate noise in the model spectrum, the flux of the model spectra was then varied randomly using the XQ-100 error spectrum flux as the standard deviation of a Gaussian distribution. Between 0 and 7 absorption systems were assigned to each XQ-100 sightline.

The identification process described above was repeated on the spectra with fake absorbers inserted, starting with the locations of the previously-identified real absorbers flagged in the model spectra. The left panel of Figure 2.2 shows the column density distribution of fake systems inserted into the XQ-100 spectra (with observed-frame Lyα absorption at wavelengths larger than λ_{LL}; grey line). The solid red bars indicate that I missed seven, logN(H I)$\leq$ 19.2 systems in my recovery analysis. However, the three missed systems with the higher column densities (logN(H I)$\geq$ 18.9) happened to be randomly inserted ontop of already identified, larger Lyα absorbers. Since the H I contribution from real overlapping systems would have already be accounted in the original fit to the larger H I systems, I do not include these three missed systems in the recovery rate derivation; therefore only systems with logN(H I)= 18.8 were missed in the recovery analysis.

For all the recovered systems, the right panel of Figure 2.2 shows the difference in logN(H I) between the measured column density of the fake absorber (N_{Meas}) and the randomly generated value (N_{Fake}). All but ten of the recovered systems (2% of the

[2] The recovery rate for DLAs in the XQ-100 dataset was previously measured at 100% in Sánchez-Ramírez et al. (2016). Given that I recovered all the previously identified DLAs, higher column densities do not need to be tested.

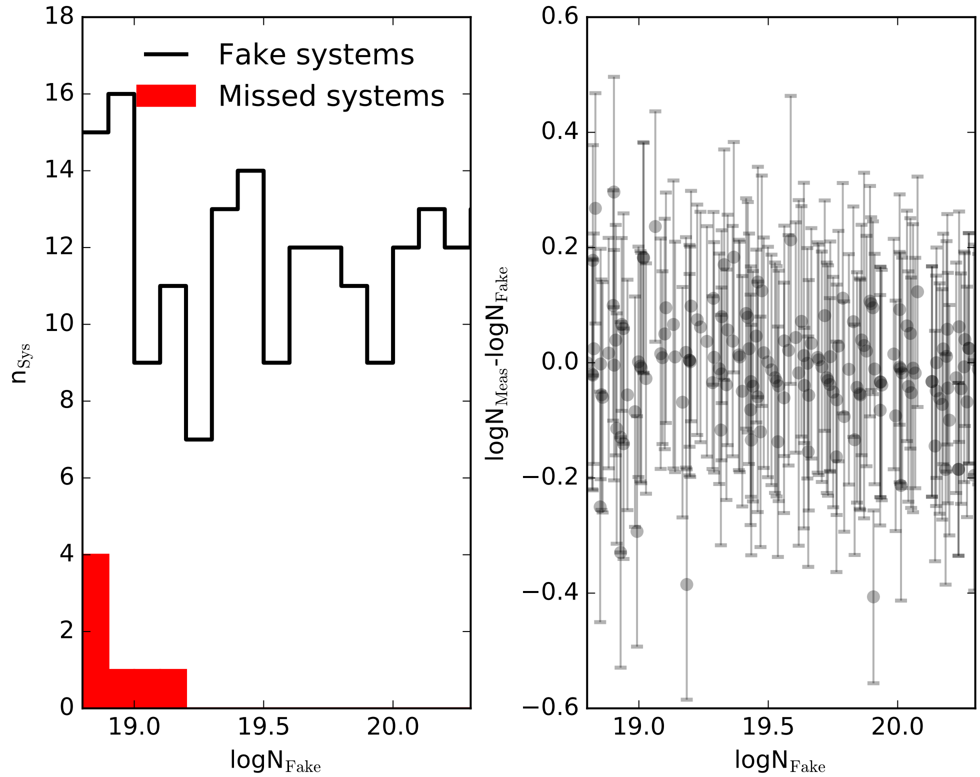

Figure 2.2 *Left panel:* Distribution of the number of fake systems of a given logN(H I) used for the recovery test (grey line) and those systems that were missed in the recovery process. Note that only systems whose Lyα is beyond $\geq \lambda_{LL}$ are included in this plot. *Right panel:* The difference in measured and fake logN(H I) column densities (i.e. $\log N_{\rm Meas}$-$\log N_{\rm Fake}$) as a function of the fake logN(H I) value.

total number of systems) have consistent column densities with $N_{\rm Fake}$. For these ten systems, the column densities are only inconsistent by ~ 0.1 dex, which is statistically consistent with the random flux errors inserted into the fake model spectra.

In summary, the H I recovery test was successful in measuring and identifying absorbers; and suggests my identification of XQ-100 absorbers is 100% complete for logN(H I)≥ 18.9, and 73% complete for logN(H I)$= 18.8$.

False positives and metal lines

In addition to ensuring that all the subDLAs and DLAs were identified in the XQ-100 dataset, it is possible that two closely-separated LLS or Lyα forest clouds can mimic a low column density subDLA, leading to falsely identified subDLA systems. The common method to remove these 'false positive' absorbers from a sample is to check higher order Ly series lines or metal lines associated with the absorber, particularly using high resolution data (Péroux et al., 2003a; O'Meara et al., 2007; Zafar et al., 2013a). However, for low-to-modest resolution spectra or low redshift absorption systems, the Ly series lines are difficult to separate from the blanket Lyman limit absorption, or the Lyβ forest. For this reason, previous studies have tended to use strong metal lines (such as C IV, Mg II, or Fe II) to confirm these systems. However, this metal line selection may artificially remove metal-poor systems with weak or no metal lines that are not easily identified, and thus lead to a biased absorber sample.

From the full sample (further abbreviated as FS) of candidate absorption systems with logN(H I)$\geq$ 18.8, I identified a subsample of metal-confirmed absorbers (further denoted as MS), where at least one of the following ionic species is detected: C IV ($\lambda\lambda$ 1548 Å & 1550 Å), Mg II ($\lambda\lambda$ 2796 Å & 2803 Å), or Fe II (λ 2344 Å, 2382 Å, & 2600 Å). Of the 358 candidate systems identified, only 149 have confirmed metals lines, with all all DLAs having detected metal lines. The systems with observed metal lines are identified in the 'Metal?' columns of Table A.1. Figure 2.3 shows the distribution of logN(H I) and $z_{\rm abs}$ for the FS (grey circles) and MS (red diamonds) absorbers. It is clear that the metal selection process preferentially removes low redshift, logN(H I)$\leq$ 19.4 candidate absorbers from the FS. I note that this high number of metal-deficient candidate absorbers identified at low redshift is in contrast with the metallicity enrichment of the Universe, where metal-poor absorbers tend to be found at higher redshifts (Pettini et al., 1999; Rafelski et al., 2014; Quiret et al., 2016).

To better understand whether the XQ-100 spectra have the capability of detecting low N(H I), metal-poor absorbers, I computed the signal-noise ratio (snr) required to detect a metal line absorption line (with rest-frame wavelength λ and oscillator strength f), at 3σ significance, for an absorber with metallicity [M/H] using

$$snr = \frac{3 m_e c \; FWHM}{\pi e_c^2 f \lambda^2} \left(N(H\ \text{I}) 10^{[M/H] + log\left(\frac{n_{\text{M}_\odot}}{n_{\text{H}_\odot}}\right)} \right)^{-1}. \tag{2.4}$$

Equation 2.4 assumes the metal line is detected at the corresponding full width half-maximum ($FWHM$; measured in the observed frame) of the instrumental resolution of the NIR arm ($R = 5300$). Note that at higher resolutions, the $FWHM$ term in

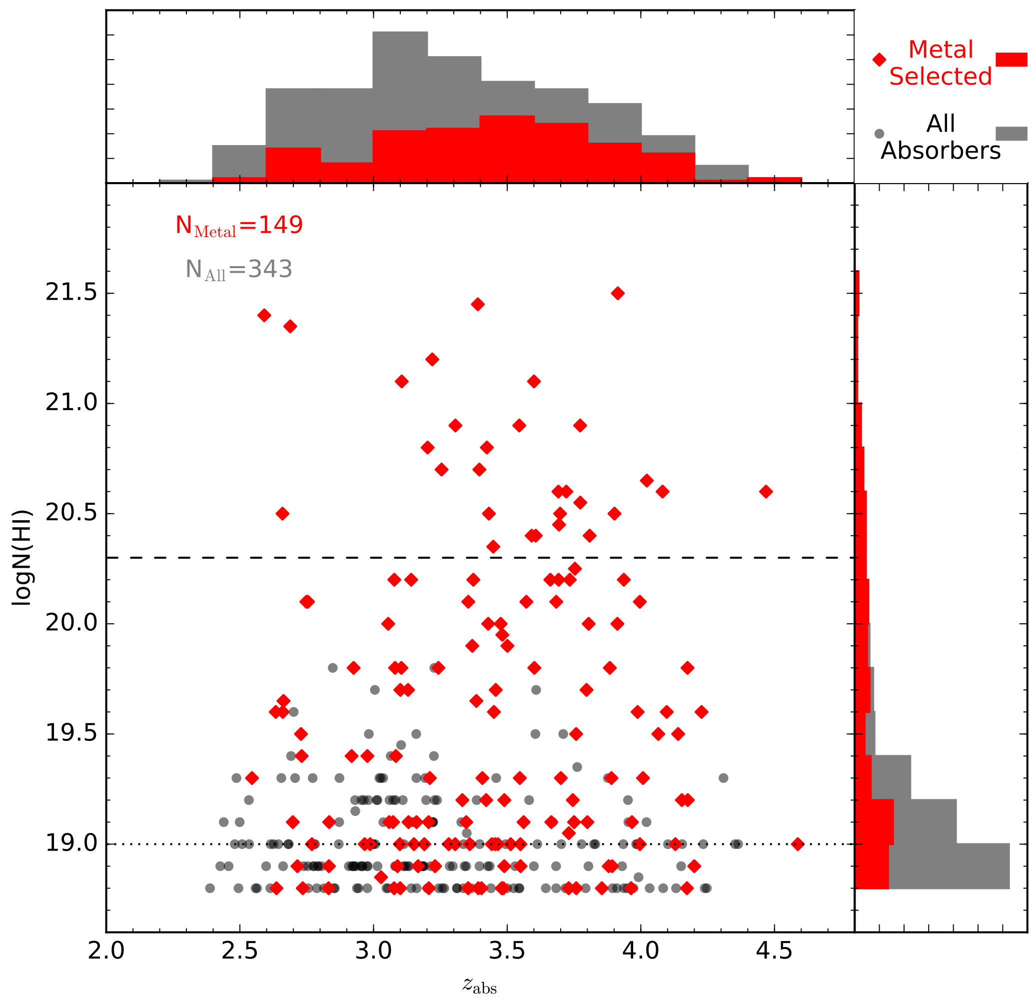

Figure 2.3 The H I column density (logN(H I) of all candidate XQ-100 absorbers (grey circles) as a function of their redshift (z_{abs}). The red diamonds indicate the XQ-100 MS absorbers. The total number of absorbers (N) for each sample are given in the top left corner of the main panel. The distributions of z_{abs} and logN(H I) are given in the top and right-most panels, using the same colour scheme for the two subsamples. For reference, the dotted and dashed horizontal lines denote the column density thresholds for subDLAs and DLAs (respectively).

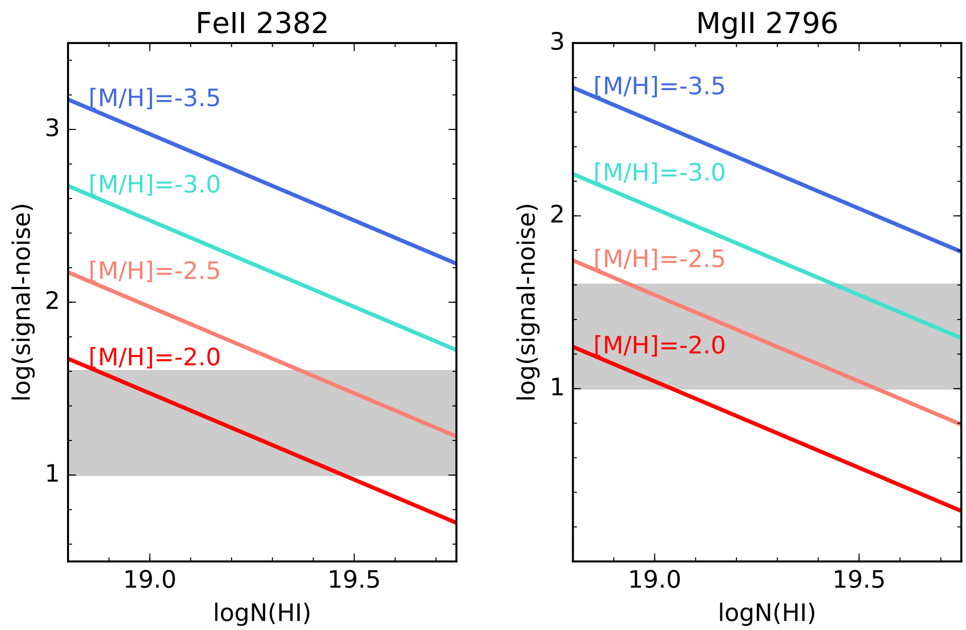

Figure 2.4 The predicted spectral signal-noise required to observe the metal lines Fe II λ 2382 Å (left panel) and Mg II λ 2796 Å (right panel) as a function of absorber logN(H I). A range in metallicities is represented by the different coloured lines. The typical range in signal-noise of the XQ-100 spectra is denoted by the light grey region.

Equation 2.4 is dictated by the smallest width of the line rather than the instrumental resolution.

Figure 2.4 shows the range of signal-noise required to detect the two strong metal lines Fe II λ 2382 Å (left panel) and Mg II λ 2796 Å (right panel) as a function of absorber logN(H I) and metallicity ([M/H]; coloured lines). For the typical range of signal-noise in the XQ-100 spectra (grey shaded region in Figure 2.4), the XQ-100 spectra can only detect metal lines down to [M/H]$\gtrsim -2.5$ for the typical subDLA absorber not included in MS (logN(H I)$\leq$ 19.4). Few subDLAs have previously been detected with [M/H]> -2 (Quiret et al., 2016). However the lack of low-metallicity subDLAs could be a result of metal-line selection effects, particularly as DLAs can probe down to [M/H]≈ -3.0 (Cooke et al., 2015; Quiret et al., 2016). Although this metal selection technique does not fully assess the false positive rate, the total number of genuine absorbers present in the XQ-100 samples should be bounded by the FS and MS absorbers.

2.3 The cosmic evolution of neutral gas

As stated in Section 2.1, the two key quantities for understanding the contribution of H I from subDLAs and DLAs are $f(N, X)$ and $\Omega_{\rm HI}$. In Sánchez-Ramírez et al. (2016), we originally computed both these quantities for the XQ-100 DLA sample and analyzed the evolution of $\Omega_{\rm HI}$. In this section, I will present the added information obtained from calculating $f(N, X)$ and $\Omega_{\rm HI}$ from the XQ-100 subsample. As in Sánchez-Ramírez et al. (2016), I restrict the XQ-100 sample to exclude systems with an absorption redshift within 5000 km s^{-1} of the QSO emission redshift. These proximate systems likely trace a different population of systems compared to their intervening counterparts, (Ellison et al., 2002, 2010; Berg et al., 2016; Perrotta et al., 2016) and are typically ignored when computing $\Omega_{\rm HI}$. To properly measure $f(N, X)$ for DLAs, a sample size much larger than the 33 DLAs identified in the XQ-100 sample must be used in order to statistically probe the high column density end of $f(N, X)$ (logN(H I)$>$ 21.5). I thus combined the XQ-100 DLA sample with literature sample of Sánchez-Ramírez et al. (2016), which consists of 1019 DLAs measured in various literature surveys across a redshift range of 1.6 $<z_{\rm abs}<$ 5.1. It is important to note that this supplementary DLAs sample does not include any subDLAs, and probes a very different redshift path than the XQ-100 subDLAs. For this reason, I will continue to separate the entire XQ-100 absorber sample into DLAs and subDLAs in the rest of this analysis.

2.3.1 The contribution of subDLAs to the HI budget

Monte Carlo Bootstrap re-sampling

To estimate the errors in deriving $f(N, X)$ and $\Omega_{\rm HI}$ from the XQ-100 dataset, the Monte Carlo bootstrap (further abbreviated MCB) resampling technique presented in Sánchez-Ramírez et al. (2016) was used. This technique provides a robust method of combining the random errors quantified for measurements (such as logN(H I)) with the sampling errors inherent to a relatively small sample size. In essence, the MCB method takes the original absorber N(H I) distribution and duplicates the sample a large number of times to create $N_{\rm samp}$ simulated mock surveys. For each mock survey, the logN(H I) of each absorbers is randomly varied within its error-bar (assuming a Gaussian error distribution) to create a 'new' set of logN(H I) measurements. From this new set of measurements, absorbers are randomly drawn (with replacements) until a new mock survey is generated with the same number of absorbers. As the drawing of values is done with replacement, this mimics the effect of sampling errors by randomly excluding or duplicating absorbers in the sample. The choice of N_{samp} is arbitrary, but needs to be very large ($\gtrsim 10000$) in order to provide a robust statistical sample.

As the XQ-100 absorber sample is split into two subsamples based on column density (subDLAs and DLAs), the MCB technique also needs to take into account the effects of removing/including systems that could be misclassified into the wrong H I absorber type (e.g. a subDLA with a measured logN(H I)$= 20.1 \pm 0.2$ could be a DLA in reality). By design, this misclassification effect is naturally implemented by the random variation in logN(H I) for each resampling. However, as the supplementary literature sample does not contain subDLAs and covers a different redshift path; only absorbers along XQ-100 sightlines are included in the sub-DLA sample, even if the supplementary literature absorber would be classified as a subDLA.

Quantifying $f(N, X)$

Using the MCB resampling of the XQ-100 and supplementary DLA samples, $f(N, X)$ was computed. Rather than using the standard bins of column density, which can hide or amplify features depending on the choice of bin, I elected to use a sliding logN(H I) bin to quantify the median $f(N, X)$ in each column density bin. The sliding bin keeps a fixed bin width, but the centre of the bin shifts by a small amount in each step to capture the effects of individual data being included and excluded from the bin. Using a logN(H I) bin width of 0.4 dex, I computed the median, 1σ and 2σ percentiles of the underlying $f(N, X)$ distribution of the 10 000 MCB samples. For the subDLAs, the centre of the bin starts at logN(H I)$= 19.2$ (such that bin edge includes logN(H I)$= 19.0$), and is then shifted by 0.05 dex until the the centre of the bin reaches logN(H I)$= 20.1$ (such that bin edge includes logN(H I)$= 20.3$). The same is done for the DLAs, but using logN(H I) bin centres from 20.5 to 21.8. Note that the sliding bins of both the DLA and subDLA samples do not pass the logN(H I)$= 20.3$ threshold due to the different redshift path coverage of the two samples. The computation of $f(N, X)$ is repeated using both the FS and MS absorbers from XQ-100.

Figure 2.5 shows the resulting median column density distribution functions of DLAs and subDLAs (solid lines) for the FS (top panel) and MS absorbers (bottom panel) in XQ-100. The 1σ and 2σ are shown as the dark and light shaded regions

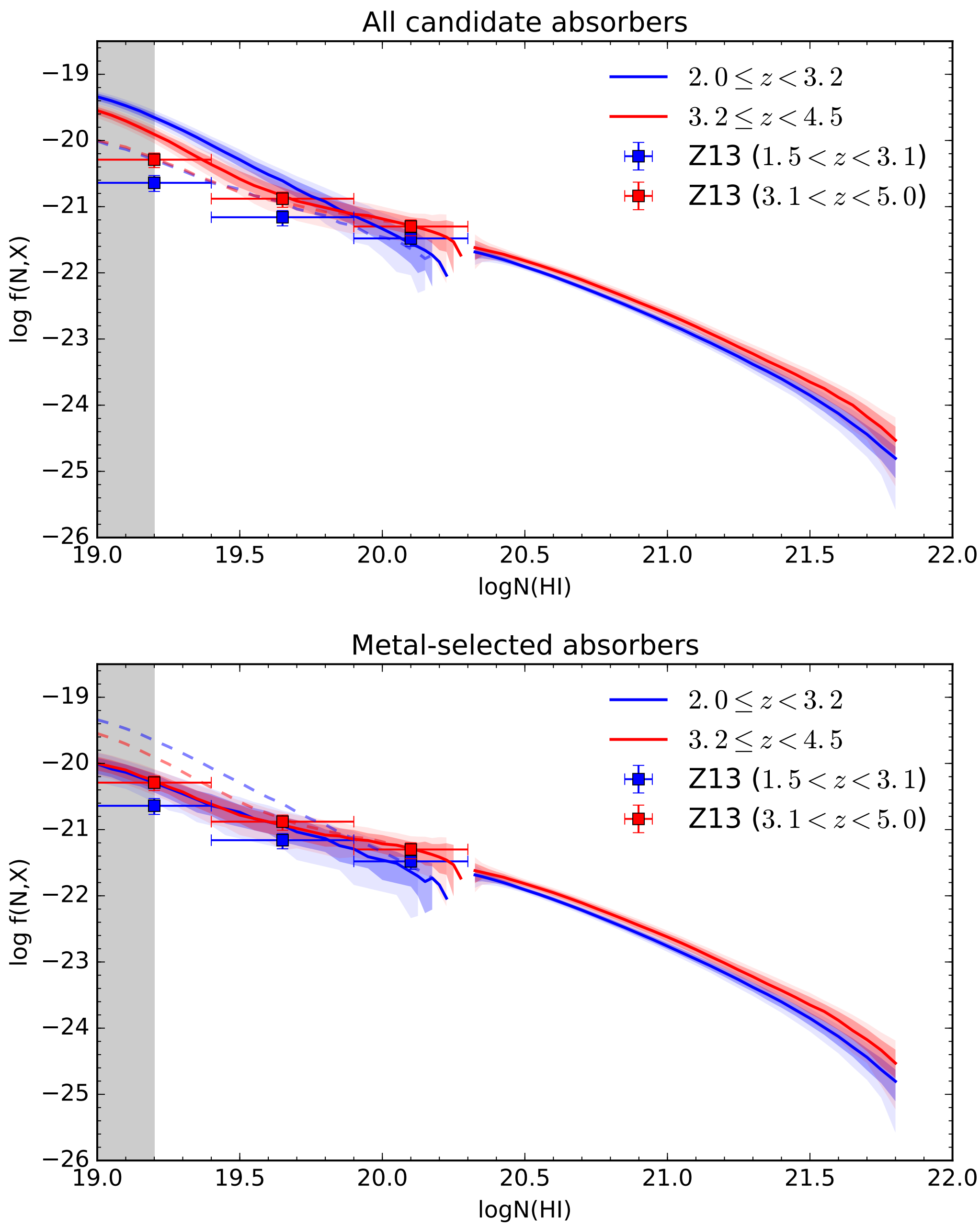

Figure 2.5 The column density distribution of subDLAs and DLAs in the XQ-100 sample. The median $f(N, X)$ is given by the solid line, while the dark and light shaded regions represent the 1σ and 2σ percentiles (respectfully). Both the DLA and subDLA samples were split by the median redshift of the XQ-100 absorbers (z_{abs}= 3.2). The top panel presents $f(N, X)$ for the FS absorbers in XQ-100, while the bottom panel shows $f(N, X)$ computed only with MS systems. For reference, the coloured dashed lines in each panel show the median subDLA $f(N, X)$ from the opposite panel. The square points denote the subDLA measurements from Zafar et al. (2013a) over a similar redshfit range. The greyed region below logN(H I)=19.2 represents the regime where the incompleteness of the XQ-100 sample could have a significant influence on the determined $f(N, X)$.

(respectfully). Each sample was split into two redshift bins by the median redshift of the XQ-100 absorbers (z_{abs}= 3.2); $f(N,X)$ for the lower and higher redshift bins are denoted by the blue and red colours (respectively).

There is a clear difference in the shape of $f(N,X)$ between all candidate subDLAs and those that have metal lines, resulting in ≈ 0.5 dex difference in $f(N,X)$ at low column densities. I emphasize again that using both the FS and MS samples should bound the true nature of $f(N,X)$ at these column densities. The derived $f(N,X)$ curves were compared with the values computed by Zafar et al. (2013a) for subDLAs over approximately the same redshift range (squares in Figure 2.5). The Zafar et al. (2013a) sample consisted of a search for subDLAs and DLAs in archival high resolution spectra taken with the UVES spectrograph on the VLT in Chile. Their identification of absorbers started with an automated search for candidate subDLAs and DLAs characterized by saturated absorption over a large range of wavelength. The absorber was confirmed as a (sub)DLA if higher order Lyman series or metal lines were present; which is analogous to the methods used in determining the XQ-100 MS absorbers. It is therefore both encouraging and not surprising that $f(N,X)$ for the MS absorbers is consistent with Zafar et al. (2013a). However, the ≈ 0.5 dex increase in $f(N,X)$ when all candidate absorbers are used suggests a potential bias of missing low column density absorbers when computing $f(N,X)$.

To attempt to better quantify the significance of the difference in $f(N,X)$ between the MS and FS subDLAs, as well as search for any evolution in $f(N,X)$ with redshift, I computed the best-fit power law fit to $f(N,X)$ (i.e. $f(N,X)= K\mathrm{N}^{\alpha}$; where K and α are the parameters of the fit). For each mock sample generated in the MCB simulation, an unweighted least-squares fit to $f(N,X)$ was computed using the sliding bin data. The median and 1σ percentile errors of α and K of all 10 000 samples least squares fits are presented in Table 2.1. Comparing the power law fit parameters α and K between the MS and FS datasets demonstrates that the power law fits between the two subDLA samples are inconsistent at the 1σ level. There is no detectable difference between the two selection techniques of DLAs, as all DLAs in the XQ-100 sample have observed metal lines[3]

Comparing the power law indices from each redshift bin, no significant evolution of α with redshift is detected at $\approx 1\sigma$ significance for both the subDLAs and DLAs (in

[3]Note that there are slight differences in the median power law fit parameters due to some subDLAs that do not have observed metal lines being classified as DLAs in the MCB resampling process.

Table 2.1 Power law fit parameters to $f(N,X)$

logN(H I)	z_{abs}	α		log(K)	
		FS absorbers	MS absorbers	FS absorbers	MS absorbers
[20.3,22.0)	[2.0,3.2)	$-2.06^{+0.127}_{-0.076}$	$-2.00^{+0.056}_{-0.133}$	$20.39^{+1.58}_{-2.62}$	$19.1^{+2.75}_{-1.14}$
	[3.2,4.5)	$-1.86^{+0.091}_{-0.127}$	$-1.90^{+0.106}_{-0.106}$	$16.3^{+2.66}_{-1.90}$	$17.2^{+2.25}_{-2.17}$
[19.0,20.3)	[2.0,3.2)	$-2.05^{+0.172}_{-0.227}$	$-1.45^{+0.209}_{-0.221}$	$19.7^{+4.44}_{-3.34}$	$7.58^{+4.30}_{-4.19}$
	[3.2,4.5)	$-1.44^{+0.159}_{-0.132}$	$-1.10^{+0.149}_{-0.224}$	$7.64^{+2.64}_{-3.07}$	$0.905^{+4.27}_{-3.02}$
[19.3,20.3)	[2.0,3.2)	$-2.15^{+0.364}_{-0.349}$	$-1.34^{+0.190}_{-0.384}$	$21.7^{+6.86}_{-7.11}$	$5.34^{+7.53}_{-3.87}$
	[3.2,4.5)	$-1.17^{+0.278}_{-0.235}$	$-0.96^{+0.236}_{-0.234}$	$2.22^{+4.71}_{-5.55}$	$-1.83^{+4.42}_{-4.85}$

both FS and MS samples). For the subDLAs, the direction of the redshift evolution depends on whether the FS or MS sample is compared. The relative direction of the redshfit evolution for the MS sample is consistent with previous work suggesting there is an increased number of subDLAs at higher redshifts (i.e. a steeper α; Péroux et al., 2003b; Zafar et al., 2013a). When using the FS however, more subDLAs are seen at lower redshifts; a result which could be (partially) explained by a high false-positive rate due to blending of low redshift Lyα with the Lyβ forest. Nevertheless, the redshift evolution of α is not strongly observed for the subDLAs; and is likely between the two evolutionary paths presented.

Previous analyses comparing the power law indices of DLAs and subDLAs has indicated a flattening in $f(N,X)$ in the subDLA regime (Péroux et al., 2005; O'Meara et al., 2007; Guimarães et al., 2009; Zafar et al., 2013a), which has been attributed to the loss of Lyα self-shielding in low N(H I) subDLA systems (Zheng & Miralda-Escudé, 2002). O'Meara et al. (2007) noted that this flattening in $f(N,X)$ at low column densities is dominated by logN(H I)$\leq$ 19.3 systems; an effect which can be seen in the power law fits to $f(N,X)$ when only logN(H I)$\geq$ 19.3 absorbers are included. I attempted to search for this flattening as well by restricting the subDLA sample only to absorbers with 19.3 $\leq$logN(H I)$<$ 20.3 and recomputing the power law fit to limited column density range (see Table 2.1 for fit parameters). The power law indices between the two logN(H I) regimes are consistent, thus I do not recover the significant flattening in $f(N,X)$ observed by O'Meara et al. (2007).

The cosmic density of HI

In addition to $f(N, X)$, $\Omega_{\rm HI}$ for the subDLA sample was also computed. Following Sánchez-Ramírez et al. (2016), $\Omega_{\rm HI}$ is computed in sliding bins of redshift. Rather than holding the bin width fixed in redshift space, Sánchez-Ramírez et al. (2016) elected to use a fixed redshift path length ΔX= 2.5, with redshift bin steps of 0.01. For consistency, I elected to use the same sliding bin setup to reproduce the observed $\Omega_{\rm HI}$ for the XQ-100 DLAs. For the derivation of $\Omega_{\rm HI}$ (Equation 2.3), I start with the same z_{min} and z_{max} used in Sánchez-Ramírez et al. (2016) for all the XQ-100 and supplementary QSO sightlines. However, due to the incompleteness of subDLA absorbers below λ_{LL} (Section 2.2.2), I increased z_{min} when necessary to remove all absorbers whose Lyα fell below λ_{LL}.

Similar to Figure 2.5, Figure 2.6 shows the redshift evolution of $\Omega_{\rm HI}$ for both the DLAs (blue; the data is nearly identical to the grey curve presented in Figure 2.1) and subDLAs (red), using both the FS (top panel) and MS absorbers (bottom panel). Although there is a slight but significant difference in the magnitude of $\Omega_{\rm HI}$ curve for the subDLAs between the two panels (detected at the $\approx 1\sigma$ level), no significant evolution in $\Omega_{\rm HI}$ with redshift is detected. If there is indeed an evolution in $f(N, X)$, any changes to the column density distribution function with time has a negligible effect on the evolution of $\Omega_{\rm HI}$. Furthermore, subDLAs only contribute a small (but still significant; $\approx$ 12–20%) amount to the total $\Omega_{\rm HI}$ probed by quasar absorption lines from 2 $<\mathrm{z_{abs}}<$ 4.3.

To estimate the relative mass contribution of subDLAs to the H I budget, I computed the relative ratio of $\Omega_{\rm HI}$ for subDLAs to DLS and subDLAs. To reduce the effects of the vastly different redshift sampling of the DLA and subDLA samples, I elected to use the median $f(N, X)$ curves (Figure 2.5) for the two redshift bins (using the discrete limit of the integral in Equation 2.3) rather than taking the ratio of the curves presented in Figure 2.6 (although note that an approximate evolution on the combined DLA and subDLA $\Omega_{\rm HI}$ is given by the black dotted lines in Figure 2.6). The estimated contribution fractions and their associated errors (estimated using the 1σ percentile curves) are tabulated in Table 2.2 for both redshift bins and absorber samples. The relative contribution of mass from subDLAs appears to be between $\approx$ 12–22%, which is consistent with estimates in the literature (Péroux et al., 2005; Guimarães et al., 2009; Zafar et al., 2013a). Although DLAs probe the bulk of H I in the Universe, subDLAs do provide a non-negligible component of the H I budget of

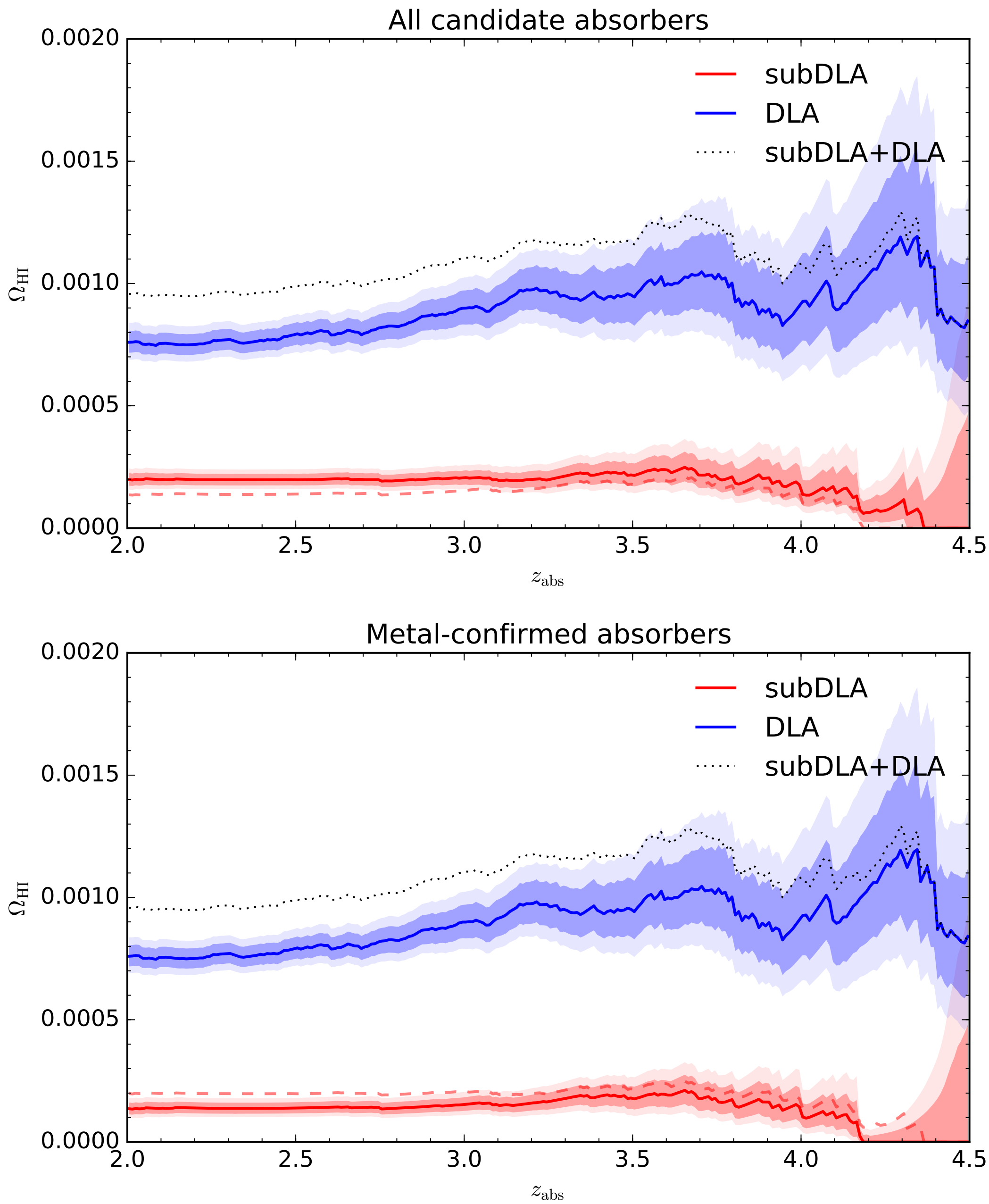

Figure 2.6 The redshift evolution of $\Omega_{\rm HI}$ as probed by DLAs (blue) and subDLAs (red) in the XQ-100 survey. The top panel presents $\Omega_{\rm HI}$ for the entire list of candidate absorbers in XQ-100, while the bottom panel shows $\Omega_{\rm HI}$ computed only with absorbers with confirmed metal lines. For reference, the coloured dashed lines in each panel show the median $\Omega_{\rm HI}$ evolutions from the opposite panel, while the black dotted line in each panel is an estimate of the combined DLA and subDLA median $\Omega_{\rm HI}$ evolution.

Table 2.2 Mass contribution fraction of subDLAs to H I budget

z_{abs}	All absorbers	Metal-confirmed
$2.0 \leq z_{abs} < 3.2$	$0.22^{+0.086}_{-0.069}$	$0.12^{+0.081}_{-0.056}$
$3.2 \leq z_{abs} < 4.5$	$0.16^{+0.082}_{-0.057}$	$0.13^{+0.075}_{-0.054}$

the Universe.

2.3.2 The influence of MgII selection on Ω_{HI}

The XQ-100 survey provides optical and near infrared coverage of blindly selected, intervening DLAs, simultaneously covering the Mg II doublet at $\lambda\lambda$ 2796, 2803 Å, and the Lyα transition. As a result of these properties, the XQ-100 DLA sample is an excellent testbed to investigate any potential sampling bias in the Mg II pre-selection technique used to identify intermediate redshift absorbers (Rao & Turnshek, 2000; Rao et al., 2006, further denoted as R00 and R06, respectively). Table 2.3 contains a summary of the intervening DLAs in XQ-100, including the measured rest-frame equivalent widths (EWs) for the Mg II λ λ 2796 Å and 2803 Å lines (W_0^{2796} and W_0^{2803}, respectively), as well as the Fe II λ 2600 Å line (W_0^{2600}). The N(H I), redshift, metallicity ([M/H]), and v_{90}[4] measurements are taken from Sánchez-Ramírez et al. (2016) and Berg et al. (2016). Additionally tabulated is the *D*-index (Ellison, 2006; Ellison et al., 2009) for each DLA. The *D*-index is defined as W_0^{2796} normalized by the velocity width of the Mg II λ 2796 Å line (ΔV). For the rest of this Mg II analysis, only the 30 DLAs with Mg II EWs that are not blended (i.e. are not upper limits in Table 2.3) are used in the analysis. More details on the metal line absorption profiles and metallicities of the DLAs will be presented in Chapter 3.

All of XQ-100 DLAs identified at $z_{abs} \lesssim 3.2$ have $W_0^{2796} \geq 0.6$ Å. For comparison, in a recent compilation of 369 Mg II systems (Rao et al., 2017), there are 70 Mg II absorbers with $0.3 \leq W_0^{2796} < 0.6$ Å, but only one of these is a DLA (S. Rao private communication). As a result, many works have typically used $W_0^{2796} \geq 0.6$ Å to pre-select potential DLA systems (R00, R06). Moreover, R06 used the EW of Fe II λ 2600 Å (W_0^{2600}) to aid in identifying DLAs, and found that their DLA sample is confined to $W_0^{2796}/W_0^{2600} < 2$, whereas their subDLAs span a larger range of W_0^{2796}/W_0^{2600}.

[4] v_{90} measures the velocity width corresponding to 90% of the integrated optical depth using one low-ion transition (Prochaska & Wolfe, 1997).

Table 2.3 XQ-100 DLA properties and equivalent widths

QSO	z_{em}	z_{abs}	logN(H I)	W_0^{2796} Å	W_0^{2803} Å	W_0^{2600} Å	[M/H] (elem)	v_{90} km s^{-1}	*D*-index (cut[a])
J0003-2603	4.12	3.3900	21.40 ± 0.10	1.393 ± 0.010	1.147 ± 0.009	...	-1.93 ± 0.12 (ZnII)	21	5.6 (3.8)
J0006-6208	4.44	3.2030	20.90 ± 0.15	0.553 ± 0.027	< 0.537	0.383 ± 0.088	-2.31 ± 0.15 (FeII)	43	5.8 (3.8)
J0006-6208	4.44	3.7750	21.00 ± 0.20	1.196 ± 0.023	0.963 ± 0.026	0.724 ± 0.034	-0.94 ± 0.20 (ZnII)	54	7.0 (3.8)
J0034+1639	4.29	3.7525	20.40 ± 0.15	0.518 ± 0.013	0.510 ± 0.022	0.369 ± 0.015	-1.88 ± 0.16 (FeII)	32	5.4 (3.8)
J0113-2803	4.31	3.1060	21.20 ± 0.10	4.377 ± 0.047	3.620 ± 0.040	2.326 ± 0.035	-1.11 ± 0.10 (SiII)	164	8.9 (3.9)
J0124+0044	3.84	2.2610	20.70 ± 0.15	1.673 ± 0.009	1.497 ± 0.009	1.054 ± 0.012	-0.85 ± 0.15 (SiII)	98	7.6 (4.2)
J0132+1341	4.15	3.9360	20.40 ± 0.15	...	...	0.235 ± 0.035	-2.04 ± 0.15 (SiII)	43	... (3.8)
J0134+0400	4.18	3.6920	20.70 ± 0.10	0.455 ± 0.008	0.405 ± 0.007	0.163 ± 0.015	-2.41 ± 0.16 (FeII)	21	6.0 (3.8)
J0134+0400	4.18	3.7725	20.70 ± 0.10	2.331 ± 0.012	2.110 ± 0.013	1.527 ± 0.012	-0.91 ± 0.10 (SiII)	98	5.8 (3.8)
J0234-1806	4.30	3.6930	20.40 ± 0.15	2.422 ± 0.054	2.101 ± 0.065	1.063 ± 0.050	-1.31 ± 0.15 (FeII)	184	5.5 (3.8)
J0255+0048	4.00	3.2555	20.90 ± 0.10	2.620 ± 0.026	2.364 ± 0.023	1.622 ± 0.036	-1.08 ± 0.10 (SiII)	208	7.7 (3.8)
J0255+0048	4.00	3.9145	21.50 ± 0.10	...	...	0.457 ± 0.052	-1.92 ± 0.11 (SII)	21	... (3.8)
J0307-4945	4.72	3.5910	20.50 ± 0.15	1.426 ± 0.015	1.191 ± 0.012	0.750 ± 0.008	-1.48 ± 0.15 (FeII)	70	3.9 (3.8)
J0307-4945	4.72	4.4665	20.60 ± 0.10	1.742 ± 0.020	1.594 ± 0.025	...	-1.52 ± 0.10 (SiII)	219	5.7 (3.8)
J0415-4357	4.07	3.8080	20.50 ± 0.20	< 2.100	> 1.647	0.755 ± 0.043	-0.28 ± 0.20 (ZnII)	131	... (3.8)
J0424-2209	4.33	2.9825	21.40 ± 0.15	0.861 ± 0.025	> 0.824	0.336 ± 0.024	-1.86 ± 0.16 (ZnII)	32	6.5 (3.9)
J0529-3552	4.17	3.6840	20.40 ± 0.15	0.375 ± 0.025	0.087 ± 0.060	...	-2.38 ± 0.16 (SiII)	21	4.9 (3.8)
J0747+2739	4.13	3.4235	20.90 ± 0.10	1.601 ± 0.021	1.431 ± 0.031	1.635 ± 0.020	-1.58 ± 0.10 (FeII)	120	7.7 (3.8)
J0747+2739	4.13	3.9010	20.60 ± 0.15	...	...	0.569 ± 0.026	-2.03 ± 0.15 (SiII)	153	... (3.8)
J0818+0958	3.66	3.3060	21.00 ± 0.10	1.776 ± 0.025	1.306 ± 0.022	...	-1.51 ± 0.10 (SiII)	76	3.9 (3.8)
J0920+0725	3.65	2.2380	20.90 ± 0.15	1.390 ± 0.012	< 1.470	0.864 ± 0.012	-1.55 ± 0.15 (FeII)	120	7.4 (4.2)
J0955-0130	4.42	4.0245	20.70 ± 0.15	...	...	1.197 ± 0.043	-1.54 ± 0.15 (FeII)	336	... (3.8)
J1020+0922	3.64	2.5920	21.50 ± 0.10	...	...	...	-1.75 ± 0.11 (SiII)	76	... (4.0)
J1024+1819	3.52	2.2980	21.30 ± 0.10	0.839 ± 0.012	< 0.873	0.631 ± 0.009	-1.45 ± 0.10 (SiII)	54	7.6 (4.2)
J1057+1910	4.13	3.3735	20.30 ± 0.10	2.456 ± 0.095	1.956 ± 0.065	...	-1.21 ± 0.14 (FeII)	153	6.8 (3.8)
J1058+1245	4.34	3.4315	20.60 ± 0.10	1.673 ± 0.020	1.330 ± 0.045	...	-1.85 ± 0.10 (SiII)	127	7.3 (3.8)
J1108+1209	3.68	3.3965	20.70 ± 0.10	0.325 ± 0.012	0.274 ± 0.027	0.235 ± 0.010	-2.49 ± 0.17 (FeII)	32	4.3 (3.8)
J1108+1209	3.68	3.5460	20.80 ± 0.15	1.810 ± 0.019	1.806 ± 0.022	...	-1.15 ± 0.15 (SII)	70	7.9 (3.8)
J1312+0841	3.73	2.6600	20.50 ± 0.10	1.237 ± 0.044	0.860 ± 0.032	0.548 ± 0.035	-1.50 ± 0.10 (FeII)	153	5.4 (4.0)
J1421-0643	3.69	3.4490	20.30 ± 0.15	0.949 ± 0.017	0.786 ± 0.019	0.320 ± 0.024	-1.40 ± 0.16 (FeII)	43	4.5 (3.8)
J1517+0511	3.56	2.6885	21.40 ± 0.10	0.807 ± 0.021	0.770 ± 0.023	0.668 ± 0.007	-2.06 ± 0.11 (SiII)	43	7.1 (4.0)
J1552+1005	3.72	3.6010	21.10 ± 0.10	0.981 ± 0.019	0.899 ± 0.021	0.665 ± 0.009	-1.75 ± 0.11 (SII)	21	7.4 (3.8)
J1633+1411	4.37	2.8820	20.30 ± 0.15	0.366 ± 0.015	0.290 ± 0.019	...	-1.78 ± 0.16 (FeII)	15	4.8 (3.9)
J1723+2243	4.53	3.6980	20.50 ± 0.10	3.888 ± 0.017	3.505 ± 0.010	1.915 ± 0.013	-1.03 ± 0.10 (FeII)	374	7.1 (3.8)
J2239-0552	4.56	4.0805	20.60 ± 0.10	> 1.512	...	0.614 ± 0.010	-1.95 ± 0.10 (SiII)	131	... (3.8)
J2344+0342	4.25	3.2200	21.30 ± 0.10	1.524 ± 0.018	1.189 ± 0.017	1.056 ± 0.023	-1.70 ± 0.32 (ZnII)	54	4.5 (3.8)

[a] The cut is obtained from Table 2 in Ellison (2006), and is based on the resolution at the Mg II λ 2796Å line (assuming R=5300). An absorber with a D-index larger than the cut value would be considered a DLA candidate.

Figure 2.7 shows how the XQ-100 measurements of W_0^{2796} (left panel), the ratio W_0^{2796}/W_0^{2600} (middle panel), and D-index (right panel) vary with logN(H I). Starting with the left panel of Figure 2.7, I found that six[5] (20% of the sample) of the XQ-100 DLAs with measured W_0^{2796} have $W_0^{2796} < 0.6$ Å (dashed line). However, *all DLAs pass the* $W_0^{2796} \geq 0.3$ *Å cut*. The middle panel of Figure 2.7 shows the W_0^{2796}/W_0^{2600} ratio for the XQ-100 and R06 samples, and demonstrates that 30% of the XQ-100 DLAs with Fe II λ 2600 Å measurements have $W_0^{2796}/W_0^{2600} > 2.0$ (DLAs above dashed line). Only one DLA (J0034+1639, $z_{abs} = 3.69$) does not satisfy both $W_0^{2796} \geq 0.6$ Å and $W_0^{2796}/W_0^{2600} < 2$ restrictions. Lastly, the right panel of Figure 2.7 shows the D-index (from Ellison, 2006) for the XQ-100 DLAs as a function of logN(H I). The minimum D-index cuts required for absorbers to be DLA candidates are derived from Ellison (2006, their Table 2), and are tabulated in Table 2.3. The D-index cuts are based on the resolution of the X-Shooter spectrum at each Mg II line (assuming a FWHM resolution of R= 5300). I note that the D-index of the XQ-100 DLAs does recover all the DLAs (i.e. points are above the grey band in the right panel of Figure 2.7). Figure 2.7 demonstrates that using the Mg II selection technique used in R03 and R06 would miss a large portion ($\approx 20\%$) of the XQ-100 DLAs; while the D-index remains robust at identifying DLAs.

Are the properties of $W_0^{2796} < 0.6$ *Å DLAs different to the higher EW systems?* The colour bar in Figure 2.7 indicates the metallicity of each DLA in the XQ-100 sample (Berg et al., 2016). Interestingly, the DLAs whose $W_0^{2796} < 0.6$ Å all have low metallicities, below $[M/H] < -1.7$. The mean metallicity of the XQ-100 DLAs subsample with $W_0^{2796} \geq 0.6$ Å is $[M/H] = -1.42 \pm 0.03$[6], whereas the entire sample has a mean metallicity of $[M/H] = -1.60 \pm 0.02$. However, the H I-weighted metallicity that is generally used to trace the evolution of DLA metallicity with cosmic time (e.g. Pettini et al., 1999; Rafelski et al., 2012) is negligibly affected, increasing from $[M/H] = -1.47 \pm 0.03$ for the full sample to $[M/H] = -1.43 \pm 0.03$ when $W_0^{2796} < 0.6$ Å absorbers are excluded. Thus, although the Mg II pre-selection tends to miss metal-poor systems, the resulting H I-weighted metallicity appears to be largely unaffected by the pre-selection.

[5] Two of these six DLAs with $W_0^{2796} < 0.6$ Å have previously been observed in the literature (DLAs towards J1108+1209 and J0134+0400), but previous observations have not covered the Mg II absorption. I also note that one of the excluded proximate DLAs (J0034+1639 at $z_{abs} = 4.25$) does not satisfy the $W_0^{2796} \geq 0.6$ Å cut. This DLA is metal-poor ($[M/H] = -2.40$) and has an equivalent width $W_0^{2796} = 0.344 \pm 0.013$ Å.

[6] All errors for mean quantities are derived using a bootstrap technique with one million iterations. The errors on individual measurements were assumed to be Gaussian.

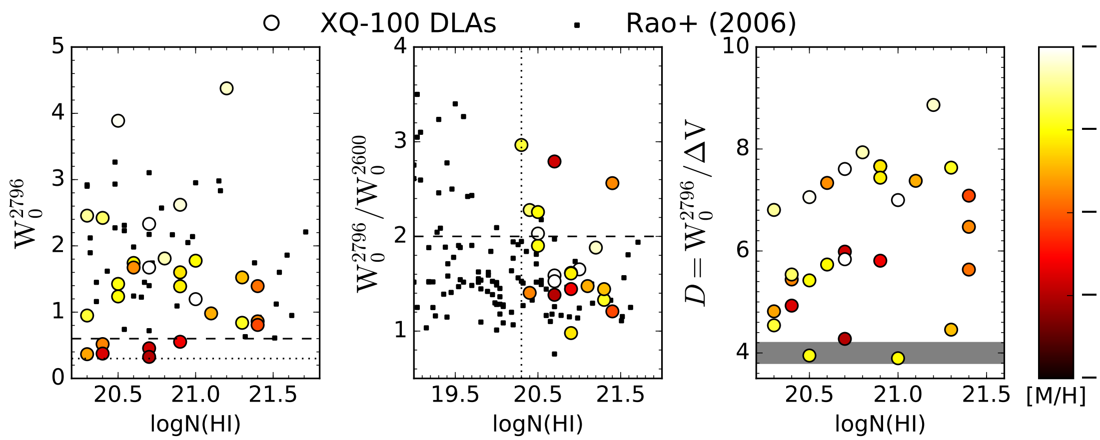

Figure 2.7 *Left Panel*: The rest-frame W_0^{2796} as a function of logN(H I) for the XQ-100 DLAs (large circles; colours indicate metallicity) and R06 data (black squares). For reference, the W_0^{2796} cuts ($W_0^{2796} \geq 0.3$ Å and $W_0^{2796} \geq 0.6$ Å) are shown as horizontal lines (dotted and dashed; respectively). Six of the 30 XQ-100 DLAs show $W_0^{2796} < 0.6$ Å. *Middle Panel*: The ratio W_0^{2796}/W_0^{2600} as a function of logN(H I) for the XQ-100 sample and R06 data. The region below the dashed line at $W_0^{2796}/W_0^{2600} \leq 2.0$ characterizes the Mg II-selected DLAs in the R06 sample, while the dotted line divides subDLAs from DLAs. 30% of the XQ-100 DLAs do not exhibit $W_0^{2796}/W_0^{2600} < 2$. *Right Panel*: The *D*-index ($W_0^{2796}/\Delta V$) as a function of logN(H I) for the XQ-100 DLA sample. The grey horizontal band represents the range of possible *D*-index cuts for the XQ-100 data. All XQ-100 DLAs pass their respective *D*-index cuts.

In addition to the metallicity, I checked for other DLA properties dependent on $W_0^{2796} \geq 0.6$ Å selection. Figure 2.8 shows the distributions of [M/H], v_{90} (which has been suggested as a proxy for mass, e.g. Prochaska & Wolfe, 1997; Haehnelt et al., 1998), z_{abs}, and logN(H I) for the XQ-100 DLAs for a selection cut of $W_0^{2796} \geq 0.6$ Å. DLAs passing the equivalent width selection cut are shown as the filled distribution, whilst DLAs that fail the selection cut are shown by the red line. DLAs with $W_0^{2796} < 0.6$ Å tend to show low metallicities, low logN(H I), and low v_{90} widths with respect to DLAs with $W_0^{2796} \geq 0.6$ Å. These properties are consistent with a 'mass-metallicity' relationship seen in DLAs (Ledoux et al., 2006; Jorgenson et al., 2010; Møller et al., 2013; Neeleman et al., 2013; Christensen et al., 2014), where narrower metal lines are typically found in lower metallicity systems. The dependence of W_0^{2796} on velocity width has been previously identified in other works (Nestor et al., 2003; Ellison, 2006; Murphy et al., 2007, R06). The *D*-index defined in Ellison (2006) potentially corrects for this bias toward low v_{90}, as the EW is normalized by the velocity width of the line. As demonstrated by the right panel of Figure 2.7, the *D*-index provides a more complete DLA sample relative to a fixed Mg II EW cut by including those absorbers with low metallicity and v_{90}.

What are the implications for the cosmological context of DLAs at $2 \leq z_{\rm abs} \leq 4$*?* The typical approach to calculating $\Omega_{\rm HI}$ uses Equation 2.3. If DLAs are missed from a Mg II-selected sample, the computed $\Omega_{\rm HI}$ from Equation 2.3 would be underestimated, as the sum of N(H I) would exclude the low Mg II EW DLAs while $\sum \Delta X_i$ remains unaffected. For the entire XQ-100 DLA sample, $\Omega_{\rm HI}$ would be *underestimated* by $\sim 5\%$ if $W_0^{2796} < 0.6$ Å DLAs were excluded.

However, R06 used a different approach to compute $\Omega_{\rm HI}$, that combines the number density of DLAs ($n_{\rm DLA}$; observed along Mg II absorber sightlines in R06) and the average N(H I) of DLAs ($\langle$N(H I)$\rangle$),

$$\Omega_{\rm HI}(z) = \frac{H_0 \mu m_H}{c \rho_{crit}} \frac{E(z)}{(1+z)^2} n_{\rm DLA}(z) \langle N(H\ \textsc{i}) \rangle, \tag{2.5}$$

where $E(z) = \sqrt{\Omega_M (1+z)^3 + (1 - \Omega_M - \Omega_\Lambda)(1+z)^2 + \Omega_\Lambda}$. With the R06 formalism, the calculation of $\Omega_{\rm HI}$ depends on two measured variables: the frequency of absorbers and their mean N(H I). As shown in Fig. 2.8, in the XQ-100 sample, DLAs with $W_0^{2796} < 0.6$ Å tend to have lower N(H I) than higher EW absorbers. If the low EW systems were not included in the XQ-100 sample statistics then $\langle$N(H I)$\rangle$ and thus $\Omega_{\rm HI}$ would be overestimated. However, this effect in our sample is minimal: the

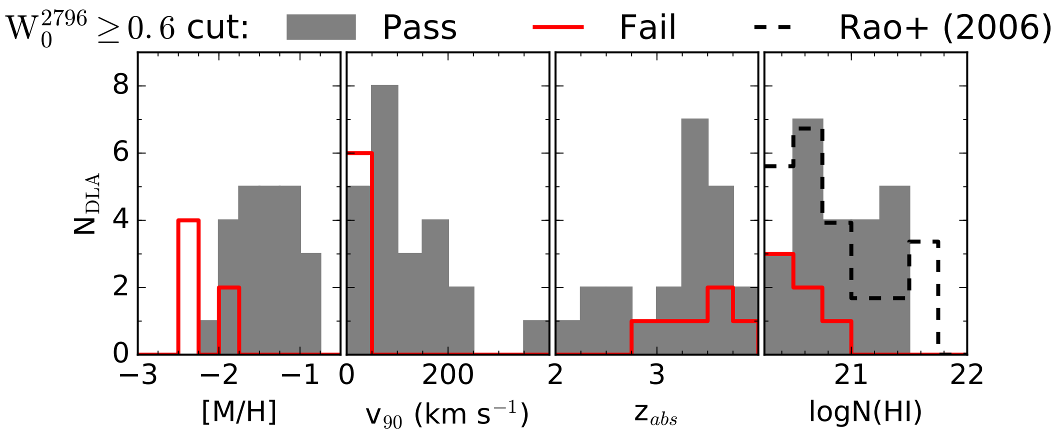

Figure 2.8 XQ-100 DLA distribution of metallicity ([M/H]), v_{90}, z_{abs}, and logN(H I) (from left to right). Different histograms are shown for DLAs that pass (shaded grey region) or fail (red line) the equivalent width cut $W_0^{2796} \geq 0.6$ Å. The simple $W_0^{2796} \geq 0.6$ Å cut clearly misses low metallicity systems, with small logN(H I) and v_{90}. For reference, the H I distribution of the R06 DLAs is shown as the dashed line. For visual purposes the R06 distribution is scaled down by a factor of ~ 1.8 to match the number of DLAs in the shaded region.

mean log(⟨ N(H I)⟩) of the XQ-100 sample increases minimally from 20.98 ± 0.03 to 21.01 ± 0.03 ($\sim 7\%$) upon exclusion of the DLAs with $W_0^{2796} < 0.6$ Å. Therefore, for a constant $n_{\rm DLA}$, $\Omega_{\rm HI}$ would be *overestimated* by $\sim 7\%$ when low EW systems are excluded.

Comparison with the properties of Mg II in DLAs at $z_{\rm abs} \leq 1.5$. In the latest compilation of 369 $z_{\rm abs} \sim 1$ Mg II absorbers (Rao et al., 2017) only 1 out of 70 ($1.4^{+3.3}_{-1.2}\%$[7]) systems with $0.3 \leq W_0^{2796} < 0.6$ Å is confirmed to be a DLA (S. Rao, private communication). In contrast, $\sim 7^{+4}_{-2}\%$ of $0.3 \leq W_0^{2796} < 0.6$ Å systems are DLAs[8] (Lopez et al. in prep). The DLA incidence for the low W_0^{2796} regime is a factor of ~ 5 higher at $z_{\rm abs} \sim 3$ than at $z_{\rm abs} \sim 1$. These incidence rates indicate a potential evolution in the Mg II properties of DLAs as a function of redshift. Whereas DLAs at low $z_{\rm abs}$ are almost uniquely associated with $W_0^{2796} \geq 0.6$ Å, at high redshift a significant fraction of DLAs (20% in our sample) can have lower values. The known relationship between W_0^{2796} and velocity spread (e.g. Ellison, 2006), as well as the relatively low values of measured v_{90} and low metallicity of the $W_0^{2796} < 0.6$ Å DLAs in the XQ-100 sample indicate that low W_0^{2796} absorbers may preferentially be probing low mass galaxies, which are less prevalent at low redshift. This is consistent with the lack of low metallicity DLAs at low redshift (Rafelski et al., 2014; Berg et al., 2015a). What is currently unknown is whether, despite their rarity, low Mg II EW DLAs at low $z_{\rm abs}$ show the same distribution of properties (metallicities, v_{90}, N(H I)) as high $z_{\rm abs}$ DLAs of the same W_0^{2796}. Based on our high $z_{\rm abs}$ results, I caution that DLAs that have been selected based on a high Mg II EW cut have the potential to be biased against low metallicity systems. Indeed, Kulkarni et al. (2007) have argued that Mg II pre-selection could select against DLAs with $[{\rm M/H}] < -2.5$. Nonetheless, the low frequency of such systems at low redshifts (and their tendency towards lower N(H I)) means that $\Omega_{\rm HI}$ and the H I-weighted metallicity is unlikely to be significantly affected.

[7]The subscript and superscript represent the Poisson 1σ confidence limits derived from Tables 1 and 2 in Gehrels (1986).

[8]I note that the DLA incidence rate for $W_0^{2796} > 0.6$ Å absorbers in the XQ-100 sample is $\sim 14^{+4}_{-3}\%$ (compared to the $\sim 22\%$ seen at $z_{\rm abs} \sim 1$; R06).

2.4 Summary

Using the XQ-100 legacy survey of 100 X-Shooter spectra of background QSO, I have found 325 new candidate subDLA absorbers with 18.8 $\leq$logN(H I)$<$ 20.3, in addition to the 33 DLA previously identified in Sánchez-Ramírez et al. (2016). Given the resolution of X-Shooter and the lack of metal line detections for 209 of the candidate absorbers, it is unclear if these systems are indeed subDLAs or blended LLS.

From the complete sample of subDLAs and DLAs, I investigated the role of using these quasar absorption line systems to trace the total H I content of the Universe at high redshift. In summary:

1. The column density distributions ($f(N, X)$) for subDLAs and DLAs show no significant evidence ($\approx 1\sigma$) of evolution across the two redshfit bins ($3.2 \leq z_{\rm abs} < 4.5$ & $2.0 \leq z_{\rm abs} < 3.2$; Figure 2.5). The nature of this evolution depends on the selection criteria used to identify subDLAs; as systems with metal lines are more numerous at high redshifts while metal-deficient candidate absorbers were more numerous at low redshifts. It is likely that many of these lower redshift, metal-deficient candidates are false-positive systems due to blending of the Lyα of the candidate absorber with Lyβ forest. Although the identification of metal-deficient systems could suffer from a high false-positive rate, the two discrepant results hint at $f(N, X)$ not evolving with redshift.

2. There is little evolution in comoving mass density of neutral gas ($\Omega_{\rm HI}$) probed by subDLAs from $2.0 \leq z_{\rm abs} < 4.5$ (Figure 2.6). Although DLAs dominate the H I content of the Universe, subDLAs contribute $\approx$12 – 22% of the H I mass in $\Omega_{\rm HI}$. This result is consistent with previous measurements (Péroux et al., 2005; Guimarães et al., 2009; Zafar et al., 2013a).

3. The mean N(H I), and hence $\Omega_{\rm HI}$, of DLAs may be over-estimated solely using the Mg II pre-selected systems ($W_0^{2796} \geq$ 0.6 Å). This is due to both a bias against low N(H I) absorbers and a possible over-representation of high N(H I) absorbers for the $W_0^{2796} \geq$ 0.6 Å DLAs (Figure 2.8). If the cosmic H I gas density is computed based on the summation of N(H I) in the DLA sample (Equation 2.3), the exclusion of $W_0^{2796} <$ 0.6 Å absorbers leads to a reduction in $\Omega_{\rm HI}$ by 5%. However, since DLAs associated with $W_0^{2796} <$ 0.6 Å absorbers tend to have lower H I column densities, using the mean N(H I) to compute the cosmic H I

gas density (e.g. Equation 2.5) results in a 7% increase in $\Omega_{\rm HI}$ if $W_0^{2796} < 0.6$ Å absorbers are excluded, relative to the full DLA sample.

4. The XQ-100 DLAs with $W_0^{2796} < 0.6$ Å tend to have lower metallicities, narrower metal lines (i.e. low v_{90}) and lower N(H I) compared to DLAs with high Mg II EW, suggesting that DLAs at $z_{\rm abs} \gtrsim 2.0$ with $W_0^{2796} < 0.6$ Å may preferentially select lower mass galaxies. There is a factor of ~ 5 more DLAs with $W_0^{2796} < 0.6$ Å at high redshifts ($z_{\rm abs} \sim 3$) compared to lower redshifts ($z_{\rm abs} \sim 1$), suggestive of an evolution in the Mg II properties of DLAs as a function of redshift. This evolution would be consistent with the deficit of low-metallicity systems observed at low redshifts.

Chapter 3

The chemical nature of DLAs

Although hydrogen and helium are the most abundant elements in the Universe, there is much additional information to be learned studying the gas traced by the other elements (also known as *metals*). Even though metals are less abundant than hydrogen, their associated absorption lines imprinted on top of quasar spectra are sensitive to the kinematic motions and the nucleosynthetic origin of the gas, which can potentially inform us of the mass and star formation history of the host galaxy. This chapter builds upon the properties of the DLAs from the XQ-100 sample (presented in Chapter 2) by studying the sample's associated metal absorption lines for 14 species (O I, C II, Mg I, Mg II, Ca II, Si II, P II, S II, Ti II, Cr II, Mn II, Fe II, Ni II, Zn II) to demonstrate the prospects of using X-Shooter to study absorption lines in the optical and NIR. The bulk of this chapter has been published in Berg et al. (2016), with a portion of the analysis concerning the dust depletion corrections of metal abundances stemming from my previous work (Berg et al., 2015a). The dataset presented in this chapter has benefited from the inclusion of the metal line velocity widths (v_{90}) computed by J. X. Prochaska.

3.1 Applications of DLA metal abundances

The chemical evolution of DLAs

DLAs are associated with star-forming galaxies (Nagamine et al., 2004; Wolfe & Chen, 2006) and can be seen out to high redshifts ($z_{abs} \sim 5$; Rafelski et al., 2014). As a result, DLAs are excellent tracers of the production of metals with cosmic time. This production of metals is typically quantified by the mean cosmic metallicity (or

H I-weighted mean metallicity; $\langle Z/Z_{\odot}\rangle$), and is given by the ratio of the metal and H I gas-mass densities of the Universe ($\frac{\Omega_{Metals}}{\Omega_{HI}}$; Lanzetta et al., 1995b). As DLAs dominate the gas-mass density of the Universe (see Section 2.1), the computation of $\langle Z/Z_{\odot}\rangle$ simplifies to:

$$\langle Z/Z_{\odot}\rangle = \frac{\Omega_{Metals}}{\Omega_{HI}} / \frac{\Omega_{Metals,\odot}}{\Omega_{HI,\odot}} = \frac{\sum_i \mathrm{N(H\ I)}_i 10^{[\mathrm{M/H}]_i}}{\sum_i \mathrm{N(H\ I)}_i}, \tag{3.1}$$

where $\mathrm{N(H\ I)}_i$ and $[\mathrm{M/H}]_i$ are the H I column density and metallicity of the i^{th} DLA of the sample.

Previous work has shown a shallow but steady increase in $\langle Z/Z_{\odot}\rangle$ with decreasing redshift (Lanzetta et al., 1995b; Pettini et al., 1999; Prochaska et al., 2003a; Rafelski et al., 2014; De Cia et al., 2017). Comparisons of the measured $\langle Z/Z_{\odot}\rangle$ to the expected metallicity obtained from the observed or simulated star formation rate of DLAs (Wolfe et al., 2003; Nagamine et al., 2004; Wolfe & Chen, 2006; Rafelski et al., 2016) show a large discrepancy, with the measured $\langle Z/Z_{\odot}\rangle$ in DLAs being up to $\sim \times 10$ lower than the expected value (Pettini et al., 1999; Prochaska et al., 2003a). This discrepant, slow evolution in the metal content of DLAs could come about from: 1) a decrease in the star formation rate efficiency of DLA gas, likely from a low molecular gas content at high redshifts (Wolfe & Chen, 2006; Noterdaeme et al., 2015; Rafelski et al., 2016); or 2) differing strengths of feedback processes within the observed and simulated host galaxies (Wolfe et al., 2003; Nagamine et al., 2004). In subDLAs however, the metallicity evolution has been shown to be much steeper than DLAs (Kulkarni et al., 2007; Quiret et al., 2016, see Figure 3.1), and could thus account for these 'missing metals' when subDLAs are combined with the DLAs to compute $\langle Z/Z_{\odot}\rangle$. However, this stronger metallicity evolution observed in sub-DLAs is heavily dependent on the presence of low redshift, high metallicity subDLAs selected using Mg II absorption, which was shown to potentially be biased in Berg et al. (2017, see Section 2.3.2).

A large portion of DLA metal studies has concentrated on more detailed abundance analyses of the host galaxies (e.g. Pettini et al., 1994; Lu et al., 1998; Centurión et al., 2000; Wolfe et al., 2003; Cooke et al., 2011; Zafar et al., 2014a; Berg et al., 2015a). As each element has unique physical properties and nucleosynthetic origins (Woosley & Weaver, 1995; McWilliam, 1997; Nomoto et al., 2013), different abundance ratios have been used to understand the star formation history and dust content of DLAs (Ledoux et al., 2002; Prochaska & Wolfe, 2002; Vladilo et al., 2011). The

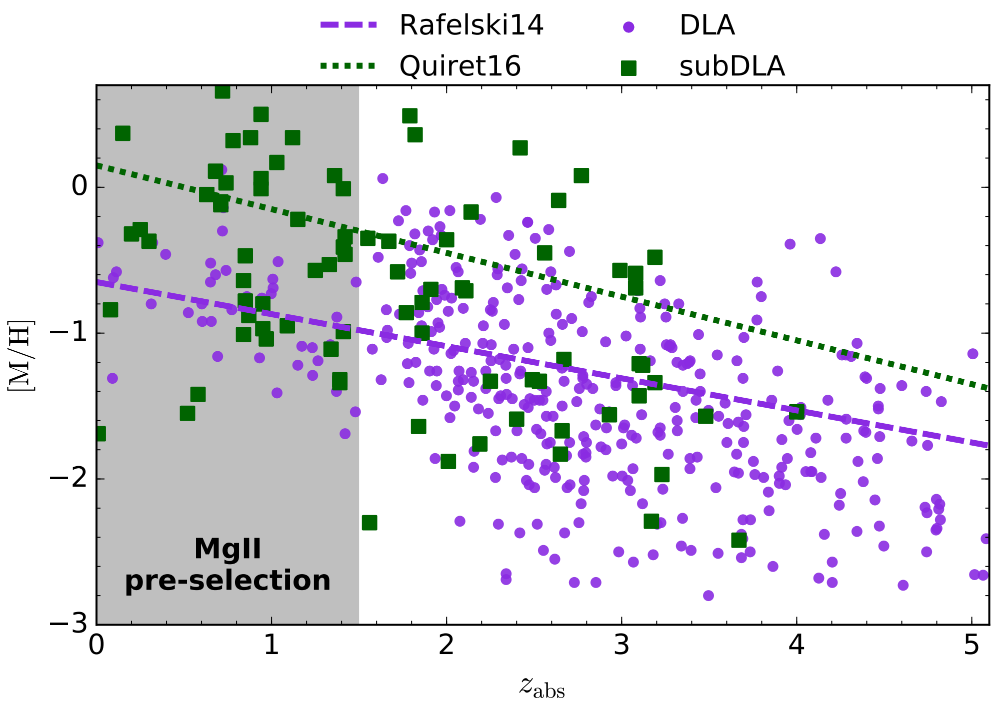

Figure 3.1 The metallicity evolution with redshift of DLAs (purple circles; Berg et al., 2015a, 2016) and subDLAs (green squares; Quiret et al., 2016). The best-fit evolution of $\langle Z/Z_{\odot}\rangle$ with $z_{\rm abs}$ for DLAs (from Rafelski et al., 2014) and subDLAs (computed by Quiret et al., 2016) are denoted by the respective dashed and dotted lines. The difference in evolution suggests that $\langle Z/Z_{\odot}\rangle$ evolves much more steeply in subDLAs than DLAs. However, this strong evolution is dominated by high-metallicity subDLAs at $z_{\rm abs} \lesssim 1.5$ where Mg II selection effects apply (grey shaded region; see Section 2.3.2).

most common ratio to probe enrichment histories is [α/Fe], which traces the star formation history due to the time-delayed contributions of Type II and Ia supernovae (Tinsley, 1979; McWilliam, 1997; Venn et al., 2004; Tolstoy et al., 2009). However elements such as Fe, Ni, and Cr are heavily depleted onto dust (Savage & Sembach, 1996), leading to overestimates of the measured gas-phase [α/Fe] in DLAs. These overestimates in [α/Fe] have led to the use of other undepleted elements that trace Fe (such as Zn) to better estimate the intrinsic [α/Fe] ratio (Pettini et al., 1997; Vladilo, 2002b). In the case of Zn, care must be taken as Zn does not necessarily trace Fe in all environments and metallicities (Prochaska et al., 2000; Chen et al., 2004; Nissen et al., 2007; Rafelski et al., 2012; Berg et al., 2015a; Skúladóttir et al., 2017).

Recently there has been a significant effort to identify the progenitors of the first stars and galaxies in nearby galaxies and the Milky Way (Cayrel et al., 2004; Beers & Christlieb, 2005; Suda et al., 2008; Spite et al., 2011; Frebel & Bromm, 2012; Norris et al., 2013; Frebel & Norris, 2015) to constrain Population III nucleosynthesis (Umeda & Nomoto, 2002; Greif et al., 2007; Heger & Woosley, 2010; Cooke et al., 2013). In tandem with the search for metal-poor stars in the Galaxy and its nearby companions (e.g. Jacobson et al., 2015; Skúladóttir et al., 2015; Starkenburg et al., 2017), work at higher redshifts focused on the identification and measurement of abundances in the most metal-poor DLAs (MPDLAs; [Fe/H]≤ -2.5; Penprase et al., 2010; Cooke et al., 2011; Becker et al., 2012; Cooke & Madau, 2014; Cooke et al., 2017). As the explosion mechanism of the supernovae models is very uncertain, measuring the chemical abundance patterns in these metal-poor regimes is required to constrain the models of Population III nucleosynthesis. In particular, the diferent supernovae explosion energies of these models influences the mass cut of the supernovae, and thus which elements escape into the ISM (Umeda & Nomoto, 2002; Nomoto et al., 2013; Cooke & Madau, 2014, see Figure 3.2 for the abundance pattern predictions). To date, abundances in the most MPDLAs tend to reflect first generation stars that have undergone moderate to low energy core-collapse supernovae (Cooke et al., 2011, 2013, 2017), but remain to be tested for a large sample of DLAs with [Fe/H]≤ -3.

The effects of environment on DLAs

The physical nature of DLAs also influences their gas phase abundances, including the role of ionizing sources (D'Odorico, 2007; Ellison et al., 2010; Zafar et al., 2014b) or the amount of dust (e.g. Pettini et al., 1994; Kulkarni et al., 1997; Akerman et al., 2005;

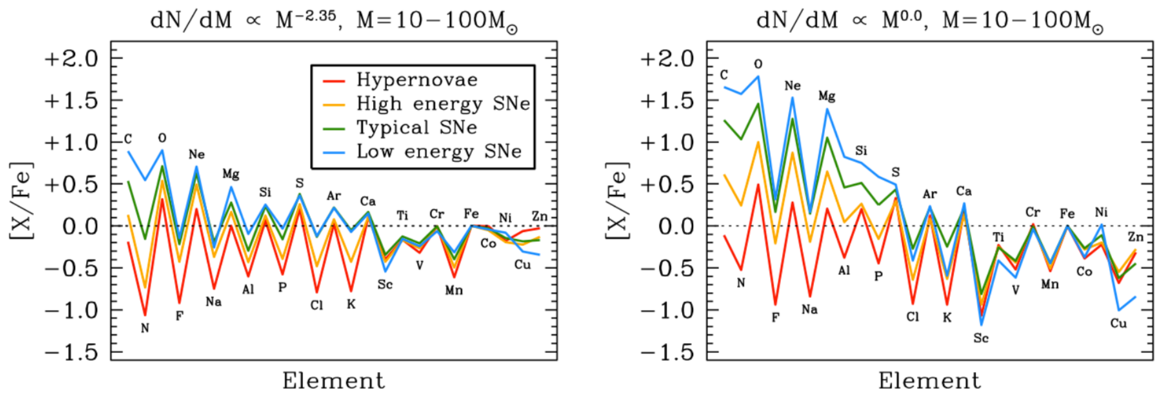

Figure 3.2 Predictions from Cooke & Madau (2014) of the expected production of various elements X (quantified in terms of [X/Fe]) from Population III stars. Each coloured line represents a different supernovae type or explosion energy model. The left and right panels show the difference in [X/Fe] for two different stellar population distributions (dN/dM). The metal-poor DLAs observed to date are most similar to the low-energy supernovae (blue curve). Figure taken with permission from Cooke & Madau (2014).

Krogager et al., 2016). There are many sub-classes of DLAs that provide opportunities to probe these differing physical environments. Proximate DLAs (PDLAs) are DLAs defined to be within a velocity separation of $\Delta v \leq 5000$ km s^{-1} of the host QSO. Δv is defined as

$$\Delta v = c\frac{R^2 - 1}{R^2 + 1}, \tag{3.2}$$

where c is the speed of light and $R = \frac{1+z_1}{1+z_2}$ (z_1 and z_2 are the redshifts of two objects, such as a DLA and background quasar). Proximate DLAs have a higher number density than intervening systems (Ellison et al., 2002; Russell et al., 2006; Prochaska et al., 2008b), and often have shown increasing metal abundances with increasing N(H I); in particular both [S/H] and [Si/H] are $\sim 3\times$ larger in four PDLAs with logN(H I)> 21.0 (Ellison et al., 2010, 2011b). Multiple DLAs (MDLAs) along the same line of sight within $500 \leq \Delta v \leq 10000$ km s^{-1} of each other have also shown different metallicity effects, with a low [α/Fe] relative to the typical DLA (Ellison & Lopez, 2001; Lopez & Ellison, 2003); an effect attributed to truncated star formation from environmental effects. However, the analyses of Lopez & Ellison (2003) and Ellison et al. (2010) suffer from low numbers of MDLAs (seven absorbers) and PDLAs (16 absorbers).

3.2 Quantifying the metal content of DLAs

The XQ-100 DLA sample used in this chapter was originally based on the sample identified in Sánchez-Ramírez et al. (2016, presented in Chapter 2). I continue to use this original sample and the corresponding H I column densities through-out this chapter. The XQ-100 X-Shooter spectra presented in Chapter 2 form the bulk of the dataset, but my analysis also includes my follow-up observations with VLT/UVES for one sightline (J0034+1639; Section 3.2.2). Table 3.1 summarizes the properties of the XQ-100 DLA sample, along with their redshifts[1], logN(H I) and line-of-sight velocity separations from the QSO (Δv_{QSO}).

3.2.1 X-Shooter dataset

Metal Column Densities

Column densities were derived using the Apparent Optical Depth Method (AODM) presented in Savage & Sembach (1991). In brief, this method sums the optical depth (τ; the log of the continuum-normalized flux) of an unsaturated absorption feature (at wavelength λ with oscillator strength f; taken from Morton, 2003), converting the total optical depth into a column density using

$$N = \frac{m_e c}{\pi e_c^2 f \lambda} \int_{v_{min}}^{v_{max}} \tau dv. \tag{3.3}$$

The constants m_e and e_c are the mass and charge of an electron (respectively). The integration limits v_{min} and v_{max} are selected such that the associated metal absorption profile is bounded by these velocity limits. I attempted to use the same velocity limits for all metal lines for a given DLA, however the velocity limits were sometimes adjusted on a line-by-line basis to exclude regions of contamination outside the metal absorption feature. If the weaker components of a shallow line are undetected, the velocity limits are purposefully made narrow to only contain associated absorption, and exclude flux contribution from the continuum. When the column density is derived using multiple clean lines for the same ion, I adopted the average value ($\log N_{adopt}$) and the standard error (with a minimum error of 0.05 dex). For features that exhibited obvious blending or saturation, I measured the AODM column density as a limit to the true value, adopting the most constraining limit as the final value. For

[1]For J0034+1639, the redshifts of the DLAs have been tweaked based on the metal lines in the UVES spectra presented in Section 3.2.2.

Table 3.1 XQ-100 DLA sample

QSO	z_{em}	z_{abs}	logN(H I)	Δv_{QSO} (km s^{-1})
J0003−2603	4.125	3.390	21.40 ± 0.10	46040
J0006−6208	4.440	3.203	20.90 ± 0.15	75670
		3.775	21.00 ± 0.20	38870
J0034+1639	4.292	3.752	20.40 ± 0.15	32110
		4.251	20.60 ± 0.10	$2349^{P\ M}$
		4.283	21.00 ± 0.10	$522^{P\ M}$
J0113−2803	4.314	3.106	21.20 ± 0.10	75650
J0124+0044	3.837	2.261	20.70 ± 0.15	112400
J0132+1341	4.152	3.936	20.40 ± 0.15	12830
J0134+0400	4.185	3.692	20.70 ± 0.10	29850^{M}
		3.772	20.70 ± 0.10	24800^{M}
J0234−1806	4.305	3.693	20.40 ± 0.15	36570
J0255+0048	4.003	3.256	20.90 ± 0.10	48100
		3.914	21.50 ± 0.10	5350
J0307−4945	4.716	3.591	20.50 ± 0.15	64680
		4.466	20.60 ± 0.10	13370
J0415−4357	4.073	3.808	20.50 ± 0.20	16070
J0424−2209	4.329	2.982	21.40 ± 0.15	84930
J0529−3552	4.172	3.684	20.40 ± 0.15	29620
J0747+2739	4.133	3.424	20.90 ± 0.10	44270
		3.901	20.60 ± 0.15	13860
J0800+1920	3.948	3.946	20.40 ± 0.10	91^{P}
J0818+0958	3.656	3.306	21.00 ± 0.10	23380
J0835+0650	4.007	3.955	20.40 ± 0.10	3099^{P}
J0920+0725	3.646	2.238	20.90 ± 0.15	103800
J0955−0130	4.418	4.024	20.70 ± 0.15	22560
J1020+0922	3.640	2.592	21.50 ± 0.10	75120
J1024+1819	3.524	2.298	21.30 ± 0.10	91730
J1057+1910	4.128	3.373	20.30 ± 0.10	47310
J1058+1245	4.341	3.432	20.60 ± 0.10	55320
J1108+1209	3.679	3.397	20.70 ± 0.10	18650
		3.546	20.80 ± 0.15	8643
J1312+0841	3.731	2.660	20.50 ± 0.10	75300
J1421−0643	3.688	3.449	20.30 ± 0.15	15670
J1517+0511	3.555	2.688	21.40 ± 0.10	62340
J1552+1005	3.722	3.601	21.10 ± 0.10	7781^{M}
		3.667	20.70 ± 0.10	$3544^{P\ M}$
J1633+1411	4.365	2.882	20.30 ± 0.15	93750
J1723+2243	4.531	3.698	20.50 ± 0.10	48510
J2239−0552	4.557	4.080	20.60 ± 0.10	26800
J2344+0342	4.248	3.220	21.30 ± 0.10	64340

^{P} – Proximate DLA

^{M} – Multiple DLA

cases where the absorption feature is severely blended, I do not consider adopting the measured column density.

The limiting spectral resolution of X-Shooter (R=5100, 8800, and 5300 for the UVB, VIS, and NIR arms; respectively) implies that there are cases where I could not determine the presence of unseen contamination or saturation visually. Cases of hidden contamination or saturation were flagged when multiple lines are measured for a given species and resulted in significantly inconsistent column densities. Using multiple Si II and Fe II lines, I have noted that these cases of hidden saturation tend to occur when the strongest absorption reaches a residual flux of ∼0.3–0.5 (similar to the ∼ 0.25 seen in the UVB arm by Krogager et al., 2016). Lines with absorption stronger than ∼ 0.5 (in units of residual flux) were inspected for inconsistent column densities with other lines. Unless the derived column density is consistent with weaker lines, any discrepant column densities were flagged as saturated. I note that all of the lines with a peak absorption at ∼ 0.5 had additional lines to constrain potential saturation. However, there may still be cases with unresolved saturation or blending unaccounted for.

When weak lines are not detected and the spectrum is uncontaminated, I measure 3σ upper limits based on the ability to detect the strongest absorption feature within the signal-noise ratio (snr) of the spectrum using

$$N = \frac{3m_e c\ FWHM}{\pi e_c^2 f \lambda^2 (1 + z_{abs}) snr} \tag{3.4}$$

where FWHM is the full-width at half-maximum of the strongest absorption feature. As the components of the absorption profile are likely limited by the resolution of the instrument ($\Delta v \sim 55$km s^{-1}) rather than the DLA kinematics ($\Delta v \sim 10$km s^{-1}; e.g. Dessauges-Zavadsky et al., 2004; Jorgenson et al., 2010; Tumlinson et al., 2010; Cooke & Madau, 2014), I assume that the FWHM of this strongest absorption feature to be equal to the resolution limit of X-Shooter in the setup with a slit width of $\sim 1''$. The signal-noise ratio for the 3σ upper-limits was computed within the bounds of the AODM limits.

As an example of data quality and coverage, Figure 3.3 shows the velocity profile for all the observed lines of the DLA in the spectrum of J0003-2603 ($z_{\rm abs}$= 3.39). The vertical dashed lines show the velocity limits used to integrate the spectrum for the AODM column density determinations. The column densities for all the measured lines for the DLA towards J0003-2603 are given in Table 3.2. Table 3.2 displays the

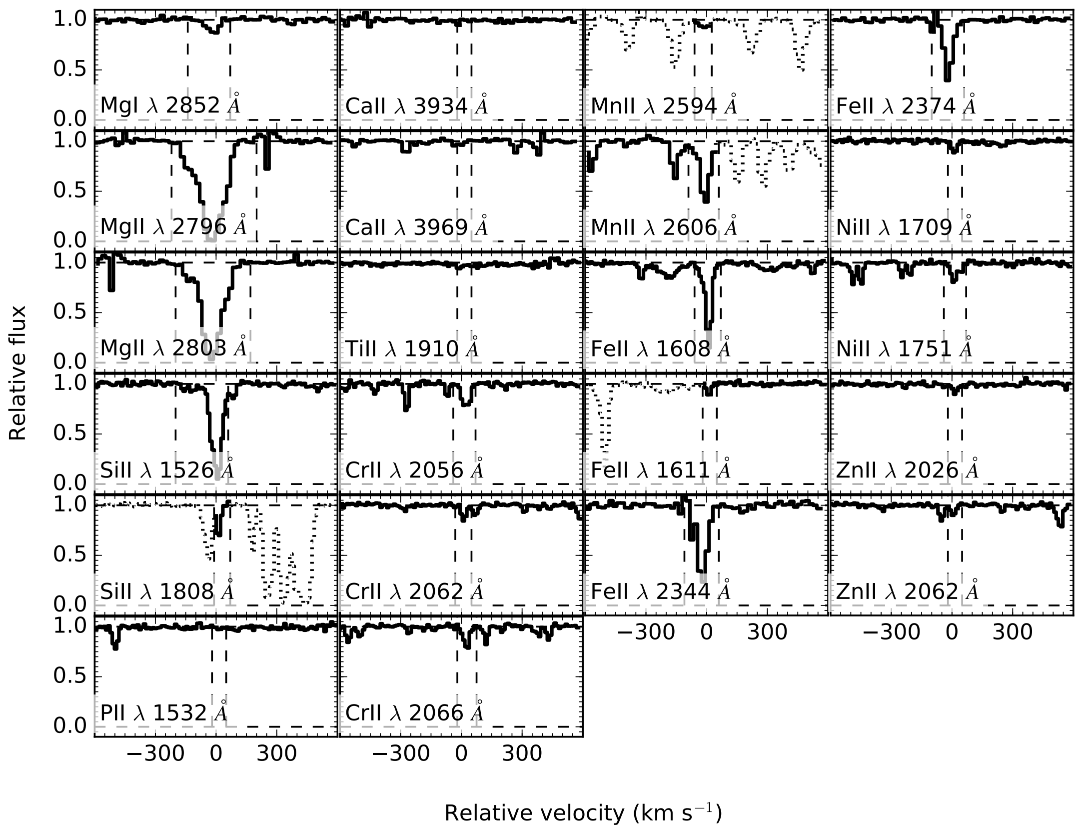

Figure 3.3 Velocity profile of the XQ-100 spectrum towards J0003-2603 (z_{abs}=3.390). The vertical dashed lines indicated the AODM velocity bounds. Regions of the spectrum that are contaminated by strong, unassociated absorption are flagged as dotted lines.

wavelength and oscillator strength of the absorption line (Morton, 2003), the velocity integration bounds of the absorption feature used (v_{min} and v_{max}), the measured column density logN(X) of the metal line, and whether the derived column density was included for the final computation of the adopted column density ($\log N_{\rm adopt}$). The adopted $\log N_{\rm adopt}$ is given for each species in the last row for the species. Appendix B.1 contains the velocity profiles (Figures B.1–B.21) and abundances (Tables B.1–B.21) for the remaining DLAs. If the adopted column density for a given species is best constrained by an upper and lower limit, the range of possible values is provided in Tables B.1–B.21.

Comparison to literature measurements

Of the DLAs studied in XQ-100, 15 DLAs have previously been observed in the literature sample of Berg et al. (2015a, further referred to as the 'literature sample' in this Chapter). The literature sample includes abundance determinations for a variety of elements[2] using high resolution spectrographs (predominantly VLT/UVES, Keck/HIRES, and Keck/ESI) for 341 DLAs between $z_{\rm abs} \sim 0-5$.

Similar to the comparison of N(H I) to the literature in Sánchez-Ramírez et al. (2016), Table 3.3 compares the metal column densities for the 15 DLAs common between the literature and XQ-100. ΔN(X) represents the difference in column density between the value determined in this work and the value in the literature sample (where a positive difference implies the XQ-100 column density is larger than what is in the literature). When both the literature and XQ-100 measurements yield a clean detection, I compared difference in column densities ($\Delta N(X)_{\rm det.}$) to the combined column density errors (summed in quadrature). Consistent values of $\Delta N(X)_{\rm det.}$ should be of the order of the combined error, although the quoted errors in metal column densities do not generally account for sources of error other than photon noise (e.g. continuum fitting) and can be larger. For most of the detections, the XQ-100 and high resolution literature values are consistent (to within 0.05 dex; the minimum error of a metal column density). The discrepant cases (the bolded ionic species in Table 3.3) are discussed in Appendix B.3. In all cases, the column densities derived in this work are adopted as they are consistent with the literature values (see Appendix B.3 for justification of discrepant cases).

For cases where both the XQ-100 and literature measurements are upper limits

[2]The elements are: N, O, Mg, Al, Si, S, Ca, Ti, Cr, Mn, Fe, Co, Ni, and Zn.

Table 3.2 X-Shooter metal column densities for J0003−2603 (z_{abs}=3.390)

Ion	Line	λ Å	f	v_{min} km s^{-1}	v_{max} km s^{-1}	logN(X)	Included	logN$_{adopt}$
MgI	2852	2852.964	1.81E+00	-140	70	11.85 ± 0.03	Y	–
MgI								11.85 ± 0.05
MgII	2796	2796.352	6.12E-01	-220	200	> 13.91	Y	–
MgII	2803	2803.531	3.05E-01	-200	170	> 14.04	Y	–
MgII								> 14.04
SiII	1526	1526.707	1.27E-01	-200	60	> 14.37	Y	–
SiII	1808	1808.013	2.19E-03	-10	70	< 14.98	Y	–
SiII								14.36–14.98
PII	1532	1532.533	7.61E-03	-20	50	< 13.73	Y	–
PII								< 13.73
CaII	3934	3934.777	6.50E-01	-20	50	< 11.81	Y	–
CaII	3969	3969.591	3.22E-01	-20	50	< 11.82	N	–
CaII								< 11.81
TiII	1910	1910.750	2.02E-01	-20	50	< 12.24	Y	–
TiII								< 12.24
CrII	2056	2056.254	1.05E-01	-40	70	< 13.34	N	–
CrII	2062	2062.234	7.80E-02	-30	50	13.07 ± 0.04	Y	–
CrII	2066	2066.161	5.15E-02	-20	75	< 13.49	N	–
CrII								13.07 ± 0.05
MnII	2594	2594.499	2.71E-01	-60	25	< 12.39	Y	–
MnII	2606	2606.462	1.93E-01	-90	60	< 13.57	N	–
MnII								< 12.39
FeII	1608	1608.451	5.80E-02	-60	70	> 14.35	N	–
FeII	1611	1611.200	1.36E-03	-20	50	14.75 ± 0.04	Y	–
FeII	2344	2344.214	1.14E-01	-110	60	> 14.02	N	–
FeII	2374	2374.461	3.13E-02	-100	60	> 14.34	N	–
FeII								14.75 ± 0.05
NiII	1709	1709.604	3.24E-02	-20	50	13.42 ± 0.04	Y	–
NiII	1751	1751.916	2.77E-02	-40	70	< 13.88	N	–
NiII								13.42 ± 0.05
ZnII	2026	2026.136	4.89E-01	-20	50	12.10 ± 0.05	Y	–
ZnII	2062	2062.664	2.56E-01	-20	50	< 12.35	N	–
ZnII								12.10 ± 0.05

($\Delta N(X)_{lim.}$; positive values indicate that the XQ-100 limit is higher than the literature), 4 of 10 XQ-100 upper limits are more constraining than the literature column density derived from Keck/ESI data with comparable resolution. For a constant signal-noise, higher-resolution instruments provide more constraining upper limits due to their ability to resolve narrower features within the fluctuations of the continuum. For all cases where the literature provides better limits (or detections, as in the case for Ni II and Zn II in J2344+0342 at z_{abs}= 3.22), I adopted the literature values.

Continuum-fitting errors

As a baseline for comparison, the spline continuum-fitting (presented in Section 2.2.1) was done two times to assess the random errors of the continuum fit. The median difference in column density for all metal lines in the two iterations is 0.0 dex, with an interquartile range of 0.02 dex and 67% of column densities being within ±0.01 dex. Although the 3σ upper limits are not included in this calculation, it is worth noting that derived column densities for these limits are sensitive to the continuum placement.

3.2.2 UVES data for J0034+1639

The X-Shooter spectrum of the z_{abs}= 4.25 DLA (Figure B.4) towards J0034+1639 suggests a very low metallicity system ([Fe/H]= -2.82 ± 0.11, fourth lowest [Fe/H] to date; Cooke et al., 2015, see Table B.5). To confirm the column densities of this metal-poor DLA are free of undetected contamination and saturation, as well as attempting to measure Fe-peak elements such as Ni II to pinpoint the underlying supernovae population (Cooke et al., 2013), I obtained VLT/UVES (Dekker et al., 2000) data towards the sightline J0034+1639. The observing program (PI: T. Berg; Program number 094.A-0223A) was organized in 5 observing blocks (OBs) of 48 min each for a total of 4 hours of on-target integration to obtain a signal-noise of 20–25 pixel^{-1}. I used the dichroic DIC-2 at the standard setting of 437+760 to obtain wavelength coverage between 6000Å–9000Å (slit width 0.8″; $R \sim 60000$). The data were reduced using the standard UVES data-reduction software in Reflex[3]. After correcting for the heliocentric velocity, the five OBs were median combined without weights using IRAF's scombine, whilst the error spectra were combined in quadrature. The

[3] http://www.eso.org/sci/software/reflex/

Table 3.3 N(X) comparison between XQ-100 and literature

QSO sightline	z_{abs}	Ion	$\log N(X)_{XQ100}$	$\log N(X)_{Lit.}$	$\Delta N(X)_{det.}$	$\Delta N(X)_{lim.}$	Lit. Instrument(s)	Ref.
J0003-2603	3.390	Cr II	13.07 ± 0.05	13.09 ± 0.03	-0.02 ± 0.06	–	UVES,HIRES	1,2
–	–	**FeII**	14.75 ± 0.05	14.87 ± 0.03	-0.12 ± 0.06	–	UVES,HIRES	1,2
–	–	Ni II	13.42 ± 0.05	13.39 ± 0.03	$+0.03 \pm 0.06$	–	UVES,HIRES	1,2
–	–	Zn II	12.10 ± 0.05	12.01 ± 0.05	$+0.09 \pm 0.07$	–	UVES,HIRES	1,2
J0134+0400	3.692	Si II	< 14.36	> 14.26	–	–	ESI,UVES	3,4
–	–	Fe II	13.44 ± 0.05	13.51 ± 0.07	-0.07 ± 0.09	–	ESI,UVES	3,4
J0134+0400	3.772	**SiII**	15.30 ± 0.05	15.46 ± 0.02	-0.16 ± 0.05	–	ESI,UVES	3,5
–	–	Cr II	< 12.83	< 13.24	–	-0.41	ESI,UVES	3,5
–	–	Fe II	14.97 ± 0.05	> 14.87	–	–	ESI,UVES	3,5
–	–	**NiII**	13.84 ± 0.05	13.98 ± 0.03	-0.14 ± 0.06	–	ESI,UVES	3,5
–	–	Zn II	12.88 ± 0.05	< 13.10	–	–	ESI,UVES	3,5
J0255+0048	3.256	Si II	15.33 ± 0.05	15.32 ± 0.04	$+0.01 \pm 0.06$	–	HIRES	2
–	–	Fe II	> 14.75	14.76 ± 0.01	–	–	HIRES	2
–	–	**NiII**	< 13.44	13.61 ± 0.07	–	–	HIRES	2
J0255+0048	3.914	Si II	15.02 ± 0.05	> 14.19	–	–	HIRES	2
–	–	S II	14.73 ± 0.05	14.72 ± 0.01	0.01 ± 0.05	–	HIRES	2
–	–	**NiII**	13.50 ± 0.05	13.27 ± 0.04	$+0.23 \pm 0.06$	–	HIRES	2
J0307-4945	4.466	Si II	14.59 ± 0.05	14.68 ± 0.07	-0.09 ± 0.09	–	UVES	6
–	–	Fe II	14.11 ± 0.05	14.21 ± 0.17	-0.10 ± 0.18	–	UVES	6
–	–	Ni II	< 13.43	< 12.60	–	0.83	UVES	6
J0424-2209	2.982	Cr II	< 13.01	< 12.90	–	$+0.11$	ESI	3
–	–	Ni II	< 13.47	< 13.37	–	0.10	ESI	3
–	–	Zn II	< 12.28	< 12.17	–	0.11	ESI	3
J0747+2739	3.424	Fe II	14.47 ± 0.05	> 14.43	–	–	ESI	3
–	–	Ni II	< 13.46	< 13.27	–	0.19	ESI	3
J0747+2739	3.901	Si II	14.08 ± 0.05	14.03 ± 0.01	$+0.05 \pm 0.05$	–	ESI	3
–	–	Fe II	14.03 ± 0.05	< 13.80	–	–	ESI	3
–	–	Ni II	< 13.45	< 13.11	–	0.34	ESI	3
J0955-0130	4.024	Fe II	14.31 ± 0.05	14.19 ± 0.08	$+0.12 \pm 0.09$	–	HIRES,ESI	2,7,8
–	–	Ni II	< 13.41	< 13.44	–	-0.03	HIRES,ESI	2,7,8
J1108+1209	3.397	SiII	< 13.77	> 13.63	–	–	ESI	9
–	–	Fe II	13.36 ± 0.05	< 13.72	–	–	ESI	9
J1421-0643	3.449	Cr II	< 12.84	< 12.71	–	0.13	UVES	5,10
–	–	**FeII**	14.05 ± 0.05	14.14 ± 0.02	-0.09 ± 0.05	–	UVES	5,10
–	–	Zn II	< 13.25	< 11.98	–	1.19	UVES	5,10
J1723+2243	3.698	Fe II	14.62 ± 0.05	> 14.57	–	–	ESI	3
–	–	Ni II	< 13.63	< 13.95	–	-0.32	ESI	3
J2239-0552	4.080	Fe II	14.00 ± 0.05	13.88 ± 0.12	$+0.12 \pm 0.13$	–	HIRES,ESI,UVES	8,11,12
–	–	Ni II	< 13.02	< 13.17	–	-0.15	HIRES,ESI,UVES	8,11,12
J2344+0342	3.220	Cr II	13.38 ± 0.05	13.34 ± 0.10	$+0.04 \pm 0.11$	–	UVES,ESI	3,13
–	–	Ni II	< 13.58	13.59 ± 0.11	–	–	UVES,ESI	3,13
–	–	Zn II	< 12.85	12.23 ± 0.30	–	–	UVES,ESI	3,13

Bolded species indicate cases of column density discrepancies between XQ-100 and the literature, and are discussed in Section B.3.

$\Delta N(X)$ is positive when the XQ-100 column density is larger than the literature value.

References – (1) Molaro et al. (2000). (2) Prochaska et al. (2001). (3) Prochaska et al. (2003b). (4) Petitjean et al. (2008). (5) Noterdaeme et al. (2008). (6) Dessauges-Zavadsky et al. (2001). (7) Prochaska & Wolfe (2000). (8) Songaila & Cowie (2002). (9) Penprase et al. (2010). (10) Akerman et al. (2005). (11) Lu et al. (1996). (12) Henry & Prochaska (2007). (13) Dessauges-Zavadsky et al. (unpublished).

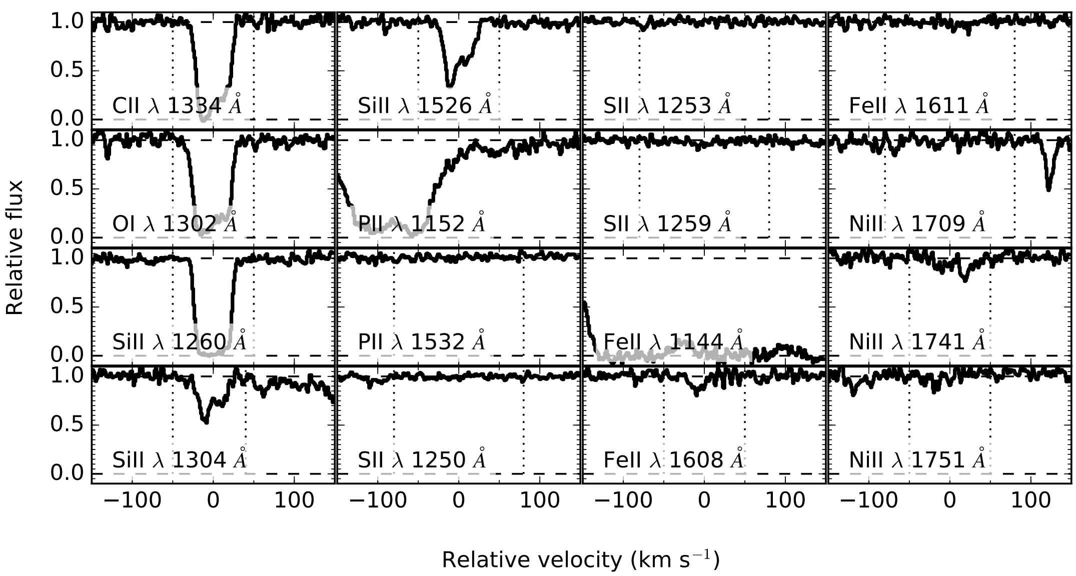

Figure 3.4 Velocity profiles of the UVES spectrum towards J0034+1639 (z_{abs}= 4.25). Vertical dashed lines represent the velocity limits of the AODM integration.

combined spectrum was then continuum normalized using the cubic spline software presented in Section 3.2.

Metal column densities for the 3 DLAs along the J0034+1639 sightline were derived using the AODM, as in Section 3.2. As UVES can resolve down to the kinematic structure of the DLA clouds ($\sim$ 10 km s^{-1}), I used the measured FWHM of the strongest component of an unsaturated metal line profile as the minimum equivalent width observable. This FWHM is used in Equation 3.4 to determine the 3σ limits in the absorber. The signal-noise ratio for the 3σ upper-limits was computed within the bounds of the AODM limits. Figure 3.4 and Table 3.4 present the velocity profiles of the absorption lines towards the MPDLA and the corresponding column densities. The data for the other absorbers are presented in the same format in Appendix B.2.

In general, I preferentially adopted the UVES column density as the higher resolution provides an accurate determination of the absorption profile and the data have a similar or higher signal-noise ratio. The one exception where we adopt the XQ-100 value is due to a lack of strong, uncontaminated Fe II lines covered in the UVES spectrum required to derive an accurate column density. We note that the absorption in the Ni II λ 1741 Å panel of Figure 3.4 is likely contaminated as it does not produce a

Table 3.4 UVES metal column densities for J0034+1639 (z_{abs}=4.251)

Ion	Line	λ Å	f	v_{min} km s^{-1}	v_{max} km s^{-1}	logN(X)	Included	logN$_{adopt}$
CII	1334	1334.532	1.28E-01	-50	50	> 14.24	Y	–
CII								> 14.24
OI	1302	1302.168	4.89E-02	-50	50	14.78 ± 0.02	Y	–
OI								14.78 ± 0.05
SiII	1260	1260.422	1.01E+00	-50	50	> 13.68	N	–
SiII	1304	1304.370	9.40E-02	-50	40	13.71 ± 0.02	Y	–
SiII	1526	1526.707	1.27E-01	-50	50	13.71 ± 0.01	Y	–
SiII								13.71 ± 0.05
PII	1532	1532.533	7.61E-03	-80	80	< 13.66	Y	–
PII								< 13.66
SII	1250	1250.584	5.43E-03	-80	80	< 13.79	N	–
SII	1253	1253.811	1.09E-02	-80	80	< 13.64	N	–
SII	1259	1259.519	1.66E-02	-80	80	13.65 ± 0.08	Y	–
SII								13.65 ± 0.08
FeII	1608	1608.451	5.80E-02	-50	50	13.23 ± 0.06	Y	–
FeII	1611	1611.200	1.36E-03	-80	80	< 14.56	N	–
FeII								13.23 ± 0.06
NiII	1709	1709.604	3.24E-02	-80	80	< 13.33	N	–
NiII	1741	1741.553	4.27E-02	-50	50	< 13.48	N	–
NiII	1751	1751.916	2.77E-02	-50	50	< 13.24	Y	–
NiII								< 13.24

consistent measurement with the derived column density limits for the Ni II λ 1709Å and 1751Å lines.

3.2.3 XQ-100 sample properties

To briefly highlight the properties of the 41 DLAs observed in the XQ-100 survey, Figure 3.5 shows the metallicity (top panel) and metallicity-redshift (bottom panel) distributions of the XQ-100 sample (red colours) relative to the DLA literature sample compiled in Berg et al. (2015a, black data). The metallicities ([M/H]; see Table 3.5) were derived following a similar scheme outlined in Rafelski et al. (2012), where they choose (in order of decreasing preference) S, Si, Zn, and Fe as the metallicity tracer. Rafelski et al. (2012) add a +0.3 dex correction to Fe to account for the difference in observed [α/Fe]. We adopt the Asplund et al. (2009) solar scale for all metallicity calculations. Figure 3.5 emphasizes that the XQ-100 DLAs are predominantly between redshifts z_{abs}=3–4.5, and as a result appear more metal-poor than the literature (which includes the lower redshift and thus higher metallicity DLAs; Rafelski et al., 2012). A Kolmogorov-Smirnov (KS) test rejects the null hypothesis that the metallicity distributions of the literature and XQ-100 DLA samples are drawn from the same distribution at 0.3% confidence. However, when both the literature and XQ-100 samples are restricted to z_{abs}=3–4.5, the KS test rejects the null hypothesis at 90.6% confidence.

Following the analysis techniques described in Prochaska & Wolfe (1997), I assessed the kinematic characteristics of the XQ-100 DLA sample. In particular, the velocity width v_{90} was calculated. v_{90} corresponds to 90% of the integrated optical depth using one low-ion transition per DLA (listed in Table 3.5). The absorption line used for calculating v_{90} for each DLA was selected according to the spectral signal-noise ratio, avoiding saturated or weak absorption profiles. The optical depth per pixel was calculated from the normalized flux values and then smoothed by a boxcar with width of 22 km s^{-1} as in Prochaska & Wolfe (1997). From these smoothed optical depth arrays, the velocity width comprising 90% of the integrated optical depth between the AODM integration bounds was calculated.

Adopting the results of Prochaska et al. (2008a) who also analyzed a set of echellette observations ($R \approx 8,000$), I have reduced the raw v_{90} values to correct for instrumental broadening. Specifically, I lowered the raw v_{90} measurements by 30, 17, and 25 km/s for the UVB, VIS, and NIR arms respectively. These corrections correspond to $\approx 40\%$ of the FWHM of the instrumental line-spread-function for our X-Shooter configuration. The final, reported v_{90} values are presented in Table 3.5.

Using the measured z_{abs} and v_{90} for the XQ-100 DLAs, we compared the derived metallicities from the [M/H]-z_{abs}-v_{90} relation in Neeleman et al. (2013) to our directly-measured [M/H]. We find good agreement between the two metallicities (mean difference of 0.02 dex), with a root-mean-squared scatter between the two metallicities (0.32 dex) that is consistent with the scatter observed in Neeleman et al. (2013, 0.37 dex).

3.3 Metal abundance analysis

3.3.1 The chemical evolution of DLAs

Cosmological metal evolution

Many of the earlier surveys of DLAs used to measure $\langle Z/Z_{\odot}\rangle$ were limited by small sample sizes or to a moderate redshift range ($z_{abs}\sim 3$). To boost the statistics of previous surveys, particularly at higher redshifts ($z_{abs}\geq 4.7$), Rafelski et al. (2012, R12) and (Rafelski et al., 2014, R14) crafted a metallicity-unbiased sample of literature and newly-observed DLAs for a total of 219 absorbing systems ($0 \leq z_{abs}\leq 5$). R12 and R14 recovered the steady metallicity evolution previously observed in the literature ($\log(\langle Z/Z_{\odot}\rangle) = (-0.2 \pm 0.03)z_{abs} - (0.68 \pm 0.09)$; Pettini et al., 1999; Prochaska et al., 2003a; Jorgenson et al., 2013), but the additional R14 observations of DLAs at $z_{abs}\geq 4.7$ indicated a distinct break in this metallicity evolution, suggesting that the metallicity of neutral gas rapidly evolved in the first couple of Gyr of the Universe, or is diluted by large cold flows of pristine gas onto the DLA host galaxies.

The sample of DLAs presented in R12 and R14[4] is the largest, blind census of DLAs observed at high enough resolution to obtain accurate metal abundances. The addition of the 41 DLAs in XQ-100 to the R14 sample grows the number of DLAs by nearly 20% across all redshift ranges, and $\sim 28\%$ when restricted to the redshift range of XQ-100 (a redshift range in which R12 states has the most influence on the evolution of $\langle Z/Z_{\odot}\rangle$). It is therefore important to assess the impact of including the XQ-100 DLAs on the evolution of $\langle Z/Z_{\odot}\rangle$.

[4]Note that the R12 and R14 datasets include a literature compilation of data used for previous computations of $\langle Z/Z_{\odot}\rangle$, including Pettini et al. (1999) and Prochaska et al. (2003a).

Table 3.5 [M/H] and v_{90} measurements for the XQ-100 DLA sample

QSO	z_{abs}	[M/H] (ion)	Transition km s^{-1}	v_{90}
J0003−2603	3.390	-1.93 ± 0.11 (ZnII)	Cr II 2066	32
J0006−6208	3.203	-2.20 ± 0.15 (FeII)	Fe II 1608	32
J0006−6208	3.775	-0.94 ± 0.20 (ZnII)	Fe II 1608	54
J0034+1639	3.755	-1.89 ± 0.15 (FeII)	Fe II 2586	32
J0034+1639	4.251	-2.10 ± 0.13 (SII)	Si II 1526	43
J0034+1639	4.283	-1.59 ± 0.11 (SII)	Fe II 1608	109
J0113−2803	3.106	-1.11 ± 0.10 (SiII)	Si II 1808	219
J0124+0044	2.261	-0.85 ± 0.15 (SiII)	Si II 1808	142
J0132+1341	3.936	-2.04 ± 0.15 (SiII)	Fe II 1608	32
J0134+0400	3.692	-2.41 ± 0.10 (FeII)	Fe II 1608	10
J0134+0400	3.772	-0.91 ± 0.10 (SiII)	Si II 1808	109
J0234−1806	3.693	-1.31 ± 0.15 (FeII)	Fe II 2344	203
J0255+0048	3.256	-1.08 ± 0.10 (SiII)	Fe II 1608	208
J0255+0048	3.914	-1.92 ± 0.10 (SII)	S II 1253	21
J0307−4945	3.591	-1.48 ± 0.15 (FeII)	Fe II 2586	51
J0307−4945	4.466	-1.52 ± 0.10 (SiII)	Si II 1304	219
J0415−4357	3.808	-0.28 ± 0.20 (ZnII)	Si II 1526	131
J0424−2209	2.982	-1.86 ± 0.16 (ZnII)	Fe II 2600	13
J0529−3552	3.684	-2.38 ± 0.15 (SiII)	Si II 1526	21
J0747+2739	3.424	-1.58 ± 0.10 (FeII)	Fe II 1608	120
J0747+2739	3.901	-2.03 ± 0.15 (SiII)	Si II 1526	153
J0800+1920	3.946	-1.87 ± 0.10 (SiII)	Si II 1304	43
J0818+0958	3.306	-1.51 ± 0.10 (SiII)	Si II 1808	76
J0835+0650	3.955	-1.81 ± 0.10 (SiII)	Si II 1304	21
J0920+0725	2.238	-1.55 ± 0.15 (FeII)	Fe II 2374	98
J0955−0130	4.024	-1.54 ± 0.15 (FeII)	Fe II 2600	336
J1020+0922	2.592	-1.75 ± 0.10 (SiII)	Si II 1808	76
J1024+1819	2.298	-1.45 ± 0.10 (SiII)	Si II 1808	54
J1057+1910	3.373	-1.25 ± 0.11 (FeII)	Fe II 1608	307
J1058+1245	3.432	-1.85 ± 0.10 (SiII)	Mg II 2803	127
J1108+1209	3.397	-2.49 ± 0.10 (FeII)	C II 1334	32
J1108+1209	3.546	-1.15 ± 0.15 (SII)	Fe II 2374	70
J1312+0841	2.660	-1.50 ± 0.10 (FeII)	Fe II 2344	153
J1421−0643	3.449	-1.40 ± 0.15 (FeII)	Fe II 1608	43
J1517+0511	2.688	-2.06 ± 0.10 (SiII)	Fe II 1608	43
J1552+1005	3.601	-1.75 ± 0.11 (SII)	S II 1253	21
J1552+1005	3.667	-1.61 ± 0.10 (FeII)	Si II 1304	230
J1633+1411	2.882	-1.78 ± 0.15 (FeII)	Mg II 2803	13
J1723+2243	3.698	-1.03 ± 0.10 (FeII)	Fe II 2586	374
J2239−0552	4.080	-1.95 ± 0.10 (SiII)	Si II 1526	131
J2344+0342	3.220	-1.70 ± 0.32 (ZnII)	Cr II 2056	54

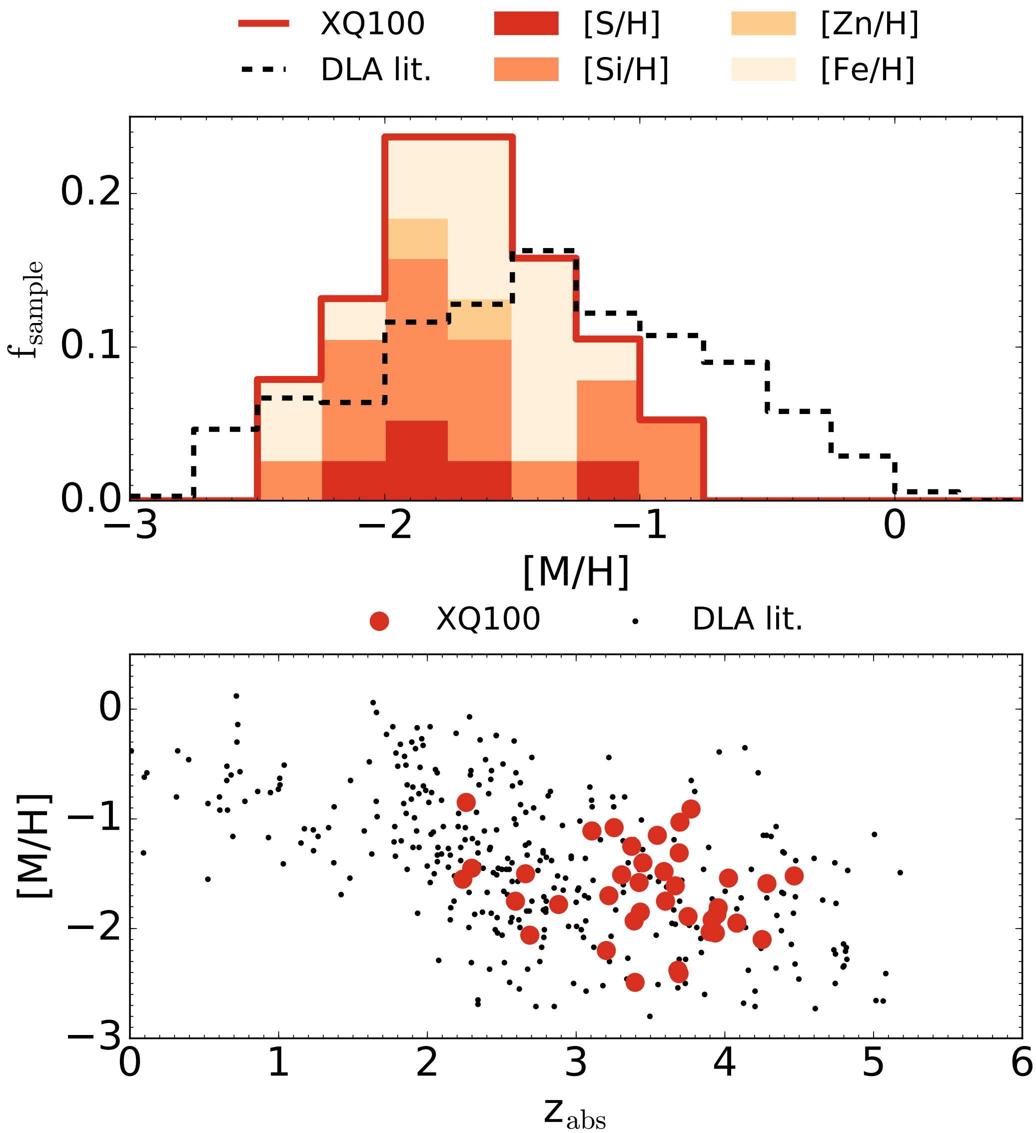

Figure 3.5 *Top Panel:* The metallicity distribution of the XQ-100 DLAs. The solid red line outlines the total metallicity distribution of the XQ-100 sample, whereas the shaded regions within each bin show the distribution of elements used as the metallicity indicator for the DLAs. The metallicity distribution of the literature DLA sample (Berg et al., 2015a) is shown by the black dashed line. *Bottom Panel:* The distribution of the XQ-100 (red circles) and literature DLAs (black points) in metallicity-redshift space.

Following the same bootstrap Monte Carlo resampling technique for computing $\Omega_{\rm HI}$ presented in Section 2.3.1, I computed $\langle Z/Z_{\odot}\rangle$ for the combined sample of XQ-100 and R14 DLAs (further denoted as XQ-100+R14 sample). In summary, for 10,000 Monte Carlo resamplings, a sample of 260 DLAs is drawn from the XQ-100+R14 sample (with replacement; note that this implies a given absorber can be reused in the same sample). For each sample, both the metallicity and H I column densities of the sample (XQ-100 values are tabulated in Tables 3.1 and 3.5) are randomly perturbed by the measurement error (assuming a Gaussian distribution), effectively creating a 'new' DLA sample. Note that this bootstrap Monte Carlo resampling is analogous to the bootstrap method presented in R12 and R14.

To compute $\langle Z/Z_{\odot}\rangle$ as a function of redshift, I used a sliding bin technique analogous to that presented in Section 2.3.1. However, rather than using a fixed redshift path as was done in Section 2.3.1, the redshift bin has a minimum width of 0.5 (e.g. $z_{\rm abs}$= 2.0 to $z_{\rm abs}$= 2.5). If there are less than 25 DLAs contained within the redshift range (the minimum number of DLAs in a redshift bin in R12), the minimum width is expanded by 0.01 until either the minimum number of DLAs is contained within the bin, or the highest redshift DLA is included in the bin. The median $\langle Z/Z_{\odot}\rangle$ (using Equation 3.1) is then computed within this redshift range, along with the percentiles of the resulting distribution corresponding to the 1σ and 2σ confidence intervals. The starting bin redshift is then shifted by 0.05 (i.e. 10% of the minimum redshift bin width), and the calculation is then repeated.

The solid blue line of Figure 3.6 shows the resulting median $\log(\langle Z/Z_{\odot}\rangle)$ evolution of the XQ-100+R14 combined DLA sample, with the dark and lighter blue shaded region representing the 1σ and 2σ confidence intervals. For reference, the R14 binned data-points are shown as the large black squares, while the translucent black and red points denote the individual R14 and XQ-100 DLAs (respectively). Using this sliding technique to compute $\langle Z/Z_{\odot}\rangle$ naturally recovers the drop in metallicity at high redshift previously seen by R14, although I note that the drop begins at a slightly lower redshift ($z_{\rm abs}\sim 4.6$[5]) than what was found previously in R12 and R14.

To compute the best-fit evolution of $\langle Z/Z_{\odot}\rangle$ as a function of $z_{\rm abs}$ and evaluate the associated errors, I reused the simulated Monte Carlo data to measure the linear evolution for all 10,000 resamplings of the simulation. For each resampled XQ-100+R14

[5]The redshift of the metallicity drop appears to be robust to a reasonable choice of redshift step size and width of the sliding bin. However, due to the low number of DLAs beyond $z_{\rm abs}\gtrsim 4.2$, choosing too large of redshift bin width (> 0.8) will wash out any metallicity drop as the bin will be dominated by the larger sample of DLAs at $z_{\rm abs}< 4.2$.

dataset, I computed an unweighted linear fit to the evaluated $\log(\langle Z/Z_{\odot}\rangle)$ within each of the sliding redshift bins. The data used in the fit was truncated by removing all redshift bins including $z_{\rm abs} \geq 4.7$, such that the best fit evolution matches the same range in redshift covered by R14. The best-fit relation was selected as the median slope and y-intercept of the 10,000 fits, with the 1σ errors using the $17^{\rm th}$ and $83^{\rm rd}$ percentiles. This resulting best-fit relation of $\log(\langle Z/Z_{\odot}\rangle) = -0.18^{+0.042}_{-0.043} z_{\rm abs} - 0.75^{+0.112}_{-0.115}$ (blue dashed line in Figure 3.6) is consistent with the best-fit relation obtained in R14 (black dotted line), given the $\sim 20\%$ increase in the DLA sample size.

Metal-poor DLA towards J0034+1639

Having examined the overall metallicity evolution of DLAs, I now focus on detailed abundance ratios to shed light on the nucleosynthetic history of DLA galaxies. Within the XQ-100 sample, I identified a MPDLA candidate towards J0034+1639 ($z_{\rm abs}=$ 4.2507), for which I followed up with higher resolution observations with VLT/UVES to confirm the derived metal column densities are free from contamination (see Section 3.2.2 for details on observations). The column densities for this MPDLA are presented in Table 3.4[6]. It is interesting to note that, although the [Fe/H] abundance (-2.82 ± 0.11) is the $4^{\rm th}$ lowest observed to date in a DLA (Cooke et al., 2015, and references therein), its metallicity using the Rafelski et al. (2012) scheme is much higher ([M/H]$= -2.40 \pm 0.11$; $24^{\rm th}$ lowest).

Table 3.6 shows the abundances for the metal-poor DLA towards J0034+1639, compared to the mean abundance derived from the metal-poor DLAs ($\langle [{\rm X/O}]_{\rm MPDLA}\rangle$) from the MPDLA sample in Cooke et al. (2011). The abundance ratios (relative to O) of C, Si, and Fe are consistent[7] with the typical MPDLA abundance pattern (although note that [Si/O] is almost 0.2 dex larger than the typical MPDLA measurement), implying consistency with yields from low-energy supernovae (Heger & Woosley, 2010; Cooke et al., 2011). Unfortunately, I was unable to place strong constraints on Ni and other Fe-peak abundances ([Ni/Fe]< 1.26), which Cooke et al. (2013, and references therein) have demonstrated to be a key discriminator of the supernovae energy.

[6] Note that most of these measurements use the UVES-derived column densities, but are supplemented by the XQ-100 column densities when there is no wavelength coverage.

[7] The [C/O] ratio is likely consistent with the typical MPDLA values, as the C II absorption is mildly saturated (see Figure 3.4).

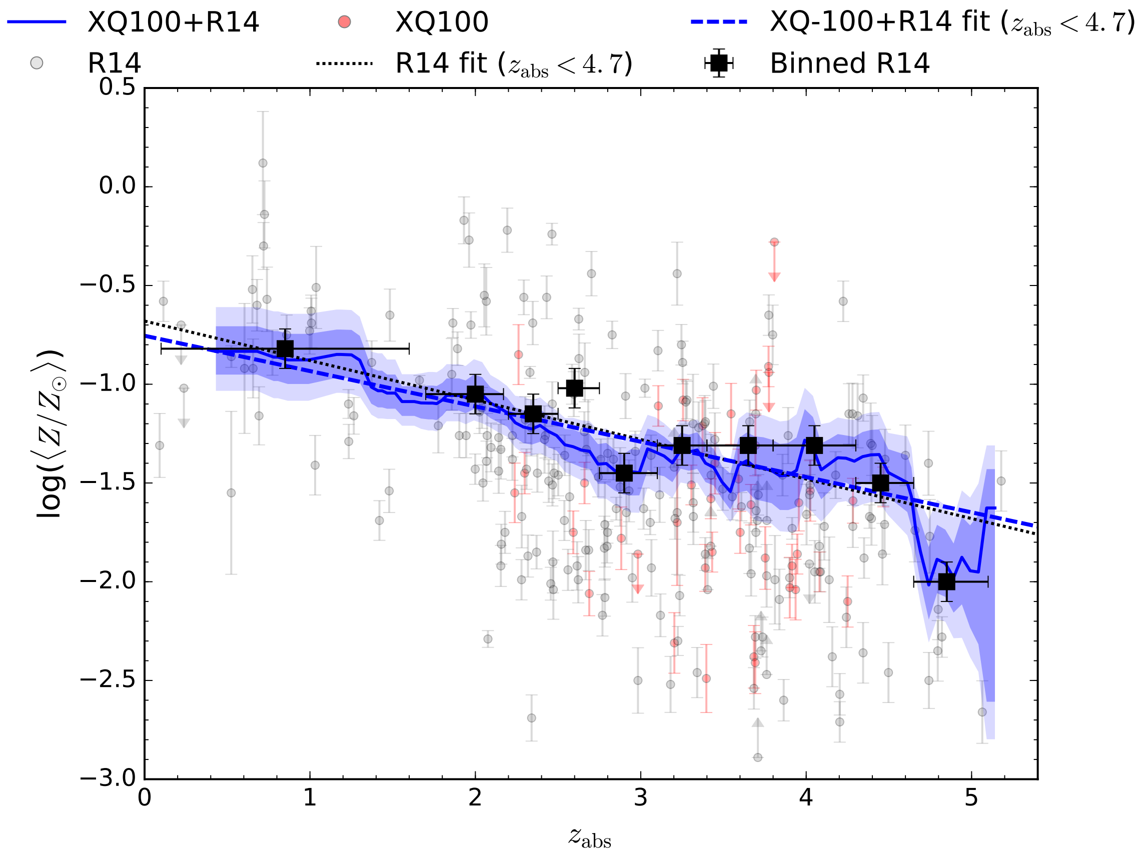

Figure 3.6 The evolution of the cosmological metallicity ($\log(\langle Z/Z_\odot \rangle)$) with redshift. The solid blue line represents the median $\log(\langle Z/Z_\odot \rangle)$ obtained from the Monte Carlo bootstrap simulation of the combined sample of XQ-100 (faded red circles) and Rafelski et al. (2014) DLAs (faded grey circles). The darker and lighter shaded regions denote the 1σ and 2σ confidence intervals (respectively) of the simulation, while the best fit metallicity evolution for the combine sample is given by the dashed blue line. For reference, the Rafelski et al. (2014) binned datapoints (black squares) and best fit metallicity evolution (black dotted line; only for systems with $z_{abs} < 4.7$) are shown.

Table 3.6 J0034+1639 MPDLA ($z_{abs} = 4.25$) abundances

Element	[X/H]	[X/O]	$\langle[X/O]_{MPDLA}\rangle^1$
O	-2.51 ± 0.12	–	–
C	> -2.79	> -0.28	-0.28 ± 0.12
Si	-2.40 ± 0.11	0.11 ± 0.16	-0.08 ± 0.10
Fe	-2.82 ± 0.11	-0.31 ± 0.16	-0.39 ± 0.12

[1]Mean MPDLA abundance from Cooke et al. (2011).

[Zn/Fe] and dust depletion

Dust depletion plagues DLA abundance analysis work, making it difficult to disentangle nucleosynthetic patterns from dust depletion effects. In particular, a dust-free Fe peak tracer is necessary to measure the intrinsic [α/Fe] ratio, an important tracer of star formation history (Tinsley, 1979; Venn et al., 2004; Tolstoy et al., 2009). In general, the quasar absorption line community has either used elements that are relatively unaffected by depletion (such as S and Zn; e.g. Pettini et al., 1997; Centurión et al., 2000; Vladilo et al., 2011) or modelled dust depletions based on chemical evolution assumptions or the uniformity of dust depletion across all galaxies (e.g. Jenkins, 2009; Vladilo et al., 2011; De Cia et al., 2016). For elements X and Y, the dust-corrected [X/Y] abundance ratio is commonly represented as:

$$[\mathrm{X/Y}]_{\mathrm{int}} = [\mathrm{X/Y}]_{\mathrm{obs}} + \delta_{[\mathrm{X/Y}]} \tag{3.5}$$

where $[\mathrm{X/Y}]_{\mathrm{int}}$ and $[\mathrm{X/Y}]_{\mathrm{obs}}$ are the respective intrinsic (i.e. dust corrected) and observed (uncorrected) abundance ratios, and $\delta_{[\mathrm{X/Y}]}$ is the relative dust depletion ratio of element X to Y.

One of the most prominent assumptions is that Zn is a dust-free proxy of the Fe peak (i.e. $[\mathrm{Zn/Fe}]_{\mathrm{int}} = 0$; Pettini et al., 1994, 1997; Vladilo, 2002a,b). The assumption that Zn traces Fe was motivated by early observations of Galactic stellar abundances showing [Zn/Fe]~ 0 over a range of metallicities (Sneden & Crocker, 1988; Sneden et al., 1991; Chen et al., 2004; Nissen et al., 2004). However, with the search for metal-poor stars extending to lower metallicities (e.g. Prochaska et al., 2000; Nissen et al., 2007), stellar [Zn/Fe] showed deviations from solar suggesting that Zn does not necessarily trace Fe; leading some authors to question whether Zn traces Fe in DLAs (such as Prochaska & Wolfe, 2000; Nissen & Schuster, 2011; Rafelski et al., 2012). Recently, both Berg et al. (2015a) and Skúladóttir et al. (2017) compared [Zn/Fe] in stars in the Milky Way and local dwarf spheroidal (dSph) galaxies, finding a large scatter of [Zn/Fe] at $-2.0 <$[Zn/H]< -0.5. In particular, many (but not all) Local Group dwarf galaxy stars exhibit subsolar [Zn/Fe] indicating that Zn is not necessarily a nucleosynthetic tracer of the Fe-peak elements at [Zn/H]≥ -1.5 (i.e. $[\mathrm{Zn/Fe}]_{\mathrm{int}} \neq 0$).

In order to investigate the possibility of intrinsically non-solar [Zn/Fe] ratios, Berg et al. (2015a) inferred the dust-corrected values of [Zn/Fe] using a novel method. Rather than using modelled corrections which require assumptions that all DLAs are identical and have similar chemical abundance patterns to the Milky Way (such as Jenkins, 2009; Vladilo et al., 2011; De Cia et al., 2016), Berg et al. (2015a) assumed two things:

1) The process of depletion onto dust is the same in all galaxies. Hence, the relative depletion pattern of any two elements should be the same in each galaxy. This assumptions was motivated by the Jenkins (2009) dust depletion correction method.

2) All α-elements trace each other in a given DLA (e.g. $[\mathrm{Si}/\alpha]_{\mathrm{int}} = 0$, for α-elements Si and α), and that the measured ratio of two α-elements can therefore be used as a tracer of dust depletion ratio of those two elements;

$$[\mathrm{Si}/\alpha]_{\mathrm{int}} = 0 = [\mathrm{Si}/\alpha]_{\mathrm{obs}} + \delta_{[\mathrm{Si}/\alpha]}, \tag{3.6}$$

and thus

$$[\mathrm{Si}/\alpha]_{\mathrm{obs}} = -\delta_{[\mathrm{Si}/\alpha]}. \tag{3.7}$$

Using the relative depletions seen toward Galactic ISM sightlines (Savage & Sembach, 1996), I noted in Berg et al. (2015a) that the relative dust depletion ratio of $\delta_{[\mathrm{Zn/Fe}]}$ is very similar to that of $\delta_{[\mathrm{Si/Ti}]}$ (to within 0.1 dex). Thus by measuring $[\mathrm{Si/Ti}]_{\mathrm{obs}}$, one could obtain a proxy of $\delta_{[\mathrm{Zn/Fe}]}$ for any galaxy or DLA system. However, I caution that assumption 1) of uniform relative depletion patterns needs to be tested in a large sample of galaxies (see measurements for the Magellanic clouds; Tchernyshyov et al., 2015).

Although the Berg et al. (2015a) analysis of dust corrected [Zn/Fe] is strongly suggestive of sub-solar ratios in DLAs, my sample was limited to the 43 systems (of which only 10 were detections) for which Ti measurements are available. This limitation is driven by the only accessible, yet weak, Ti II λ 1910 Å line in optical spectra for the majority of the DLA sample. Previous surveys of Mg II abundances with high resolution spectroscopy have been limited to $z_{\mathrm{abs}}\sim$2–3 DLAs (e.g. Prochaska et al., 2003b; Dessauges-Zavadsky et al., 2006; Prochaska et al., 2007; Noterdaeme et al., 2008). With the additional IR coverage that X-Shooter provides, I have unprecedented access to absorption lines of α-elements that are not typically observed in the optical; particularly in absorbers at redshifts 3–4. These lines include: Mg, Ca, as well as stronger Ti lines (relative to Ti II λ 1910Å; Ti II λ 3073Å, 3242Å, and 3384Å).

With the XQ-100 DLA sample I can further test the intrinsic [Zn/Fe] ratio of DLAs, by using the new Ti II abundances, as well as other α-elements ratios ([Mg/Si] and [Ca/Si]) as additional dust-depletion proxies. Figure 3.7 shows the DLA dust-corrected [Zn/Fe] abundances (coloured circles) as a function of metallicity using [Si/Ca] (top panel), [Si/Mg] (middle panel), and [Si/Ti] (bottom panel) as tracers for $\delta_{[Zn/Fe]}$. For reference, the Galactic (grey points) and dSph (grey squares) stellar trends of [Zn/Fe] are shown in each panel.

The difficulty of using Mg II and Ca II is that the differential depletions $\delta_{[Si/Mg]}$ and $\delta_{[Si/Ca]}$ are much different than $\delta_{[Zn/Fe]}$ in Galactic ISM sightlines (differences of +0.8 and −1.4 dex, respectively; Savage & Sembach, 1996). The two horizontal dashed lines in each panel constrain the region where the dust-corrected [Zn/Fe] could be consistent with solar [Zn/Fe] based on the difference in differential depletions $\delta_{[Si/\alpha]}$ and $\delta_{[Zn/Fe]}$ in the Milky Way. DLA points below the lowest line are consistent with intrinsically subsolar [Zn/Fe], and DLAs above the higher line likely have supersolar [Zn/Fe].

Unfortunately, the addition of Ti abundances from the XQ-100 DLA sample (red circles) does not provide much additional insight on the intrinsic nature of [Zn/Fe] in DLAs previously identified by Berg et al. (2015a) (blue circles). One of the XQ-100 DLAs has a dust-corrected [Zn/Fe]$\sim$ 0.3 dex. Although supersolar, this one system is consistent with both Milky Way and dSphs stellar [Zn/Fe] abundances (Berg et al., 2015a). Although the Ti II lines accessible in the NIR are nominally stronger than those in the optical, the typical detection limits of Ti II from the lower resolution X-Shooter spectra are not as sensitive as the measurements available from UVES or HIRES. It is worth noting that of the 38 cases where Ti II abundances were measured in the XQ-100 DLAs, 28 abundances were preferentially adopted based on the Ti II lines in the NIR arm rather than the Ti II λ 1910Å line. Therefore the use of NIR lines can be a useful tool to obtain more constraining Ti II abundances in DLAs.

The additional 5 Ca II robust upper limits (to the single detection in the literature) in the left panel of Figure 3.7 further support that DLAs span the same range of [Zn/Fe] as dSphs seen by Berg et al. (2015a), suggesting that DLAs share a similar nucleosynthetic history as Galactic dSphs. It is worth noting that Ca II (excitation potential of 11.87eV) is not the dominant ionization state of Ca in DLAs (e.g. Wild et al., 2006), suggesting that the measured N(Ca II) may require significant ionization corrections.

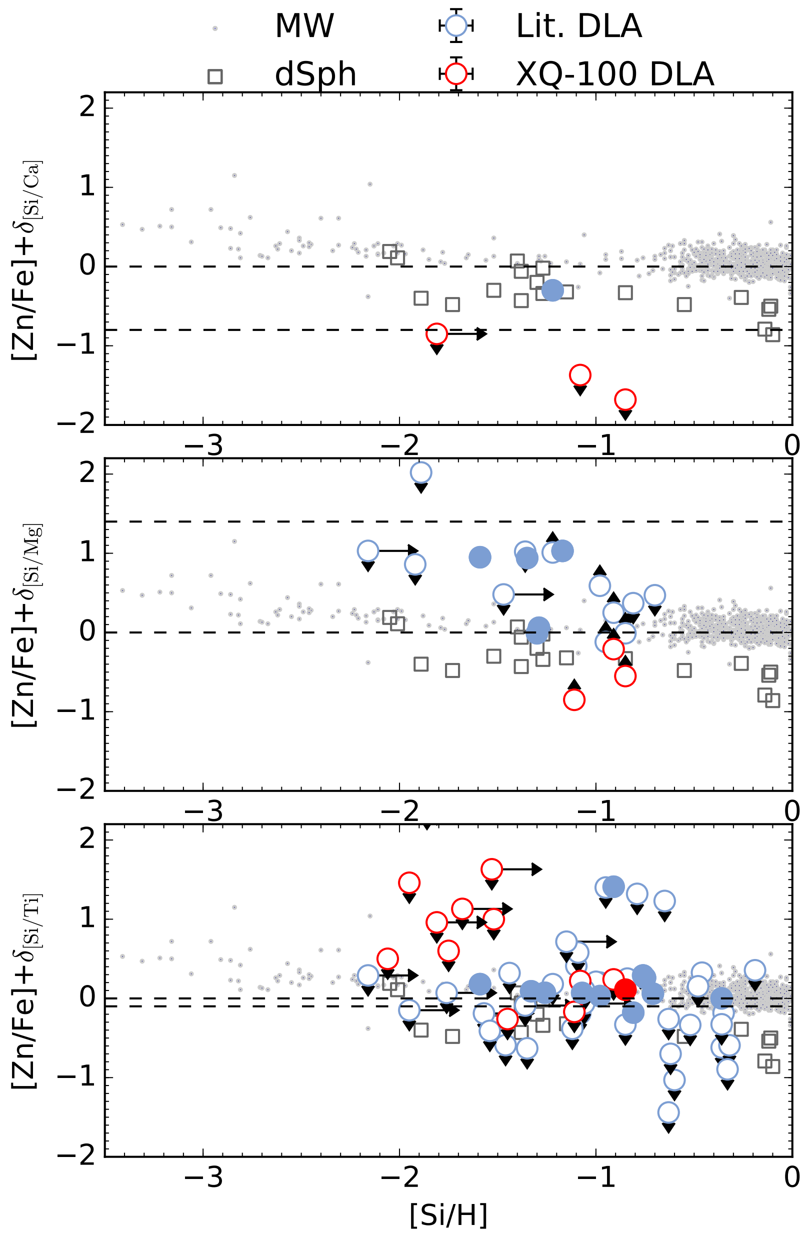

Figure 3.7 Dust-corrected [Zn/Fe] DLA abundances (XQ-100 are in red, literature DLAs in blue) relative to stellar [Zn/Fe] (grey points are the Milky Way, dark grey squares are dSphs) from Berg et al. (2015a). Larger, filled DLA circles represent detections, whereas the unfilled circles are limits. The dust correction is determined by subtracting the ratio of two α-elements of different relative dust depletions ([Si/Ca] top panel; [Si/Mg] middle panel; [Si/Ti] bottom panel). The two dashed lines bound the region where [Zn/Fe] may be consistent with solar, such that measurements below the line are consistent with subsolar [Zn/Fe]. In addition to [Si/Ti], [Si/Ca] can also constrain the intrinsic [Zn/Fe] in DLAs. Both of these ratios indicate that DLAs are consistent with the subsolar values seen in dSphs (Berg et al., 2015a). This subsolar [Zn/Fe] is likely nucleosynthetic in origin.

3.3.2 Signatures of environment in DLA abundances

Multiple DLAs

Previous work by Lopez & Ellison (2003) on 3 MDLA systems found a slight deficit of [α/Fe] relative to the typically observed DLA. They suggested that the low [α/Fe] is due to environmental effects truncating star formation. With the large increase in DLA abundance measurements over the past decade, the robustness of these results can be tested. Following Lopez & Ellison (2003), I identified MDLAs in the XQ-100 and in the Berg et al. (2015a) literature DLA samples as systems of two or more absorbers within 500 km $s^{-1} \leq \Delta v \leq 10,000$ km s^{-1} of each other. 6 and 21 MDLAs from the XQ-100 and the literature samples (respectively) were identified (Table 3.1). Using the measured [α/Fe] from literature and XQ-100 DLAs, I tested the potential enhancement by comparing each MDLA galaxy with a control-matched sample of intervening DLAs from the literature sample. The control matching technique accounts for the intrinsic evolution of similar DLAs, allowing a comparative test of different environments.

The control matching was completed for each MDLA by selecting all DLAs within the pool of literature DLAs with a redshifts and metallicity identical to the MDLA, within a prescribed tolerance. I imposed that the DLA control pool are not classified as MDLAs or PDLAs ($\Delta v_{\rm QSO} < 5000$ km s^{-1} from the QSO) to not include any potential metallicity bias (Ellison et al., 2010). The matching tolerance for metallicity was set by the error in the MDLA's metallicity. The matching tolerance for redshift was adopted based on the known redshift evolution of mean metallicity ([M/H]$\propto -0.2$ $z_{\rm abs}$; Pettini et al., 1997; Rafelski et al., 2012, 2014). The error in metallicity provides a relative spread in redshifts for a DLA to have undergone a similar metal-enrichment history. Using the slope of the redshift-metallicity evolution, I calculated the redshift tolerance ($\delta z_{\rm abs}$) using $\delta z_{\rm abs} = \frac{\delta[\rm M/H]}{0.2}$, where δ[M/H] is the error in the metallicity of the MDLA.

To ensure a representative control-matched sample, I required that each MDLA had at least 5 matched control DLAs. Each of the matched control DLAs must have at least 5 detections of both Si and Fe to compute a median [α/Fe]. If these criteria were not met within the initial tolerances, the size of the two matching criteria are repeatedly increased in small increments until a sufficient number of control matched DLAs were obtained. The metallicity bin grew by ± 0.025 dex increments (15–25% of the typical error in metallicity), while the redshift criteria grew by ± 0.125 ($\sim$20% of the associated error due to metallicity evolution). However, expansions were stopped after 10 iterations to ensure that the control-matched sample still resembles the MDLA, effectively matching within $\sim 3\sigma$ of $z_{\rm abs}$ and [M/H]. These criteria result in controls samples being identified for all MDLAs, with only 3 MDLAs requiring more than 2 expansions. The median number of matched control DLAs is 14 per MDLA, with 25% of MDLAs having 19 or more (up to 37) control DLAs matched.

The left panel of Figure 3.8 shows the relative change of [α/Fe] (Δ[α/Fe]) in MDLAs compared to their control-matched counterparts, as a function of N(H I). Δ[α/Fe] is computed as the difference in [Si/Fe] between the MDLA absorber and median [Si/Fe] of the control-matched DLAs, such that a positive Δ[α/Fe] implies that the MDLA has a higher [α/Fe] than its control sample. Note that, although all MDLAs are matched, only 14 of the 27 MDLAs have measured Δ[α/Fe] due to lack of Si and Fe column densities. Although Fe is depleted onto dust, the relative comparison of [α/Fe] of MDLAs and control DLAs at a fixed metallicity should remove the effects of dust depletion, as the depletion of refractory elements appears to scale with metallicity in DLAs (e.g. Pettini et al., 1997; Ledoux et al., 2002; Prochaska & Wolfe, 2002; Berg et al., 2015a; De Cia et al., 2016). For reference, the MDLAs from Lopez & Ellison (2003) are shown as large squares, and are included in the analysis. The grey points are the measured Δ[α/Fe] from repeating the matching procedure on all control DLAs. The errors on the MDLA points were derived from the spread in the [α/Fe] of the control sample using the jackknife technique;

$$\sigma_{jack} = \sum_{i=1}^{N} \sqrt{\frac{N-1}{N}(med(N) - med(N-1))^2} \tag{3.8}$$

where N is the number of DLAs, $med(N)$ is the median of the entire sample, and $med(N-1)$ is the median of the sample with the $i^{\rm th}$ DLA removed. The colour of the MDLA points indicates the velocity separation of the MDLAs from their counterpart (Table 3.1). The median Δ[α/Fe] (and σ_{jack}) for the MDLAs and control sample are 0.06 ± 0.01 dex and -0.01 ± 0.00[8] dex (respectively).

The right panel of Figure 3.8 shows the distribution of Δ[α/Fe] for both the MDLA and control samples. The p-value from the Anderson-Darling (AD) test ($p_{\rm AD}$)[9] rejects the null hypothesis that the two samples are drawn from the same parent sample at

[8] σ_{jack} is much smaller than 0.01 dex, and is thus quoted to be 0 dex.

[9] I preferentially used the AD test over a KS test as the AD test is independent of the shape of the distribution, and is more sensitive to discrepancies in the tails of the distribution.

$\sim$ 31% confidence. This test suggests MDLAs likely do not show any deficit (or enhancement) in [α/Fe] relative to the typical DLA, underscoring the need for a more robust comparison of MDLAs to single intervening DLAs in comparison to the work done in Lopez & Ellison (2003).

Note that the Berg et al. (2015a) literature sample includes surveys that have purposefully observed DLAs of specific properties and may have a biased representation of these properties, such as high or low metallicity. As a test of robustness of these results, I limited the control-matched samples to DLAs from the relatively unbiased Rafelski et al. (2012) literature sample, and re-computed Δ[α/Fe]. Only 6 of the 27 MDLAs were matched, and still showed no deficit in [α/Fe] ($p_{AD} \sim 0.86$).

It is worth pointing out that the upper velocity limit of MDLAs defined in Lopez & Ellison (2003, 10000 km s^{-1}) is much larger than the typical galaxy cluster velocity dispersion (values are typically smaller than 2000 km s^{-1}; Ruel et al., 2014). Reducing the definition of an MDLA to a separation of 2000 km s^{-1} limits the sample to one MDLA system, which shows a Δ[α/Fe] of $\sim +0.2$dex. Unfortunately more MDLAs are required to further test if a smaller velocity separation does have an impact on the MDLA abundances.

Proximate DLAs

The XQ-100 DLA catalogue from Sánchez-Ramírez et al. (2016) showed that 5 DLAs are PDLAs ($\Delta v_{\rm QSO} \leq 5000$ km s^{-1}). The properties of the complete set of associated absorbers in XQ-100, not just limited to DLAs, can be found in Perrotta et al. (2016). With the addition of 41 PDLAs in the literature sample (Berg et al., 2015a), I tested the effect of proximity of a DLA to its host QSO for 46 absorbers. Improving upon the analysis of 16 PDLAs in Ellison et al. (2010), I compared the relative abundance of a given PDLA to a control-matched sample of intervening DLAs.

The control matching was undertaken in an identical manner as for the MDLAs, with the exception that DLAs were matched by logN(H I) and redshift. In addition, I required the control sample to have at least 5 measured abundances for each of the following elements: S, Si, Fe, and Zn[10]. The tolerance for the logN(H I) match was set by the error in the PDLA's logN(H I). If required, the logN(H I) selection tolerance grew by $\pm$0.025 dex increments (15–25% of the typical error). The same criteria for

[10]The requirement of having 5 abundances for each element is the most restrictive criterion; but is required to ensure that DLAs are compared to the same control pool for each element. Without this criterion, all matching is completed within at most 4 expansions.

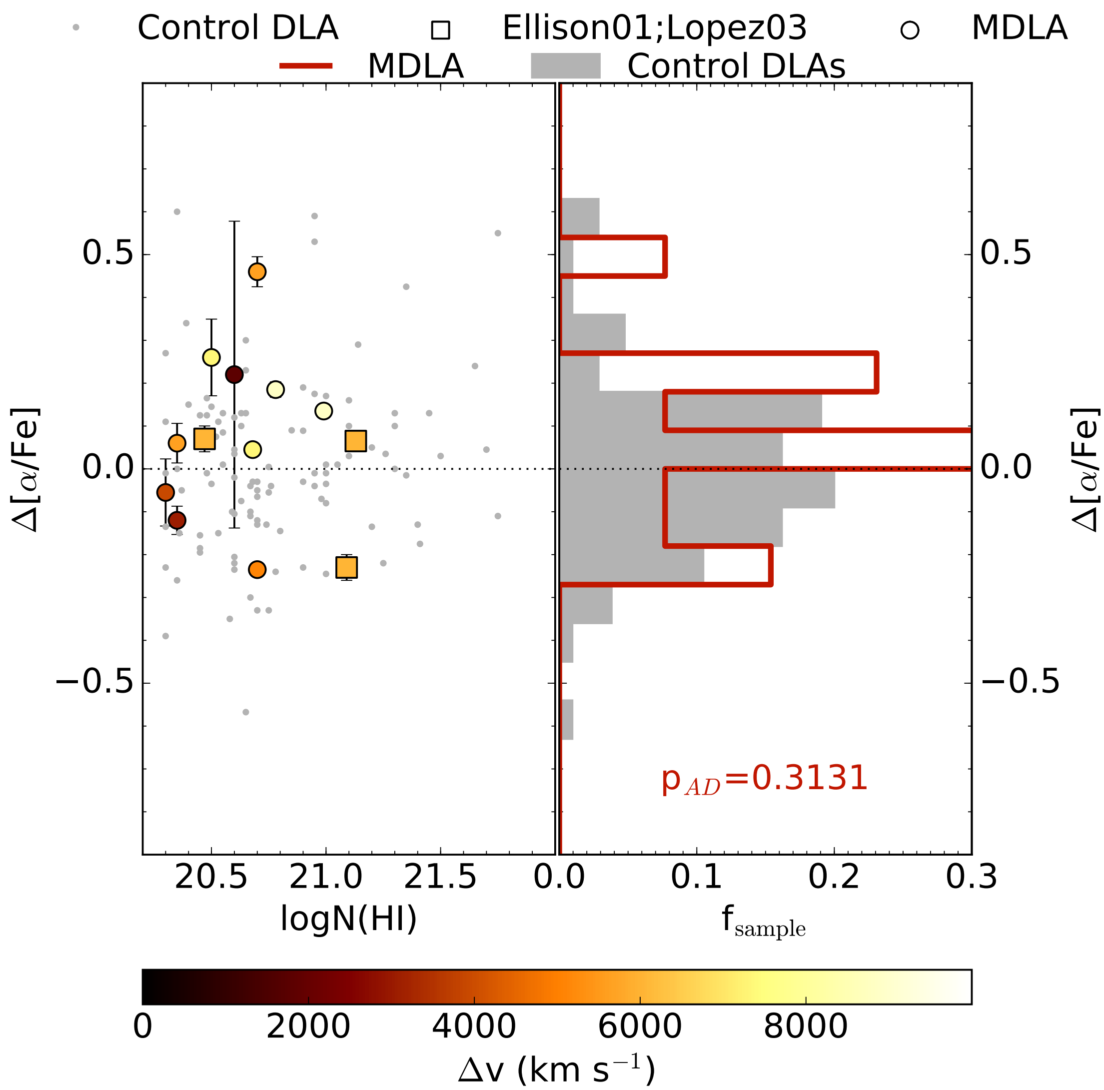

Figure 3.8 The relative change in [α/Fe] for MDLAs ($\Delta[\alpha/\mathrm{Fe}]$) as a function of logN(H I). The left panel show $\Delta[\alpha/\mathrm{Fe}]$ in MDLA sightlines (coloured by their velocity separation Δv) compared to the control-matched sample (small grey points). For reference, the MDLAs observed in Lopez & Ellison (2003) are shown as large squares. The colour of the MDLA points represent the velocity separation of the DLAs along the sightline. The right panel shows the distribution of $\Delta[\alpha/\mathrm{Fe}]$ for the MDLA (red) and control (grey) samples. The p-value from the Anderson-Darling test for the two MDLA samples relative to the control sample is displayed; suggesting that the MDLA and control DLAs are likely drawn from the same parent sample.

redshift used for the MDLAs was imposed for the PDLAs as well. This matching procedure resulted in successful matches for all 46 PDLAs, with 25 PDLAs being matched within 3 expansions, and 6 PDLAs requiring 9 expansions. Each PDLA had at least 12 control matches. The median number of matched controls is 35.5 per PDLA, with 25% of PDLAs having 52 or more controls matches.

The main science result from the control-matching analysis for PDLAs is presented in Figure 3.9. I defined Δ[X/H] as the difference in the PDLA abundance [X/H] relative to the median abundance of control-matched sample; such that a negative Δ[X/H] would imply that the PDLA has a lower [X/H] than the control-matched sample. The left-most panels of Figure 3.9 show Δ[X/H] as a function of logN(H I) for elements (in order from top to bottom rows) S, Si, Fe, and Zn. The error bars represent σ_{jack} of the control-matched sample. The colour of the points indicate the velocity separation ($\Delta v_{\rm QSO}$; km s^{-1}) from the host QSO. PDLAs from Ellison et al. (2010) are shown as large squares, and are included in the analysis. For comparison to the DLAs in the control pool, the smaller grey points are the Δ[X/H] obtained from repeating the control match on all control DLAs. The left panels of Figure 3.9 visually hint at a possible deficit of [X/H] for PDLAs with logN(H I)$\lesssim$ 21.0, and an enhanced [X/H] at logN(H I)$\gtrsim$ 21.0 (the enhancement was first identified for [S/H] and [Si/H] in Ellison et al., 2010).

To quantitatively test the possibility of a correlation between Δ[X/H] and logN(H I) in PDLAs, I performed the Pearson-r test. However, the test did not show any significant correlation of Δ[X/H] with logN(H I) (r =0.33, 0.18, 0.08, 0.00 for S, Si, Fe, and Zn; respectively). Despite the lack of correlation, the AD statistic will additionally constrain whether the PDLAs are drawn from a different distribution of Δ[X/H] compared to the intervening control DLAs. The AD test was performed in three regimes: all logN(H I), logN(H I)$<$ 21.0 , and logN(H I)$>$ 21.0. The distributions of Δ[X/H] (along with the associated $p_{\rm AD}$) for each regime is displayed in the second, third, and fourth column of Figure 3.9 (respectively). The $p_{\rm AD}$ measurements suggest that PDLAs are likely drawn from a different distribution than the control DLAs for [S/H] (null hypothesis rejected at $\sim$ 6% confidence) and [Fe/H] ($\sim$ 32% confidence) for logN(H I)$<$ 21.0, as well as [S/H] ($\sim$ 14% confidence) and [Si/H] ($\sim$ 26% confidence) for logN(H I)$>$ 21.0.

As with the MDLAs, I attempted to assess the potential biases of using the Berg et al. (2015a) literature DLAs by only adopting control DLAs from the Rafelski et al. (2012) sample. Unfortunately only two PDLAs were matched at logN(H I)$>$ 21.0,

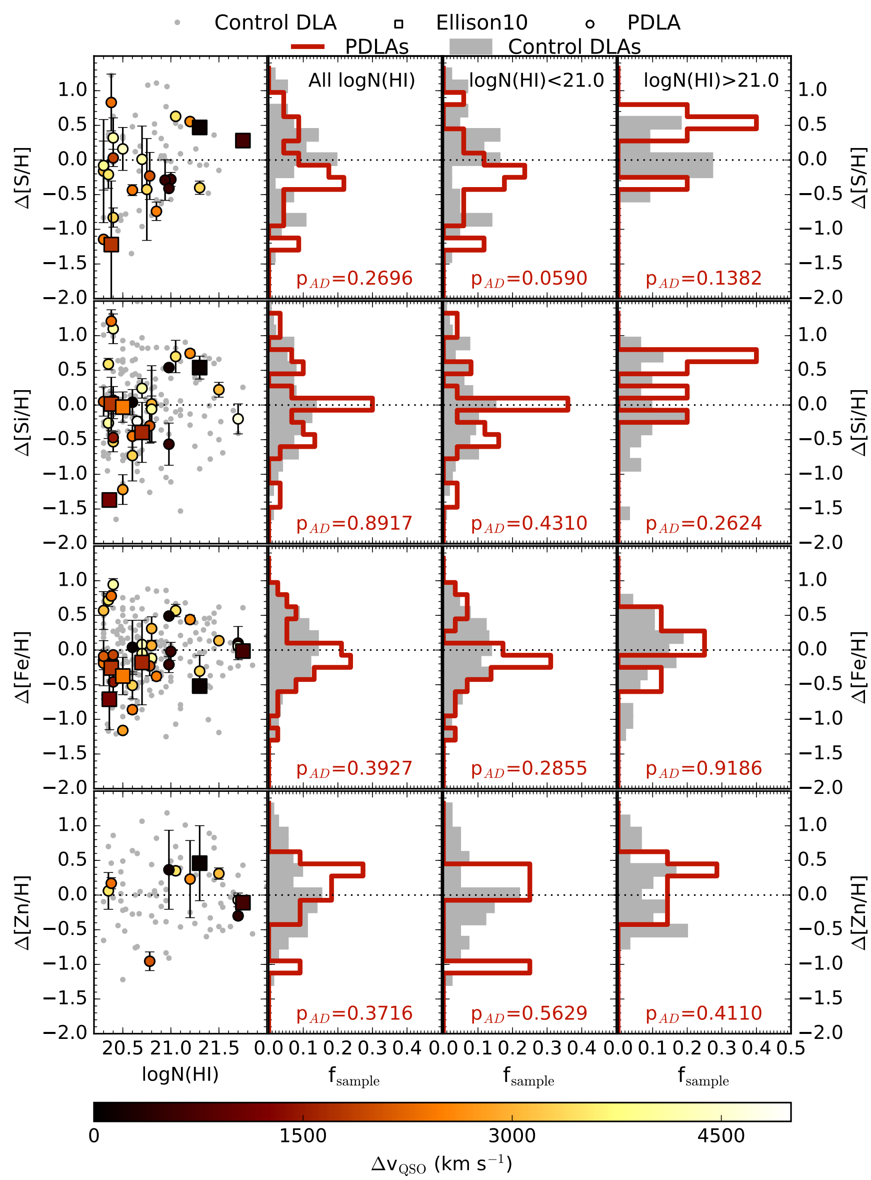

Figure 3.9 *First column:* The relative change in the PDLA abundances compared to a sample of DLAs matched in redshift and logN(H I) (Δ[X/H]) as a function of logN(H I). Each row is Δ[X/H] for S, Si, Fe, and Zn (top to bottom). The notation is the same as Figure 3.8, with the colour coding of the PDLA points now referring to Δv_{QSO}. In all panels, the data from Ellison et al. (2010) is highlighted as large squares for comparison. *Second column:* The fractional distribution of Δ[X/H] for each element in PDLAs (red line) and the control sample (grey shaded region). *Third column:* The fractional distribution of Δ[X/H] for each element, restricting both samples to DLAs with only logN(H I)$<$ 21.0. *Fourth column:* The fractional distribution of Δ[X/H] for each element, restricting both samples to DLAs with logN(H I)$>$ 21.0. All PDLA distributions are compared to the control-sample distribution using the Anderson-Darling test, showing the p-value (p_{AD}) that the two distributions are drawn from the same parent sample.

and are unable to test how robust the results are. Similarly for logN(H I)< 21.0, only 7 PDLAs had measured Δ[S/H], 6 of which had Δ[S/H]≤ 0. Again, by matching the controls in logN(H I) should remove any effects caused by H I selection of control sample DLAs, whilst taking the median value of the control sample should remove any outlaying DLAs. A larger unbiased sample of DLAs is required to further evaluate the robustness of our results.

To test whether the Δ[X/H] offsets seen in PDLAs could occur by chance in a sample of this modest size, I ran a Monte Carlo simulation with 10,000 iterations, drawing a random sample of control DLAs[11] of the same size as the PDLAs sample for each element and logN(H I) cut. At each iteration, I computed the median Δ[X/H] for each logN(H I) criteria. The distribution of medians is shown in Figure 3.10. To understand the likelihood of observing any potential Δ[X/H] offset by chance, I calculated the frequency of observing a median Δ[X/H] that is identical or further offset from zero than the median Δ[X/H] observed for the PDLAs. Table 3.7 provides the median Δ[X/H] of the PDLA sample, and summarizes the frequencies of this simulation for all four elements[12]. The deficit of [S/H] and [Fe/H] for logN(H I)< 21.0 was seen 3.2% and 5.4% of the time (respectively), suggesting it is unlikely the deficit in the observations is observed by random chance. The excess of [S/H] at logN(H I)> 21.0 is also unlikely to be caused by random chance, since *none* of the iterations demonstrated a similar median of Δ[S/H]. The excess of [Si/H] is seen slightly frequently 9.7% of the time. Therefore there is observational evidence that PDLAs exhibit different abundances than intervening DLAs as previously suggested by Ellison et al. (2010).

I now consider the possible source of distinct abundances between PDLAs and intervening systems. The deficit of S and Fe in PDLA abundances at low logN(H I) might arise from ionization effects as the hard ionizing spectrum of the quasar is more likely to penetrate the self-shielding effect of DLAs at low logN(H I). A natural assumption might be that PDLAs closer to the QSO ($\Delta v_{\rm QSO} \leq 1500$ km s^{-1} Ellison et al., 2010) may be more influenced by the higher radiation field. The mean and scatter in Δ[S/H] and Δ[Si/H] for logN(H I)< 21.0 is the same across all Δv, suggesting that the velocity separation of a PDLA has little effect.

[11] The randomly generated sample in each iteration does not contain the same DLA more than once; however the same DLA can appear in the samples of other iterations.

[12] To estimate the uncertainty on the simulation, I recomputed the frequencies of observing a Δ[X/H], taking into account the σ_{jack} of the PDLA Δ[X/H] to make the offset weaker. These recomputed frequencies are provided in parentheses in Table 3.7.

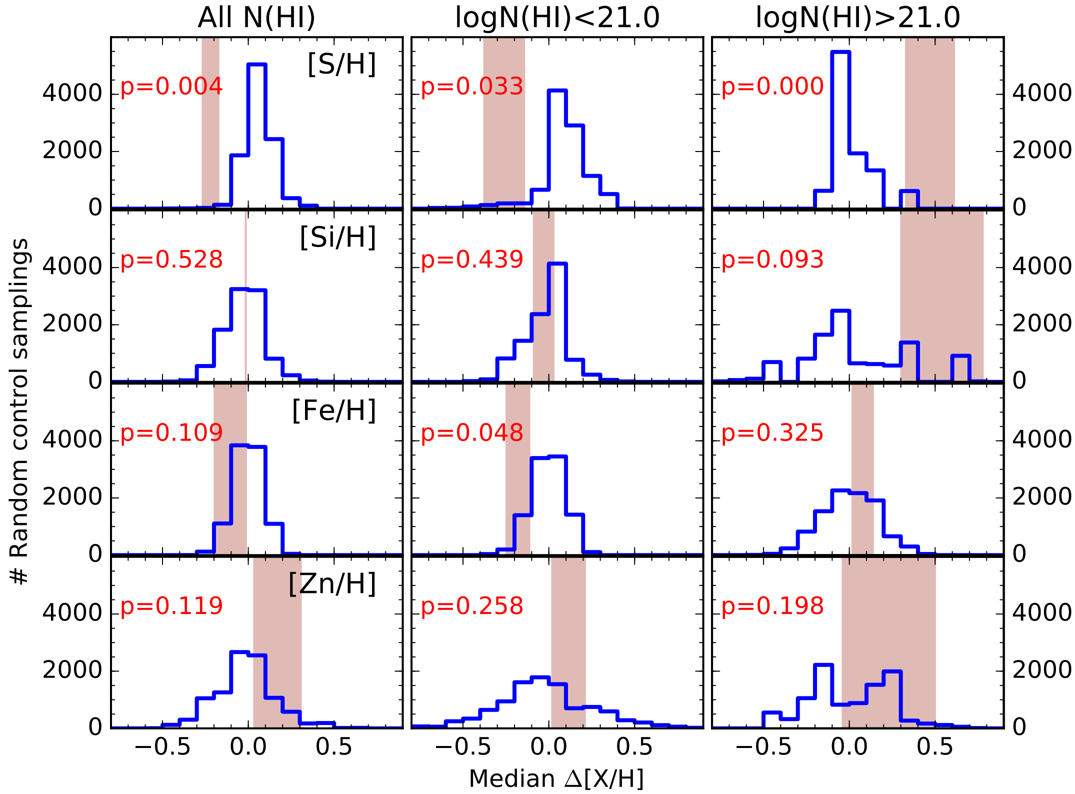

Figure 3.10 The frequency (of 10 000 iterations) of observing a median Δ[X/H] in a randomly-selected control sample of the same size as the PDLA sample. Each row is for the elements S, Si, Fe, and Zn (top to bottom; respectively), while each column is the logN(H I) cut on the sample (all N(H I), logN(H I)< 21.0, and logN(H I)> 21.0; left to right, respectively). The red band indicates the median Δ[X/H] of the PDLA sample, whose half-width is given by σ_{jack} of the PDLA Δ[X/H]. The probability (p) of observing a median Δ[X/H] of the same magnitude (or further offset from 0) as the PDLA median Δ[X/H] is displayed.

Table 3.7 Frequencies of obtaining median PDLA Δ[X/H] from control DLA resampling.

	All N(H I)		logN(H I)< 21.0		logN(H I)> 21.0	
X	Median Δ[X/H]	Freq. (%)	Median Δ[X/H]	Freq. (%)	Median Δ[X/H]	Freq. (%)
[S/H]	-0.22 ± 0.05	0.4 (0.5)[1]	-0.26 ± 0.12	3.3 (5.8)[1]	0.47 ± 0.14	0.0 (6.2)[1]
[Si/H]	-0.02 ± 0.00	52.8 (53.0)[1]	-0.03 ± 0.06	43.9 (62.4)[1]	0.54 ± 0.24	9.3 (23.1)[1]
[Fe/H]	-0.10 ± 0.09	10.9 (43.6)[1]	-0.18 ± 0.07	4.8 (14.0)[1]	0.08 ± 0.06	32.5 (47.6)[1]
[Zn/H]	0.17 ± 0.14	11.9 (38.4)[1]	0.12 ± 0.10	25.8 (39.6)[1]	0.23 ± 0.27	19.8 (58.5)[1]

[1]Frequency including PDLA σ_{jack} in median Δ[X/H].

Table 3.8 Literature PDLA ionization corrections

[X/H]	logN(H I)= 20.35[1] $U=-4.2^{H}$ (dex)	$U=-2.2^{S}$ (dex)	$U=-1.7^{S}$ (dex)	logN(H I)= 20.75[1] $U=-4.8^{H}$ (dex)	$U=-2.2^{S}$ (dex)	$U=-1.7^{S}$ (dex)	logN(H I)= 20.8[2] $U=-4.0^{H}$ (dex)	$U=-2.0^{H}$ (dex)
[Si/H]	−0.04	−0.09	−0.16	−0.01	−0.03	−0.07	−0.02	−0.09
[S/H]	+0.15	−0.20	−0.15	+0.09	−0.07	−0.09	+0.03	+0.26
[Fe/H]	−0.04	−0.02	−0.02	−0.01	−0.01	−0.01	−0.01	−0.05
[Zn/H]	+0.32	−0.35	−0.73	+0.16	−0.17	−0.44	+0.15	+0.58

[1] Vladilo et al. (2001).
[2] Rix et al. (2007).
[S] Soft, stellar-type ionization spectrum.
[H] Hard, QSO-like ionization spectrum.

It is worth noting that the uncertainty in QSO's systemic z_{em} can be large (depending on which emission lines are used, e.g. Gaskell, 1982; Tytler & Fan, 1992), leading to a scatter in Δv_{QSO} determinations from tens to a couple of hundred km s^{-1} (for QSOs identified with the Sloan Digital Sky Survey; see Ellison et al., 2010; Hewett & Wild, 2010; Pâris et al., 2011). In addition, the error in z_{abs} for the DLAs will also contribute to the precision of the Δv_{QSO} measurements. For the XQ-100 sample, the scatter in z_{abs} derived from H I absorption (Table 3.1) and the metal lines is ±47 km s^{-1}. However, the lack of a strong correlation between Δ[X/H] and Δv suggests that higher precision measurements Δv_{QSO} are not required.

To further explore the possibility of ionization effects at logN(H I)< 21.0, the observed Δ[X/H] were compared to abundance discrepancies observed in QSO-like radiation models from the literature. Both Vladilo et al. (2001) and Rix et al. (2007) modelled the effect of radiation fields (for a variety of ionization strengths U) on abundances in DLAs; with their ionization abundance corrections shown in Table 3.8 (where positive corrections imply the observed abundances are underestimated relative to the true value). As a reference, the soft stellar-like ionizing spectrum (denoted by ^{S} in Table 3.8) from Vladilo et al. (2001) is also included. For a hard, QSO-like ionizing field (flagged by ^{H} in Table 3.8); Vladilo et al. (2001) found that [Fe/H] is *over-predicted* by a factor of 0.01–0.04 dex; whereas I found that [Fe/H] is *underestimated* in PDLAs. The corrections for the single PDLA modelled by Rix et al. (2007) are qualitatively similar. Both sets of models suggest that the deficit of [Fe/H] in PDLAs *cannot* be explained by ionization; and I rule out ionization as a possible explanation. However, the deficit for [S/H] could be explained by ionization corrections for logN(H I)< 21.0; but not for the excess seen at logN(H I)> 21.0 (Ellison et al., 2010).

A suggestion in Ellison et al. (2010) is that PDLAs are typically probing more massive galaxies (relative to intervening systems). To test this explanation for the observed metallicity effect, I checked whether the v_{90} parameter (a proxy for mass in DLAs; Prochaska & Wolfe, 1997; Ledoux et al., 2006; Møller et al., 2013; Neeleman et al., 2013) is substantially larger in PDLAs than in the control sample. In addition to the v_{90} measurements of the XQ-100 sample (Table 3.5), I also adopted the 139 v_{90} measurements from HIRES data for DLAs in the literature (Neeleman et al., 2013; Berg et al., 2015b) for the control-matched sample.

Figure 3.11 shows the difference in v_{90} for a PDLA relative to its control matched sample (Δv_{90}; a positive value implying the PDLA has a large v_{90} than the matched controls). Again, the smaller grey points show the scatter within the control sample. There is no significant discrepancy between the v_{90} in PDLAs relative to the control, suggesting no dependence on mass; assuming v_{90} is a good proxy for mass.

3.4 Summary

I have computed the column densities for a variety of metals in the 41 DLAs in the XQ-100 sample. This unbiased sample of DLAs provides coverage of the redshift range z_{abs}= 3–4, an important redshift range for computing $\langle Z/Z_{\odot}\rangle$ but only contains a modest sampling of DLAs in the literature. After increasing the sample of metal-unbiased DLAs of Rafelski et al. (2014) by $\sim$ 20%, we find a steady decrease in $\langle Z/Z_{\odot}\rangle$ with increasing redshift consistent with previous studies.

The additional coverage from the NIR arm of X-Shooter provides coverage of rarely detected lines at $z_{abs}= 3 - 4$ in abundance studies such as Mg II, Ca II, and strong Ti II lines. With the addition of dust-depleted α-elements, I was able to test the dust-corrected [Zn/Fe] to see if [Zn/Fe] is solar in DLAs. I have shown in Section 3.3.1 that [Zn/Fe] is not necessarily solar in DLAs, and that [Zn/Fe] shows the same range of values as seen in the dSphs of the Local Group (in agreement with Berg et al., 2015a; Skúladóttir et al., 2017).

In combination with a sample of DLAs drawn from the literature, I have provided a statistical analysis of proximate DLAs (within $\Delta v_{\rm QSO} \leq 5000$ km s^{-1} of the host QSO) and multiple DLAs (two or more DLAs separated by $500 \leq \Delta v \leq 10000$ km s^{-1}) by comparing to a control-matched sample of individual, intervening absorbers. I do not find any suppression in [α/Fe] in multiple DLAs, suggesting that there is no evidence for truncated star formation between nearby DLAs based on their [α/Fe] abundance. Relative to a control sample of DLAs, I note a mildly elevated [S/H]

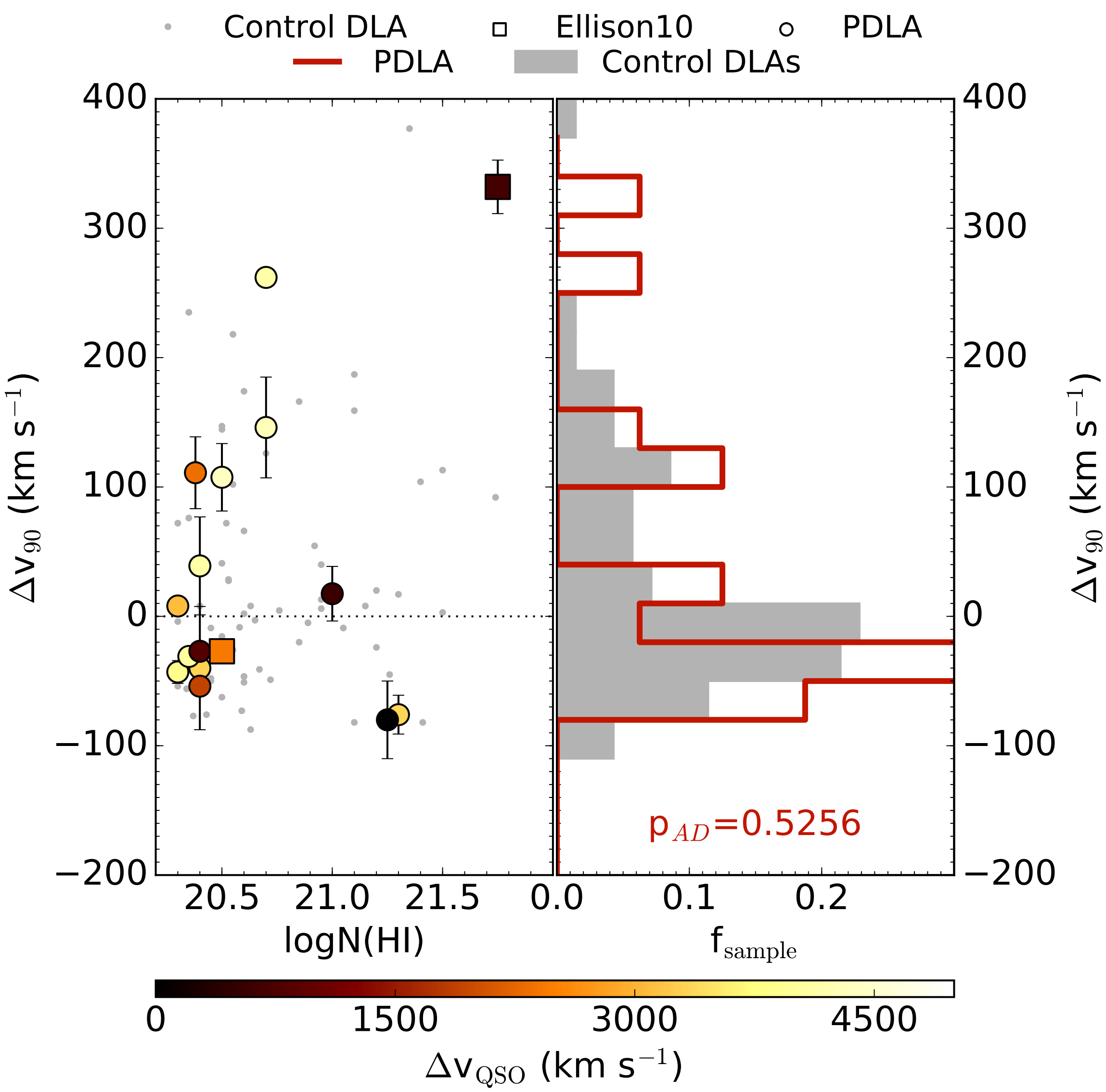

Figure 3.11 *Left Panel:* The difference in v_{90} between a given PDLA and control-matched sample (Δv_{90}), as a function of logN(H I). The notation is the same as Figure 3.9. *Right Panel:* distributions of Δv_{90} for the PDLA sample (red line) compared to the control sample (grey bars). The Anderson-Darling p-value is shown for the comparison of the two distributions.

and [Si/H] for high logN(H I)> 21.0 proximate DLAs (Anderson Darling test rejects the null hypothesis at 14% and 26% confidence; respectively), as previously seen by Ellison et al. (2010); however I also detected a deficit in [S/H] and [Fe/H] (null hypothesis rejected at 6% and 32% confidence, respectively) for proximate DLAs with logN(H I)< 21.0. These abundance discrepancies appear to be independent of velocity separation of the host QSO and the mass proxy v_{90}. It is possible to explain the deficit of [S/H] at low logN(H I) through ionization corrections, but not the deficit of [Fe/H].

I have also presented UVES observations of 3 DLAs towards J0034+1639 in order to investigate a metal-poor DLA candidate at $z_{abs} \sim 4.25$ with a [Fe/H]$= -2.82 \pm 0.11$. This metal-poor DLA is consistent with abundances in the typical metal-poor DLA (Cooke et al., 2011). Metal-poor DLAs such as the one towards J0034+1639 prime targets for easily detecting Ni and other discriminating elements in future follow-up observations with 30-m class telescopes.

Chapter 4

The circumgalactic medium of Active Galactic Nuclei hosts

To form new stars over cosmic time, galaxies need vast supplies of gas to feed their growth. As suggested by the slow evolution of $\Omega_{\rm HI}$ with cosmic time in comparison with the evolution of the cosmic star formation density (see Chapter 2; Figure 2.1), there appears to be a constant replenishment of gas from the intergalactic medium. The interface between the intergalactic medium and galaxies' interstellar medium, known as the *circum-galactic medium*, is host to a large reservoir of gas that is thought to be responsible for maintaining fuel for star formation. When astrophysical processes shut off star formation in galaxies, a question arises of how these processes impact the replenishment of gas and thus the circum-galactic medium?

One of the suggested processes for shutting off star formation in a galaxy is the rapid, active growth of the super-massive black hole (AGN) that resides in the centre of large galaxies. AGN are thought to disrupt star formation processes by heating and removing gas from the galaxy. This chapter presents a systematic analysis of the effects of active galactic nuclei on the circum-galactic medium of galaxies hosting Type II Seyfert AGN (which I will simply refer to as AGN in this chapter). The simulations presented in Section 4.4.1 were created and processed by Ben Oppenheimer and Ryan Horton, although I guided the design of the simulated experiment and what data products were needed. The material presented in this chapter is published in Berg et al. (2018). Throughout the chapter, I assumed a flat ΛCDM Universe with $H_0 = 67.8$ km s^{-1} Mpc^{-1} and $\Omega_M = 0.308$ (Planck Collaboration et al., 2015).

4.1 Properties of the circum-galactic medium

The circum-galactic medium (CGM) is the interface between cold flows from the intergalactic medium onto a galaxy, and hosts hot halo gas and material ejected from galaxies (for reviews, see Putman et al., 2012; Tumlinson et al., 2017). With various processes in galaxy evolution consuming (e.g. star formation) and removing (e.g. winds) gas, the CGM is shaped by the processes internal to the galaxy. Early progress in the study of the CGM came from connecting absorption lines in QSO spectra with galaxies imaged in the foreground, tracing the extent and properties of the CGM gas as a function of the host galaxy's properties (e.g. Bergeron, 1986; Bowen et al., 1995; Lanzetta et al., 1995a; Adelberger et al., 2005; Chen et al., 2010; Steidel et al., 2010; Bordoloi et al., 2011; Prochaska et al., 2011; Turner et al., 2014). Building on these foundations, our understanding of the CGM has been significantly improved through surveys with the Hubble Space Telescope's (HST) Cosmic Origins Spectrograph (COS; Green et al., 2012). The first of several surveys of the CGM surrounding low redshift galaxies was the COS-Halos survey (Tumlinson et al., 2013) which targetted the CGM around 44 $\sim$L* galaxies, demonstrating that the properties of the CGM differ depending on whether the central galaxy is passive or star-forming (defined using a specific star formation rate[1] cut of sSFR= 10^{-11}yr^{-1}; Tumlinson et al., 2011; Werk et al., 2013; Borthakur et al., 2016). The COS-Halos team found a distinct lack of O VI around passive galaxies, while H I was found at the same strength around all galaxies (Tumlinson et al., 2011; Thom et al., 2012). Additionally, connections have been made between the CGM and properties of the host galaxy, including: increased H I content of the CGM with larger ISM gas masses (COS-GASS; Borthakur et al., 2015), the presence of extended gas reservoirs around galaxies of all stellar mass (COS-Dwarfs; Bordoloi et al., 2014b), and enhanced metal content around starbursting hosts (COS-Burst; Borthakur et al., 2013; Heckman et al., 2017).

Active galactic nuclei and their impact on the CGM

An important stage in the evolution of galaxies is when their central supermassive black holes are actively accreting material. These AGN may be responsible for the removal of gas from star forming reservoirs within galaxies via winds and outflows (Veilleux et al., 2005; Tremonti et al., 2007; Sturm et al., 2011; Woo et al., 2017), and

[1] The specific star formation rate is defined as the ratio of the active star-formation rate to the total mass of stars within the galaxy.

has been associated with the evolution of galaxies off the star-forming main sequence to passive galaxies (Springel et al., 2005a; Schawinski et al., 2007; Fabian, 2012; Bluck et al., 2014, 2016). In addition, radio-mode feedback and radiation from the AGN keeps the CGM hot, buoyant, and consistently ionized (McNamara & Nulsen, 2007; Bower et al., 2017; Hani et al., 2017), as well as preventing gas from returning to the host galaxy. Such processes have been proposed to be responsible for O VI bimodality seen in the CGM by COS-Halos without an active AGN (Oppenheimer et al., 2017).

Observationally linking the environmental and feedback effects of AGN hosts with their CGM has primarily been done through the use of projected QSO-QSO pairs at higher redshifts. This technique has the added benefit of looking at the role of a stronger and weaker QSO radiation fields located in the respective transverse (background QSO) and line-of-sight (foreground QSO; i.e. along the outflow) CGM (Bowen et al., 2006; Farina et al., 2013; Johnson et al., 2015). Cool gas traced by H I and Mg II is anisotropically distributed about the QSO, with larger column densities of H I preferentially found along the transverse direction (Hennawi et al., 2006; Farina et al., 2013); suggesting that radiation from the QSO does not affect the transverse medium (Hennawi & Prochaska, 2007; Prochaska et al., 2014; Farina et al., 2014). An excess of cool gas (relative to the intergalactic medium) has been found all the way out to one Mpc, with a stronger enhancement at smaller impact parameters (Prochaska et al., 2013). When the QSO-QSO pairs are split by the bolometric luminosity of the QSO host, the Mg II covering fraction[2] is larger for high-luminosity QSOs (covering fraction of $\approx 60\%$ for luminosities of $L_{Bol} \geq 45.5$ erg s^{-1}) compared to low luminosity QSOs ($\approx 20\%$, $L_{Bol} \leq 45.5$ erg s^{-1}; Johnson et al., 2015). All of these observations of excess cool gas around luminous QSOs is suggestive of either a viewing angle effect with the ionizing radiation exciting cool gas along the line of sight to the QSO, or an environmental effect of haloes hosting massive QSOs such as debris from galaxy interactions fuelling QSO activity (Prochaska et al., 2013; Farina et al., 2014; Johnson et al., 2015).

Most of the work described above has focused on high luminosity quasars. However, there has been little focus on how the less luminous but more common Seyfert-like AGN shape their surrounding CGM. In the only observational study of the CGM surrounding Seyfert galaxies, Kacprzak et al. (2015) found a low (10%) Mg II λ 2796

[2]The covering fraction refers to the incidence of detecting gas (above a column density or equivalent width threshold) over the surface area of the sky. For quasar absorption line studies, this is typically measured as the fraction of sightlines that have detected gas above the given threshold.

Å covering fraction around 14 AGN (between 100 and 200 kpc) in the transverse direction relative to field and QSO host galaxies, but a reservoir of cool gas still exists along the line of sight to the AGN. They suggest that AGN-driven outflows are destroying the cool gas in the transverse direction (i.e. along the outflow), suggesting that the difference between their observations of the CGM of AGN-dominated galaxies with previous observations of QSOs (e.g. Prochaska et al., 2013) is caused by the viewing angle of the AGN.

Predictions from zoom-in simulations of galaxies taken from the EAGLE cosmological simulation (Schaye et al., 2015) suggest that radiative feedback from the AGN should ionize the gas out to a distance of two virial radii (Oppenheimer & Schaye, 2013; Segers et al., 2017). After implementing non-equilibrium ionization into their models, Oppenheimer & Schaye (2013) have predicted that AGN *proximity fossil zones* exist around galaxies that host (or have hosted) bright AGN, where the metals remain in an over ionized state for several megayears (depending on the luminosity duty cycle and lifetime of the AGN; Segers et al., 2017; Oppenheimer et al., 2018). However, the detailed CGM properties in simulations can be quite sensitive to the size of the CGM clouds, implementation of feedback, and different recipes between codes (Stinson et al., 2012; Gutcke et al., 2017; Nelson et al., 2017).

4.2 The COS-AGN survey

Although the impact of AGN on the CGM has been quantified over a large range of AGN luminosities (Prochaska et al., 2013; Kacprzak et al., 2015; Johnson et al., 2015), the respective studies have been limited to only using neutral gas tracers (i.e. H I and Mg II). To expand upon this previous work and provided a systematic comparison of AGN and non-AGN host haloes, the COS-AGN survey observed 20 QSO sightlines through the CGM of foreground AGN-hosts to search for the predicted effects of AGN feedback on the CGM (Oppenheimer & Schaye, 2013; Segers et al., 2017).

4.2.1 Sample selection and properties

The COS-AGN QSO sightlines were selected by cross-matching coordinates of Sloan Digital Sky Survey (SDSS; Abazajian et al., 2009) galaxies hosting AGN with the locations of UV-bright QSOs ($17 < m_{FUV} < 18.9$) identified in the Galaxy Evolution

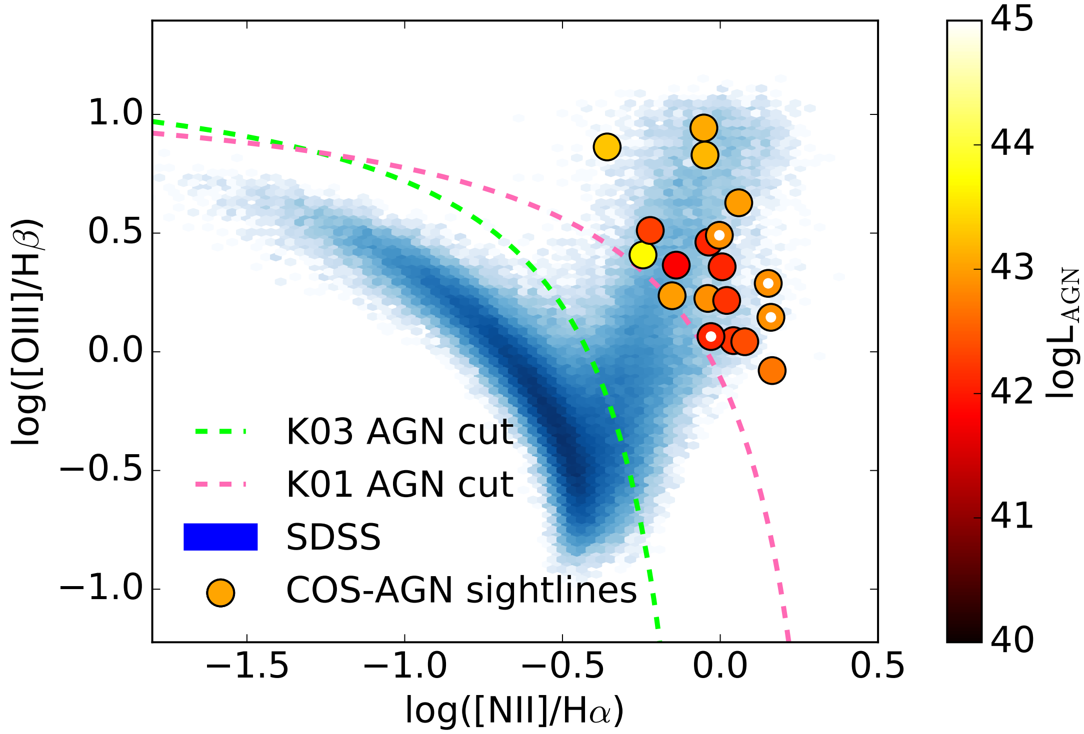

Figure 4.1 The BPT diagram of all SDSS galaxies with spectroscopic observations (blue shaded region; only showing SDSS galaxies with $> 5\sigma$ detections of diagnostic emission lines). The solid circles show the COS-AGN galaxies, and are coloured based on their AGN luminosity. The dashed pink and green lines denote the Kewley et al. (2001, K01) and Kauffmann et al. (2003, K03) cuts typically used to select AGN and composite galaxies. LINERS classified using the Kewley et al. (2006b) emission line metrics (see Table 4.1) are denoted with a white dot on top of the datapoint.

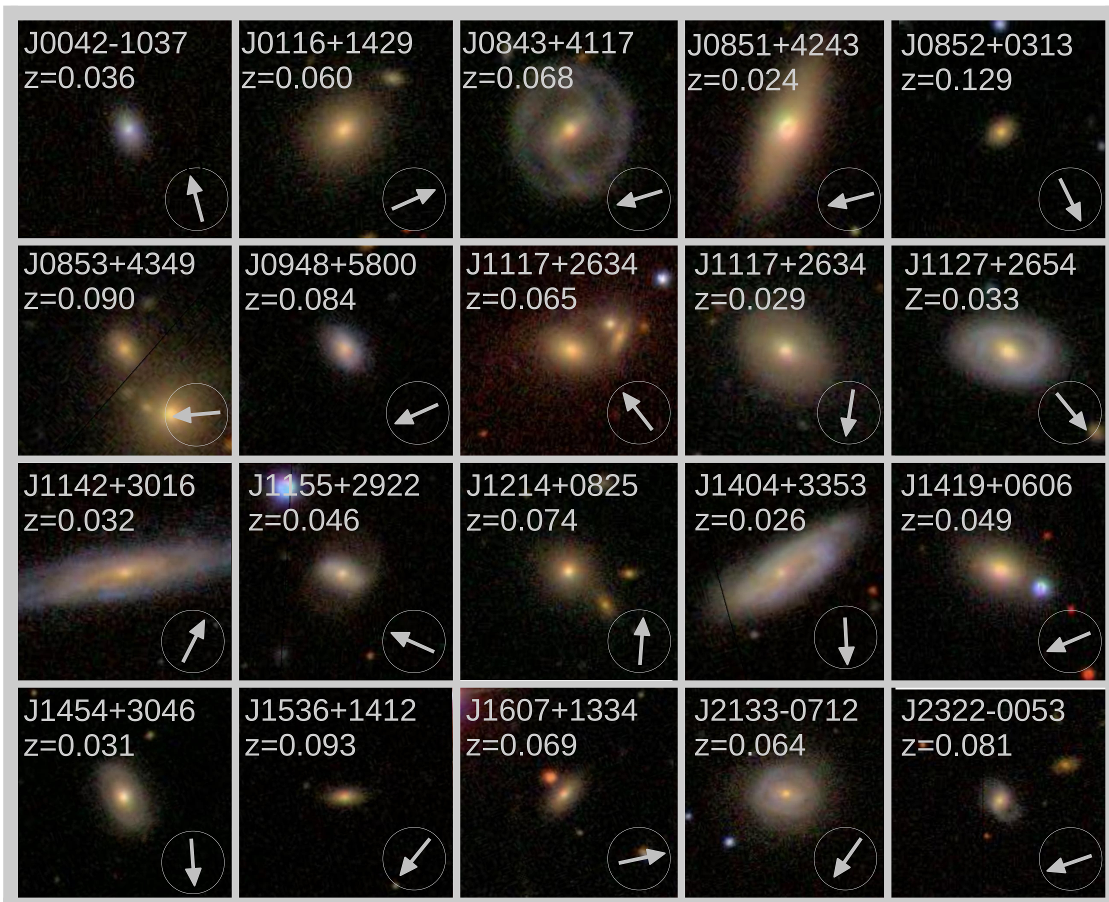

Figure 4.2 SDSS postage stamp images of the entire COS-AGN sample. Each image is 50 arcsec × 50 arcsec. The QSO name and AGN host galaxy redshift are provided in each panel. For reference, the arrow in the bottom right of each panel gives the relative direction of the background QSO from the centre of the galaxy.

Explorer (GALEX) catalogue[3] (Martin et al., 2005). AGN were selected using the emission line ratios [N II/Hα] and [O III/Hβ] measured in the SDSS[4] following the line ratio diagnostics provided in Kewley et al. (2001). I required that all four emission lines be detected at $\geq 5\sigma$, and that the background QSO sightline must probe within 300 kpc of the AGN host galaxy. Using these criteria, I identified ten AGN-QSO pairs (along nine QSO sightlines) that had been previously observed with HST whose data are located in the Hubble Spectroscopic Legacy Archive (HSLA; data release 1[5]). In addition, ten more QSO sightlines were selected to probe the inner 175 kpc of the CGM surrounding AGN, which were observed with HST/COS in Cycle-22 (PI: S. Ellison). These combined 19 sightlines probing 20 AGN host galaxies make up the COS-AGN sample. Descriptions of the observations are presented in Section 4.2.2. Figure 4.1 shows the so-called BPT diagram (Baldwin et al., 1981) of the COS-AGN host galaxies (coloured circles) compared to SDSS galaxies (blue shaded region), whilst Figure 4.2 shows the SDSS thumbnail images of each AGN host. Of the 20 COS-AGN host galaxies, four are classified as low-ionization nuclear emission-line regions (LINERS) based on the diagnostics presented in Kewley et al. (2006b, equations 1–15) that encompass both the classic BPT diagram (Figure 4.1) and line ratios that include [O II] $\lambda\lambda$ 3726Å & 3729Å, and [S II] $\lambda\lambda$ 6717Å & 6731Å. Although the LINER category was originally envisaged to identify low luminosity AGN (Heckman, 1980; Ho et al., 1997), alternative ionization mechanisms can also produce extended LINER-like emission (Yan & Blanton, 2012; Belfiore et al., 2016). I therefore kept these sightlines in the COS-AGN sample as they may be bona fide AGN, but are flagged through-out the analysis to assess the effects of including or removing LINERs from the sample.

The properties of the COS-AGN galaxies are given in Table 4.1. I adopted the SDSS spectroscopic redshifts as the systemic redshifts of the galaxy ($z_{\rm gal}$). Stellar masses were taken from Mendel et al. (2014), which are based on spectral energy distribution fits to the SDSS g and r-band photometry of a single Sérsic fit to the galaxy, and assume a Chabrier (2003) initial mass function. The most commonly adopted SFRs for SDSS galaxies are those provided in the MPA/JHU catalogues (Brinchmann et al., 2004; Salim et al., 2007). These SFRs are nominally based on fits to emission lines for star forming galaxies. However, it is well known that the standard

[3]http://galex.stsci.edu/

[4]Emission line fluxes were taken from http://www.mpa-garching.mpg.de/SDSS/.

[5]https://archive.stsci.edu/hst/spectral_legacy/

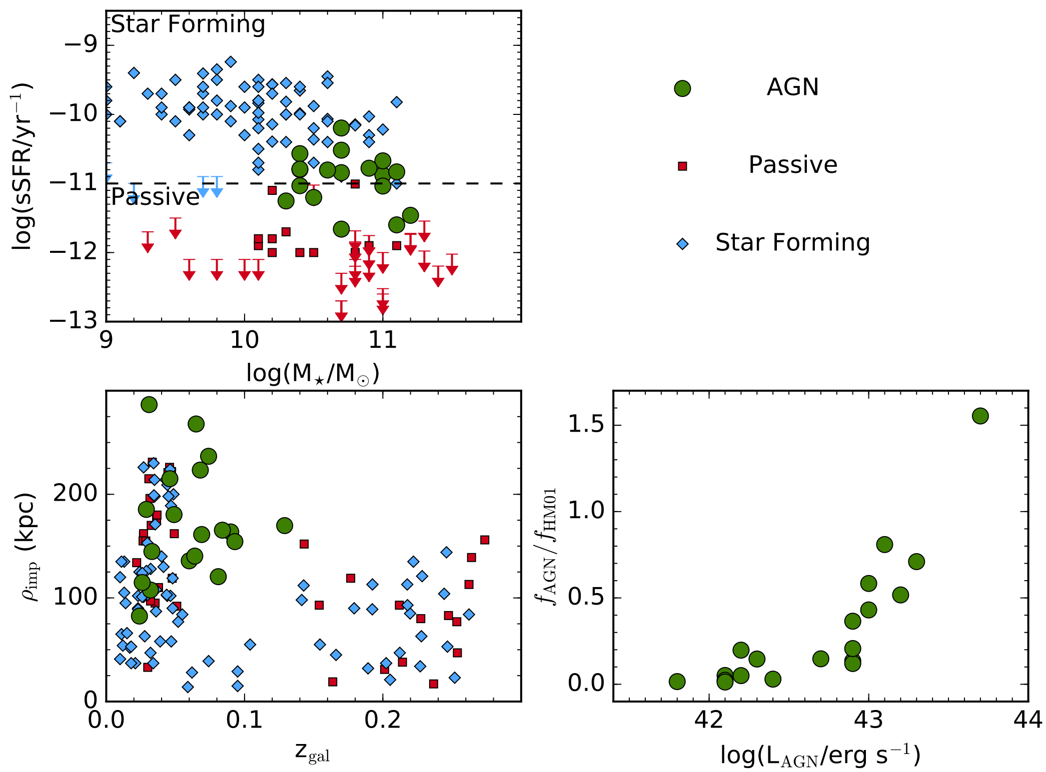

Figure 4.3 Top left: sSFR vs $M_\star$ for the COS-AGN sample (green circles) compared to star-forming (blue diamonds) and passive (red squares) galaxies from the literature. Bottom left: Impact parameter (ρ_{imp}) vs galaxy redshift (z_{gal}) for the COS-AGN and literature sample. Bottom right: the strength of Lyα ionizing radition of the AGN relative to the UV background (f_{AGN}/f_{HM01}) as a function of the bolometric luminosity of the AGN (L_{bol}) for the COS-AGN sample.

SFR conversions (e.g. Kennicutt, 1998) will be incorrect when AGN contribute to emission line fluxes. Therefore, for galaxies with an AGN, the MPA/JHU catalog presents a SFR based on the correlation between the 4000 Å break and sSFR in star forming galaxies. However, SFRs derived from the 4000 Å break have large uncertainties, and it has been recently shown that the far-IR can be used to obtain more accurate values (Rosario et al., 2016). I therefore used the infrared luminosity (L_{IR}) of the SDSS galaxies predicted by an artificial neural network (Ellison et al., 2016a) to calculate log(sSFR) using the conversion $\log(\mathrm{sSFR/yr^{-1}}) = \log L_{IR} - 43.951 - \log(M_\star/M_\odot)$. All of the COS-AGN galaxies have a predicted L_{IR} confidence of ≈ 0.1 dex, passing the adopted quality control cut in Ellison et al. (2016a). The bolometric luminosity of the AGN (L_{bol}) is calculated based on the AGN's [O III] line luminosity following Kauffmann & Heckman (2009), where the bolometric luminosity of the AGN is 600× the [O III] line luminosity. The projected proper impact parameter of the QSO sightline (ρ_{imp}) is calculated at the systemic redshift of the AGN host galaxy. Lastly, the AGN type from the Kewley et al. (2006b) classification is also tabulated.

To provide a systematic comparison between the properties of the CGM of galaxies with and without an AGN, I have compiled a non-AGN literature sample of EWs from all galaxies observed in the COS-Halos (Tumlinson et al., 2013; Werk et al., 2013, 2014), COS-Dwarfs (Bordoloi et al., 2014b), and COS-GASS (Borthakur et al., 2015, 2016) surveys. Figure 4.3 compares the properties of the non-AGN literature sample to the COS-AGN galaxies (green data) in terms of sSFR as a function of $M_\star$ (top left), and ρ_{imp} vs z_{gal} (bottom left). The non-AGN literature sample is separated into star-forming (blue diamonds) and passive galaxies (red squares) using a $\log(\mathrm{sSFR/yr^{-1}}) = -11$ cut. I note that the measured SFR values in this literature sample have been derived using different methods for COS-Halos (Werk et al., 2012), COS-GASS (Borthakur et al., 2013), and COS-Dwarfs (Bordoloi et al., 2014b). However, small differences (up to a few tenths of dex) will not affect the analyses presented in this chapter as sSFR is only used to classify galaxies as star-forming or passive. To demonstrate the properties of the AGN in the COS-AGN sample, the bottom right panel of Figure 4.3 shows the distributions of L_{bol} and the strength of the H I ionizing flux from the AGN (Sazonov et al., 2004) relative to the UV background (Haardt & Madau, 2001)[6] at the ρ_{imp} of each sightline (f_{AGN}/f_{HM01}). The distribution of f_{AGN}/f_{HM01} shows the UV background is the dominant source of ionizing

[6] I adopted the Haardt & Madau (2001) UV background to be consistent with what I use in our zoom-in simulations (see Section 4.4.1).

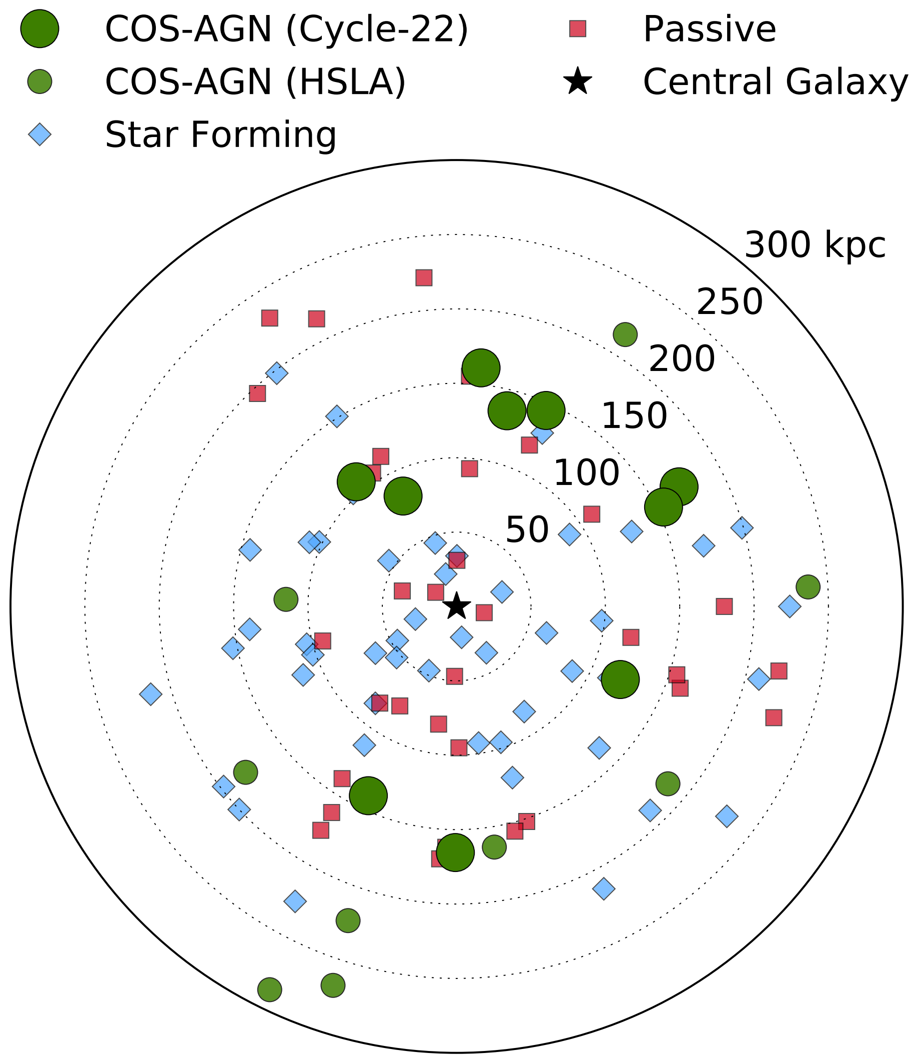

Figure 4.4 The map of QSO sightlines that probe the CGM of AGN-dominated (green circles), star-forming (red squares), and passive galaxies (blue diamonds). All the sightlines are shown relative to the central galaxy being probed (black star). The larger and smaller circles respectively represent sightlines observed in our Cycle 22 program, and previously observed in the HSLA. The passive and star-forming galaxies are from the COS-Halos, COS-Dwarfs, and COS-GASS surveys. The angular position of the points are based on the position angle of the galaxy relative to the background QSO.

radiation for most of these sightlines except for the sightline towards J0948+5800 ($f_{\rm AGN}/f_{\rm HM01}$= 1.56). In addition, Figure 4.4 shows the distribution of QSO sightlines observed for the COS-AGN sample (our Cycle-22 observations are the larger green circles; archival sightlines are the smaller circles) about the central galaxy (black star).

In order to identify additional absorbers that could potentially contribute to the CGM of the AGN hosts, I searched for possible spectroscopic companions in the SDSS for each of the 20 COS-AGN hosts using the catalogue of galaxy companions compiled by Patton et al. (2016). The catalogue from Patton et al. (2016) finds the nearest spectroscopic companion in the SDSS DR7 with a stellar mass greater than 10% of the galaxy in question. In order to flag the possibility of contaminating absorption, I further required that the background QSO be within 300 kpc of the companion, and within $\pm$1000 km s^{-1} of the AGN host such that any contribution from the CGM gas of the companion would be found in the absorption search window. Five of the COS-AGN galaxies have companions that match these requirements (see Table 4.1), and are situated between 193 $\leq\rho_{\rm imp}\leq$ 274 kpc from the targetted QSO. I have repeated all of the analysis presented here with and without these five systems, and find that my results do not change qualitatively; I therefore kept these systems with companions in my sample and visually flag their data in relevant figures. I note that 13 of the remaining 15 sightlines still contain a lower mass companion (M$_{\star}$< 10% of the AGN host mass) within $\pm$1000 km s^{-1} of the AGN host and 300 kpc projected separation from the background QSO. However, given the low mass of these 13 systems I suspect that the CGM will be dominated by the AGN host.

Table 4.1 COS-AGN sightline properties

QSO name	z_{gal}	Galaxy SDSS objid	Gal. R.A. [°]	Gal. Dec. [°]	$\log(M_\star)$ $[\log(M_\odot)]$	log(sSFR) $[\log(yr^{-1})]$	$\log(L_{AGN})$ $[\log(erg\ s^{-1})]$	ρ_{imp} [kpc]	Program	Companion?	AGN type⋆
J0042−1037	0.036	587727178454007913	10.562	−10.738	9.5	−10.2	42.8	299	COS−Halos	N	—
J0116+1429	0.060	587724232641544435	19.126	14.482	11.1	−11.6	42.9	136	COS−AGN	N	LINER
J0843+4117	0.068	587732048403824840	130.898	41.308	11.0	−10.9	42.9	223	COS−Dwarfs	N	LINER
J0851+4243	0.024	587732048404676666	132.757	42.736	10.7	−11.7	42.2	82	COS−AGN	Y	—
J0852+0313	0.129	587728880331194569	133.255	3.240	11.0	−10.7	42.7	170	COS−AGN	N	—
J0853+4349	0.090	587731886277197945	133.357	43.820	11.0	−11.0	42.2	164	HSLA	Y	—
J0948+5800	0.084	587725468527231140	147.118	58.022	10.7	−10.2	43.7	165	COS−AGN	N	—
J1117+2634	0.065	587741708880773130	169.437	26.526	11.2	−11.5	42.4	268	COS−Dwarfs	Y	—
J1117+2634	0.029	587741602026029237	169.461	26.657	10.4	−11.0	41.8	185	COS−Dwarfs	Y	—
J1127+2654	0.033	587741602027012125	171.943	26.960	10.5	−11.2	42.1	145	COS−AGN	N	—
J1142+3016	0.032	587741490911576221	175.575	30.230	10.4	−10.6	42.3	108	COS−AGN	N	Seyfert
J1155+2922	0.046	587741532251685053	178.903	29.351	10.4	−10.8	42.1	215	COS−GASS	N	LINER
J1214+0825	0.074	588017726547361972	183.630	8.374	11.2	. . .	42.9	237	HSLA	N	LINER
J1404+3353	0.026	587739131343929515	211.122	33.953	10.4	−10.8	43.1	115	HSLA	N	Seyfert
J1419+0606	0.049	587730022252675197	214.909	6.135	10.9	−10.8	42.9	180	HSLA	N	—
J1454+3046	0.031	587739131885649936	223.612	30.909	10.3	−11.3	42.1	287	COS−GASS	Y	—
J1536+1412	0.093	587742551760765148	234.172	14.227	10.7	−10.8	43.3	154	COS−AGN	N	Seyfert
J1607+1334	0.069	587742614562603047	241.824	13.565	10.6	−10.8	43.2	161	COS−AGN	N	Seyfert
J2133−0712	0.064	587726878878073213	323.473	−7.180	11.1	−10.8	43.0	140	COS−AGN	N	Seyfert
J2322−0053	0.081	587731185126080831	350.730	−0.893	10.7	−10.5	43.0	121	COS−AGN	N	—

⋆The AGN are classified as LINERs or Seyferts using the SDSS emission line diagnostics presented in Kewley et al. (2006b, Equations 1-15). Cases where the classification is either ambiguous, or the emission line data quality is poor (signal-noise ratio < 3 for any emission line) are denoted by blank entries.

4.2.2 Cycle 22 Observations

Observations for the ten newly targeted sightlines were completed with HST/COS during Cycle-22 (program ID 13774; PI S. Ellison). To probe a range of ionization species, I required wavelength coverage to probe the prominent lines of H I λ 1215 Å, Si II λ 1260 Å, C IV λ 1548 Å, Si IV λ 1393 Å, and N V λ 1238 Å. This required observations using both the G130M and G160M gratings on COS. I note that the G130M data used for three of these ten sightlines were previously obtained by the COS-GASS program (Borthakur et al., 2015), and were not re-observed in our program. For each individual sightline, the central wavelengths were selected to ensure coverage of these lines, and all four FP-POS offsets were used to minimize gaps in the wavelength coverage and reduce the fixed pattern noise. Exposure times were selected to obtain a similar signal-noise ratio of ≈ 10 to the COS-Halos survey across the entire wavelength range (Tumlinson et al., 2013). To ensure homogeneity in signal-noise ratio amongst the archival HSLA sample and our Cycle-22 observations, I required a signal-noise ratio $\gtrsim 4$ near absorption lines of interest for the archival sightlines. It is important to note that the HSLA sightlines do not have the same wavelength coverage as the Cycle-22 sample. A summary of the observational details of all 19 COS-AGN sightlines is provided in Table 4.2.

4.2.3 Data reduction and equivalent width measurements

To provide a systematic comparison to the EWs measured in COS-Halos and COS-GASS, I used the same data reduction technique as COS-Halos (Tumlinson et al., 2013). In brief, the final CALCOS (version 3.1) extracted 1D spectra (x1d files) are taken from the HST archive[7], and are coadded and rebinned to contain ≈ 6 pixels per resolution element. The QSO continuum is fitted locally (± 1500 pixels) around each absorption feature using fifth-order Legendre polynomials.

Following the COS-Halos methodology, all absorption located within ± 500 km s^{-1} of the systemic redshift of the galaxy is assumed to be associated with the CGM of the galaxy. Within the ± 500 km s^{-1} window, the wavelength integration limits (λ_{min} and λ_{max}) of the equivalent width derivation are chosen on a line by line basis to avoid any regions of contamination, whilst limiting the amount of clean continuum within the integration bounds. The measured EW is given by

[7] `https://archive.stsci.edu/hst/`

Table 4.2 Summary of QSO observations

QSO ID	R.A. [°]	Dec. [°]	Grating	Central wavelength(s) [Å]	Exposure time [s]	signal-noise ratio[a] [pixel^{-1}]	Program ID[b]
				COS-AGN Cycle-22 sightlines			
J0116+1429	19.096	14.495	G130M	1309	5239	5–7	13774
			G160M	1577	11338	10	13774
J0851+4243	132.817	42.725	G130M	1318	5408	6–12	13774
			G160M	1611	11696	7–12	13774
J0852+0313	133.247	3.222	G130M	1291,1327	2232	3–12	12603
			G160M	1600	8135	6–15	13774
J0948+5800	147.167	58.011	G130M	1291	8834	5–10	13774
			G160M	1589	18676	4–11	13774
J1127+2654	171.902	26.914	G130M	1291	2255	5–18	12603
			G160M	1577	8193	8–15	13774
J1142+3016	175.551	30.270	G130M	1291,1327	4790	4–14	12603
			G160M	1577	11466	8–14	13774
J1536+1412	234.187	14.208	G130M	1291	4251	4–9	13774
			G160M	1600	6232	5–9	13774
J1607+1334	241.791	13.572	G130M	1318	4265	4–7	13774
			G160M	1577	6218	3–7	13774
J2133−0712	323.491	−7.205	G130M	1309	8245	7–9	13774
			G160M	1577	11322	4–9	13774
J2322−0053	350.750	−0.900	G130M	1291	5242	7	13774
			G160M	1600	11326	4–10	13774
				COS-AGN HSLA sightlines			
J0042−1037	10.593	−10.629	G130M	1291	2448	5–7	11598
			G160M	1600,1623	2781	9	11598
J0843+4117	130.956	41.295	G130M	1291,1309	4359	2–9	12248
			G160M	1577,1623	7010	4–9	12248
J0853+4349	133.393	43.817	G130M	1222	14809	5–10	13398
J1117+2634	169.476	26.571	G160M	1577,1600	4783	4–16	12248
J1155+2922	178.970	29.377	G130M	1300,1327	10916	3–9	12603
J1214+0825	183.627	8.419	G130M	1300	4813	6–8	11698
J1404+3353	211.118	33.895	G130M	1309,1327	7706	4–7	12603
J1419+0606	214.956	6.115	G130M	1291	11028	5–7	13473
			G160M	1600	8735	3–6	13473
J1454+3046	223.601	30.783	G130M	1291,1327	7712	3–8	12603

[a] – Range of continuum signal-noise ratio measured at the wavelengths of Lyα and metal species listed in Section 4.2.3.
[b] – HST MAST archive program ID. Notable program IDs include: Cycle 22 COS-AGN (13774), COS-Halos (11598), COS-Dwarfs (12248), and COS-GASS (12603).

$$\text{EW} = \int_{\lambda_{min}}^{\lambda_{max}} 1 - F \, d\lambda, \tag{4.1}$$

where F is the continuum-normalized flux.

To determine if the absorption within this ± 500 km s^{-1} window is indeed associated with the CGM of the host galaxy, I confirmed that there was neither contamination from the Galaxy's ISM nor from intervening absorbers at other redshifts more than 1000 km s^{-1} from the AGN. In cases where multiple lines are covered for a given species, contamination was also flagged by comparing the strengths of the lines relative to the ratio of oscillator strengths (f), as well as requiring similar velocity profiles.

For five of the COS-AGN sightlines, I was uncertain if the absorption detected at the expected location of Lyα or Si III is associated with the CGM of the COS-AGN host galaxy as there are no other absorption lines to confirm its velocity or structure. I have conservatively not adopted the corresponding EW measurements in my analysis for these lines, but note (when relevant) how the results change if these EW measurements are adopted. Appendix C presents the measured EWs for these line and the justification for why these cases are not included.

When no absorption is detected without signs of blending, 3σ EW upper limits on these undetected lines are derived using the error spectrum within a ± 50 km s^{-1} interval of clean continuum near the systemic redshift of the AGN-dominated galaxy. The EW for lines that are visually detected but were $< 3\sigma$ above the noise were automatically set to the 3σ noise threshold and flagged as upper limits. All EW upper limits adopted from the literature are converted to 3σ values for consistency.

The derived EWs and velocity profiles are given in Appendix C. An example is given for the sightline towards J0852+0313 (the sightline with the strongest metal lines); Table 4.3 gives the EW and the associated data quality flags for each absorption line shown in Figure 4.5. The data quality flags represent a sum of whether or not the line is adopted (+1), blended (+2), undetected (+4), or saturated (+8).

4.2.4 Control matching

To provide a fair comparison between the CGM properties of AGN and non-AGN host galaxies, I implement a control-matching scheme that matches galaxies from the literature sample (COS-Halos, COS-GASS and COS-Dwarf galaxies) to each COS-AGN

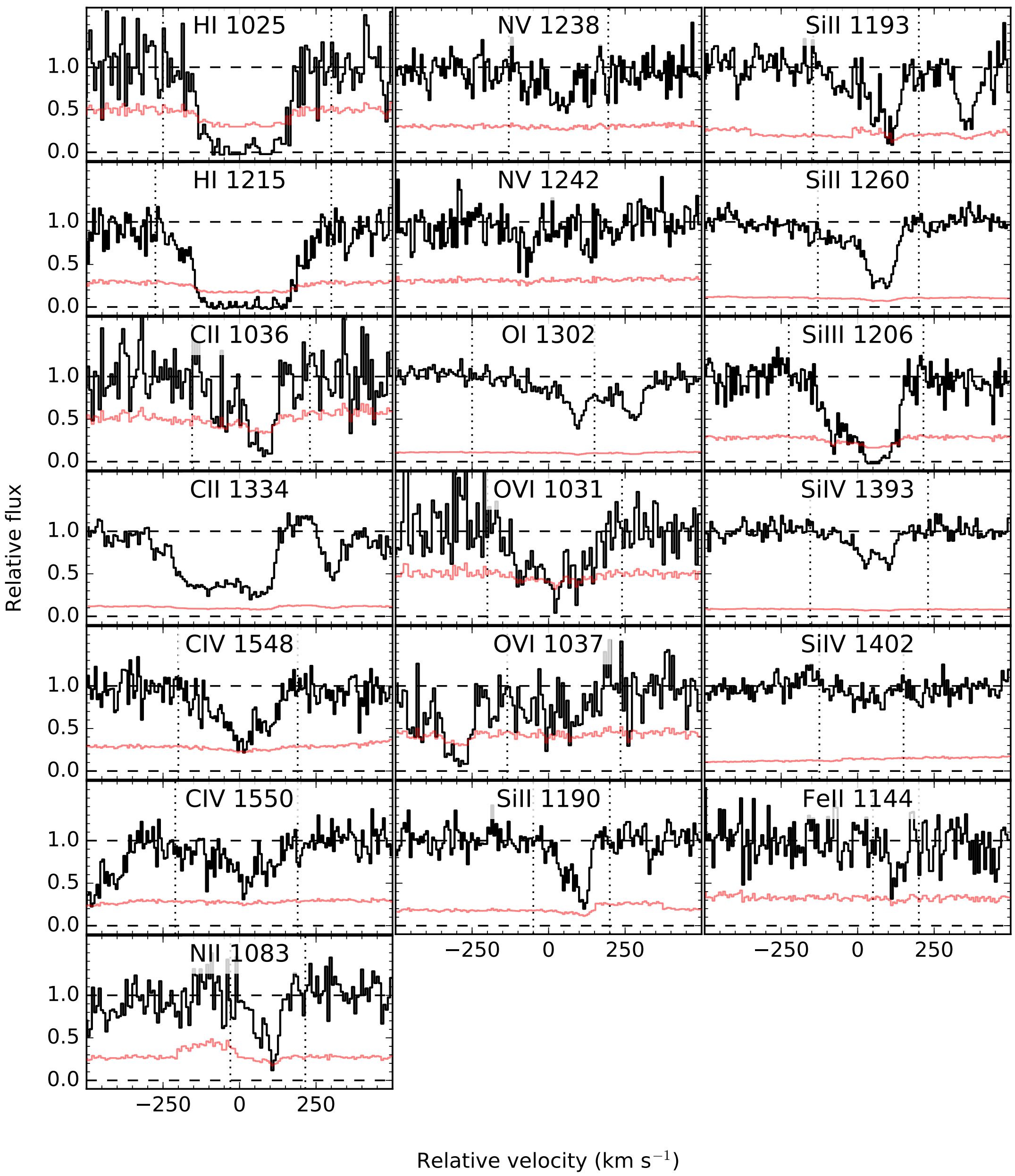

Figure 4.5 Velocity profiles for the sightline towards J0852+0313 (z_{gal}=0.129). The vertical dotted lines show the integration limits for determining the EW for adopted lines only. The red line shows the associated error spectrum.

Table 4.3 Measured EWs for J0852+0313 (z=0.129)

Ion	λ [Å]	f	$v_{\rm min}$ [km s^{-1}]	$v_{\rm max}$ [km s^{-1}]	EW [mÅ]	flag*
H I	1025.722	7.912E-02	-250	300	752 ± 91	**9**
H I	1215.670	4.164E-01	-275	300	1356 ± 56	**9**
C II	1036.337	1.231E-01	-155	230	< 366	**11**
C II	1334.532	1.278E-01	-315	215	. . .	2
C IV	1548.195	1.908E-01	-200	190	657 ± 66	**1**
C IV	1550.770	9.522E-02	-210	190	474 ± 71	**1**
N II	1083.990	1.031E-01	-30	215	200 ± 41	**1**
N V	1238.821	1.570E-01	-130	195	260 ± 56	**1**
N V	1242.804	7.823E-02	0	100	. . .	2
O I	1302.168	4.887E-02	-250	150	< 264	**3**
O VI	1031.926	1.329E-01	-200	240	< 451	**11**
O VI	1037.617	6.609E-02	-135	235	273 ± 80	**1**
Si II	1190.416	2.502E-01	-50	200	234 ± 30	**1**
Si II	1193.290	4.991E-01	-145	200	378 ± 40	**9**
Si II	1260.422	1.007E+00	-130	200	458 ± 18	**1**
Si III	1206.500	1.660E+00	-225	215	804 ± 52	**9**
Si IV	1393.755	5.280E-01	-155	230	235 ± 19	**1**
Si IV	1402.770	2.620E-01	-125	150	115 ± 28	**1**
Fe II	1144.938	1.060E-01	50	200	87 ± 39	**1**

*The data quality flags represent a sum of whether or not the line is: adopted (+1), blended (+2), undetected (+4), or saturated (+8).

galaxy. By adopting the literature sample as a pool for the control galaxies, I assume that these galaxies are representative of galaxies that do not host AGN. As the EW of a given species in the CGM has tentatively been shown to scale with a combination of $\rho_{\rm imp}$ and the host's $M_\star$ (Chen et al., 2010; Werk et al., 2014; Borthakur et al., 2016), I used $M_\star$ and $\rho_{\rm imp}$ as the control matching parameters, thus simultaneously removing the effects from these observed scaling relations in the EW analysis.

The combination of the large range in $M_\star$ and $\rho_{\rm imp}$ of both the literature and COS-AGN galaxies (see Figure 4.3) makes selecting a large but representative control sample difficult. Ideally the control-matching criteria should maximize the number of matches for each COS-AGN sightline, whilst removing any potential EW differences resulting from small but significant changes in $M_\star$ and $\rho_{\rm imp}$ (see trends observed in Chen et al., 2010; Werk et al., 2014; Borthakur et al., 2016). However, these previously derived EW relations are empirically determined for an individual species, and cannot easily be generalized to all species into a simple control matching methodology.

The adopted control matching scheme in this work uses a fixed maximum tolerated offset in both $M_\star$ and $\rho_{\rm imp}$ between a given control sightline and the AGN sightline ($\Delta\log(M_\star/M_\odot)$ and $\Delta\log(R_{\rm imp}/{\rm kpc})$; where $\Delta X = X_{control} - X_{AGN}$ for the matched parameter X). Figure 4.6 shows $\Delta\log(M_\star/M_\odot)$ and $\Delta\log(R_{\rm imp}/{\rm kpc})$ for all potential AGN-control pairs. These two offsets are combined into a single matching parameter r^2, which is given by the sum of the squares of $\Delta\log(M_\star/M_\odot)$ and $\Delta\log(R_{\rm imp}/{\rm kpc})$, i.e.

$$r^2 = \Delta\log(M_\star/M_\odot)^2 + \Delta\log(R_{\rm imp}/{\rm kpc})^2, \tag{4.2}$$

such that r provides a single factor of how far off each control match is from the AGN value. Adopting a tolerance of 0.2 dex in each $\Delta\log(M_\star/M_\odot)$ and $\Delta\log(R_{\rm imp}/{\rm kpc})$ (and thus a tolerance in $r = 0.28$ dex) provides matching within a factor of two of the COS-AGN sightline's $\rho_{\rm imp}$ and $M_\star$. Given that the COS-AGN sample tends to probe higher $\rho_{\rm imp}$ and $\log(M_\star/M_\odot)$ relative to the literature sample (e.g. see Figure 4.6), I computed the skewness for both $\Delta\log(M_\star/M_\odot)$ and $\Delta\log(R_{\rm imp}/{\rm kpc})$ (independently) to confirm that the adopted tolerances do not lead to a biased control sample. The skewness tests reveal that the selected r tolerance is similar to a Gaussian distribution at $\geq 95\%$ confidence, suggesting that the initial tolerance does not select a significantly skewed sample. Thus I adopted a cut of $r = 0.28$ as my control matching tolerance, which selects at least five different control sightlines for over 80% of the COS-AGN sample.

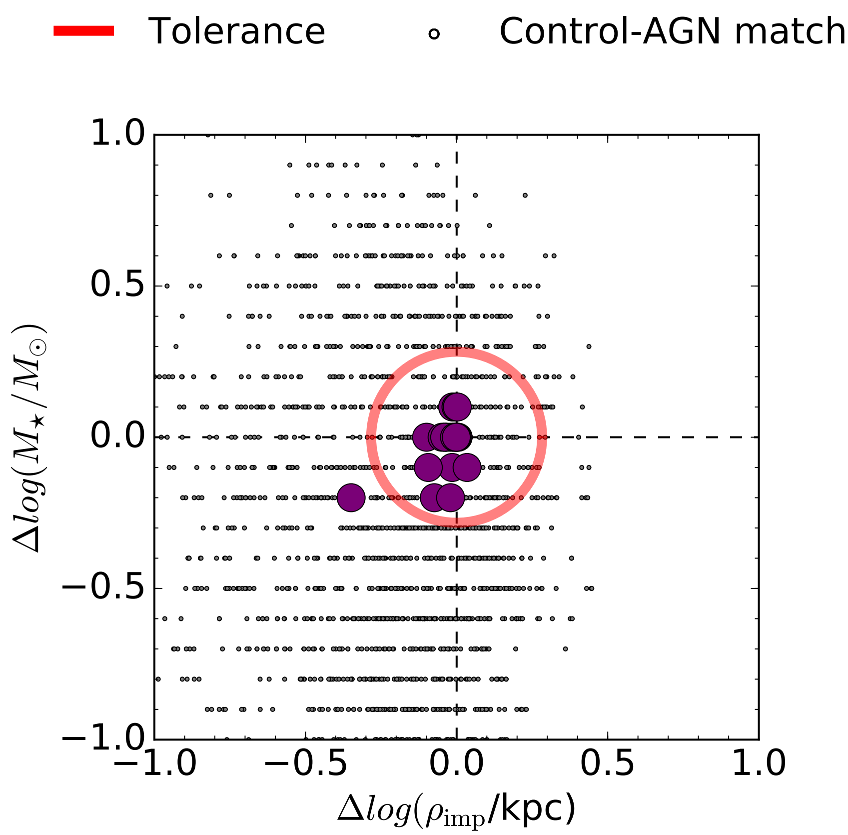

Figure 4.6 The offsets $\Delta\log(M_\star/M_\odot)$ and $\Delta\log(R_{\rm imp}/{\rm kpc})$ computed for all possible control-AGN matches (small circles). For reference, the larger purple circles represent the best control match (in terms of the matching parameter r) for each COS-AGN galaxy. The thick red circle denotes the adopted tolerance of $r = 0.28$ dex.

I point out that this broad tolerance allows for any of the literature galaxies to be matched to multiple COS-AGN galaxies. As one COS-AGN absorber does not have a single control match within the adopted tolerance range (J0042-1037; z=0.036, $\log(M_\star/M_\odot)$=9.5, and $\rho_{\rm imp}$= 299 kpc, see purple point outside red circle in Figure 4.6); I do not include this sightline in the analysis. I note that the adopted tolerance in r is similar to the one required to match the scatter of the Mg II-$\rho_{\rm imp}$ relation computed by Chen et al. (2010).

In addition to $M_\star$ and $\rho_{\rm imp}$, the comparison sample could potentially benefit from controlling additional parameters. For example, the sSFR appears to play a key role in the EW distribution of O VI (Tumlinson et al., 2011; Werk et al., 2014), however an alternative suggestion for the paucity of metals around passive galaxies is related to the halo mass rather than the sSFR of a galaxy (Oppenheimer et al., 2016). Figure 4.3 demonstrates that many of the COS-AGN galaxies have a sSFR that is intermediate to the star-forming and passive galaxies (these lower SFR for Seyfert AGN relative to star-forming galaxies have previously been seen in the SDSS; Ellison et al., 2016b; Leslie et al., 2016). The lack of overlap between the COS-AGN sSFR distribution and that of the control pool prevents a matching within meaningful tolerances of sSFR. However, we can simply distinguish between star-forming and passive galaxies in the control sample based on the log(sSFR / yr^{-1})= -11.0 cut adopted by COS-Halos, and draw comparisons between AGN and star-forming or passive galaxies independently. Later, I will implement this sSFR cut into the analysis.

Environment may also influence the CGM of galaxies (Bordoloi et al., 2011; Stocke et al., 2014; Burchett et al., 2016). Environment can be quantified using a metric such as δ_5, a measure of the surface density of galaxies (Σ_5) within the distance to the 5^{th} nearest neighbour (d_5) relative to the average surface density across the sky at that redshift, i.e.

$$\delta_5 \equiv \frac{\Sigma_{5,gal}}{\Sigma_{5,sky}} = \left(\frac{d_{5,sky}}{d_{5,gal}}\right)^2, \tag{4.3}$$

where $\Sigma_{5,gal}$ and $d_{5,gal}$ are measured for the host galaxy (within ± 1000 km s^{-1} of the host's redshift) and $\Sigma_{5,sky}$ and $d_{5,sky}$ are the average values measured across the sky at the host's redshift. Since I do not have a robust measurement of environment consistently quantified across the control and COS-AGN samples, I am unable to control for environment. However, I have compared the distribution of δ_5 measured in the SDSS (Baldry et al., 2006) for all AGN galaxies to the distribution for star-forming galaxies with matching stellar mass and redshift distributions and find that the resulting δ_5 distributions between these two galaxy populations are similar to within a couple of per cent at all values of $\mathrm{M}_\star$ (see Figure 4.7). The consistent distributions suggests that, on average, the star-forming and the SDSS AGN galaxies occupy similar environments, thus I do not need to match for environment in the control sample.

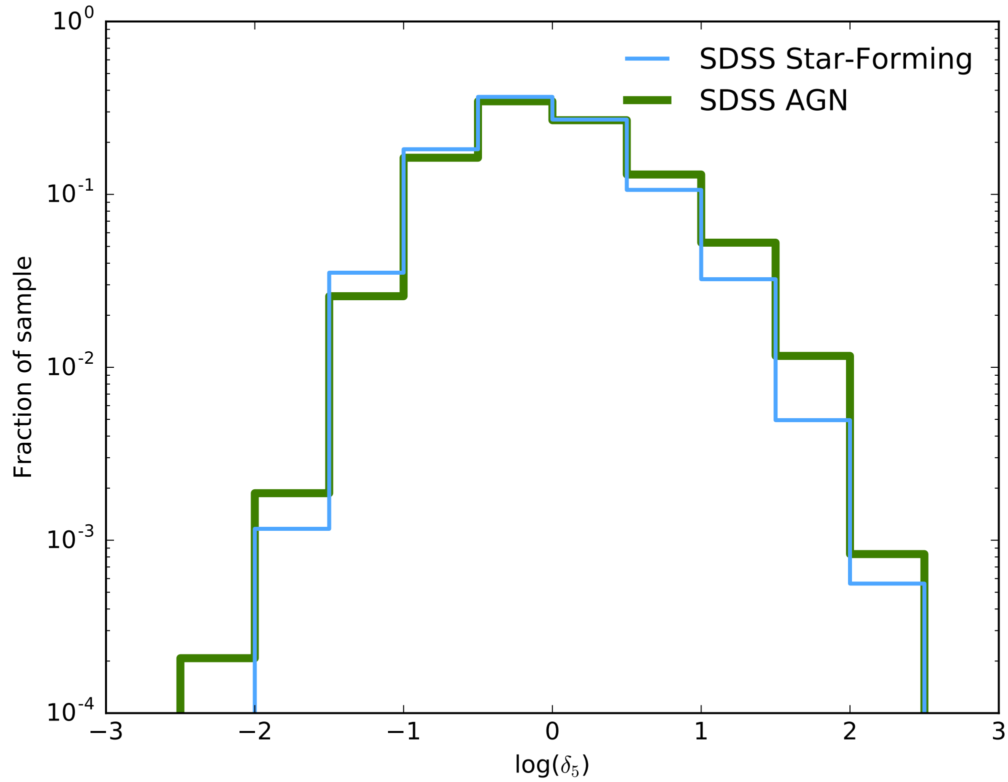

Figure 4.7 The normalized distributions of δ_5 computed for all star-forming (blue) and AGN host (green) galaxies in the SDSS over the same redshift and mass range as the COS-AGN sample.

4.3 Results

4.3.1 Kinematics

To study the kinematics of the CGM gas, I was limited to using the saturated Lyα absorption as many of the typically unsaturated metal lines are frequently undetected in the COS-AGN sample (the covering fractions of metal lines will be further discussed in the following section). I first assessed whether or not the CGM gas is bound to the host galaxy by comparing the relative velocity of the Lyα absorption ($v_{\mathrm{Ly}\alpha}$) to the systemic velocity of the galaxy (v_{Gal}). As the dark matter halo mass ($\mathrm{M_{Halo}}$) is required to assess the escape velocity of the galaxy halo, I used the $\mathrm{M_\star}$-$\mathrm{M_{Halo}}$ relation provided by Moster et al. (2010) to calculate the halo mass of each galaxy, namely

$$\frac{\mathrm{M_\star}}{\mathrm{M_{Halo}}} = 2\left(\frac{\mathrm{M_\star}}{\mathrm{M_{Halo}}}\right)_0 \left[\left(\frac{\mathrm{M_{Halo}}}{M_1}\right)^{-\beta} + \left(\frac{\mathrm{M_{Halo}}}{M_1}\right)^{\gamma}\right]^{-1}, \tag{4.4}$$

where $M_1 = 10^{11.884} M_\odot$, $\left(\frac{\mathrm{M_\star}}{\mathrm{M_{Halo}}}\right)_0 = 0.0282$, $\beta = 1.057$, and $\gamma = 0.556$ (i.e. the best fit parameters from table 1 in Moster et al., 2010). The escape velocity of the halo (calculated from ρ_{imp} of the QSO sightline) is found using

$$v_{\mathrm{Esc}} = \left[2\int_{\rho_{\mathrm{imp}}}^{\infty} \frac{\mathrm{GM_{Halo}}(< \rho)}{\rho^2}\mathrm{d}\rho\right]^{0.5}, \tag{4.5}$$

assuming the halo mass is distributed following a Navarro et al. (1997) dark matter profile with a concentration parameter of 15.

The top panel of Figure 4.8 compares the kinematic extent of the Lyα profile to the escape velocity of the halo for both the COS-AGN (thick bars) and control samples (thin lines). The horizontal lines denote the escape velocity of the halo, such that any gas located beyond these lines is *likely not bound* to the host galaxy. The colour coding of the vertical bars in the top panel of Figure 4.8 represents the optical depth of the velocity profile of the Lyα line, such that dark colours show the strongest components of the line. The bulk of the gas in the COS-AGN is within the escape velocity of hosts' haloes, and is likely bound to the host galaxy. I note that the gas probed by the control sightlines also appears bound (grayscale lines; Werk et al., 2013; Borthakur et al., 2016)

The only AGN host that shows gas likely moving at speeds greater than the escape velocity is J1117+2634 (absorber at z= 0.029; see Figure C.8). I note that in this system the ± 500 km s^{-1} absorption search window for Lyα contains two absorption features: Galactic S II λ 1250 Å absorption at ≈ -100 km s^{-1}, and the unidentified absorption assumed to be Lyα between 250 km s^{-1} and 400 km s^{-1} (see Appendix C). Without additional detected metal lines to attempt to confirm the absorption at 250–400 km s^{-1}, it is possible the proposed absorption towards J1117+2634 at z= 0.029 is not from gas actually associated with the AGN host.

To compare the bulk motion of the CGM surrounding AGN hosts to their control match sample, I computed the flux-weighted velocity centroid of the Lyα absorption profiles ($v_{\rm CGM}$) to look for any kinematic differences between the AGN and non-AGN populations. The bottom panel of Figure 4.8 shows the distributions of kinematic offset between the CGM gas and the systemic redshift of the host ($|v_{\rm CGM} - v_{\rm Gal}|$) for the COS-AGN (green shaded region) and control samples (black line). The inset panel shows the distribution of the same $|v_{\rm CGM} - v_{\rm Gal}|$ data, but normalized by $v_{\rm Esc}$. Note that the majority of the COS-AGN sightlines probe gas within 100 km s^{-1} of their host galaxy that is likely bound to the host galaxies. A KS test rejects the null hypothesis that the two distributions of $|v_{\rm CGM} - v_{\rm Gal}|$ are similar at 75% confidence (61% for the $v_{\rm Esc}$-normalized distribution of the inset panel), suggesting there is likely no difference in the bulk motions of the AGN gas compared to their control-matched counterparts. Therefore the kinematics of the gas traced by Lyα around AGN hosts suggests the material is likely bound and has bulk motion properties similar to the CGM surrounding non-AGN hosts in the control sample.

4.3.2 EW analysis

Since many of the detected absorption lines are potentially saturated, my analysis is limited to using EWs, rather than column densities. In this sub-section, I present a number of complementary analyses to investigate both the strength and frequency of absorption features in the COS-AGN sample, relative to the matched control sightlines.

Covering Fractions

Covering fractions are determined as the number of CGM sightlines that have a detection of a given species greater than some EW threshold (EW$_{\rm thrsh}$) relative to the total number of sightlines in a given sample with the adopted EW measurements

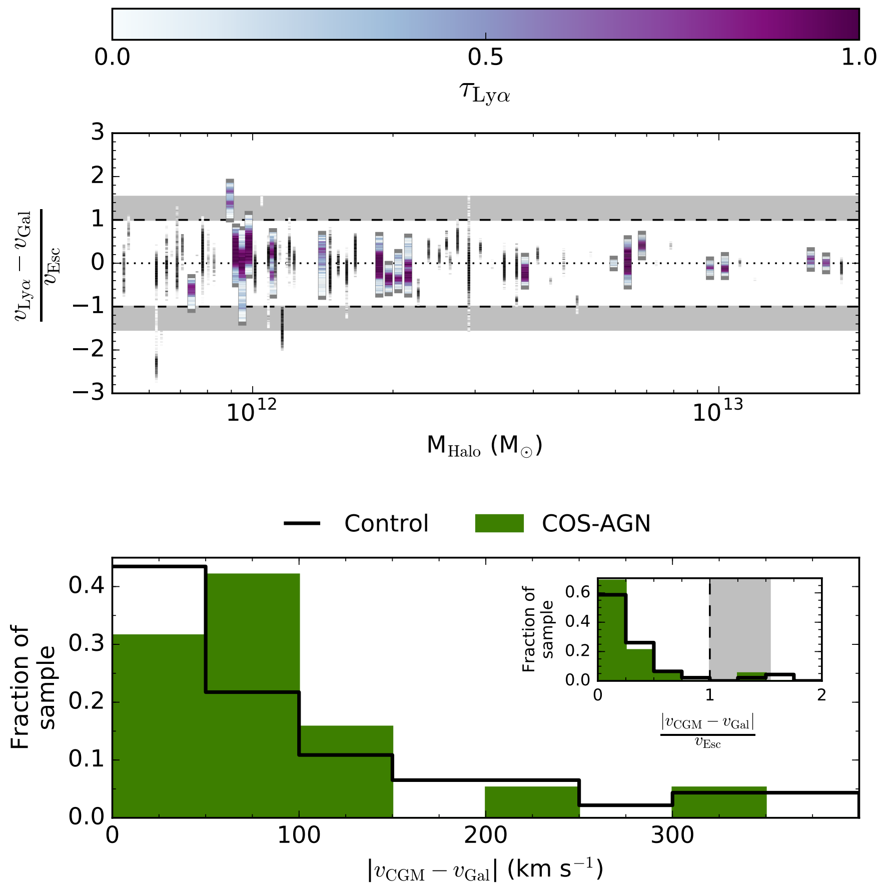

Figure 4.8 The top panel shows the velocity span of the Lyα profiles (within ± 500 km s^{-1} of the host galaxy) from COS-AGN and the control sample as a function of halo mass ($\mathrm{M_{Halo}}$). The COS-AGN sightlines are denoted by the thicker coloured lines, while the control sample are shown as thin grey lines. The velocity is normalized by the escape velocity from the halo at the observed ρ_{imp}. The horizontal dashed lines denotes the relative velocity for which gas at a distance of ρ_{imp} from the galaxy becomes unbound. As the precise location of the gas along the line of sight is not known, the grey band shows where gas becomes unbounded within a $\pm\rho_{\mathrm{imp}}$ region along the sightline from the perpendicular. Each line is colour-coded by the optical depth of the Lyα profile to indicate the velocity of all the observed components. For visualization, all galaxies of the same halo mass are offset horizontally by a small amount. The bottom panel displays the distribution of the velocity centroid offsets of the Lyα absorption profile relative to the systemic velocity of the galaxy for the COS-AGN (green bars) and control (black line) samples. The inset panel shows the distribution of $|v_{\mathrm{CGM}} - v_{\mathrm{Gal}}|$ data normalized by the escape velocity of the halo. As in the top panel, the shaded region denotes the approximate value where the gas may become unbound from the host galaxy. A KS test suggests there is no difference between the AGN and control sample distributions.

Table 4.4 Covering Fractions

Ion	λ	EW_{thrsh}	Covering Fraction		
	[Å]	[mÅ]	AGN	SF controls	P controls
H I	1215	124	$0.94^{+0.06}_{-0.23}$	$1.00^{+0.00}_{-0.21}$	$0.75^{+0.25}_{-0.21}$
		200⋆	$0.88^{+0.12}_{-0.23}$	$0.86^{+0.14}_{-0.20}$	$0.69^{+0.28}_{-0.20}$
Si II	1260	197	$0.06^{+0.14}_{-0.05}$	$0.18^{+0.24}_{-0.12}$	$0.25^{+0.33}_{-0.16}$
		150⋆	$0.12^{+0.16}_{-0.08}$	$0.27^{+0.27}_{-0.15}$	$0.25^{+0.33}_{-0.16}$
Si III	1206	234	$0.23^{+0.22}_{-0.13}$	$0.27^{+0.27}_{-0.15}$	$0.18^{+0.24}_{-0.12}$
		100⋆	$0.31^{+0.24}_{-0.15}$	$0.55^{+0.33}_{-0.22}$	$0.36^{+0.29}_{-0.17}$
Si IV	1393	218	$0.07^{+0.15}_{-0.06}$	$0.08^{+0.19}_{-0.07}$	$0.40^{+0.53}_{-0.26}$
		100⋆	$0.13^{+0.18}_{-0.09}$	$0.33^{+0.26}_{-0.16}$	$0.40^{+0.53}_{-0.26}$
C IV	1548	272	$0.15^{+0.20}_{-0.10}$	...	...
N V	1238	151	$0.07^{+0.16}_{-0.06}$	$0.00^{+0.18}_{-0.00}$	$0.00^{+0.31}_{-0.00}$

⋆ COS-Halos EW threshold.

presented in Section 4.2.3. Similar to Werk et al. (2013), the EW_{thrsh} are selected based on the lowest signal-noise ratio near the species of interest such that all 3σ non-detections from COS-AGN are below this threshold. As the signal-noise ratio of some of the spectra is lower than for COS-Halos, the EW_{thrsh} are different than those used in Werk et al. (2013). Table 4.4 lists the covering fractions calculated for the entire COS-AGN and control-matched sample (split by sSFR into star-forming [SF] and passive [P] controls; blue diamonds and red squares respectively in Figure 4.9) using my EW_{thrsh} as well as the threshold adopted by COS-Halos for reference (note that when using the COS-Halos thresholds, upper limits above the threshold are removed from the covering fraction calculations). I elected to use my EW_{thrsh} for consistency with my data quality. Due to the low number of sightlines, I used the 1σ binomial confidence intervals in the Poisson regime (tabulated in Gehrels, 1986) for the covering fraction errors. These covering fractions using the EW_{thrsh} are plotted in the top panel of Figure 4.9 for a variety of species, spanning a range of ionization states.

The bottom six panels of Figure 4.9 present the covering fractions in bins of ρ_{imp} (split by the median ρ_{imp} of the COS-AGN sample; 164 kpc). The covering fractions of the COS-AGN sample are the green circles. For reference, the covering fractions of the literature galaxies that were matched to the COS-AGN galaxies are shown as blue diamonds (for star-forming controls) and red squares (passive controls).

The error bars on all of the data points overlap, indicating no significant difference between the AGN sightlines and the controls for any of the species. Nonetheless, I note three tentative differences. The first is that the H I covering fraction of the COS-AGN sightlines (94^{+6}_{-23}%) is most similar to the covering fraction of the star-forming control galaxies (100^{+0}_{-21}%), and higher that the control-matched passive galaxies (75^{+25}_{-21}%). Secondly, the covering fraction for Si III λ 1206 Å is 29^{+38}_{-18}% for the COS-AGN sample at high impact parameters, which is larger than the covering fraction of the control samples at the same distance (0%; $164 \leq \rho_{\rm imp} < 300$ kpc). Lastly, the inner 164 kpc bin shows no detections of Si II and Si IV in the COS-AGN sample while the control sample has non-zero covering fractions at those impact parameters ($\approx$ 25%, and 10–40%; respectively).

Although the covering fraction of N V in the COS-AGN sample is 7^{+16}_{-6}% for the entire range of $\rho_{\rm imp}$, the sightline towards J0852+0313 (see Figure 4.5) represents the only detection of N V in COS-AGN (1/20) and the controlled matched galaxies from COS-Halos (0/16 sightlines) and COS-GASS (0/30; S. Borthakur, private communication). I note however that COS-Halos detected N V in four of their 44 sightlines.

The 94^{+6}_{-23}% covering fraction measured for Lyα in the COS-AGN galaxies may initially appear to be in tension with the conclusions of Kacprzak et al. (2015), who used Mg II as a neutral gas tracer and found much smaller 10% covering fraction (EW> 300mÅ) between 100 and 200 kpc of the AGN. The Mg II EW threshold adopted by Kacprzak et al. (2015) is typical of that used to select strong H I absorbers at low redshifts ($\log(N(\text{H I})/\text{cm}^{-2}) \gtrsim 18.5$; Rao et al., 2006). Translating this Mg II EW threshold into a corresponding Lyα EW theshold for these column densities of gas yields a much higher than the threshold used in this work (EW $\gtrsim$ 1300 mÅ — assuming a minimum broadening parameter of 5 km s^{-1} — compared to EW > 124 mÅ for COS-AGN). Using this larger threshold, only one of the COS-AGN sightlines has an EW $\gtrsim$ 1300 mÅ, giving a consistent result with the observations from Kacprzak et al. (2015).

Relative EW analysis

Figure 4.10 shows the raw EW values for a variety of ionic species as a function of $\rho_{\rm imp}$. The COS-AGN points are colour-coded by their $L_{\rm bol}$. The control-matched sample is shown as black points, while the grey points are the remaining un-matched literature sightlines. The bold COS-AGN points are CGM sightlines that have spectroscopic

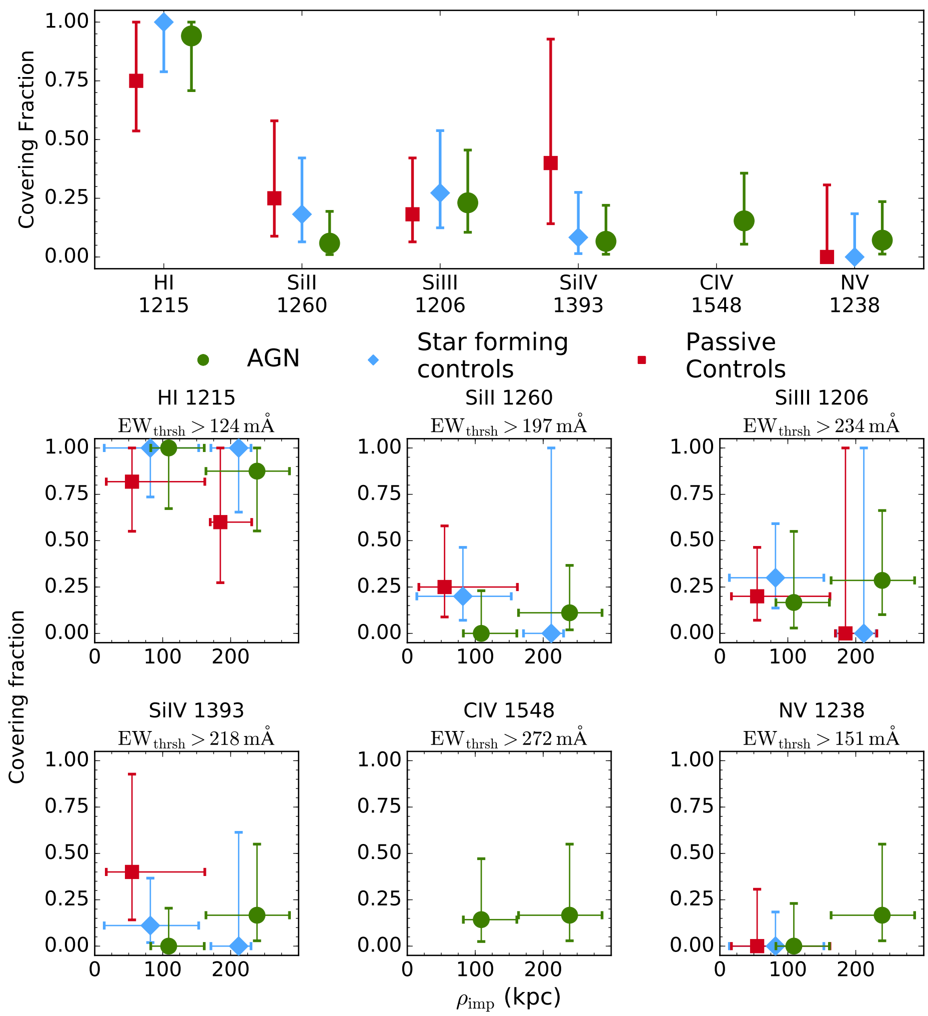

Figure 4.9 Covering fractions (with 1σ errors) of gas within ±500 km s^{-1} of the host galaxy for a variety of species measured in COS-AGN and control-matched samples. Top panel: The global covering fractions measured across all impact parameters from Table 4.4 are shown for the COS-AGN galaxies (green circles), and the control-matched passive (red squares) and star-forming (blue diamonds) galaxies. Bottom panels: The covering fractions of an individual species as a function of impact parameter (ρ_{imp}), split into two bins by the median ρ_{imp} of the COS-AGN sample (164 kpc). The EW thresholds (EW$_{thrsh}$) used to determine the covering fraction for each species (including the measurements presented in the top panel) are given above the corresponding species panel in the bottom two rows. The horizontal error bars represent the entire range of ρ_{imp} probed by each sample within the respective bin. The three points are offset from the centre of each bin by a small amount for clarity. No points are shown for a species that do not have spectral coverage of the corresponding absorption line.

companions (see Section 4.2.1). The top left panel demonstrates that the Lyα EWs for the COS-AGN follow the general trend of decreasing EW as a function of $\rho_{\rm imp}$ seen in previous low redshift studies (Chen et al., 2010; Werk et al., 2014; Borthakur et al., 2016). For metal species, the lack of detections in both the COS-AGN and control sample makes a comparative analysis difficult. For the remainder of this section, I will focus only on the Lyα EWs.

In order to quantify any difference between the COS-AGN and control samples, I calculated Δlog(EW/mÅ), which is defined as $\Delta\log(\mathrm{EW/m\AA}) = \log[\mathrm{EW_{AGN}}/\mathrm{median}(\mathrm{EW_{Controls}})]$, such that a positive Δlog(EW/mÅ) would imply that the CGM surrounding the AGN has a larger EW than the median of its control-matched galaxies. The left panel of Figure 4.11 shows Δlog(EW) for Lyα as a function of $\rho_{\rm imp}$ for the COS-AGN galaxies. For reference, the grey band represents the interquartile range of Δlog(EW) for the entire literature sample matched to itself. The right panel shows the distributions of Δlog(EW) for the COS-AGN (orange) and literature (grey) galaxies, with medians of the distributions indicated by the arrows.

To include the non-detections of the controls in the analysis, I calculated the median EW of the controls twice: once including limits as if they were detections, and once setting the non-detected EWs to 0 mÅ. These median EWs span the range of true median EW if the absorption lines were actually detected. For this calculation, I only include non-detections when the upper limits are more sensitive (i.e. smaller) than the largest detected EW as these limits are constraining enough to affect the median value. The corresponding Δlog(EW) range is shown on Figure 4.11 as the thick grey errorbars. The 1σ jackknife errors on Δlog(EW) are typically smaller than the size of the points.

The median Δlog(EW) of the COS-AGN sample is enhanced by $+0.10 \pm 0.13$ dex relative to the controls. Repeating this control-matching experiment for the literature sample yields a median Δlog(EW) of $0.00{\pm}0.28$. Note that the errors on these median Δlog(EW) represent the median absolute deviation of the distribution. A KS test rejects the null hypothesis that the distributions of Δlog(EW) for the COS-AGN and control samples are same at 20% confidence. When the LINER galaxies are removed from the COS-AGN sample, the median Δlog(EW) changes to $+0.10 \pm 0.15$, and the KS test yields a rejection of the null hypothesis at 14% confidence.

To check if there is any effect from splitting the control sample into star-forming and passive galaxies, I measured the Δlog(EW) for all star-forming galaxies in the non-AGN literature sample to their control-matched passive counterparts. The me-

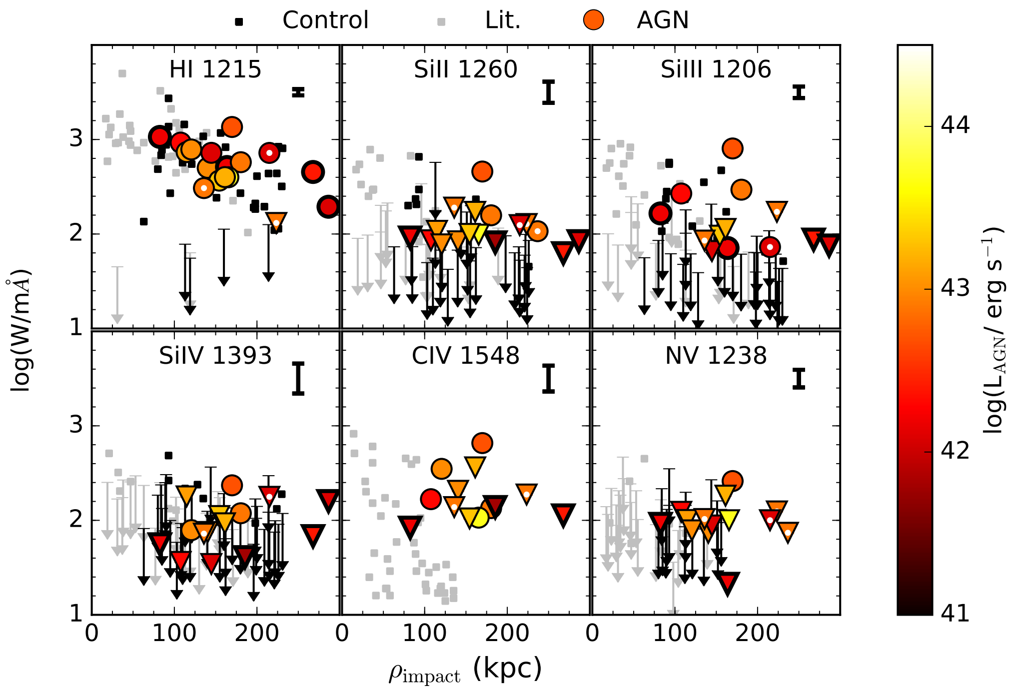

Figure 4.10 The rest-frame equivalent widths (within ±500 km s^{-1} of the host galaxy) as a function of impact parameter. The coloured circles (EW detections) and triangles (EW upper limits) represent the COS-AGN sample, and are colour coded by the bolometric luminosity of the AGN (L_{bol}). The median error bar on the COS-AGN EW measurements is given by the black error bar in the top right region of each panel. The black squares show the EW values of the control-matched galaxies, while the grey squares denote the rest of the literature comparison sample. Data outlined with a thick black line represent COS-AGN systems with nearby galaxies. COS-AGN galaxies flagged as LINERs are indicated by small white dots on top of the respective data points.

dian Δlog(EW) obtained for star-forming galaxies relative to the matched passive controls is $+0.03 \pm 0.26$, while a KS-test reveals the null hypothesis of the Δlog(EW) distributions for the star-forming and passive galaxies are the same is rejected at 38% confidence. Therefore there is no significant difference in the offset of the AGN hosts from the controls that would be caused by the star formation rate.

Stacked Spectra

The results in the previous sub-section indicate a possible (but not significant) difference in the Lyα absorption properties of the COS-AGN sample, and possibly in some of the metal species as well. However, that analysis is limited by the modest signal-noise ratio of the data, the small sample size and lack of detections of metal species. Therefore, in this section I consolidated the data by stacking all of the COS-AGN spectra and comparing it to a stack of the control sample. In brief, all spectra are shifted to the rest-frame (using the redshift of the strongest component of the H I absorption profile) and rebinned to a linear dispersion of 0.064 Å pixel^{-1} (similar to the resolution of the COS-AGN spectra). These rebinned spectra are mean combined without any weighting. I note that either using the systemic redshifts of the galaxies or using different weighting schemes does not significantly change the results.

Table 4.5 gives the measured EWs of the various absorption lines of interest from the final stacked COS-AGN spectrum. I required that the absorption line be detected at $> 3\sigma$, otherwise the EW is set to a 3σ upper limit. The stacked EW errors are calculated using a standard jackknife approach by removing each COS-AGN sightline from the stacked spectrum and recalculating the EW. The numbers in brackets in each column give the EW offsets from removing the 'strongest' ($jack, min$) and 'weakest' ($jack, max$) absorber sightline from the stack in a jackknife fashion (i.e. these are the maximal variations in the EW from the jackknife), as well as the number of sightlines that contributed to the stack (N_{spec}). The four columns on the right are the measured EWs when the stacking process is only applied to COS-AGN sightlines split into two bins of log($L_{\rm bol}$) and $\rho_{\rm imp}$ at the median value of the COS-AGN sample (log($L_{\rm bol}$/erg s^{-1})= 42.9 and $\rho_{\rm imp}$= 164 kpc; respectively).

A similar procedure was completed for all the spectra in the literature sample that were used in the control sample. Each control sightline in the stacked spectrum was weighted by the number of times the sightline was matched to a unique AGN host (such that the most frequently matched control sightline was given a higher

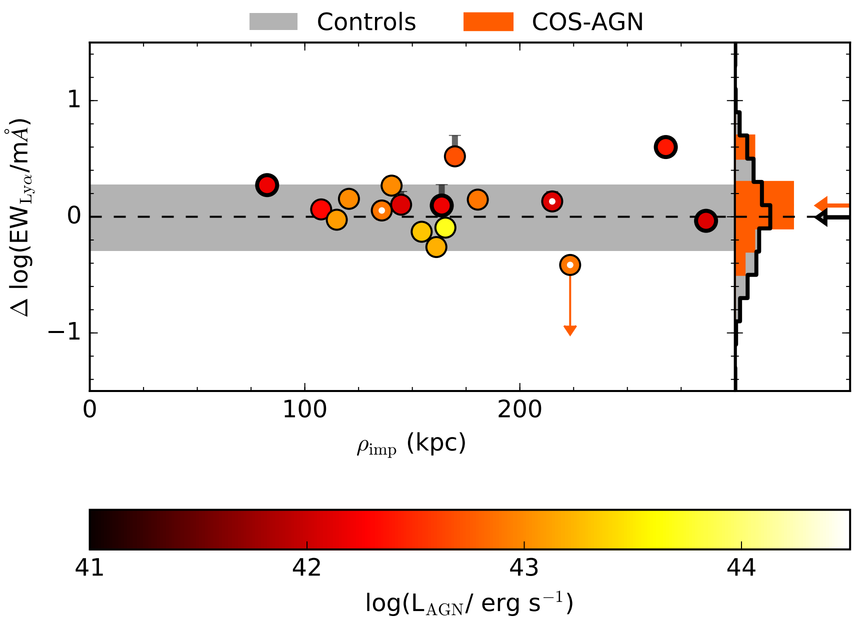

Figure 4.11 The difference in the Lyα equivalent width of the COS-AGN sightlines relative to their control matched counterparts (Δlog(EW/mÅ)) as a function of impact parameter (ρ_{imp}). The EW measure material within $\pm$500 km s^{-1} of the host galaxy. The points are colour-coded by the bolometric luminosity of the AGN (L_{bol}). The errorbars denote how the maximal shift on including control matched EW upper limits in the calculation of Δlog(EW/mÅ). For reference, the horizontal grey band represents the interquartile range of ΔEW of the literature sample control matched with itself. The normalized distributions of ΔEW for both the COS-AGN and control galaxies are shown in the right panel, with the median of each histogram given by an arrow. Data outlined by a thick black line are COS-AGN sightlines flagged as having nearby galaxies. COS-AGN galaxies flagged as LINERs are indicated by small white dots on top of the respective data points.

Table 4.5 Measured EW of stacked spectra

Ion	Line	Stacked EW ($^{jack,max}_{jack,min}$; N_{spec}) [mÅ]				
	[Å]	All sight-lines	log(L_{bol}/erg s^{-1})≤42.9	log(L_{bol}/erg s^{-1})>42.9	ρ_{imp}≤164 kpc	ρ_{imp}>164 kpc
H I	1215	739±25 ($^{+44}_{-69}$; 14)	937±53 ($^{+77}_{-116}$; 7)	539±38 ($^{+70}_{-66}$; 7)	799±41 ($^{+73}_{-68}$; 7)	680±66 ($^{+87}_{-176}$; 7)
C II	1036	<80 (2)	<80 (2)	. . .	. . .	<80 (2)
C II	1334	<37 (11)	<53 (6)	<50 (5)	<54 (5)	<51 (6)
C IV	1548	194±13 ($^{+20}_{-40}$; 11)	236±38 ($^{+61}_{-89}$; 5)	<194 (6)	185±17 ($^{+29}_{-38}$; 6)	205±39 ($^{+53}_{-96}$; 5)
C IV	1550	131±9 ($^{+15}_{-24}$; 13)	132±21 ($^{+21}_{-56}$; 6)	<167 (7)	<132 (7)	159±24 ($^{+33}_{-52}$; 6)
N V	1238	<32 (13)	<42 (6)	<47 (7)	<47 (7)	<43 (6)
N V	1242	<38 (10)	<46 (5)	<60 (5)	<51 (6)	<54 (4)
O I	1302	<31 (12)	<45 (5)	<42 (7)	<47 (6)	<39 (6)
O VI	1037	<379 (1)	<379 (1)	. . .	. . .	<379 (1)
SiII	1190	<29 (10)	<36 (5)	<46 (5)	<61 (3)	<32 (7)
Si II	1190	<32 (9)	<44 (4)	<46 (5)	<61 (3)	<37 (6)
Si II	1260	88±8 ($^{+11}_{-28}$; 15)	94±28 ($^{+30}_{-75}$; 6)	84±10 ($^{+15}_{-17}$; 9)	<101 (6)	103±18 ($^{+21}_{-47}$; 9)
Si III	1206	152±16 ($^{+18}_{-62}$; 12)	211±37 ($^{+33}_{-98}$; 8)	<120 (4)	<98 (6)	238±40 ($^{+32}_{-112}$; 6)
Si IV	1393	<44 (11)	<69 (4)	<57 (7)	<59 (6)	<66 (5)
Fe II	1144	<29 (12)	<34 (7)	<52 (5)	<49 (5)	<35 (7)
Fe II	1608	<102 (8)	<94 (2)	<134 (6)	<129 (5)	<168 (3)

Table 4.6 Measured EW of stacked control spectra

Ion	Line	Stacked EW ($^{jack,max}_{jack,min}$; N_{spec}) [mÅ]				
	[Å]	All sight-lines	log(sSFR/yr^{-1})< −11	log(sSFR/yr^{-1})≥ −11	ρ_{imp}≤164 kpc	ρ_{imp}>164 kpc
H I	1215	577±12 ($^{+24}_{-39}$; 43)	485±30 ($^{+52}_{-84}$; 19)	649±21 ($^{+40}_{-65}$; 24)	781±20 ($^{+50}_{-50}$; 25)	239±15 ($^{+30}_{-37}$; 18)
C II	1334	36±3 ($^{+6}_{-11}$; 43)	<29 (19)	46±5 ($^{+9}_{-20}$; 24)	62±5 ($^{+10}_{-18}$; 25)	<31 (18)
Si II	1190	<22 (15)	<39 (5)	<26 (10)	<22 (15)	. . .
Si II	1260	56±4 ($^{+7}_{-14}$; 33)	85±10 ($^{+17}_{-28}$; 16)	<42 (17)	103±6 ($^{+8}_{-20}$; 23)	<55 (10)
Si III	1206	98±4 ($^{+9}_{-15}$; 39)	77±9 ($^{+14}_{-28}$; 21)	126±8 ($^{+15}_{-24}$; 18)	156±7 ($^{+14}_{-20}$; 25)	<47 (14)
Si IV	1393	<35 (37)	<44 (17)	<55 (20)	58±5 ($^{+14}_{-15}$; 23)	<65 (14)
Si IV	1402	<27 (37)	<34 (17)	<41 (20)	<33 (21)	<44 (16)

weighting). Although there is very little difference in the measured EW without such a weighting, I elected to use this weighting scheme such that the derived jackknife errors represent the true range in EWs when a given sightline is excluded. The EWs measured from the stacked spectrum of the control galaxies is given in Table 4.6. I repeated the stacked EW calculations of splitting the controls by the median $\rho_{\rm imp}$ of the COS-AGN sample and log(sSFR/yr^{-1})= -11 (i.e. whether the controls are star-forming or passive; see Table 4.6). Note that the COS-GASS results (Borthakur et al., 2015, 2016) focus on a smaller subset of species (H I, C II, Si II, Si III, and Si IV), thus I was only able to provide a stacked spectrum for these species. I point out that the Si IV EW of the control stacked spectrum is poorly constrained due to an uncertain continuum in some of the literature sample spectra.

I repeated a similar differential EW analysis as above, where I calculated δlog(EW)= log(EW$_{\rm AGN}$) $-$ log(EW$_{\rm Control}$) using the EWs derived from the respective stacked spectra (Tables 4.5 and 4.6). The top panel of Figure 4.12 provides a comparison of EW between all the AGN sightlines and all controls (black points). The errorbars represent the combination of the maximal jackknife errors, providing the entire range of possible δlog(EW) from removing a single sightline from each sample. The stacking confirms the results from Figure 4.11, where the COS-AGN sightlines have an enhanced Lyα relative to the controls, with an enhancement of δlog(EW)$\approx$ 0.17 dex. However, there is a negligible difference in δlog(EW) for the metal species detected at all impact parameters. Removing the absorption surrounding the LINER galaxies does not change the qualitative picture presented in Figure 4.11; the measured δEW from the LINER-free stacks shift $\leq$ 0.08 dex (in either direction) for all species.

The additional red and blue points in the top panel of Figure 4.12 show the values of δlog(EW) calculated only when including only sightlines with $\rho_{\rm imp}$ smaller or larger than the median value of the COS-AGN sample (164 kpc; respectively). Splitting the stacking into the 'inner' and 'outer' CGM around AGN hosts uncovers that the enhancement seen in the Lyα δlog(EW) is driven by the the COS-AGN sightlines that probe $\rho_{\rm imp}\geq$ 164 kpc (δlog(EW)= $+0.45 \pm 0.05$ dex; using standard jackknife EW errors). This enhancement in the outer CGM gas is also seen by the detections of the cool gas tracers Si II (δlog(EW)$>$ 0.27 dex) and Si III (δlog(EW)$>$ 0.75 dex) in COS-AGN, even after removing the strongest metal absorber (towards QSO J0852+0313; see Figure 4.5), whilst these species are not detected in the stacked spectrum of the control galaxies. I remind the reader that this enhancement was suggested in the covering fraction analysis of Si III (Figure 4.9). For the inner CGM, the stacked

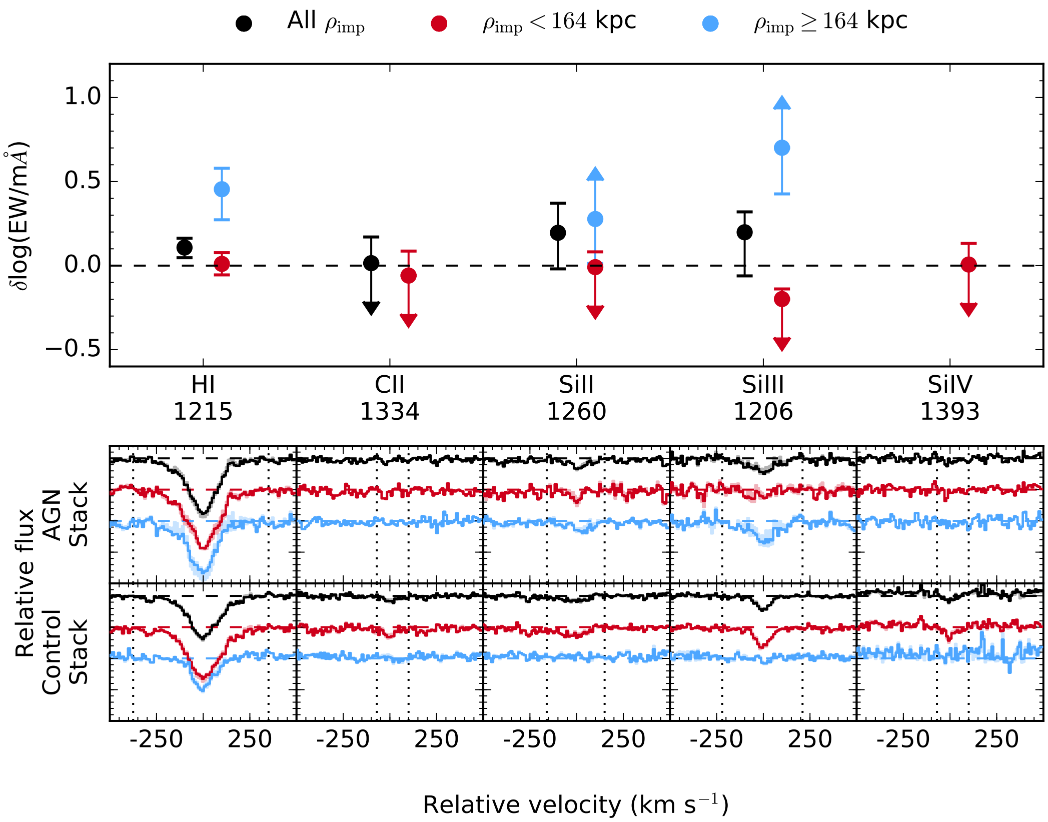

Figure 4.12 δlog(EW) measured from the stacked spectra for a variety of detected species. Top panel: The δlog(EW) is shown for the COS-AGN sightlines relative to: all controls (black circles), AGN and controls for small ($\rho_{\rm imp}$< 164 kpc; red circles) and large ($\rho_{\rm imp}\geq$ 164 kpc; blue circles) impact parameters. Errorbars on all points represent the possible range in δlog(EW) spanned by the maximal jackknife errors (i.e. $^{+jack,max}_{-jack,min}$). Upper and lower limits are plotted when an absorption line is detected in either the COS-AGN or control stack (respectively), but not the other. I note that the lower errorbar on the $>$ 164 kpc δlog(EW) for Si III λ 1206 Å line represents how shallow the lower limit becomes upon including the jackknife errors. The bottom ten panels show the absorption profiles of the stacked spectra (the COS-AGN spectrum in the middle row; the control spectrum in the bottom row) for each element. The colour coding of which sightlines are included is the same as in the top panel. The absorption lines are offset vertically by 0.5 in relative flux for clarity.

spectrum hints that there is a deficit of metal species around AGN galaxies relative to the control sample. The combination of the excess Lyα EW and tentative Si II and Si III EW enhancements at high $\rho_{\rm imp}$ is suggestive that these EW enhancement are tracing the cool gas phase of the CGM, rather than just the H I gas kinematics. I note that the inner CGM distribution has a slightly higher median $M_\star$ than the outer CGM bin ($\log(M_\star/M_\odot)$ of 10.8 dex relative to 10.5 dex), and the inner and outer CGM bins contain approximately the same ratio of passive and star-forming galaxies. I remind the reader that this discrepancy in the median $M_\star$ of each bins is on the order of the size of the control matching tolerance.

4.4 Discussion

In the previous section, I demonstrated that based on an analysis of the individual spectra, the CGM around AGN hosts is not much different than the control-matched non-AGN hosts. However, statistically significant differences are found in the analysis of the stacked spectrum; the COS-AGN systems have a higher EW of Lyα (and potentially Si II and Si III as well) relative to their non-AGN host counterparts at high impact parameters ($\rho_{\rm imp} \geq 164$ kpc; $\delta\log(\mathrm{EW/m\AA}) = +0.45 \pm 0.05$ dex). The kinematics of the gas traced by the absorption show the gas is likely bound to the halo, whilst no strong kinematic offsets relative to their host are present. I now consider whether these observations are a result of the AGN directly influencing the CGM of the host galaxy, or an effect of the environments (either internal or external to the host galaxy) in which AGN are typically found.

4.4.1 Are we seeing the effects of AGN feedback?

Mock COS-AGN simulation

The radiation field of the AGN may be expected to have a profound effect on the ionization structure of the CGM, by enhancing the ionizing radiation field to which the surrounding gas is subjected, and in the case of metals even long after the AGN has turned off (Oppenheimer & Schaye, 2013; Segers et al., 2017; Oppenheimer et al., 2018). To quantify the expected effects of turning on and off the AGN ionizing radiation spectrum on the CGM of a COS-AGN galaxy, were created a mock COS-AGN survey using previously run cosmological zoom-in hydrodynamical simulations with an additional AGN ionizing source following previous work on non-equilibrium ionization effects (Oppenheimer & Schaye, 2013; Oppenheimer et al., 2016). The purpose of these simulations is to isolate the effect of adding a constant AGN ionizing radiation source versus a control sample without AGN ionizing radiation to study the effect of the changed ionization structure of the CGM. This exploration is not meant to model or consider the effect of AGN feedback mechanically transforming the CGM via superwinds as the inclusion of the AGN radiation is not tied to the accretion onto the central super massive black hole. The AGN radiation is added to these simulations at the position of the central super massive black hole and only alters the ionization states of the CGM.

For our simulation suite we selected three representative galaxy haloes from Oppenheimer et al. (2016) that were chosen from the EAGLE volume (Crain et al., 2015; Schaye et al., 2015). These three halos are representative of the properties of the COS-AGN sample at $z = 0.075$ [log($M_\star/M_\odot$)= 10.3, 10.9, 11.0, log(sSFR / yr^{-1})= −10.3, −10.7, −11.0, residing in haloes log($M_{200}/M_\odot$)= 12.1, 12.8, 13.3; respectively]. The haloes were run by B. Oppenheimer and R. Horton at EAGLE HiRes resolution (gas particle mass of 2.3×10^5 $M_\odot$, dark matter particle mass of 1.2×10^6 $M_\odot$, and softening length of 350 proper pc) using the Recal feedback prescription (Schaye et al., 2015) and are zooms Gal001, Grp003, and Grp008 listed in Table 1 of Oppenheimer et al. (2016) from the initial conditions ($z = 127$).

To include the effects of the AGN ionizing spectrum on the CGM at different luminosities, we inserted an additional AGN ionizing source (with an ionizing spectrum from Sazonov et al., 2004) placed at the centre of the galaxy, instantaneously affecting the radiation field from $z = 0.1$ onwards and reaches equilibrium at $z = 0.075$. I note that this AGN radiation model has no dynamical effect on the gas accretion or outflows from the AGN, and is not tied to the accretion of material onto the central super-massive black hole. A range of AGN luminosities was used to match the COS-AGN luminosities (log(L_{AGN}/erg s^{-1})=42–44 dex, in increments of 0.5 dex), and a control run with no AGN radiation was included for creating the control sample. The time-dependent ionization from the AGN in addition to the Haardt & Madau (2001)[8] ultra-violet background is followed using the Richings et al. (2014) ionization network.

A mock COS-AGN sample was then generated from this simulation suite to match

[8]The Haardt & Madau (2001) background is adopted as it better reproduces the statistics of the Lyα forest in the EAGLE volumes and other simulations (Rahmati et al., 2015; Kollmeier et al., 2014).

the properties of the COS-AGN sample. For each observed galaxy in COS-AGN, a simulated galaxy was selected by matching the stellar mass (with a $\log(M_\star/M_\odot)= \pm0.5$ dex tolerance), star formation rate ($\log(\mathrm{sSFR}\ /\ \mathrm{yr}^{-1})= \pm0.5$ dex tolerance), and AGN luminosity ($\log(L_{\mathrm{AGN}}/\mathrm{erg\ s}^{-1})= \pm0.25$ dex) of the simulated haloes to each COS-AGN galaxy. If multiple matches were identified, a random simulated halo was selected such that a mock sample contains the same number of galaxies as the actual COS-AGN sample (20 galaxies). A mock spectrum was generated for each galaxy using the SpecWizard package (Theuns et al., 1998; Schaye et al., 2003) by placing a randomly oriented quasar sightline through the CGM at the corresponding impact parameter of the matched COS-AGN galaxy sightline. A control sample was generated in a similar fashion, but all AGN ionizing sources in the simulated galaxies were set to $L_{\mathrm{bol}}= 0$ erg s^{-1}. The above procedure was repeated 200 times (including choosing another random halo if multiple haloes were matched), in order to produce 200 mock survey samples for both the AGN and control samples. These 200 realizations of the COS-AGN survey were needed to reproduce the range in measured EW variations for the metal species between the mock samples, and are used to quantify the expected spread in EWs from different orientations and from halo to halo variations. Further details on how these mock spectra were generated will be presented in a forthcoming paper (Horton et al., in prep.).

Stacked mock COS-AGN spectra

We assessed the relative impact of the AGN ionizing radiation on the measured simulated EWs by repeating the stacking procedure above, but with the simulated data. R. Horton computed the relative EW ratio $\delta\log(\mathrm{EW})$ in the same way that I did for the observations. Note that this relative EW analysis removes any systematic differences between the observed and simulated EWs caused by assumptions in the physics models (e.g. feedback) or ability to resolve small clouds in the simulations (Schaye et al., 2007; Stinson et al., 2012; Crighton et al., 2015; Gutcke et al., 2017; Nelson et al., 2017). A quantitative comparison between the simulated and observed EWs will be presented in Horton et al. (in prep.), although we note that the simulations produce a systematically weaker H I EW compared with the observations, while metal lines show better agreement with the observed data (see Oppenheimer et al., 2016, 2017).

The simulated stacked sightline spectra were created from the mocks by center-

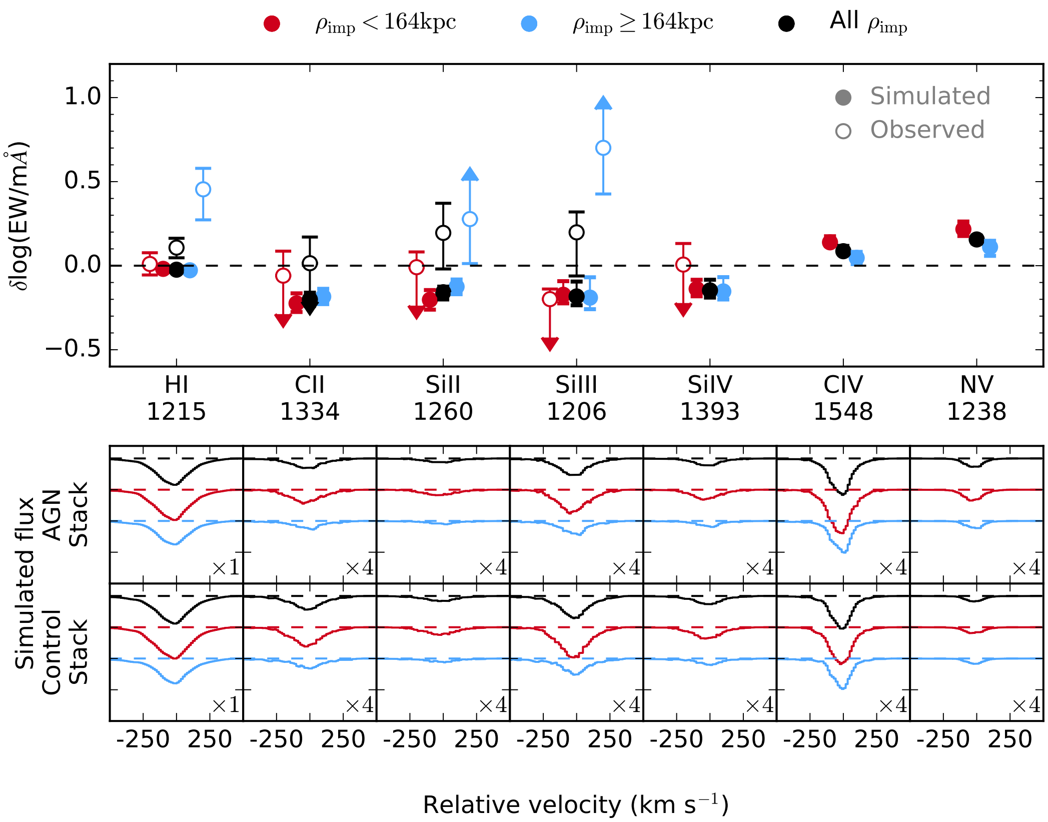

Figure 4.13 The top panel shows the measured δEW using a stacked spectrum from the zoom-in simulations of AGN hosts, split into bins of $\rho_{\rm imp}$ (all $\rho_{\rm imp}$, < 164 kpc and ≥ 164 kpc; black, red and blue points, respectively). The respective open symbols show the δEW measured in the observations (i.e. identical points presented in the top panel of Figure 4.12). Errorbars were calculated using the jackknife approach identical to that used for the observations. The bottom panels show the simulated stacked velocity profiles for each species for the AGN (middle row) and non-AGN control run (bottom row). The dashed lines represent the continuum levels of the absorption profiles. The Lyα are staggered by 0.5 in relative flux for clarity. The relative flux scale has been enlarged by a factor of four for the metal line profiles (indicated by a $\times 4$ in the bottom right of each panel), with the dashed continuum lines separated by a relative flux of 0.125. For the outer CGM, the simulations predict little change in the EW of H I and Si III due to the ionizing radiation from the AGN, which is in stark contrast to the COS-AGN observations similarly presented in Figure 4.12.

ing the velocity profile on the redshift of the simulated galaxy, rebinning the mock spectra to 15 km s^{-1}, and mean stacking these rebinned spectra. Three simulated stacked spectra were created for the same three bins of impact parameters that were previously used for the observed data: all $\rho_{\rm imp}$, $\rho_{\rm imp}$< 164 kpc, and $\rho_{\rm imp}$≥ 164 kpc. Jackknife errors on the measured EWs were computed by removing all 200 mock spectra associated with the matched COS-AGN sightline which contributed the most and least to the derived EW. This approach for calculating the simulated jackknife error is identical to that used for the observations. Using the same analysis as was used for the COS-AGN sightlines, Figure 4.13 presents the δlog(EW) analysis for these simulated stacked spectra (solid points in the top panel) to quantify the effect of including AGN radiation on the CGM relative to the control simulations. The inclusion of an AGN ionizing spectrum results in a negligible change in the EW of Lyα as a function of impact parameter. At high impact parameters ($\rho_{\rm imp}$≥ 164 kpc), the simulated results are in contrast to the observations (open points on Figure 4.13) where the COS-AGN sample shows a significant enhancement in the Lyα EW relative to the control sample, as well as a potential enhancement for Si II and Si III. I do note that for the inner impact parameter bin, the results from the simulation are consistent with the lack of metal species detected in the COS-AGN stacked spectrum ($\rho_{\rm imp}$< 164 kpc; Figure 4.12).

Compounded by the fact that the H I ionizing radiation from a Sazonov et al. (2004) AGN at the observed $\rho_{\rm imp}$ of the COS-AGN sample is weaker ($\lesssim$ 25%) than the ionizing radiation from the UV background (Haardt & Madau, 2001) at most of the impact parameters probed by COS-AGN (see the bottom right panel of Figure 4.3), the results from these simulations indicate that it is unlikely that photoionizing radiation from the AGN is responsible for the observed difference in EWs between the COS-AGN and the control samples. I note that at the impact parameters of COS-AGN, the light travel time of radiation from the AGN ($\sim 5\times10^5$ yr) is comparable to the AGN's lifetime ($\lesssim 10^6$ yr; Schirber et al., 2004; Gonçalves et al., 2008; Furlanetto & Lidz, 2011; Keel et al., 2012), implying that photoionization events caused by an AGN likely require previous AGN cycle(s) to have ionized the CGM gas, and have remained in the predicted long-lived fossil zone around the AGN (Oppenheimer & Schaye, 2013; Segers et al., 2017) provided an AGN has been active within the last several Myrs. Unfortunately, our simulations predict that low ionization species cannot distinguish the presence of fossil zones in COS-AGN due to the low intensity of the photo-ionizing radiation.

Despite being unable to probe the effects of the lower ionization species, ions such as C IV, N V, and O VI are better indicators of these proximity zone fossil. I highlight that in the simulated COS-AGN haloes, C IV and N V are still sensitive to the ionizing radiation of the harder AGN ionizing spectrum relative to the Haardt & Madau (2001) UV background (see figure 3 in Segers et al., 2017), as demonstrated by the enhanced EWs for these ionization species out to 300 kpc. However, to observe such an excess with N V λ 1238 Å would require spectra with signal-noise ratio of $\sim$ 30 to detect an absorption line of the predicted strength displayed in Figure 4.13. The excess EW of C IV λ 1548 Å would be an excellent test of the effects of the AGN ionizing field as I have already detected absorption in the stacked COS-AGN spectra (Table 4.5). Such a test would required observing the C IV λ 1548 Å covering fraction in the CGM of non-AGN galaxies from the control-matched sample.

AGN-driven winds and outflows

An alternative form of feedback is AGN-driven winds or outflows (Concas et al., 2017; Fiore et al., 2017; Woo et al., 2017). As the typical lifetime of an AGN ($\lesssim 10^6$ yr) is much smaller than the expected travel time of winds out to the impact parameters probed by COS-AGN ($\sim 10^8$ yr, assuming a constant, maximum velocity of 1000 km s^{-1}; e.g. Tremonti et al., 2007; Veilleux et al., 2013; Ishibashi & Fabian, 2015), any signatures of winds or outflowing material would likely trace material expelled from a previous cycles of AGN activity or star-formation in the host galaxy (e.g. Nedelchev et al., 2017; Kauffmann et al., 2017; Woo et al., 2017). The typically observed signatures of outflowing winds from a galaxy manifest as kinematic offsets of ionized emission or absorption lines from the host galaxy (e.g. Bordoloi et al., 2014a; Rubin et al., 2014; Woo et al., 2016; Heckman et al., 2017; Perna et al., 2017), but as demonstrated in Figure 4.8, the Lyα gas that I am probing in the COS-AGN sightlines does not have any strong bulk motion away from the host galaxy relative to the control matched sample. If such winds or outflows were driven by previous AGN or star-forming activity, the lack of kinematic offsets from the host galaxy suggests that these winds have dissipated over time, and should have deposited metals into the CGM (e.g. Muzahid et al., 2015; Turner et al., 2015). The low metal covering fraction at low impact parameter ($\leq$ 164 kpc; Figure 4.9) suggests an absence of outflowing material polluting the CGM with metals, rejecting the notion that any recent (within 160 Myr) AGN-driven winds have enhanced the CGM. I note that the Lyα EW at these column densities is more sensitive to the kinematics of the gas than to the amount of gas. Although I have rejected the possibility that AGN-driven winds are responsible for my results, it is possible that the gas is more turbulent in the CGM of AGN hosts compared to their control matches. To estimate the effects of turbulence, I would require observations of unsaturated low ionization metal absorption lines to verify if the EW enhancements are from enhanced column densities or kinematic broadening.

Given that AGN-driven winds can affect the absorption line profile by up to $\approx \pm 1000$ km s^{-1}, the adopted search window of ± 500 km s^{-1} (Section 4.2.3) could potentially miss gas present in a wind. I searched for the Lyα profiles within ± 1000 km s^{-1} and found two systems (J1214+0825 and J2133−0712) with minimal absorption outside the original window not associated with other absorption systems or the Galaxy. These two additional absorption components do not show any associated metal line absorption. As these missed components are small and narrow, the calculated flux-weighted velocity centroids presented in Figure 4.8 would still be contained within the already identified absorption component. However, I remind the reader that the adopted search window of ± 500 km s^{-1} is adopted to be consistent with methods used in the literature and control samples.

Rather than AGN feedback, it is possible that the observed effects are from a different process co-eval or prior to the onset of AGN accretion. Several works have pointed out that AGN activity coincide with a recent starburst; with the AGN having significant accretion events at least ~ 200 Myr after the starburst has occurred (Wild et al., 2007; Davies et al., 2007; Wild et al., 2010; Yesuf et al., 2014) giving the neutral material time to propagate out to the impact parameters probed by COS-AGN (Heckman et al., 2017). With a sample of QSO sightlines probing the CGM around 17 low-redshift starburst and post-starburst galaxies, Heckman et al. (2017) have observed a similar signature of enhanced EWs of Lyα, Si III, and C IV (the latter of which is not measured in the control sample) relative to a control-matched sample (matched in stellar mass and impact parameter). In the range of impact parameters and stellar masses probed by COS-AGN, the strength of the enhanced EW signature is consistent with the values probed by Heckman et al. (2017). However, the results of Heckman et al. (2017) show strong offsets in the kinematics of the gas from the host galaxy (≈ 100 km s^{-1}; see figure 5 from Heckman et al., 2017), whereas the COS-AGN sightlines do not (bottom panel of Figure 4.8). Assuming the AGN activity was triggered by the starburst, a minimum delay time of 200 Myr could allow for any starburst-driven winds to dissipate and kinematic offsets to no longer be present at the impact parameters of the COS-AGN sample. Although this starburst picture provides a possible explanation of my observations, I caution that starbursts are not the only astrophysical event linked to AGN accretion activity. For example, mergers that trigger the AGN (Ellison et al., 2011a, 2013; Satyapal et al., 2014; Silverman et al., 2014; Goulding et al., 2017) could potentially affect the surrounding CGM gas. Past and future work focussing on the CGM of galaxy mergers can further test this result (Johnson et al., 2014; Hani et al., 2017, Bordoloi et al. in prep.).

4.4.2 Are we seeing the effects from environment or other galaxy properties?

If the AGN (or host galaxy) is not responsible for the observed differences in the CGM, an alternative is that the circumgalactic environment in which an AGN host is found is different. Results from *Quasars probing Quasars* (Prochaska et al., 2013), Farina et al. (2014), and Johnson et al. (2015) have all suggested that the excess of cool gas seen in the CGM out to 1 Mpc around $z \approx 1$ quasars is a result of residing in group environments. Although the excess of cool gas around quasars goes in the same direction as the 0.1 dex enhancement found in the outer CGM of $z \approx 0.1$ COS-AGN galaxies (though I *do not* see an excess in the Lyα EW in the inner CGM of AGN hosts, as seen for QSOs), the dark matter haloes of the AGN in the sample are typically an order of magnitude smaller than group dark matter haloes that host quasars. As stated in Section 4.2.4, the δ_5 parameter provides an estimate of the environment. Given that differences in the distributions of δ_5 between AGN and star-forming galaxies in the SDSS vary on the order of a percent for a given stellar mass, it is likely that the enhanced EW of cool gas is not due to the contribution from a difference in the galaxy environment.

Given that I found an excess in the H I content of the outer CGM around AGN hosts, the results from Borthakur et al. (2013) which find a connection between the ISM and CGM gas properties would imply that the ISM would also host a large reservoir of H I gas. Such an enhancement in the ISM gas mass (relative to non-AGN galaxies) has been previously seen in AGN hosts (e.g. Vito et al., 2014), where an excess of ~ 0.2 dex in gas mass is seen for AGN hosts similar to those probed in the sample. If such large gas reservoirs do exist in the ISM of AGN hosts, the AGN could be fuelled by the excess cool gas in the ISM, which in turn is fed by the cool CGM gas surrounding the AGN host. I note that other works such as Fabello et al. (2011) have found that the ISM of optically-selected AGN hosts contain the same H I gas mass as their star-forming counterparts. However, ∼50% of the Fabello et al. (2011) AGN sample are so-called 'composite' AGN (galaxies whose emission lines contain contributions from both star formation and AGN activity), which are not representative of the AGN hosts selected in the COS-AGN sample.

A further test of this accretion picture would be to look for any orientation effects. If the COS-AGN sightlines are probing the gas reservoirs that are fuelling the AGN, we are likely to find the accreting gas along the major axis of the galaxy (e.g. Kacprzak et al., 2012; Nielsen et al., 2015; Ho et al., 2017). Unfortunately, I do not have the ability to measure robust inclinations for many of the COS-AGN galaxies from SDSS imaging (see Figure 4.2), and have too small of a sample size to produce a significant statistic. In addition, the Ho et al. (2017) sample are at much closer impact parameters ($\lesssim$ 50 kpc) whereas Borthakur et al. (2015) showed that at higher impact parameters (such as those probed by COS-AGN) there is no evidence of orientation effects for galaxies in COS-GASS. However, I do note that for the 4–5 sightlines that are probing along the edge of the disc relative to the 2–3 that are perpendicular to the disc, there is no significant difference in the median $\Delta\log(\mathrm{EW})$. A larger sample would be required to test this explicitly.

4.5 Summary

Using a sample of 19 quasar sightlines through the CGM of 20 Type II Seyfert AGN and LINERs, I have demonstrated that there are mild differences in the rest-frame equivalent widths of cool CGM gas around AGN hosts relative to their non-AGN counterparts. After matching AGN and non-AGN galaxies by their stellar mass and impact parameter, I found:

1. The covering fraction of Lyα gas for the AGN is 94^{+6}_{-23}%, which is comparable to the star-forming control galaxies (100^{+0}_{-21}%) and consistent with passive galaxies (75^{+25}_{-21}%). The covering fractions of metal species (C II, Si II, Si III, C IV, Si IV, and N V) are consistent with the control-matched galaxies (Figure 4.9).

2. An insignificant increase in the Lyα EW for AGN relative to control-matched galaxies on a sightline by sightline basis. The measured median EW offset between these two population is $+0.10 \pm 0.13$ dex (Figure 4.11).

3. After stacking the spectra, the observed EW enhancement of low ionization species for AGN is seen only at high impact parameters ($\rho_{\rm imp} \geq 164$ kpc; the median impact parameter of COS-AGN) for both Lyα (δlog(EW)$= +0.45 \pm 0.05$) and cool metal line tracers (Si II λ 1260 Å [δlog(EW)> 0.27 dex] and Si III λ 1206 Å [δlog(EW)> 0.75 dex]; Figure 4.12). These results are inconsistent with the expected effects from AGN feedback seen in our zoom-in simulations at high impact parameters (Figure 4.13). At lower impact parameters ($\rho_{\rm imp} < 164$ kpc), my results are consistent with the simulations.

4. The Lyα line kinematics for the COS-AGN sightlines does not differ significantly from what is observed around the control-matched sample, suggesting there is no strong bulk motion in the CGM due to the presence of an AGN (Figure 4.8). As all but one system show gas within the escape velocity of the host halo, the probed material is likely bound to the AGN host.

These results suggest that the circumgalactic environments that host AGN show little difference than their non-AGN hosts on a sightline-by-sightline basis, likely attributed to my small sample size. I only detected a significant difference in the amount of cool gas in the stacked spectrum at high impact parameters ($\rho_{\rm imp} \geq 164$ kpc), which I used to interpret the results. Given the lack of signatures (in both EW and kinematic diagnostics) of recent AGN feedback on the CGM from winds and ionizing radiation, I speculate that possible causes for these stacked spectrum results could be from the accretion of cool gas to feed the AGN, or a remnant effect from previous evolutionary activity of the host galaxy (such as starbursts) prior to the AGN accretion phase.

Chapter 5

The current and future roles of quasar absorption lines

The diverse study of gas probed by quasar sightlines is a powerful tool to provide orthogonal investigations of galaxy evolution over a large portion of cosmic time. In this thesis, I have presented a subset of the applications of quasar absorption line systems to understand the evolution of gaseous reservoirs. In brief, I have:

- Assessed the impact of selecting H I absorbing systems with commonly-used metal line tracers on quantifying the density of H I gas in the Universe (Chapter 2).

- Developed a novel method for correcting the dust depletion present in gas-phase abundance measurements (Chapter 3). These corrections are made on an absorber-by-absorber basis, and make use of Ti II typically observed in the NIR.

- Studied the chemical nature of various subclasses of DLAs to understand the role they potentially play in chemical evolution studies (Chapter 3).

- Quantified the nature of CGM gas surrounding AGN host galaxies in comparison with their non-AGN counterparts (Chapter 4).

As discussed in more detail in the following subsections, the results of this thesis offer a stepping stone to further assess the gas reservoirs of galaxies as probed by quasar absorption lines.

The contribution of subDLAs to gas reservoirs

As demonstrated in Chapter 2, subDLAs account for a small, but significant, portion of neutral gas in the Universe ($\approx 10 - 20\%$; Figure 2.6); making it important to construct unbiased samples of subDLAs over a large range of redshifts to accurately measure both their contribution to the H I budget of the Universe, and their role in chemical evolution (see Figure 3.1).

Of particular interest are the 209 candidate subDLA absorbers in the XQ-100 catalogue with no strong metal lines. Although these systems are likely to be blends of lower column density absorption lines, it is possible that a fraction of these systems could be bona fide galaxy-class absorbers that probe metal-poor environments (see the signal-noise constraints on metallicity in Figure 2.4). However, I have demonstrated that requiring metal lines (such as Mg II, see Figure 2.7) to identify or confirm absorbers can impact the nature of the evolution of H I systems (Figures 2.1 and 2.5). To confirm these systems in an unbiased fashion, new higher resolution spectroscopic observations are needed, in addition to already existing archival data for some sightlines (e.g. Zafar et al., 2013b,a), to better constrain the H I profiles and determine if these are real absorbers.

Furthermore, there has been little work on studying the detailed chemical abundances of the lower H I column density LLS and subDLAs, in particular their global metallicity evolution (Cooper et al., 2015; Lehner et al., 2016; Quiret et al., 2016; Wotta et al., 2016). Many of these previous studies have selected absorbers to be peculiar in their metal content, or have been derived from archival data which suffers from a complex selection function; complicating the interpretation of their chemical content in a cosmological context (with respect to DLAs, i.e. Figures 3.1 and 3.6; Quiret et al., 2016). Deriving the metal abundances for the identified subDLAs in the absorber-blind XQ-100 survey, as well as extending this analysis to other LLS, will provide an unbiased census of the metallicity evolution, particularly in the redshift regime $3.5 \lesssim z_{\rm abs} \lesssim 4.5$ where metals abundances have not been studied to date.

Of particular interest in the understanding of chemical evolution is the nature of the first stars. Quasar absorption line studies have only focused on DLAs (Section 3.3.1, Cooke et al., 2015), but metal-poor environments have also been identified in a handful of lower H I column density systems (e.g. Morrison et al., 2016; Crighton et al., 2016). An increasing carbon-oxygen ratio ([C/O]) with decreasing metallicity is a proposed identifying signature of the first stars (Jacobson et al., 2015). As this signature is only seen in DLA populations (Cooke et al., 2015) and not with most LLS (Lehner et al., 2016), it is proposed that LLS are preferentially tracing this carbon-enriched ejecta from first generation stars in dwarf galaxies (Lehner et al., 2016). The higher redshift XQ-100 sample is expected to have three times as many LLS as Lehner et al. (2016) for just as many quasars, providing an unbiased census of [C/O] distribution as a function of redshift. Such an analysis would be timely as the proposed [C/O] signature of first stars is currently under investigation in the Milky Way's stellar halo (Starkenburg et al., 2017). Therefore, studying the distribution individual elements within subDLAs and LLSs will informs us how this gas is cycled in galaxies at early times, as well as place constraints on chemical evolution.

An intrinsic method to applying dust corrections

Understanding the chemical nature of DLAs is complicated by either the significant amount of dust depletion of well studied elements (such as Fe and potentially Si), or the unknown nucleosynthetic origin of volatile elements (e.g. Zn). I have proposed a novel method to measure the intrinsic dust-depletion on an absorber-by-absorber basis by comparing the abundance of two α-elements, providing a correction independent of nucleosynthetic effects. Using this method, I have shown that [Zn/Fe], the commonly used tracer of dust depletion in DLAs as it is solar in the Milky Way (Pettini et al., 1997; De Cia et al., 2017), might not necessarily be solar in DLAs; a feature similar to dwarf galaxies (Figure 3.7; see also Berg et al., 2015a; Skúladóttir et al., 2017). High resolution, near infra-red spectrographs are ideal to assess dust depletion as the strongest lines for refractory α-elements tend to be at observed-frame infra-red wavelengths for $z_{\rm abs} \approx 2-4$ absorbers. However, many of the constraints on subsolar [Zn/Fe] in DLAs come from non-detections of Ti, which only provide an upper limit on the amount of dust depletion. Obtaining deeper, higher signal-to-noise observations for a handful of these systems to detect Ti II in the most constraining systems would confirm whether [Zn/Fe] should not be used as a dust depletion tracer, as well as understand the types of galactic systems DLAs are probing in parallel to imaging techniques.

The origin of excess HI gas surrounding AGN hosts

The COS-AGN survey have demonstrated an apparent excess of cool gas surrounding AGN hosts (relative to their non-AGN counterparts; Figure 4.12). The origin of this excess is unclear, as there appears to be no signature of bulk motion from winds, or strong ionization expected from AGN radiation (Figure 4.13). I have speculated this may be tied to previous starburst or merger events, but it could also be the result of having a limited sample of both AGN and non-AGN galaxies to work with. As shown in Figure 4.13, the enhancement of C IV at low impact parameters would confirm whether the AGN ionizing radiation has any effect on the CGM. Follow-up measurements of C IV around the non-AGN control galaxies are imperative to address the nature of the high-ionization gas phase while the Hubble Space Telescope, our only access to high resolution UV spectroscopy, is still in operation. These observations would confirm or deny the role of AGN photoionization on the CGM. In addition, these C IV measurements in the COS-Halos and COS-GASS galaxies (which are rapidly becoming the gold standard datasets of CGM work) would provide an excellent comparison set to future high redshift studies, as C IV would likely be the absorption line of choice due to its strength and is typically not found in the Lyα forest.

Given the unknown lifetime of the Hubble Space Telescope and no immediate successor UV telescope, further expanding these samples of AGN host galaxies requires pushing to higher redshifts where: high star-formation rates and AGN are more common, bright background quasars are frequently found, and identical observations can be made with ground-based optical telescopes. Identifying suitable galaxy-quasar pairs for such observations has not yet been achieved at high redshift, as quasars typically outshine galaxies along their line of sight and the samples of previously observed foreground galaxies is sparse. However high-redshift AGN or highly star-forming galaxies are bright in the rest-frame infra-red (observed-frame sub-millimeter; Chapman et al., 2005), a wavelength regime where the contrast of the background quasar is much reduced, making the identification of foreground galaxies easier. Instruments like X-Shooter can provide simultaneous coverage of the necessary absorption lines (H I, Si III, and C IV) to further understand how the presence of high star-formation rates or AGN have on the CGM. Current and future surveys of galaxy fields at higher redshifts with Atacama Large Millimeter Array (Hodge et al., 2013) will be monumental to finding more SMG-quasar pairs.

The role of upcoming facilities

The future of this field relies on the advent of the thirty-metre class telescopes (e.g Thirty Meter Telescope, Extremely Large Telescope, or Giant Magellan Telescope) with high resolution spectroscopy capabilities to provide higher signal-noise spectra in shorter exposures to build up statistical samples of high redshift absorbers. The Sloan Digital Sky Survey revolutionized the study of H I gas available in DLAs (Prochaska et al., 2005; Noterdaeme et al., 2012), but did not have the resolution to explore lower column density systems or the associated detailed chemical makeup. Upcoming surveys using dedicated higher resolution spectroscopy (relative to Sloan Digital Sky Survey, such as the Mauna Kea Spectroscopic Explorer; MSE) will improve upon the statistics of lower H I column density absorbers and their associated metal abundance profiles with high resolution spectroscopy of ≈ 5000 quasars. With the limited lifetime of the Hubble Space Telescope and its UV capabilities, there will unfortunately be a large set-back in what can be studied in the local Universe; likely leaving COS-Halos (Tumlinson et al., 2013), COS-GASS (Borthakur et al., 2015), and COS-Dwarfs (Bordoloi et al., 2014b) surveys as the legacy datasets of the CGM of lower redshift galaxies. Analogous studies now must be pushed to the high redshift Universe, where identification of the absorbing galaxy is tricky to confirm (e.g. Prochaska et al., 2011) until the next generation of space-based UV telescopes (e.g. the Large UV Optical InfraRed telescope; LUVOIR) are available. Beyond quasar absorption lines, H I can still be detected through 21 cm emission and absorption. New radio facilities such as the Square Kilometer Array and all of its many H I surveys will provide a low to intermediate redshift survey of the presence of H I in and around all types of galaxies, providing yet another complementary picture of the gas surrounding galaxies.

Bibliography

Abazajian, K. N. et al. 2009, Astrophysical Journal, Supplement Series, 182, 543

Adelberger, K. L., Shapley, A. E., Steidel, C. C., Pettini, M., Erb, D. K., & Reddy, N. A. 2005, Astrophysical Journal, 629, 636

Akerman, C. J. 2005, PhD thesis, University of Cambridge

Akerman, C. J., Ellison, S. L., Pettini, M., & Steidel, C. C. 2005, Astronomy and Astrophysics, 440, 499

Asplund, M., Grevesse, N., Sauval, A. J., & Scott, P. 2009, Annual Review of Astronomy and Astrophysics, 47, 481

Asplund, M., Lambert, D. L., Nissen, P. E., Primas, F., & Smith, V. V. 2006, Astrophysical Journal, 644, 229

Baldry, I. K., Balogh, M. L., Bower, R. G., Glazebrook, K., Nichol, R. C., Bamford, S. P., & Budavari, T. 2006, Monthly Notices of the RAS, 373, 469

Baldry, I. K., Glazebrook, K., Brinkmann, J., Ivezić, Ž., Lupton, R. H., Nichol, R. C., & Szalay, A. S. 2004, Astrophysical Journal, 600, 681

Baldwin, J. A., Phillips, M. M., & Terlevich, R. 1981, Publications of the ASP, 93, 5

Becker, G. D., Sargent, W. L. W., Rauch, M., & Carswell, R. F. 2012, Astrophysical Journal, 744, 91

Beers, T. C. & Christlieb, N. 2005, Annual Review of Astronomy and Astrophysics, 43, 531

Belfiore, F. et al. 2016, Monthly Notices of the RAS, 461, 3111

Berg, T. A. M. et al. 2017, Monthly Notices of the RAS, 464, L56

Berg, T. A. M., Ellison, S. L., Prochaska, J. X., Venn, K. A., & Dessauges-Zavadsky, M. 2015a, Monthly Notices of the RAS, 452, 4326

Berg, T. A. M. et al. 2016, Monthly Notices of the RAS, 463, 3021

Berg, T. A. M., Ellison, S. L., Tumlinson, J., Oppenheimer, B. D., Horton, R., Bordoloi, R., & Schaye, J. 2018, Monthly Notices of the RAS, 478, 3890

Berg, T. A. M., Neeleman, M., Prochaska, J. X., Ellison, S. L., & Wolfe, A. M. 2015b, Publications of the ASP, 127, 167

Bergeron, J. 1986, Astronomy and Astrophysics, 155, L8

Bergeron, J. & Boissé, P. 1991, Astronomy and Astrophysics, 243, 344

Bethe, H. A. 1939, Physical Review, 55, 434

Bi, H. & Davidsen, A. F. 1997, Astrophysical Journal, 479, 523

Bluck, A. F. L., Mendel, J. T., Ellison, S. L., Moreno, J., Simard, L., Patton, D. R., & Starkenburg, E. 2014, Monthly Notices of the RAS, 441, 599

Bluck, A. F. L. et al. 2016, Monthly Notices of the RAS, 462, 2559

Bordoloi, R. et al. 2014a, Astrophysical Journal, 794, 130

— 2011, Astrophysical Journal, 743, 10

— 2014b, Astrophysical Journal, 796, 136

Borthakur, S., Heckman, T., Strickland, D., Wild, V., & Schiminovich, D. 2013, Astrophysical Journal, 768, 18

Borthakur, S. et al. 2016, Astrophysical Journal, 833, 259

— 2015, Astrophysical Journal, 813, 46

Bouché, N., Murphy, M. T., Péroux, C., Csabai, I., & Wild, V. 2006, Monthly Notices of the RAS, 371, 495

Bowen, D. V., Blades, J. C., & Pettini, M. 1995, Astrophysical Journal, 448, 634

Bowen, D. V. et al. 2006, Astrophysical Journal, Letters to the Editor, 645, L105

Bower, R. G., Schaye, J., Frenk, C. S., Theuns, T., Schaller, M., Crain, R. A., & McAlpine, S. 2017, Monthly Notices of the RAS, 465, 32

Brinchmann, J., Charlot, S., White, S. D. M., Tremonti, C., Kauffmann, G., Heckman, T., & Brinkmann, J. 2004, Monthly Notices of the RAS, 351, 1151

Bromm, V. & Larson, R. B. 2004, Annual Review of Astronomy and Astrophysics, 42, 79

Burbidge, E. M., Burbidge, G. R., Fowler, W. A., & Hoyle, F. 1957, Reviews of Modern Physics, 29, 547

Burchett, J. N. et al. 2016, Astrophysical Journal, 832, 124

Cashman, F. H., Kulkarni, V. P., Kisielius, R., Ferland, G. J., & Bogdanovich, P. 2017, Astrophysical Journal, Supplement Series, 230, 8

Cayrel, R. et al. 2004, Astronomy and Astrophysics, 416, 1117

Cen, R., Miralda-Escudé, J., Ostriker, J. P., & Rauch, M. 1994, Astrophysical Journal, Letters to the Editor, 437, L9

Centurión, M., Bonifacio, P., Molaro, P., & Vladilo, G. 2000, Astrophysical Journal, 536, 540

Chabrier, G. 2003, Publications of the ASP, 115, 763

Chapman, S. C., Blain, A. W., Smail, I., & Ivison, R. J. 2005, Astrophysical Journal, 622, 772

Chen, H.-W., Helsby, J. E., Gauthier, J.-R., Shectman, S. A., Thompson, I. B., & Tinker, J. L. 2010, Astrophysical Journal, 714, 1521

Chen, Y. Q., Nissen, P. E., & Zhao, G. 2004, Astronomy and Astrophysics, 425, 697

Christensen, L., Møller, P., Fynbo, J. P. U., & Zafar, T. 2014, Monthly Notices of the RAS, 445, 225

Christensen, L. et al. 2017, Astronomy and Astrophysics, 608, A84

Concas, A., Popesso, P., Brusa, M., Mainieri, V., Erfanianfar, G., & Morselli, L. 2017, ArXiv e-prints

Cooke, R., Pettini, M., Jorgenson, R. A., Murphy, M. T., Rudie, G. C., & Steidel, C. C. 2013, Monthly Notices of the RAS, 431, 1625

Cooke, R., Pettini, M., Steidel, C. C., Rudie, G. C., & Nissen, P. E. 2011, Monthly Notices of the RAS, 417, 1534

Cooke, R. J. & Madau, P. 2014, Astrophysical Journal, 791, 116

Cooke, R. J., Pettini, M., & Jorgenson, R. A. 2015, Astrophysical Journal, 800, 12

Cooke, R. J., Pettini, M., & Steidel, C. C. 2017, Monthly Notices of the RAS, 467, 802

— 2018, Astrophysical Journal, 855, 102

Cooper, T. J., Simcoe, R. A., Cooksey, K. L., O'Meara, J. M., & Torrey, P. 2015, Astrophysical Journal, 812, 58

Crain, R. A. et al. 2015, Monthly Notices of the RAS, 450, 1937

Crighton, N. H. M., Hennawi, J. F., Simcoe, R. A., Cooksey, K. L., Murphy, M. T., Fumagalli, M., Prochaska, J. X., & Shanks, T. 2015, Monthly Notices of the RAS, 446, 18

Crighton, N. H. M., O'Meara, J. M., & Murphy, M. T. 2016, Monthly Notices of the RAS, 457, L44

Cyburt, R. H., Fields, B. D., & Olive, K. A. 2008, Journal of Cosmology and Astroparticle Physics, 11, 012

Davies, R. I., Müller Sánchez, F., Genzel, R., Tacconi, L. J., Hicks, E. K. S., Friedrich, S., & Sternberg, A. 2007, Astrophysical Journal, 671, 1388

De Cia, A., Ledoux, C., Mattsson, L., Petitjean, P., Srianand, R., Gavignaud, I., & Jenkins, E. B. 2016, Astronomy and Astrophysics, 596, A97

De Cia, A., Ledoux, C., Petitjean, P., & Savaglio, S. 2017, ArXiv e-prints

Dekker, H., D'Odorico, S., Kaufer, A., Delabre, B., & Kotzlowski, H. 2000, in Society of Photo-Optical Instrumentation Engineers (SPIE) Conference Series, Vol. 4008, Optical and IR Telescope Instrumentation and Detectors, ed. M. Iye & A. F. Moorwood, 534–545

Dessauges-Zavadsky, M., Calura, F., Prochaska, J. X., D'Odorico, S., & Matteucci, F. 2004, Astronomy and Astrophysics, 416, 79

Dessauges-Zavadsky, M., D'Odorico, S., McMahon, R. G., Molaro, P., Ledoux, C., Péroux, C., & Storrie-Lombardi, L. J. 2001, Astronomy and Astrophysics, 370, 426

Dessauges-Zavadsky, M., Ellison, S. L., & Murphy, M. T. 2009, Monthly Notices of the RAS, 396, L61

Dessauges-Zavadsky, M., Péroux, C., Kim, T.-S., D'Odorico, S., & McMahon, R. G. 2003, Monthly Notices of the RAS, 345, 447

Dessauges-Zavadsky, M., Prochaska, J. X., D'Odorico, S., Calura, F., & Matteucci, F. 2006, Astronomy and Astrophysics, 445, 93

Di Matteo, P., Combes, F., Melchior, A.-L., & Semelin, B. 2007, Astronomy and Astrophysics, 468, 61

D'Odorico, V. 2007, Astronomy and Astrophysics, 470, 523

Dressler, A. 1980, Astrophysical Journal, 236, 351

Ellison, S. L. 2006, Monthly Notices of the RAS, 368, 335

Ellison, S. L. & Lopez, S. 2001, Astronomy and Astrophysics, 380, 117

Ellison, S. L., Mendel, J. T., Patton, D. R., & Scudder, J. M. 2013, Monthly Notices of the RAS, 435, 3627

Ellison, S. L., Murphy, M. T., & Dessauges-Zavadsky, M. 2009, Monthly Notices of the RAS, 392, 998

Ellison, S. L., Patton, D. R., Mendel, J. T., & Scudder, J. M. 2011a, Monthly Notices of the RAS, 418, 2043

Ellison, S. L., Patton, D. R., Simard, L., & McConnachie, A. W. 2008, Astronomical Journal, 135, 1877

Ellison, S. L., Prochaska, J. X., Hennawi, J., Lopez, S., Usher, C., Wolfe, A. M., Russell, D. M., & Benn, C. R. 2010, Monthly Notices of the RAS, 406, 1435

Ellison, S. L., Prochaska, J. X., & Mendel, J. T. 2011b, Monthly Notices of the RAS, 412, 448

Ellison, S. L., Teimoorinia, H., Rosario, D. J., & Mendel, J. T. 2016a, Monthly Notices of the RAS, 455, 370

— 2016b, Monthly Notices of the RAS, 458, L34

Ellison, S. L. et al. 2006, Monthly Notices of the RAS, 372, L38

Ellison, S. L., Yan, L., Hook, I. M., Pettini, M., Wall, J. V., & Shaver, P. 2002, Astronomy and Astrophysics, 383, 91

Fabello, S., Kauffmann, G., Catinella, B., Giovanelli, R., Haynes, M. P., Heckman, T. M., & Schiminovich, D. 2011, Monthly Notices of the RAS, 416, 1739

Fabian, A. C. 2012, Annual Review of Astronomy and Astrophysics, 50, 455

Farina, E. P., Falomo, R., Decarli, R., Treves, A., & Kotilainen, J. K. 2013, Monthly Notices of the RAS, 429, 1267

Farina, E. P., Falomo, R., Scarpa, R., Decarli, R., Treves, A., & Kotilainen, J. K. 2014, Monthly Notices of the RAS, 441, 886

Ferrarese, L. & Merritt, D. 2000, Astrophysical Journal, Letters to the Editor, 539, L9

Fiore, F. et al. 2017, Astronomy and Astrophysics, 601, A143

Fox, A. J. et al. 2016, Astrophysical Journal, Letters to the Editor, 816, L11

Frebel, A. & Bromm, V. 2012, Astrophysical Journal, 759, 115

Frebel, A. & Norris, J. E. 2015, Annual Review of Astronomy and Astrophysics, 53, 631

Fumagalli, M., O'Meara, J. M., Prochaska, J. X., Rafelski, M., & Kanekar, N. 2015, Monthly Notices of the RAS, 446, 3178

Furlanetto, S. R. & Lidz, A. 2011, Astrophysical Journal, 735, 117

Fynbo, J. P. U. et al. 2013, Monthly Notices of the RAS, 436, 361

Gaskell, C. M. 1982, Astrophysical Journal, 263, 79

Gehrels, N. 1986, Astrophysical Journal, 303, 336

Giovanelli, R. et al. 2005, Astronomical Journal, 130, 2598

Gonçalves, T. S., Martin, D. C., Menéndez-Delmestre, K., Wyder, T. K., & Koekemoer, A. 2012, Astrophysical Journal, 759, 67

Gonçalves, T. S., Steidel, C. C., & Pettini, M. 2008, Astrophysical Journal, 676, 816

Gould, R. J. & Salpeter, E. E. 1963, Astrophysical Journal, 138, 393

Goulding, A. D. et al. 2017, ArXiv e-prints

Green, J. C. et al. 2012, Astrophysical Journal, 744, 60

Greif, T. H., Johnson, J. L., Bromm, V., & Klessen, R. S. 2007, Astrophysical Journal, 670, 1

Guimarães, R., Petitjean, P., de Carvalho, R. R., Djorgovski, S. G., Noterdaeme, P., Castro, S., Poppe, P. C. D. R., & Aghaee, A. 2009, Astronomy and Astrophysics, 508, 133

Gunn, J. E. & Peterson, B. A. 1965, Astrophysical Journal, 142, 1633

Gutcke, T. A., Stinson, G. S., Macciò, A. V., Wang, L., & Dutton, A. A. 2017, Monthly Notices of the RAS, 464, 2796

Haardt, F. & Madau, P. 2001, in Clusters of Galaxies and the High Redshift Universe Observed in X-rays, ed. D. M. Neumann & J. T. V. Tran

Haehnelt, M. G., Steinmetz, M., & Rauch, M. 1998, Astrophysical Journal, 495, 647

Hani, M. H., Sparre, M., Ellison, S. L., Torrey, P., & Vogelsberger, M. 2017, MNRAS, stx3252

Häring, N. & Rix, H.-W. 2004, Astrophysical Journal, Letters to the Editor, 604, L89

Hayashi, C. 1950, Progress of Theoretical Physics, 5, 224

Heckman, T., Borthakur, S., Wild, V., Schiminovich, D., & Bordoloi, R. 2017, ArXiv e-prints

Heckman, T. M. 1980, Astronomy and Astrophysics, 87, 152

Heckman, T. M., Lehnert, M. D., Strickland, D. K., & Armus, L. 2000, Astrophysical Journal, Supplement Series, 129, 493

Heger, A. & Woosley, S. E. 2010, Astrophysical Journal, 724, 341

Hennawi, J. F. & Prochaska, J. X. 2007, Astrophysical Journal, 655, 735

Hennawi, J. F. et al. 2006, Astrophysical Journal, 651, 61

Henry, R. B. C. & Prochaska, J. X. 2007, Publications of the ASP, 119, 962

Hernquist, L., Katz, N., Weinberg, D. H., & Miralda-Escudé, J. 1996, Astrophysical Journal, Letters to the Editor, 457, L51

Hewett, P. C. & Wild, V. 2010, Monthly Notices of the RAS, 405, 2302

Ho, L. C., Filippenko, A. V., & Sargent, W. L. W. 1997, Astrophysical Journal, 487, 591

Ho, S. H., Martin, C. L., Kacprzak, G. G., & Churchill, C. W. 2017, Astrophysical Journal, 835, 267

Hodge, J. A. et al. 2013, Astrophysical Journal, 768, 91

Huang, Y.-H., Chen, H.-W., Johnson, S. D., & Weiner, B. J. 2016, Monthly Notices of the RAS, 455, 1713

Hubble, E. P. 1926, Astrophysical Journal, 64

Iršič, V. et al. 2017a, Monthly Notices of the RAS, 466, 4332

— 2017b, Phys. Rev. D, 96, 023522

Ishibashi, W. & Fabian, A. C. 2015, Monthly Notices of the RAS, 451, 93

Jacobson, H. R. et al. 2015, Astrophysical Journal, 807, 171

Jeans, J. H. 1902, Philosophical Transactions of the Royal Society of London Series A, 199, 1

Jenkins, E. B. 2009, Astrophysical Journal, 700, 1299

Jenkins, E. B. & Tripp, T. M. 2006, Astrophysical Journal, 637, 548

Johnson, S. D., Chen, H.-W., & Mulchaey, J. S. 2015, Monthly Notices of the RAS, 452, 2553

Johnson, S. D., Chen, H.-W., Mulchaey, J. S., Tripp, T. M., Prochaska, J. X., & Werk, J. K. 2014, Monthly Notices of the RAS, 438, 3039

Johnson-Groh, M., Marois, C., & Ellison, S. L. 2016, Astrophysical Journal, 831, 49

Jorgenson, R. A., Murphy, M. T., & Thompson, R. 2013, Monthly Notices of the RAS, 435, 482

Jorgenson, R. A. & Wolfe, A. M. 2014, Astrophysical Journal, 785, 16

Jorgenson, R. A., Wolfe, A. M., & Prochaska, J. X. 2010, Astrophysical Journal, 722, 460

Kacprzak, G. G., Churchill, C. W., Murphy, M. T., & Cooke, J. 2015, Monthly Notices of the RAS, 446, 2861

Kacprzak, G. G., Churchill, C. W., & Nielsen, N. M. 2012, Astrophysical Journal, Letters to the Editor, 760, L7

Kashikawa, N., Misawa, T., Minowa, Y., Okoshi, K., Hattori, T., Toshikawa, J., Ishikawa, S., & Onoue, M. 2014, Astrophysical Journal, 780, 116

Kauffmann, G. & Heckman, T. M. 2009, Monthly Notices of the RAS, 397, 135

Kauffmann, G. et al. 2003, Monthly Notices of the RAS, 346, 1055

Kauffmann, G., Nelson, D., Ménard, B., & Zhu, G. 2017, Monthly Notices of the RAS, 468, 3737

Kauffmann, G., White, S. D. M., Heckman, T. M., Ménard, B., Brinchmann, J., Charlot, S., Tremonti, C., & Brinkmann, J. 2004, Monthly Notices of the RAS, 353, 713

Keel, W. C. et al. 2012, Monthly Notices of the RAS, 420, 878

Kennicutt, Jr., R. C. 1998, Astrophysical Journal, 498, 541

Kewley, L. J., Geller, M. J., & Barton, E. J. 2006a, Astronomical Journal, 131, 2004

Kewley, L. J., Groves, B., Kauffmann, G., & Heckman, T. 2006b, Monthly Notices of the RAS, 372, 961

Kewley, L. J., Heisler, C. A., Dopita, M. A., & Lumsden, S. 2001, Astrophysical Journal, Supplement Series, 132, 37

Kippenhahn, R. & Weigert, A. 1994, Stellar Structure and Evolution

Kirchhoff, G. 1860, Annalen der Physik, 185, 275

Knapen, J. H., Cisternas, M., & Querejeta, M. 2015, Monthly Notices of the RAS, 454, 1742

Kollmeier, J. A. et al. 2014, Astrophysical Journal, Letters to the Editor, 789, L32

Krogager, J.-K. et al. 2013, Monthly Notices of the RAS

Krogager, J.-K., Fynbo, J. P. U., Noterdaeme, P., Zafar, T., Møller, P., Ledoux, C., Krühler, T., & Stockton, A. 2016, Monthly Notices of the RAS, 455, 2698

Kulkarni, V. P., Fall, S. M., & Truran, J. W. 1997, Astrophysical Journal, Letters to the Editor, 484, L7

Kulkarni, V. P., Khare, P., Péroux, C., York, D. G., Lauroesch, J. T., & Meiring, J. D. 2007, Astrophysical Journal, 661, 88

Lambas, D. G., Tissera, P. B., Alonso, M. S., & Coldwell, G. 2003, Monthly Notices of the RAS, 346, 1189

Lan, T.-W. & Fukugita, M. 2017, Astrophysical Journal, 850, 156

Lanzetta, K. M., Bowen, D. V., Tytler, D., & Webb, J. K. 1995a, Astrophysical Journal, 442, 538

Lanzetta, K. M., Wolfe, A. M., & Turnshek, D. A. 1995b, Astrophysical Journal, 440, 435

Ledoux, C., Bergeron, J., & Petitjean, P. 2002, Astronomy and Astrophysics, 385, 802

Ledoux, C., Petitjean, P., Fynbo, J. P. U., Møller, P., & Srianand, R. 2006, Astronomy and Astrophysics, 457, 71

Lehner, N. et al. 2013, Astrophysical Journal, 770, 138

Lehner, N., O'Meara, J. M., Howk, J. C., Prochaska, J. X., & Fumagalli, M. 2016, Astrophysical Journal, 833, 283

Leslie, S. K., Kewley, L. J., Sanders, D. B., & Lee, N. 2016, Monthly Notices of the RAS, 455, L82

López, S. et al. 2016, Astronomy and Astrophysics, 594, A91

Lopez, S. & Ellison, S. L. 2003, Astronomy and Astrophysics, 403, 573

Lu, L., Sargent, W. L. W., & Barlow, T. A. 1998, Astronomical Journal, 115, 55

Lu, L., Sargent, W. L. W., Barlow, T. A., Churchill, C. W., & Vogt, S. S. 1996, Astrophysical Journal, Supplement Series, 107, 475

Madau, P. & Dickinson, M. 2014, Annual Review of Astronomy and Astrophysics, 52, 415

Marois, C., Lafrenière, D., Doyon, R., Macintosh, B., & Nadeau, D. 2006, Astrophysical Journal, 641, 556

Martin, A. M., Papastergis, E., Giovanelli, R., Haynes, M. P., Springob, C. M., & Stierwalt, S. 2010, Astrophysical Journal, 723, 1359

Martin, D. C. et al. 2005, Astrophysical Journal, Letters to the Editor, 619, L1

— 2007, Astrophysical Journal, Supplement Series, 173, 342

McKee, C. F. & Ostriker, E. C. 2007, Annual Review of Astronomy and Astrophysics, 45, 565

McNamara, B. R. & Nulsen, P. E. J. 2007, Annual Review of Astronomy and Astrophysics, 45, 117

McQuinn, M. 2016, Annual Review of Astronomy and Astrophysics, 54, 313

McWilliam, A. 1997, Annual Review of Astronomy and Astrophysics, 35, 503

Mendel, J. T., Simard, L., Palmer, M., Ellison, S. L., & Patton, D. R. 2014, Astrophysical Journal, Supplement Series, 210, 3

Mihos, J. C. & Hernquist, L. 1994, Astrophysical Journal, Letters to the Editor, 437, L47

Molaro, P., Bonifacio, P., Centurión, M., D'Odorico, S., Vladilo, G., Santin, P., & Di Marcantonio, P. 2000, Astrophysical Journal, 541, 54

Møller, P., Fynbo, J. P. U., Ledoux, C., & Nilsson, K. K. 2013, Monthly Notices of the RAS, 430, 2680

Morrison, S., Kulkarni, V. P., Som, D., DeMarcy, B., Quiret, S., & Péroux, C. 2016, Astrophysical Journal, 830, 158

Morton, D. C. 2003, Astrophysical Journal, Supplement Series, 149, 205

Moster, B. P., Somerville, R. S., Maulbetsch, C., van den Bosch, F. C., Macciò, A. V., Naab, T., & Oser, L. 2010, Astrophysical Journal, 710, 903

Murphy, M. T., Curran, S. J., Webb, J. K., Ménager, H., & Zych, B. J. 2007, Monthly Notices of the RAS, 376, 673

Muzahid, S., Kacprzak, G. G., Churchill, C. W., Charlton, J. C., Nielsen, N. M., Mathes, N. L., & Trujillo-Gomez, S. 2015, Astrophysical Journal, 811, 132

Nagamine, K., Springel, V., & Hernquist, L. 2004, Monthly Notices of the RAS, 348, 435

Navarro, J. F., Frenk, C. S., & White, S. D. M. 1997, Astrophysical Journal, 490, 493

Nedelchev, B., Sarzi, M., & Kaviraj, S. 2017, ArXiv e-prints

Neeleman, M., Kanekar, N., Prochaska, J. X., Rafelski, M., Carilli, C. L., & Wolfe, A. M. 2017, Science, 355, 1285

Neeleman, M., Prochaska, J. X., Ribaudo, J., Lehner, N., Howk, J. C., Rafelski, M., & Kanekar, N. 2016a, Astrophysical Journal, 818, 113

Neeleman, M. et al. 2016b, Astrophysical Journal, Letters to the Editor, 820, L39

Neeleman, M., Wolfe, A. M., Prochaska, J. X., & Rafelski, M. 2013, Astrophysical Journal, 769, 54

Nelson, D. et al. 2017, ArXiv e-prints

Nestor, D. B., Rao, S. M., Turnshek, D. A., & Vanden Berk, D. 2003, Astrophysical Journal, Letters to the Editor, 595, L5

Nielsen, N. M., Churchill, C. W., Kacprzak, G. G., & Murphy, M. T. 2013, Astrophysical Journal, 776, 114

Nielsen, N. M., Churchill, C. W., Kacprzak, G. G., Murphy, M. T., & Evans, J. L. 2015, Astrophysical Journal, 812, 83

Nissen, P. E., Akerman, C., Asplund, M., Fabbian, D., Kerber, F., Kaufl, H. U., & Pettini, M. 2007, Astronomy and Astrophysics, 469, 319

Nissen, P. E., Chen, Y. Q., Asplund, M., & Pettini, M. 2004, Astronomy and Astrophysics, 415, 993

Nissen, P. E. & Schuster, W. J. 2011, Astronomy and Astrophysics, 530, A15

Nomoto, K., Kobayashi, C., & Tominaga, N. 2013, Annual Review of Astronomy and Astrophysics, 51, 457

Norris, J. E. et al. 2013, Astrophysical Journal, 762, 25

Noterdaeme, P., Ledoux, C., Petitjean, P., & Srianand, R. 2008, Astronomy and Astrophysics, 481, 327

Noterdaeme, P. et al. 2012, Astronomy and Astrophysics, 547, L1

Noterdaeme, P., Petitjean, P., & Srianand, R. 2015, Astronomy and Astrophysics, 578, L5

O'Meara, J. M., Prochaska, J. X., Burles, S., Prochter, G., Bernstein, R. A., & Burgess, K. M. 2007, Astrophysical Journal, 656, 666

Oppenheimer, B. D. et al. 2016, Monthly Notices of the RAS, 460, 2157

Oppenheimer, B. D. & Schaye, J. 2013, Monthly Notices of the RAS, 434, 1063

Oppenheimer, B. D., Schaye, J., Crain, R. A., Werk, J. K., & Richings, A. J. 2017, ArXiv e-prints

Oppenheimer, B. D., Segers, M., Schaye, J., Richings, A. J., & Crain, R. A. 2018, Monthly Notices of the RAS, 474, 4740

Pâris, I. et al. 2011, Astronomy and Astrophysics, 530, A50

Patton, D. R., Ellison, S. L., Simard, L., McConnachie, A. W., & Mendel, J. T. 2011, Monthly Notices of the RAS, 412, 591

Patton, D. R., Qamar, F. D., Ellison, S. L., Bluck, A. F. L., Simard, L., Mendel, J. T., Moreno, J., & Torrey, P. 2016, Monthly Notices of the RAS, 461, 2589

Penprase, B. E., Prochaska, J. X., Sargent, W. L. W., Toro-Martinez, I., & Beeler, D. J. 2010, Astrophysical Journal, 721, 1

Penzias, A. A. & Wilson, R. W. 1965, Astrophysical Journal, 142, 419

Perna, M., Lanzuisi, G., Brusa, M., Mignoli, M., & Cresci, G. 2017, Astronomy and Astrophysics, 603, A99

Péroux, C., Bouché, N., Kulkarni, V. P., York, D. G., & Vladilo, G. 2011, Monthly Notices of the RAS, 410, 2237

Péroux, C., Deharveng, J.-M., Le Brun, V., & Cristiani, S. 2004, Monthly Notices of the RAS, 352, 1291

Péroux, C., Dessauges-Zavadsky, M., D'Odorico, S., Kim, T.-S., & McMahon, R. G. 2003a, Monthly Notices of the RAS, 345, 480

Péroux, C., Dessauges-Zavadsky, M., D'Odorico, S., Sun Kim, T., & McMahon, R. G. 2005, Monthly Notices of the RAS, 363, 479

Péroux, C., McMahon, R. G., Storrie-Lombardi, L. J., & Irwin, M. J. 2003b, Monthly Notices of the RAS, 346, 1103

Perrotta, S. et al. 2016, Monthly Notices of the RAS, 462, 3285

Petitjean, P., Ledoux, C., & Srianand, R. 2008, Astronomy and Astrophysics, 480, 349

Pettini, M., Ellison, S. L., Steidel, C. C., & Bowen, D. V. 1999, Astrophysical Journal, 510, 576

Pettini, M., Smith, L. J., Hunstead, R. W., & King, D. L. 1994, Astrophysical Journal, 426, 79

Pettini, M., Smith, L. J., King, D. L., & Hunstead, R. W. 1997, Astrophysical Journal, 486, 665

Pettini, M., Zych, B. J., Murphy, M. T., Lewis, A., & Steidel, C. C. 2008, Monthly Notices of the RAS, 391, 1499

Planck Collaboration et al. 2015, ArXiv e-prints

Prochaska, J. X., Chen, H.-W., Wolfe, A. M., Dessauges-Zavadsky, M., & Bloom, J. S. 2008a, Astrophysical Journal, 672, 59

Prochaska, J. X., Gawiser, E., Wolfe, A. M., Castro, S., & Djorgovski, S. G. 2003a, Astrophysical Journal, Letters to the Editor, 595, L9

Prochaska, J. X., Gawiser, E., Wolfe, A. M., Cooke, J., & Gelino, D. 2003b, Astrophysical Journal, Supplement Series, 147, 227

Prochaska, J. X., Hennawi, J. F., & Herbert-Fort, S. 2008b, Astrophysical Journal, 675, 1002

Prochaska, J. X. et al. 2013, Astrophysical Journal, 776, 136

Prochaska, J. X., Herbert-Fort, S., & Wolfe, A. M. 2005, Astrophysical Journal, 635, 123

Prochaska, J. X., Lau, M. W., & Hennawi, J. F. 2014, Astrophysical Journal, 796, 140

Prochaska, J. X., Naumov, S. O., Carney, B. W., McWilliam, A., & Wolfe, A. M. 2000, Astronomical Journal, 120, 2513

Prochaska, J. X., Weiner, B., Chen, H.-W., Mulchaey, J., & Cooksey, K. 2011, Astrophysical Journal, 740, 91

Prochaska, J. X. & Wolfe, A. M. 1997, Astrophysical Journal, 487, 73

— 2000, Astrophysical Journal, Letters to the Editor, 533, L5

— 2002, Astrophysical Journal, 566, 68

— 2009, Astrophysical Journal, 696, 1543

Prochaska, J. X., Wolfe, A. M., Howk, J. C., Gawiser, E., Burles, S. M., & Cooke, J. 2007, Astrophysical Journal, Supplement Series, 171, 29

Prochaska, J. X. et al. 2001, Astrophysical Journal, Supplement Series, 137, 21

Putman, M. E., Peek, J. E. G., & Joung, M. R. 2012, Annual Review of Astronomy and Astrophysics, 50, 491

Quiret, S. et al. 2016, Monthly Notices of the RAS, 458, 4074

Rafelski, M., Gardner, J. P., Fumagalli, M., Neeleman, M., Teplitz, H. I., Grogin, N., Koekemoer, A. M., & Scarlata, C. 2016, Astrophysical Journal, 825, 87

Rafelski, M., Neeleman, M., Fumagalli, M., Wolfe, A. M., & Prochaska, J. X. 2014, Astrophysical Journal, Letters to the Editor, 782, L29

Rafelski, M., Wolfe, A. M., Prochaska, J. X., Neeleman, M., & Mendez, A. J. 2012, Astrophysical Journal, 755, 89

Rahmati, A., Schaye, J., Bower, R. G., Crain, R. A., Furlong, M., Schaller, M., & Theuns, T. 2015, Monthly Notices of the RAS, 452, 2034

Rao, S. M. & Turnshek, D. A. 2000, Astrophysical Journal, Supplement Series, 130, 1

Rao, S. M., Turnshek, D. A., & Nestor, D. B. 2006, Astrophysical Journal, 636, 610

Rao, S. M., Turnshek, D. A., Sardane, G. M., & Monier, E. M. 2017, Monthly Notices of the RAS, 471, 3428

Rhee, J., Lah, P., Chengalur, J. N., Briggs, F. H., & Colless, M. 2016, Monthly Notices of the RAS, 460, 2675

Richings, A. J., Schaye, J., & Oppenheimer, B. D. 2014, Monthly Notices of the RAS, 440, 3349

Rix, S. A., Pettini, M., Steidel, C. C., Reddy, N. A., Adelberger, K. L., Erb, D. K., & Shapley, A. E. 2007, Astrophysical Journal, 670, 15

Rosario, D. J., Mendel, J. T., Ellison, S. L., Lutz, D., & Trump, J. R. 2016, Monthly Notices of the RAS, 457, 2703

Rubin, K. H. R., Prochaska, J. X., Koo, D. C., Phillips, A. C., Martin, C. L., & Winstrom, L. O. 2014, Astrophysical Journal, 794, 156

Ruel, J. et al. 2014, Astrophysical Journal, 792, 45

Russell, D. M., Ellison, S. L., & Benn, C. R. 2006, Monthly Notices of the RAS, 367, 412

Salim, S. et al. 2007, Astrophysical Journal, Supplement Series, 173, 267

Salpeter, E. E. 1952, Astrophysical Journal, 115, 326

Sánchez-Ramírez, R. et al. 2016, Monthly Notices of the RAS, 456, 4488

Satyapal, S., Ellison, S. L., McAlpine, W., Hickox, R. C., Patton, D. R., & Mendel, J. T. 2014, Monthly Notices of the RAS, 441, 1297

Savage, B. D. & Sembach, K. R. 1991, Astrophysical Journal, 379, 245

— 1996, Annual Review of Astronomy and Astrophysics, 34, 279

Sazonov, S. Y., Ostriker, J. P., & Sunyaev, R. A. 2004, Monthly Notices of the RAS, 347, 144

Scannapieco, C. et al. 2012, Monthly Notices of the RAS, 423, 1726

Schawinski, K., Thomas, D., Sarzi, M., Maraston, C., Kaviraj, S., Joo, S.-J., Yi, S. K., & Silk, J. 2007, Monthly Notices of the RAS, 382, 1415

Schawinski, K. et al. 2014, Monthly Notices of the RAS, 440, 889

Schaye, J., Aguirre, A., Kim, T.-S., Theuns, T., Rauch, M., & Sargent, W. L. W. 2003, Astrophysical Journal, 596, 768

Schaye, J., Carswell, R. F., & Kim, T.-S. 2007, Monthly Notices of the RAS, 379, 1169

Schaye, J. et al. 2015, Monthly Notices of the RAS, 446, 521

Schiminovich, D. et al. 2007, Astrophysical Journal, Supplement Series, 173, 315

Schirber, M., Miralda-Escudé, J., & McDonald, P. 2004, Astrophysical Journal, 610, 105

Scudder, J. M., Ellison, S. L., Torrey, P., Patton, D. R., & Mendel, J. T. 2012, Monthly Notices of the RAS, 426, 549

Searle, L. & Zinn, R. 1978, Astrophysical Journal, 225, 357

Segers, M. C., Oppenheimer, B. D., Schaye, J., & Richings, A. J. 2017, ArXiv e-prints

Shapiro, P. R. & Field, G. B. 1976, Astrophysical Journal, 205, 762

Shetrone, M., Venn, K. A., Tolstoy, E., Primas, F., Hill, V., & Kaufer, A. 2003, Astronomical Journal, 125, 684

Silverman, J. D., Miniati, F., Finoguenov, A., Carollo, C. M., Cibinel, A., Lilly, S. J., & Schawinski, K. 2014, Astrophysical Journal, 780, 67

Skúladóttir, Á., Tolstoy, E., Salvadori, S., Hill, V., & Pettini, M. 2017, Astronomy and Astrophysics, 606, A71

Skúladóttir, Á., Tolstoy, E., Salvadori, S., Hill, V., Pettini, M., Shetrone, M. D., & Starkenburg, E. 2015, Astronomy and Astrophysics, 574, A129

Sneden, C. & Crocker, D. A. 1988, Astrophysical Journal, 335, 406

Sneden, C., Gratton, R. G., & Crocker, D. A. 1991, Astronomy and Astrophysics, 246, 354

Songaila, A. & Cowie, L. L. 2002, Astronomical Journal, 123, 2183

Spite, F. & Spite, M. 1982, Astronomy and Astrophysics, 115, 357

Spite, M. et al. 2011, Astronomy and Astrophysics, 528, A9

Springel, V., Di Matteo, T., & Hernquist, L. 2005a, Astrophysical Journal, Letters to the Editor, 620, L79

Springel, V. et al. 2005b, Nature, 435, 629

Starkenburg, E. et al. 2017, Monthly Notices of the RAS, 471, 2587

Steidel, C. C., Erb, D. K., Shapley, A. E., Pettini, M., Reddy, N., Bogosavljević, M., Rudie, G. C., & Rakic, O. 2010, Astrophysical Journal, 717, 289

Stinson, G. S. et al. 2012, Monthly Notices of the RAS, 425, 1270

Stocke, J. T. et al. 2014, Astrophysical Journal, 791, 128

Storrie-Lombardi, L. J. & Wolfe, A. M. 2000, Astrophysical Journal, 543, 552

Strateva, I. et al. 2001, Astronomical Journal, 122, 1861

Sturm, E. et al. 2011, Astrophysical Journal, Letters to the Editor, 733, L16

Suda, T. et al. 2008, Publications of the ASJ, 60, 1159

Tchernyshyov, K., Meixner, M., Seale, J., Fox, A., Friedman, S. D., Dwek, E., & Galliano, F. 2015, Astrophysical Journal, 811, 78

Theuns, T., Leonard, A., & Efstathiou, G. 1998, Monthly Notices of the RAS, 297, L49

Thom, C. et al. 2012, Astrophysical Journal, Letters to the Editor, 758, L41

Timmes, F. X., Woosley, S. E., & Weaver, T. A. 1995, Astrophysical Journal, Supplement Series, 98, 617

Tinsley, B. M. 1979, Astrophysical Journal, 229, 1046

Tolstoy, E., Hill, V., & Tosi, M. 2009, Annual Review of Astronomy and Astrophysics, 47, 371

Torrey, P., Cox, T. J., Kewley, L., & Hernquist, L. 2012, Astrophysical Journal, 746, 108

Tremonti, C. A., Moustakas, J., & Diamond-Stanic, A. M. 2007, Astrophysical Journal, Letters to the Editor, 663, L77

Tumlinson, J. et al. 2010, Astrophysical Journal, Letters to the Editor, 718, L156

Tumlinson, J., Peeples, M. S., & Werk, J. K. 2017, Annual Review of Astronomy and Astrophysics, 55, 389

Tumlinson, J. et al. 2013, Astrophysical Journal, 777, 59

— 2011, Science, 334, 948

Turner, M. L., Schaye, J., Steidel, C. C., Rudie, G. C., & Strom, A. L. 2014, Monthly Notices of the RAS, 445, 794

— 2015, Monthly Notices of the RAS, 450, 2067

Tytler, D. & Fan, X.-M. 1992, Astrophysical Journal, Supplement Series, 79, 1

Tytler, D., Fan, X.-M., & Burles, S. 1996, Nature, 381, 207

Umeda, H. & Nomoto, K. 2002, Astrophysical Journal, 565, 385

Veilleux, S., Cecil, G., & Bland-Hawthorn, J. 2005, Annual Review of Astronomy and Astrophysics, 43, 769

Veilleux, S. et al. 2013, Astrophysical Journal, 776, 27

Venemans, B. P. et al. 2015, Monthly Notices of the RAS, 453, 2259

Venn, K. A., Irwin, M., Shetrone, M. D., Tout, C. A., Hill, V., & Tolstoy, E. 2004, Astronomical Journal, 128, 1177

Venn, K. A. et al. 2012, Astrophysical Journal, 751, 102

Vernet, J. et al. 2011, Astronomy and Astrophysics, 536, A105

Vito, F. et al. 2014, Monthly Notices of the RAS, 441, 1059

Vladilo, G. 2002a, Astrophysical Journal, 569, 295

— 2002b, Astronomy and Astrophysics, 391, 407

Vladilo, G., Abate, C., Yin, J., Cescutti, G., & Matteucci, F. 2011, Astronomy and Astrophysics, 530, A33

Vladilo, G., Centurión, M., Bonifacio, P., & Howk, J. C. 2001, Astrophysical Journal, 557, 1007

Vogelsberger, M. et al. 2014, Monthly Notices of the RAS, 444, 1518

Wagoner, R. V., Fowler, W. A., & Hoyle, F. 1967, Astrophysical Journal, 148, 3

Wakker, B. P. & Savage, B. D. 2009, Astrophysical Journal, Supplement Series, 182, 378

Walker, T. P., Steigman, G., Kang, H.-S., Schramm, D. M., & Olive, K. A. 1991, Astrophysical Journal, 376, 51

Weinmann, S. M., van den Bosch, F. C., Yang, X., & Mo, H. J. 2006, Monthly Notices of the RAS, 366, 2

Werk, J. K., Prochaska, J. X., Thom, C., Tumlinson, J., Tripp, T. M., O'Meara, J. M., & Meiring, J. D. 2012, Astrophysical Journal, Supplement Series, 198, 3

Werk, J. K., Prochaska, J. X., Thom, C., Tumlinson, J., Tripp, T. M., O'Meara, J. M., & Peeples, M. S. 2013, Astrophysical Journal, Supplement Series, 204, 17

Werk, J. K. et al. 2014, Astrophysical Journal, 792, 8

White, S. D. M. & Rees, M. J. 1978, Monthly Notices of the RAS, 183, 341

Wild, V., Heckman, T., & Charlot, S. 2010, Monthly Notices of the RAS, 405, 933

Wild, V., Hewett, P. C., & Pettini, M. 2006, Monthly Notices of the RAS, 367, 211

Wild, V., Kauffmann, G., Heckman, T., Charlot, S., Lemson, G., Brinchmann, J., Reichard, T., & Pasquali, A. 2007, Monthly Notices of the RAS, 381, 543

Willett, K. W. et al. 2013, Monthly Notices of the RAS, 435, 2835

Wolfe, A. M. & Chen, H.-W. 2006, Astrophysical Journal, 652, 981

Wolfe, A. M., Gawiser, E., & Prochaska, J. X. 2005, Annual Review of Astronomy and Astrophysics, 43, 861

Wolfe, A. M., Prochaska, J. X., & Gawiser, E. 2003, Astrophysical Journal, 593, 215

Wolfe, A. M., Turnshek, D. A., Smith, H. E., & Cohen, R. D. 1986, Astrophysical Journal, Supplement Series, 61, 249

Woo, J.-H., Bae, H.-J., Son, D., & Karouzos, M. 2016, Astrophysical Journal, 817, 108

Woo, J.-H., Son, D., & Bae, H.-J. 2017, Astrophysical Journal, 839, 120

Woosley, S. E. & Weaver, T. A. 1995, Astrophysical Journal, Supplement Series, 101, 181

Wotta, C. B., Lehner, N., Howk, J. C., O'Meara, J. M., & Prochaska, J. X. 2016, Astrophysical Journal, 831, 95

Wright, G. S., James, P. A., Joseph, R. D., & McLean, I. S. 1990, Nature, 344, 417

Yan, R. & Blanton, M. R. 2012, Astrophysical Journal, 747, 61

Yesuf, H. M., Faber, S. M., Trump, J. R., Koo, D. C., Fang, J. J., Liu, F. S., Wild, V., & Hayward, C. C. 2014, Astrophysical Journal, 792, 84

Zafar, T., Centurión, M., Péroux, C., Molaro, P., D'Odorico, V., Vladilo, G., & Popping, A. 2014a, Monthly Notices of the RAS, 444, 744

Zafar, T., Péroux, C., Popping, A., Milliard, B., Deharveng, J.-M., & Frank, S. 2013a, Astronomy and Astrophysics, 556, A141

Zafar, T., Popping, A., & Péroux, C. 2013b, Astronomy and Astrophysics, 556, A140

Zafar, T., Vladilo, G., Péroux, C., Molaro, P., Centurión, M., D'Odorico, V., Abbas, K., & Popping, A. 2014b, Monthly Notices of the RAS, 445, 2093

Zheng, Z. & Miralda-Escudé, J. 2002, Astrophysical Journal, Letters to the Editor, 568, L71

Zwaan, M. A., Meyer, M. J., Staveley-Smith, L., & Webster, R. L. 2005, Monthly Notices of the RAS, 359, L30

Appendix A

XQ-100 absorber catalogue

This appendix contains the XQ-100 H I absorber catalogue presented in Chapter 2. Table A.1 contains all the H I column densities and redshifts of the absorbers, while Figures A.1 – A.15 show the Lyα velocity profiles, and the best-fitting Voit profiles for each of these absorbers.

Table A.1: XQ-100 H I absorbers

QSO	z_{abs}	logN(H I)	Metal?	QSO	z_{abs}	logN(H I)	Metal?
J0003-2603	2.78140	19.00±0.20	N	J0003-2603	3.05490	20.00±0.15	Y
J0003-2603	3.16080	19.10±0.15	Y	J0003-2603	3.39020	21.45±0.05	Y
J0003-2603	3.43470	18.90±0.10	N	J0006-6208	3.16890	18.90±0.20	N
J0006-6208	3.18430	18.90±0.15	N	J0006-6208	3.20250	20.80±0.20	Y
J0006-6208	3.45890	19.30±0.20	N	J0006-6208	3.77300	20.90±0.15	Y
J0006-6208	3.79683	19.70±0.15	Y	J0030-5129	3.35400	18.80±0.20	Y
J0034+1639	2.99540	19.00±0.15	N	J0034+1639	3.02170	19.30±0.15	N
J0034+1639	3.12750	18.90±0.20	N	J0034+1639	3.22750	19.80±0.15	N
J0034+1639	3.47970	18.80±0.20	Y	J0034+1639	3.75350	20.25±0.15	Y
J0034+1639	3.82470	19.00±0.20	N	J0034+1639	4.22715	19.60±0.20	Y
J0034+1639	4.25163	21.10±0.20	Y	J0034+1639	4.28360	21.20±0.10	Y
J0042-1020	2.68090	19.00±0.20	N	J0042-1020	2.68290	19.00±0.20	N
J0042-1020	2.75482	20.10±0.15	Y	J0048-2442	3.75800	19.50±0.25	Y
J0056-2808	2.72863	19.50±0.15	Y	J0100-2708	3.24270	19.80±0.10	Y
J0113-2803	3.07400	19.20±0.20	N	J0113-2803	3.10550	21.10±0.10	Y
J0113-2803	3.39726	19.00±0.15	N	J0113-2803	3.89000	19.30±0.20	Y
J0117+1552	3.17670	18.90±0.25	N	J0117+1552	4.13166	18.80±0.10	N
J0121+0347	2.87250	19.30±0.20	N	J0121+0347	2.95176	18.90±0.15	N
J0121+0347	2.97700	19.40±0.15	Y	J0121+0347	3.36000	19.00±0.20	Y
J0121+0347	3.79347	18.80±0.15	N	J0124+0044	2.83320	18.90±0.20	Y
J0124+0044	2.98750	19.00±0.15	Y	J0124+0044	3.07770	20.20±0.15	Y
J0124+0044	3.39200	18.80±0.15	Y	J0124+0044	3.55000	18.90±0.15	Y
J0132+1341	3.05980	19.20±0.20	N	J0132+1341	3.08204	19.20±0.25	N
J0132+1341	3.09983	18.80±0.20	Y	J0132+1341	3.28489	18.90±0.20	N
J0132+1341	3.93640	20.20±0.20	Y	J0134+0400	2.94367	18.80±0.20	N
J0134+0400	3.08042	18.90±0.20	N	J0134+0400	3.23010	18.90±0.20	Y
J0134+0400	3.69159	20.60±0.15	Y	J0134+0400	3.75850	18.80±0.20	N
J0134+0400	3.77345	20.55±0.20	Y	J0134+0400	3.94917	18.80±0.20	N
J0134+0400	3.95341	19.10±0.20	N	J0134+0400	3.99630	20.10±0.15	Y
J0134+0400	4.02108	19.10±0.15	N	J0134+0400	4.11270	18.80±0.20	Y

Continued on next page

Table A.1 – continued from previous page

QSO	z_{abs}	logN(H I)	Metal?	QSO	z_{abs}	logN(H I)	Metal?
J0137-4224	3.07313	19.10±0.20	Y	J0137-4224	3.10030	19.70±0.20	Y
J0137-4224	3.39627	18.90±0.20	N	J0137-4224	3.54628	18.80±0.25	N
J0137-4224	3.66516	19.10±0.20	Y	J0153-0011	2.99368	19.00±0.25	N
J0153-0011	3.01484	19.20±0.20	N	J0153-0011	3.03616	19.30±0.20	N
J0153-0011	3.38570	19.20±0.15	N	J0153-0011	3.87670	19.30±0.20	N
J0153-0011	4.12822	18.80±0.20	N	J0211+1107	3.11780	18.90±0.20	N
J0211+1107	3.14080	20.20±0.20	Y	J0211+1107	3.50080	19.90±0.20	Y
J0211+1107	3.87986	18.90±0.20	Y	J0214-0517	2.76992	19.00±0.20	N
J0214-0517	2.95904	18.90±0.15	N	J0214-0517	3.08439	18.90±0.15	N
J0214-0517	3.08966	18.90±0.15	Y	J0214-0517	3.22189	19.10±0.20	N
J0214-0517	3.72110	20.60±0.20	Y	J0234-1806	3.00500	19.70±0.25	N
J0234-1806	3.25732	18.80±0.20	N	J0234-1806	3.34870	19.05±0.20	N
J0234-1806	3.36450	19.00±0.20	N	J0234-1806	3.69403	20.45±0.20	Y
J0234-1806	4.22700	19.40±0.20	Y	J0244-0134	2.85146	18.80±0.20	N
J0244-0134	2.91910	18.90±0.20	N	J0244-0134	2.93176	19.15±0.20	N
J0244-0134	3.92982	18.90±0.20	N	J0244-0134	3.96680	19.10±0.15	Y
J0247-0556	3.03668	19.10±0.20	N	J0247-0556	3.10946	19.20±0.20	N
J0247-0556	3.11344	19.00±0.20	N	J0247-0556	3.33643	19.00±0.20	N
J0247-0556	3.99141	18.85±0.20	N	J0247-0556	4.13958	19.50±0.20	Y
J0248+1802	3.16955	18.90±0.20	N	J0248+1802	3.32810	19.10±0.20	N
J0248+1802	3.70260	19.00±0.20	N	J0248+1802	3.93685	18.80±0.20	N
J0248+1802	4.03307	18.80±0.20	N	J0248+1802	4.12920	19.00±0.15	Y
J0255+0048	2.79119	18.90±0.20	N	J0255+0048	2.87008	19.00±0.20	N
J0255+0048	3.25453	20.70±0.15	Y	J0255+0048	3.45038	19.60±0.15	Y
J0255+0048	3.91400	21.50±0.20	Y	J0307-4945	3.35450	20.10±0.20	Y
J0307-4945	3.49416	19.00±0.20	N	J0307-4945	3.59170	20.40±0.25	Y
J0307-4945	3.60826	19.70±0.25	N	J0307-4945	3.71772	18.80±0.20	N
J0307-4945	4.36390	19.00±0.20	N	J0307-4945	4.46840	20.60±0.10	Y
J0307-4945	4.58726	19.00±0.20	Y	J0311-1722	3.73420	20.20±0.20	Y
J0311-1722	3.85420	18.80±0.20	Y	J0311-1722	3.97845	18.90±0.20	N
J0403-1703	3.20617	19.10±0.15	Y	J0403-1703	3.54373	18.80±0.20	N
J0403-1703	4.10146	19.00±0.20	N	J0415-4357	2.81455	18.80±0.20	N

Continued on next page

Table A.1 – continued from previous page

QSO	z_{abs}	logN(H I)	Metal?	QSO	z_{abs}	logN(H I)	Metal?
J0415-4357	2.84749	19.80±0.20	N	J0415-4357	2.93399	18.90±0.20	N
J0415-4357	3.02721	19.30±0.20	N	J0415-4357	3.05382	18.80±0.20	N
J0415-4357	3.29662	18.90±0.20	N	J0415-4357	3.80850	20.40±0.20	Y
J0415-4357	4.03473	20.05±0.30	Y	J0424-2209	3.04835	18.80±0.20	N
J0424-2209	3.14142	18.80±0.20	N	J0424-2209	3.15974	19.50±0.20	N
J0424-2209	3.24419	18.80±0.20	N	J0424-2209	3.36663	18.80±0.20	N
J0424-2209	3.60541	19.50±0.20	N	J0424-2209	3.64458	18.80±0.20	N
J0424-2209	3.93433	19.00±0.20	N	J0424-2209	4.17561	19.20±0.15	Y
J0525-3343	3.07538	18.80±0.20	N	J0525-3343	3.09793	18.80±0.20	N
J0525-3343	3.13246	18.90±0.20	N	J0525-3343	3.20174	18.80±0.15	N
J0529-3526	3.06433	19.40±0.20	N	J0529-3526	3.19297	19.30±0.20	N
J0529-3526	3.31146	18.80±0.20	N	J0529-3526	3.57170	20.10±0.15	Y
J0529-3526	3.76200	19.35±0.20	N	J0529-3526	3.89440	18.80±0.20	N
J0529-3552	2.97530	18.90±0.20	N	J0529-3552	3.01493	18.90±0.20	N
J0529-3552	3.68360	20.10±0.20	Y	J0529-3552	3.70972	19.50±0.20	N
J0529-3552	3.99650	19.00±0.20	Y	J0529-3552	4.06530	19.50±0.15	Y
J0714-6455	3.10313	19.45±0.20	N	J0714-6455	3.21970	19.10±0.20	N
J0714-6455	3.26472	18.80±0.15	N	J0714-6455	3.31292	18.80±0.20	N
J0714-6455	3.74562	19.20±0.20	Y	J0714-6455	3.75020	19.10±0.10	Y
J0714-6455	4.38971	18.80±0.20	Y	J0747+2739	2.91793	19.40±0.20	Y
J0747+2739	2.99956	19.00±0.20	N	J0747+2739	3.42400	20.80±0.15	Y
J0747+2739	3.90134	20.50±0.20	Y	J0755+1345	3.09850	19.00±0.20	Y
J0800+1920	2.75564	18.80±0.20	N	J0800+1920	2.95673	18.90±0.20	N
J0800+1920	3.42900	20.00±0.20	Y	J0800+1920	3.56152	19.10±0.20	Y
J0800+1920	3.73076	19.05±0.20	Y	J0818+0958	2.56424	18.80±0.20	N
J0818+0958	3.02811	18.85±0.20	Y	J0818+0958	3.30631	20.90±0.20	Y
J0818+0958	3.45449	19.00±0.20	Y	J0833+0959	2.80570	18.90±0.20	N
J0835+0650	2.77229	19.30±0.20	N	J0835+0650	2.77647	18.90±0.20	N
J0835+0650	2.79340	18.90±0.20	N	J0835+0650	2.87150	19.10±0.20	N
J0835+0650	2.96430	19.20±0.20	N	J0835+0650	2.97858	18.90±0.20	N
J0835+0650	3.19004	19.00±0.20	Y	J0835+0650	3.51317	19.00±0.20	Y
J0835+0650	3.60160	19.80±0.20	Y	J0835+0650	3.95570	20.35±0.20	Y

Continued on next page

Table A.1 – continued from previous page

QSO	z_{abs}	logN(H I)	Metal?	QSO	z_{abs}	logN(H I)	Metal?
J0839+0318	3.43922	18.80±0.20	N	J0839+0318	4.09690	19.60±0.20	Y
J0920+0725	3.05873	19.10±0.20	Y	J0920+0725	3.54962	19.00±0.20	Y
J0937+0828	2.71534	18.90±0.20	Y	J0937+0828	3.12919	19.70±0.30	Y
J0955-0130	3.16128	18.80±0.20	N	J0955-0130	3.20670	19.30±0.15	N
J0955-0130	3.23765	19.20±0.20	N	J0955-0130	3.47570	20.00±0.20	Y
J0955-0130	3.91050	18.80±0.20	N	J0955-0130	3.95186	19.20±0.20	N
J0955-0130	3.98709	19.00±0.20	N	J0955-0130	4.02250	20.65±0.20	Y
J0955-0130	4.17243	18.80±0.20	Y	J0955-0130	4.23885	18.80±0.20	N
J0959+1312	2.92544	18.90±0.20	N	J0959+1312	3.14507	19.10±0.20	N
J0959+1312	3.91230	20.00±0.10	Y	J1013+0650	2.78778	18.80±0.20	N
J1013+0650	3.01137	19.20±0.20	N	J1013+0650	3.48930	19.20±0.20	Y
J1018+0548	2.50832	19.00±0.20	N	J1018+0548	2.83192	18.80±0.20	Y
J1018+0548	3.38470	19.65±0.20	Y	J1020+0922	2.59127	21.40±0.20	Y
J1020+0922	2.74873	20.10±0.20	Y	J1020+0922	3.47980	18.80±0.20	N
J1024+1819	2.53488	19.00±0.20	N	J1024+1819	2.69809	19.10±0.20	Y
J1024+1819	3.18451	18.90±0.20	N	J1024+1819	3.40393	18.80±0.20	Y
J1032+0927	3.80480	20.00±0.15	Y	J1034+1102	3.34668	18.90±0.20	N
J1036-0343	3.46553	19.00±0.20	N	J1036-0343	3.67068	19.10±0.20	N
J1036-0343	4.15340	19.20±0.20	Y	J1036-0343	4.17470	19.80±0.20	Y
J1037+0704	3.28155	19.00±0.20	Y	J1037+0704	3.77820	19.00±0.20	N
J1037+0704	3.89280	18.90±0.20	Y	J1037+2135	2.93761	18.80±0.20	N
J1054+0215	3.97758	19.00±0.20	Y	J1057+1910	3.22329	19.10±0.20	N
J1057+1910	3.37340	20.20±0.15	Y	J1057+1910	3.79985	19.10±0.20	Y
J1057+1910	4.00818	19.30±0.20	Y	J1058+1245	3.20690	18.80±0.20	Y
J1058+1245	3.22850	19.20±0.20	N	J1058+1245	3.43160	20.50±0.20	Y
J1058+1245	3.59987	18.90±0.20	N	J1103+1004	2.48702	19.30±0.20	N
J1103+1004	3.13101	19.10±0.20	Y	J1103+1004	3.53240	18.90±0.20	N
J1108+1209	2.53374	19.20±0.20	N	J1108+1209	2.63670	18.80±0.20	Y
J1108+1209	2.65507	19.30±0.20	N	J1108+1209	2.66164	18.90±0.20	N
J1108+1209	2.73522	18.80±0.20	Y	J1108+1209	3.39594	20.70±0.15	Y
J1108+1209	3.48574	18.80±0.20	Y	J1108+1209	3.54530	20.90±0.15	Y
J1111-0804	2.70126	19.60±0.20	N	J1111-0804	2.98005	19.20±0.20	N

Continued on next page

Table A.1 – continued from previous page

QSO	z_{abs}	logN(H I)	Metal?	QSO	z_{abs}	logN(H I)	Metal?
J1111-0804	3.48180	19.95±0.15	Y	J1111-0804	3.60690	20.40±0.15	Y
J1111-0804	3.75820	18.80±0.20	Y	J1117+1311	2.73896	18.90±0.20	N
J1126-0124	2.61480	19.00±0.20	N	J1126-0124	3.68281	18.90±0.20	N
J1202-0054	2.66046	19.60±0.15	Y	J1202-0054	2.76953	19.00±0.15	Y
J1202-0054	3.15122	19.00±0.20	Y	J1248+1304	2.62589	19.00±0.20	N
J1248+1304	3.40724	19.30±0.15	Y	J1249-0159	2.48080	19.00±0.15	N
J1249-0159	2.49471	18.80±0.20	N	J1249-0159	3.52476	18.80±0.20	N
J1249-0159	3.52963	18.90±0.15	N	J1304+0239	2.75477	18.90±0.15	N
J1304+0239	3.21063	19.30±0.20	Y	J1304+0239	3.33631	18.80±0.20	N
J1312+0841	2.65950	20.50±0.20	Y	J1320-0523	2.83411	19.10±0.20	Y
J1323+1405	2.92550	19.80±0.20	Y	J1330-2522	2.77513	18.90±0.20	N
J1330-2522	2.90758	18.90±0.20	N	J1330-2522	3.08060	19.80±0.20	Y
J1332+0052	2.38831	18.80±0.20	N	J1332+0052	3.08365	19.40±0.20	Y
J1332+0052	3.42120	19.20±0.20	Y	J1336+0243	2.69140	19.40±0.20	N
J1352+1303	3.16676	18.90±0.20	Y	J1401+0244	3.34057	18.90±0.20	N
J1416+1811	2.59808	18.90±0.20	N	J1416+1811	2.66330	19.65±0.20	Y
J1421-0643	2.55859	18.80±0.20	N	J1421-0643	3.16020	19.30±0.20	N
J1421-0643	3.44802	20.35±0.15	Y	J1503+0419	2.49915	19.10±0.20	N
J1517+0511	2.42657	18.90±0.20	N	J1517+0511	2.43960	19.10±0.20	N
J1517+0511	2.45773	18.90±0.20	N	J1517+0511	2.61383	18.80±0.20	N
J1517+0511	2.68838	21.35±0.15	Y	J1524+2123	2.54540	19.30±0.20	Y
J1524+2123	2.63417	19.60±0.15	Y	J1524+2123	2.73116	19.40±0.15	Y
J1542+0955	2.76560	19.00±0.20	N	J1542+0955	3.33235	19.20±0.30	Y
J1542+0955	3.61287	19.00±0.25	N	J1542+0955	3.90500	18.90±0.20	N
J1552+1005	2.64396	19.00±0.20	N	J1552+1005	2.97674	18.80±0.20	N
J1552+1005	3.07712	18.80±0.20	Y	J1552+1005	3.44240	19.00±0.20	Y
J1552+1005	3.60030	21.10±0.20	Y	J1552+1005	3.66550	21.00±0.20	Y
J1621-0042	3.10423	19.80±0.15	Y	J1633+1411	3.34678	19.10±0.20	Y
J1633+1411	4.15083	18.90±0.20	N	J1658-0739	2.70650	19.30±0.20	N
J1658-0739	2.95470	19.20±0.20	N	J1658-0739	3.54728	19.30±0.20	Y
J1658-0739	3.68892	19.00±0.15	N	J1658-0739	3.69580	19.10±0.15	Y
J1723+2243	3.19667	19.20±0.20	N	J1723+2243	3.42745	18.90±0.20	N

Continued on next page

Table A.1 – continued from previous page

QSO	z_{abs}	logN(H I)	Metal?	QSO	z_{abs}	logN(H I)	Metal?
J1723+2243	3.69800	20.50±0.15	Y	J1723+2243	3.97228	18.80±0.15	N
J1723+2243	3.98250	19.00±0.15	N	J1723+2243	4.08350	18.80±0.15	N
J1723+2243	4.15470	19.00±0.20	N	J1723+2243	4.23341	19.00±0.20	N
J1723+2243	4.24700	18.80±0.15	N	J1723+2243	4.35246	19.00±0.20	N
J2215-1611	2.77623	19.00±0.20	N	J2215-1611	2.85521	18.80±0.20	N
J2215-1611	2.93093	19.20±0.20	N	J2215-1611	2.96694	19.00±0.20	Y
J2215-1611	3.00628	19.00±0.20	N	J2215-1611	3.22585	19.40±0.20	N
J2215-1611	3.30557	19.00±0.20	Y	J2215-1611	3.46525	19.00±0.15	Y
J2215-1611	3.48904	18.90±0.20	Y	J2215-1611	3.49991	18.80±0.20	N
J2215-1611	3.66150	20.20±0.15	Y	J2215-1611	3.70080	19.30±0.15	Y
J2216-6714	3.11219	18.90±0.20	N	J2216-6714	3.15509	19.10±0.20	N
J2216-6714	3.21393	18.90±0.15	N	J2216-6714	3.36940	19.90±0.15	Y
J2216-6714	3.68304	18.80±0.20	N	J2216-6714	3.73025	18.80±0.20	Y
J2216-6714	4.30920	19.30±0.15	N	J2239-0552	3.18862	18.90±0.15	N
J2239-0552	3.82975	19.00±0.20	N	J2239-0552	4.08130	20.60±0.10	Y
J2239-0552	4.19986	18.90±0.15	Y	J2251-1227	2.98253	19.50±0.30	N
J2251-1227	3.23384	18.90±0.20	N	J2251-1227	3.45717	19.70±0.20	Y
J2251-1227	3.98793	19.60±0.15	Y	J2344+0342	3.21980	21.20±0.20	Y
J2344+0342	3.88400	19.80±0.15	Y	J2349-3712	2.92570	18.90±0.15	N
J2349-3712	3.58203	19.20±0.20	N	J2349-3712	3.69250	20.20±0.10	Y
J2349-3712	3.80387	18.90±0.15	N	J2349-3712	3.96340	18.80±0.15	Y

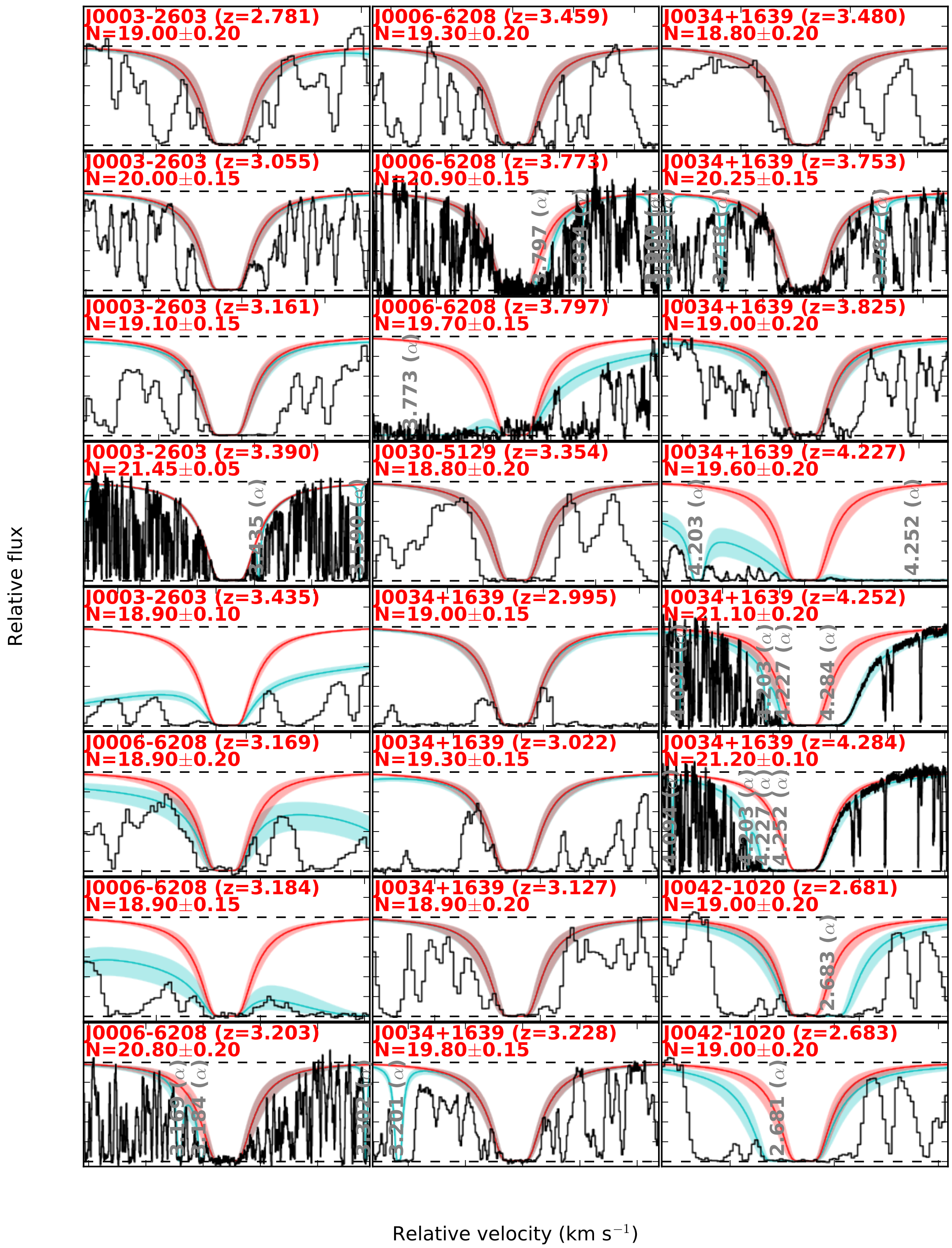

Figure A.1 The velocity profiles (black data) for the Lyα absorption lines of subDLAs and DLAs identified in the XQ-100 spectra. The text at the top of each panel denotes the host QSO, $z_{\rm abs}$, and logN(H I) of the absorber displayed. The best-fitting Voigt profile is shown in red, with the shaded red region denoting the error on the fit. The model H I fitted spectra for the entire sightline is shown in cyan. Nearby absorption lines at different redshifts are labelled with vertical text. To maintain the same scale over the diverse range of column densities probed, the velocity axis is arbitrarily scaled such that the Voigt profile reaches a relative flux of 0.97 on the edges of each panel.

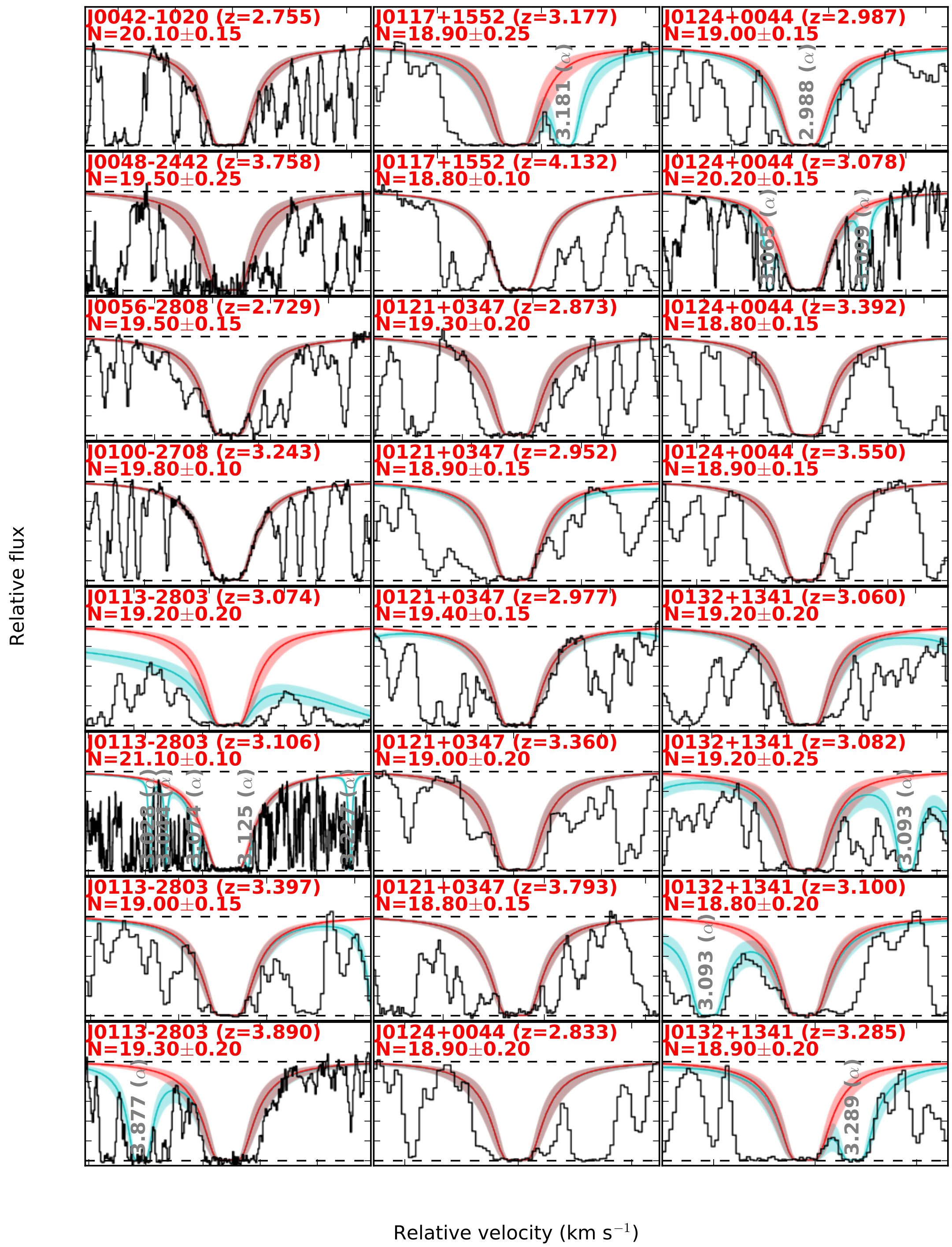

Figure A.2 The velocity profiles for the Lyα absorption lines of subDLAs and DLAs identified in the XQ-100 spectra. The notation is the same as Figure A.1.

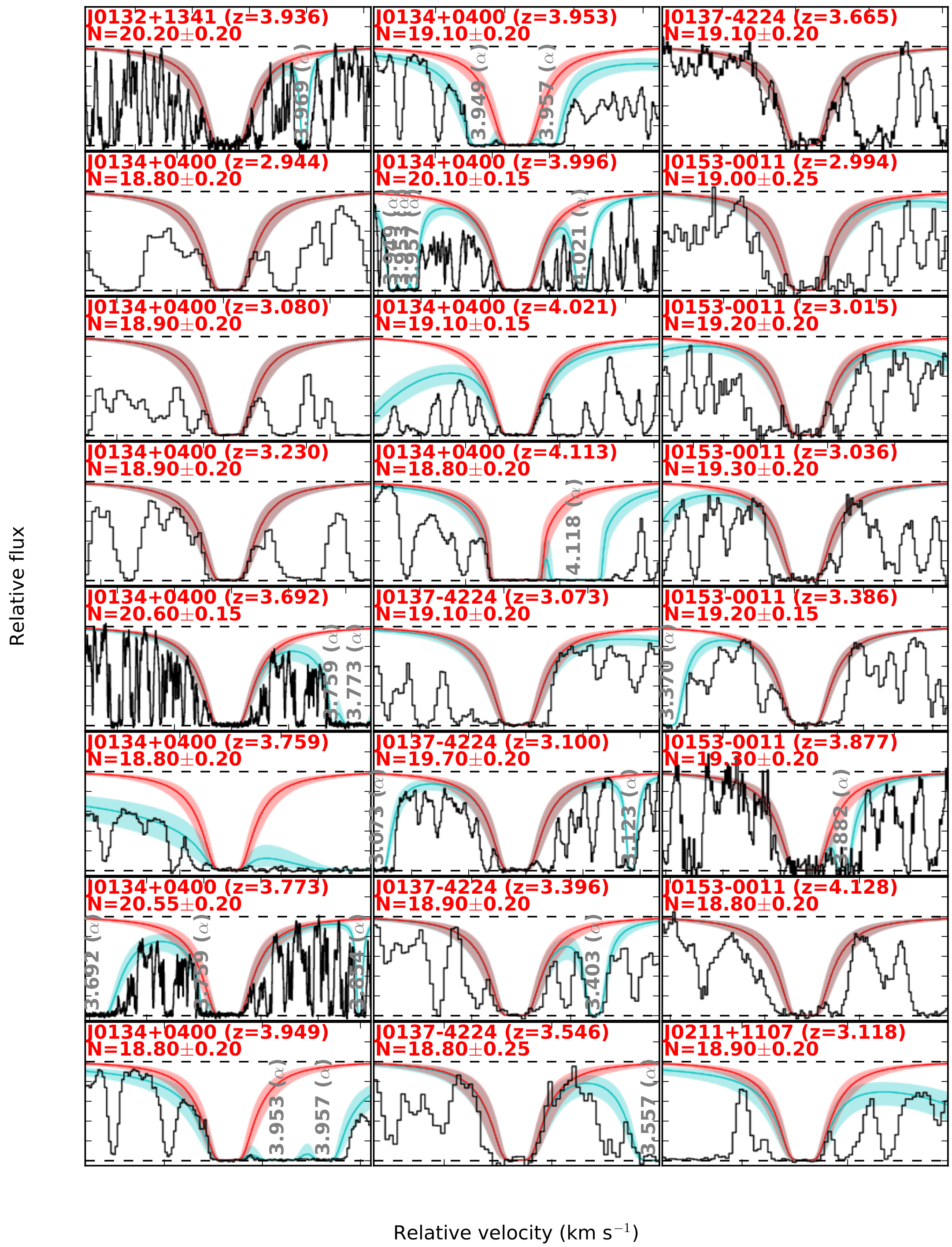

Figure A.3 The velocity profiles for the Lyα absorption lines of subDLAs and DLAs identified in the XQ-100 spectra. The notation is the same as Figure A.1.

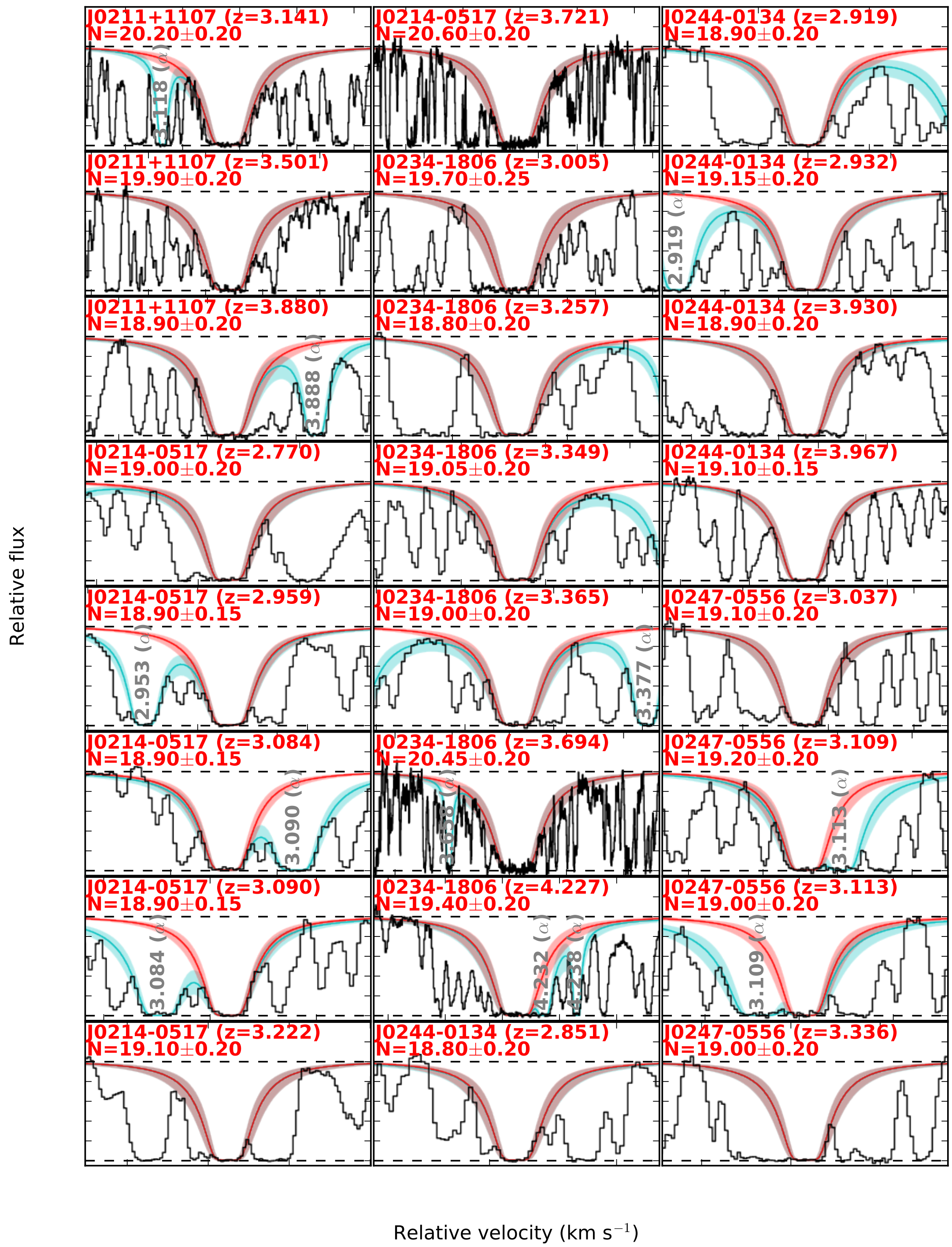

Figure A.4 The velocity profiles for the Lyα absorption lines of subDLAs and DLAs identified in the XQ-100 spectra. The notation is the same as Figure A.1.

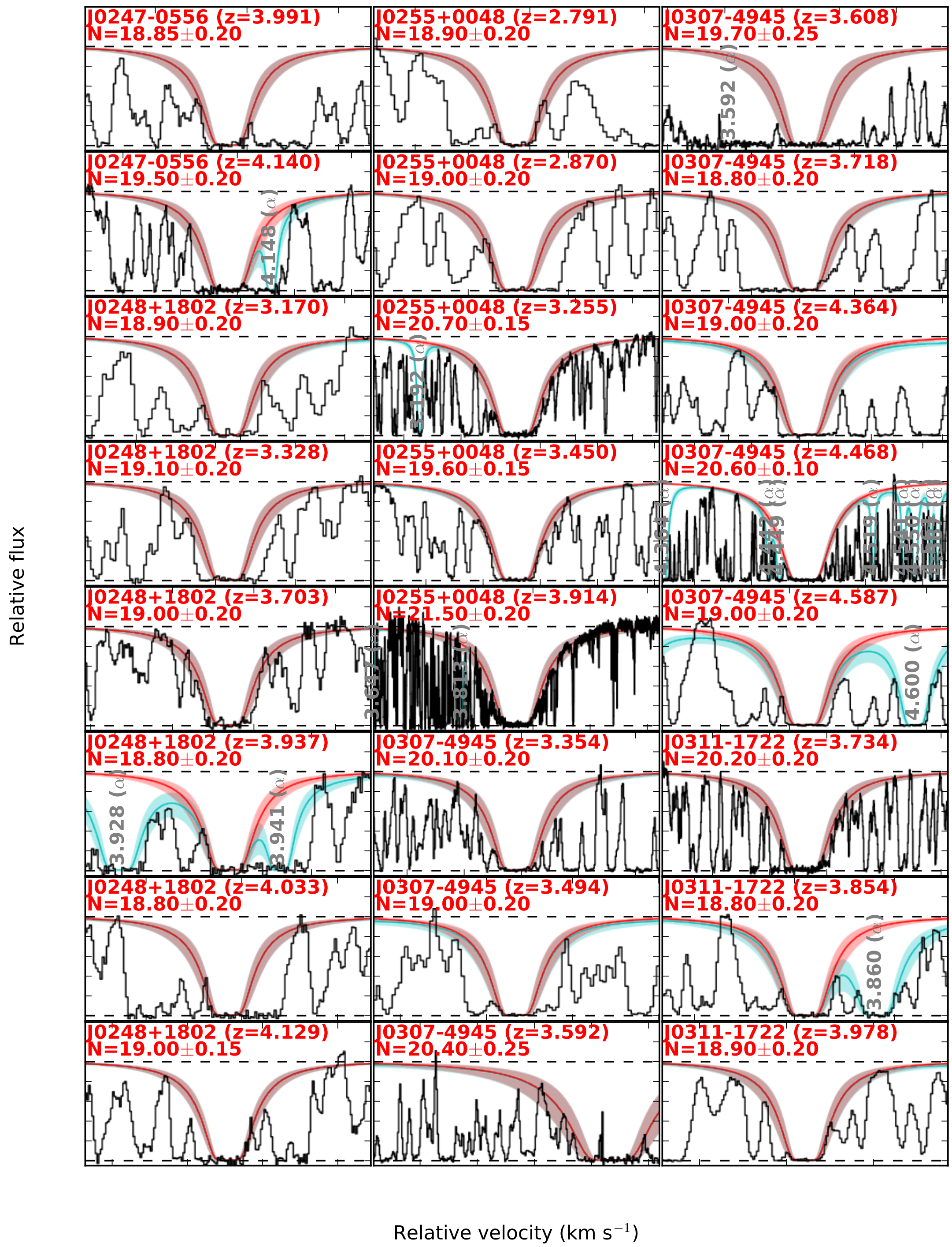

Figure A.5 The velocity profiles for the Lyα absorption lines of subDLAs and DLAs identified in the XQ-100 spectra. The notation is the same as Figure A.1.

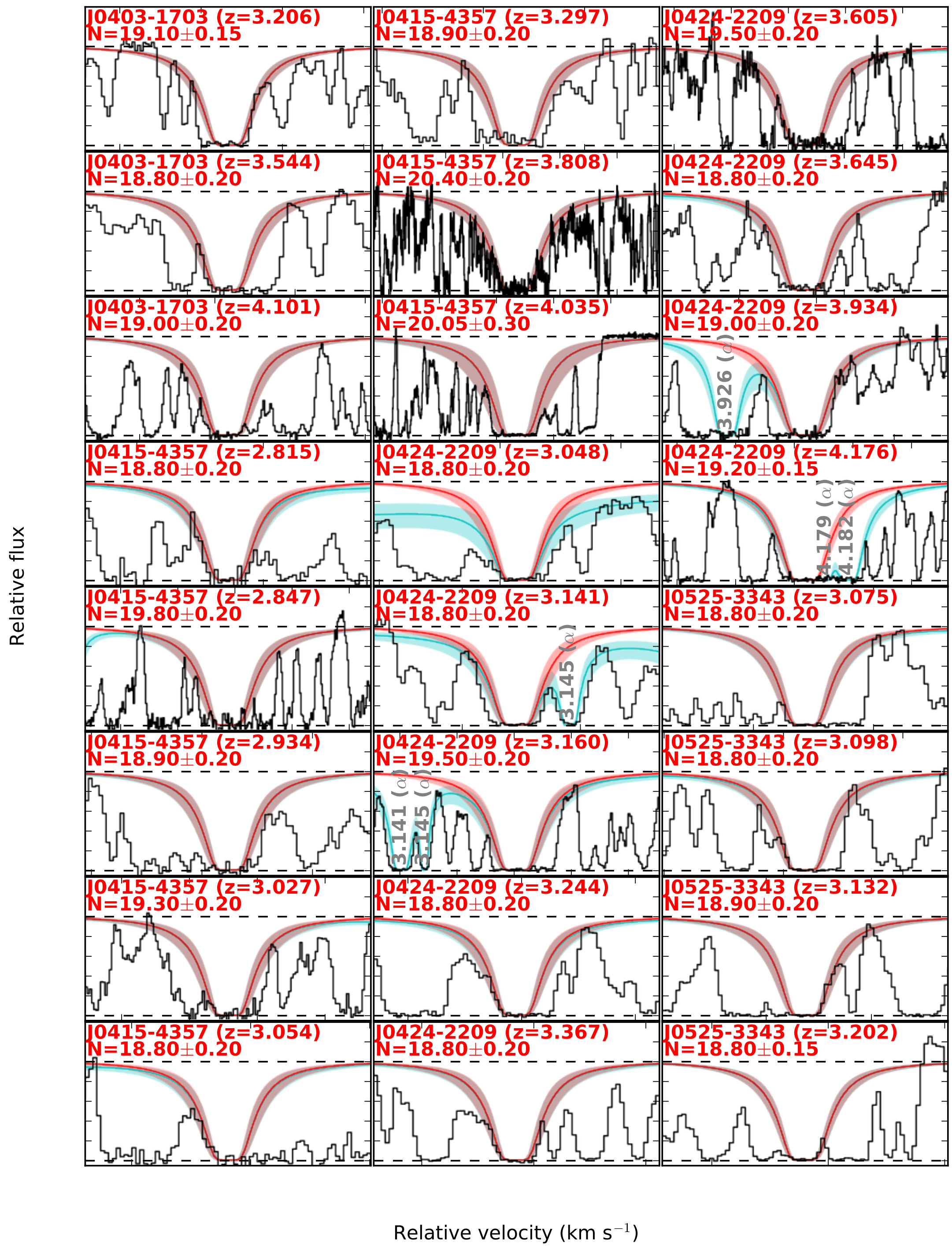

Figure A.6 The velocity profiles for the Lyα absorption lines of subDLAs and DLAs identified in the XQ-100 spectra. The notation is the same as Figure A.1.

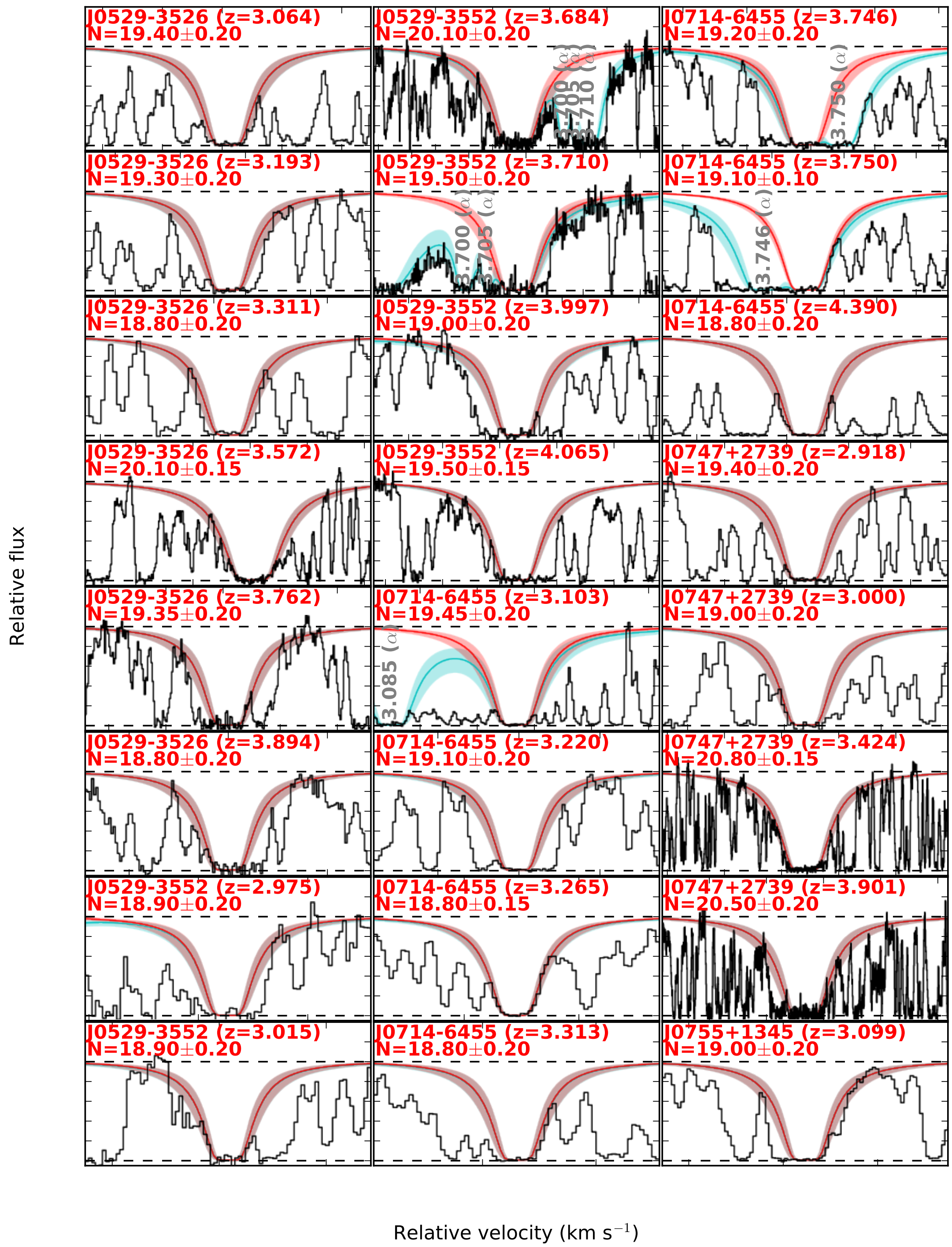

Figure A.7 The velocity profiles for the Lyα absorption lines of subDLAs and DLAs identified in the XQ-100 spectra. The notation is the same as Figure A.1.

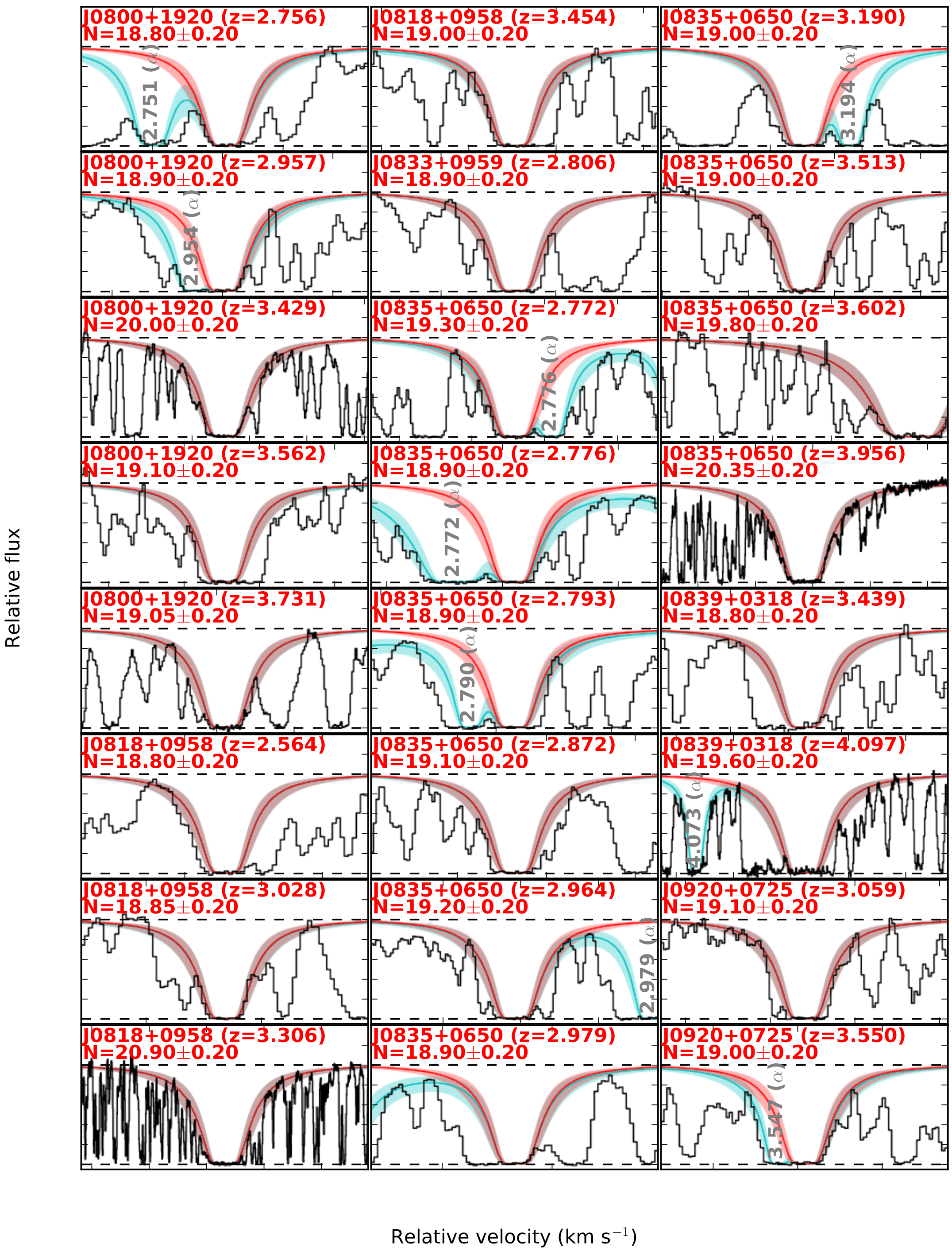

Figure A.8 The velocity profiles for the Lyα absorption lines of subDLAs and DLAs identified in the XQ-100 spectra. The notation is the same as Figure A.1.

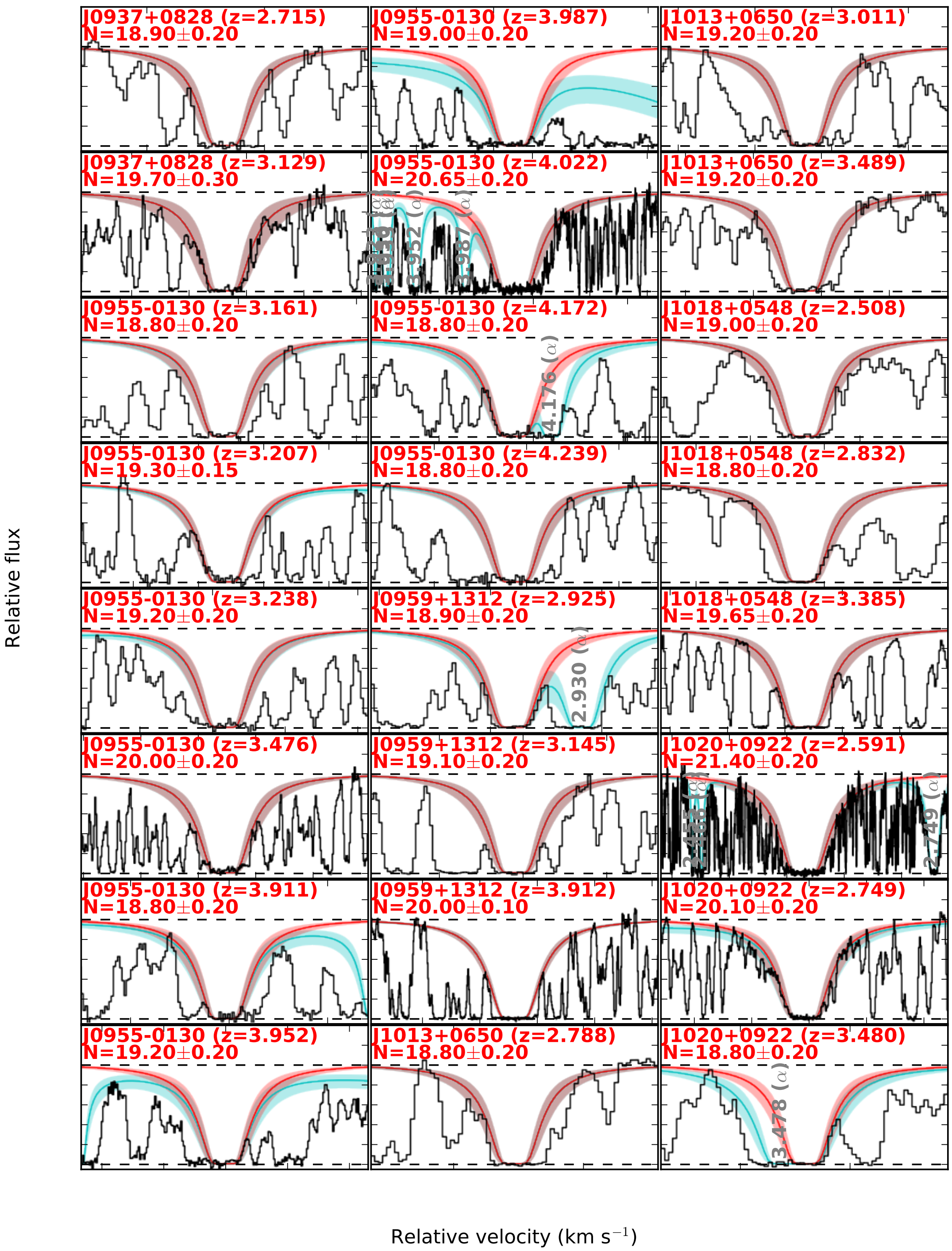

Figure A.9 The velocity profiles for the Lyα absorption lines of subDLAs and DLAs identified in the XQ-100 spectra. The notation is the same as Figure A.1.

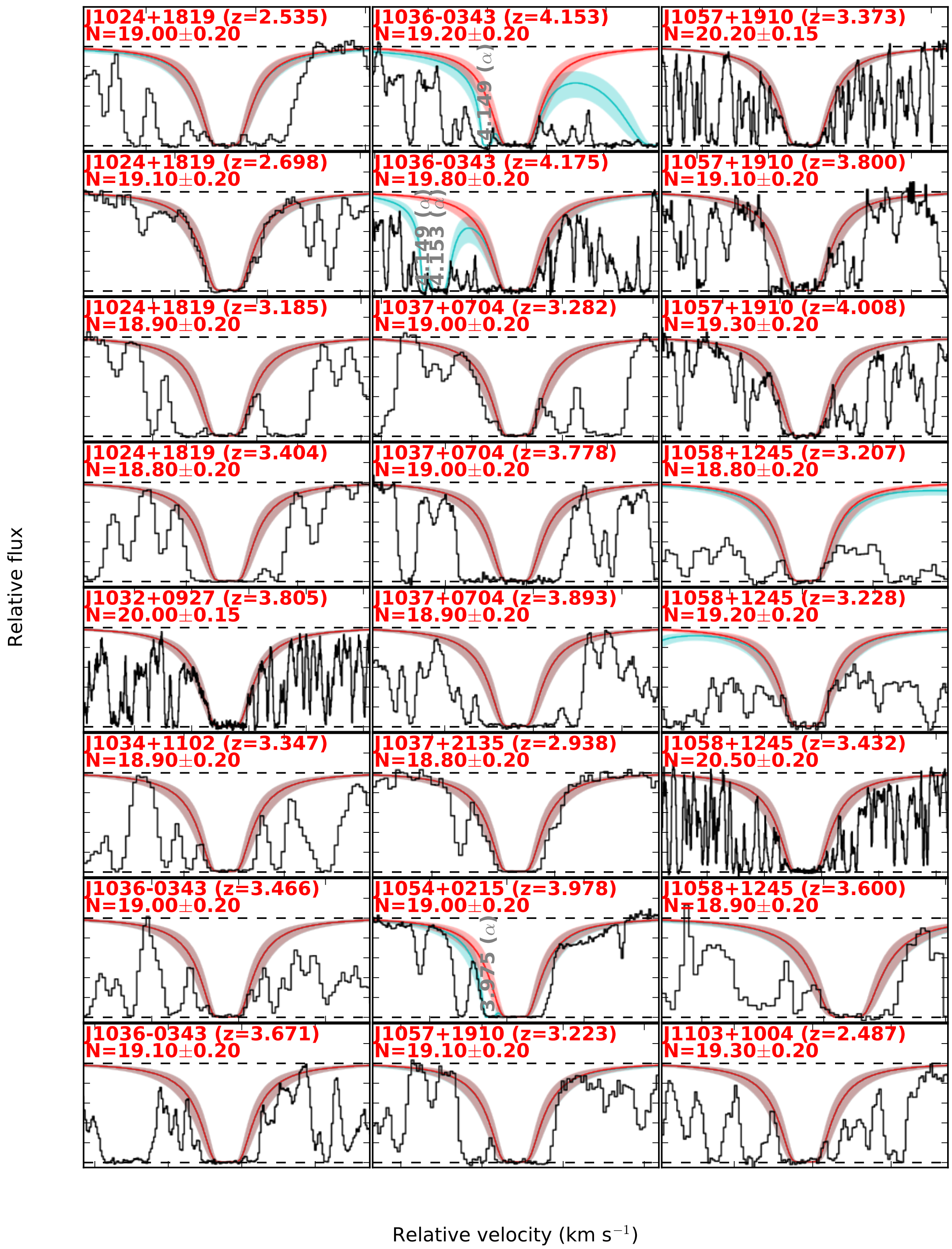

Figure A.10 The velocity profiles for the Lyα absorption lines of subDLAs and DLAs identified in the XQ-100 spectra. The notation is the same as Figure A.1.

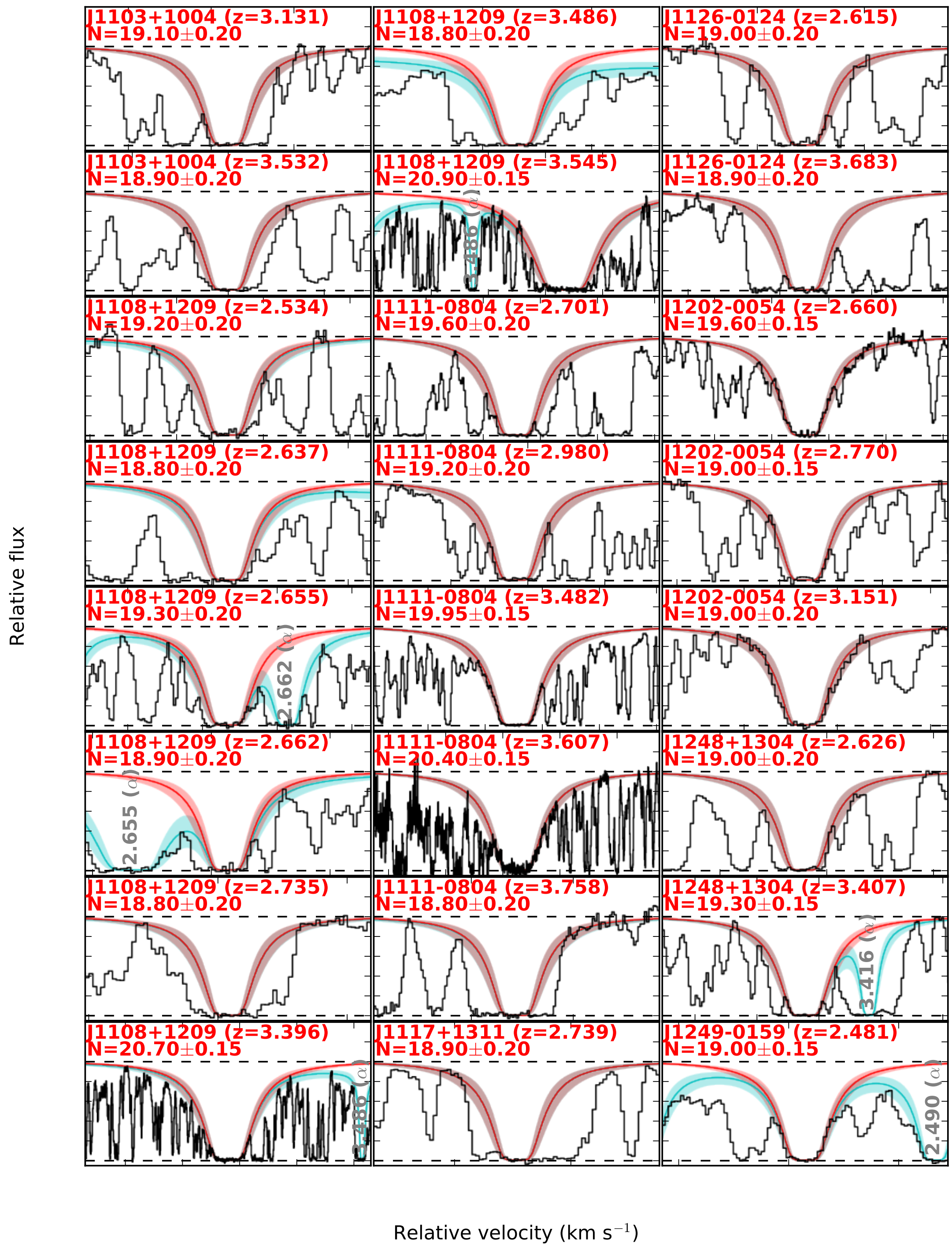

Figure A.11 The velocity profiles for the Lyα absorption lines of subDLAs and DLAs identified in the XQ-100 spectra. The notation is the same as Figure A.1.

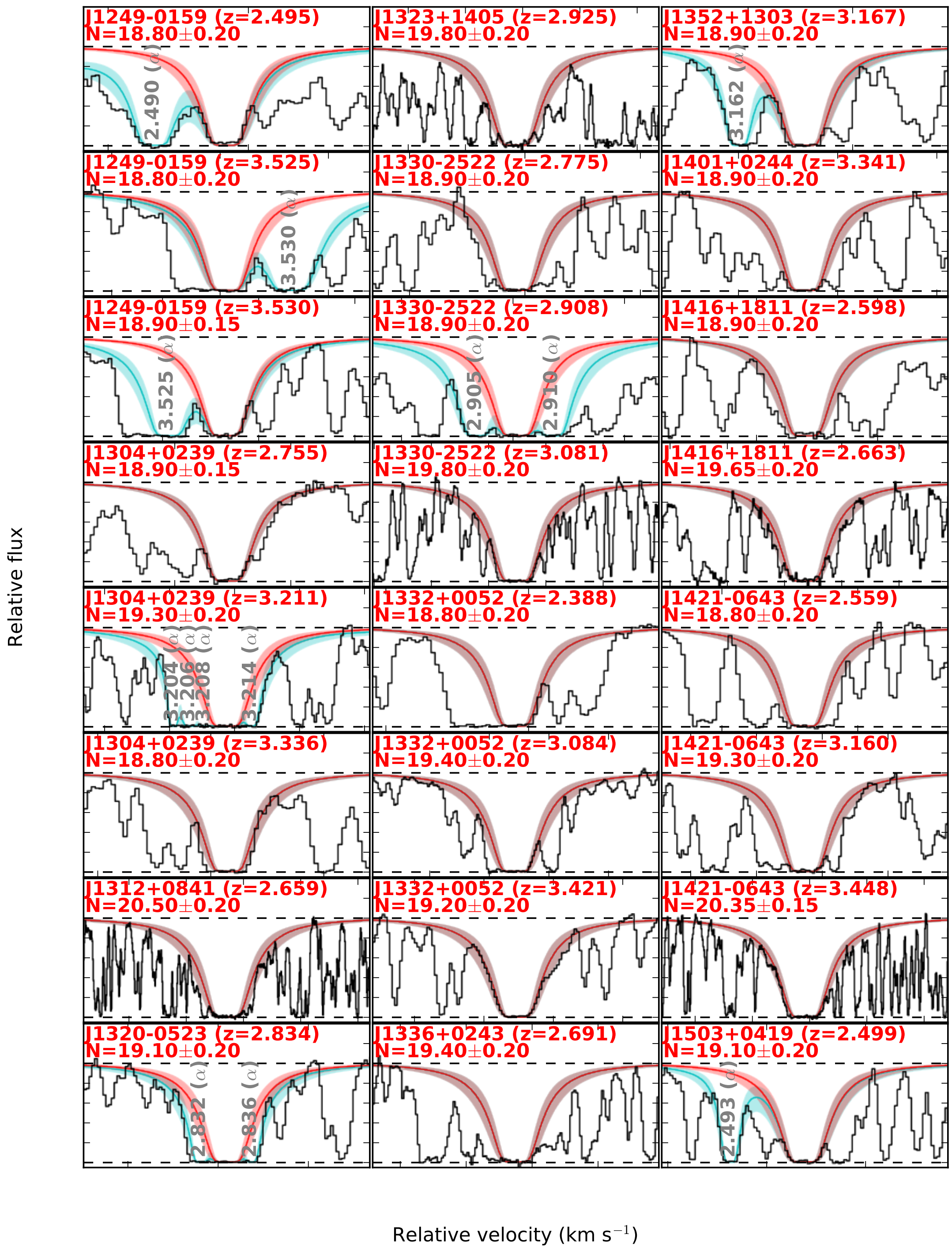

Figure A.12 The velocity profiles for the Lyα absorption lines of subDLAs and DLAs identified in the XQ-100 spectra. The notation is the same as Figure A.1.

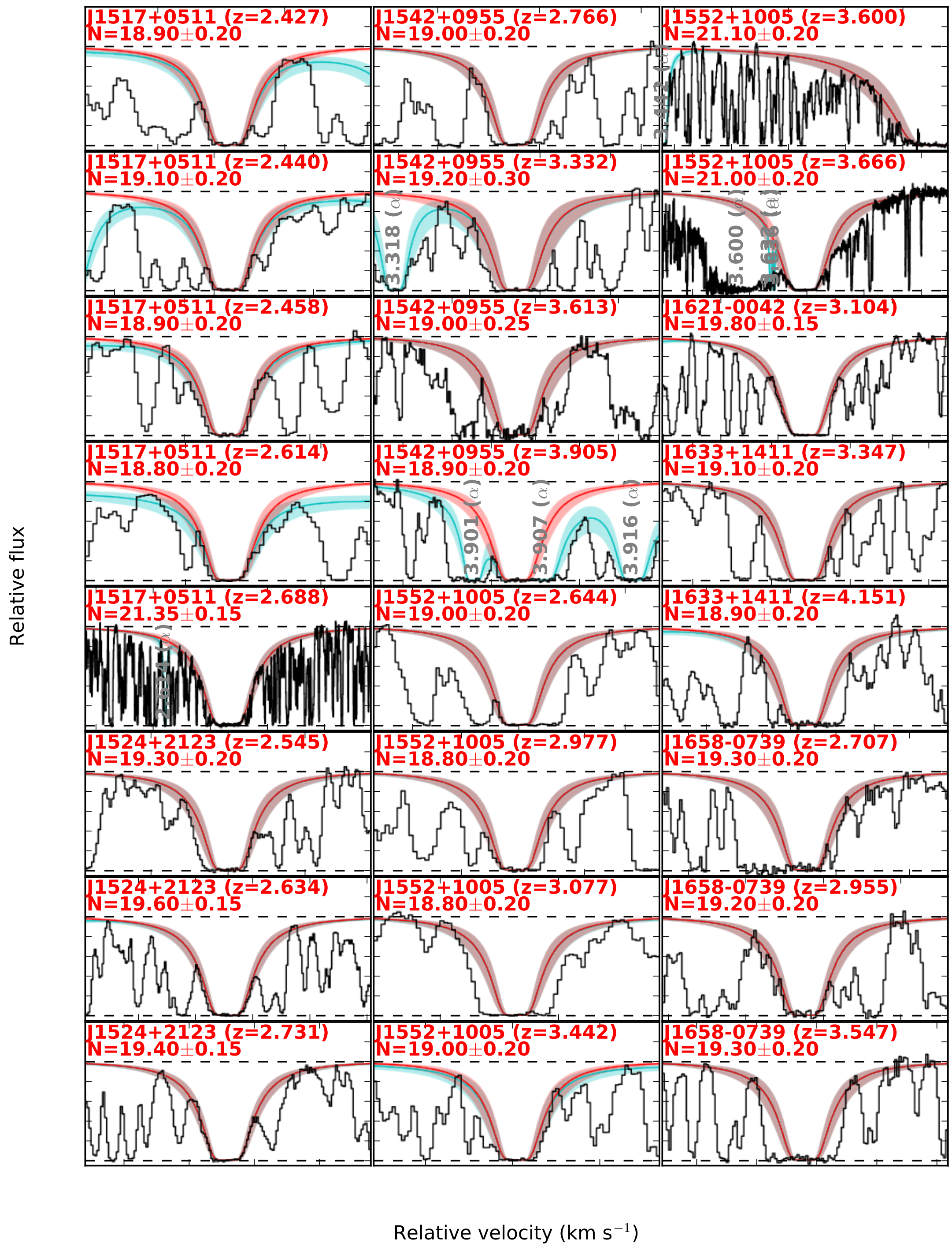

Figure A.13 The velocity profiles for the Lyα absorption lines of subDLAs and DLAs identified in the XQ-100 spectra. The notation is the same as Figure A.1.

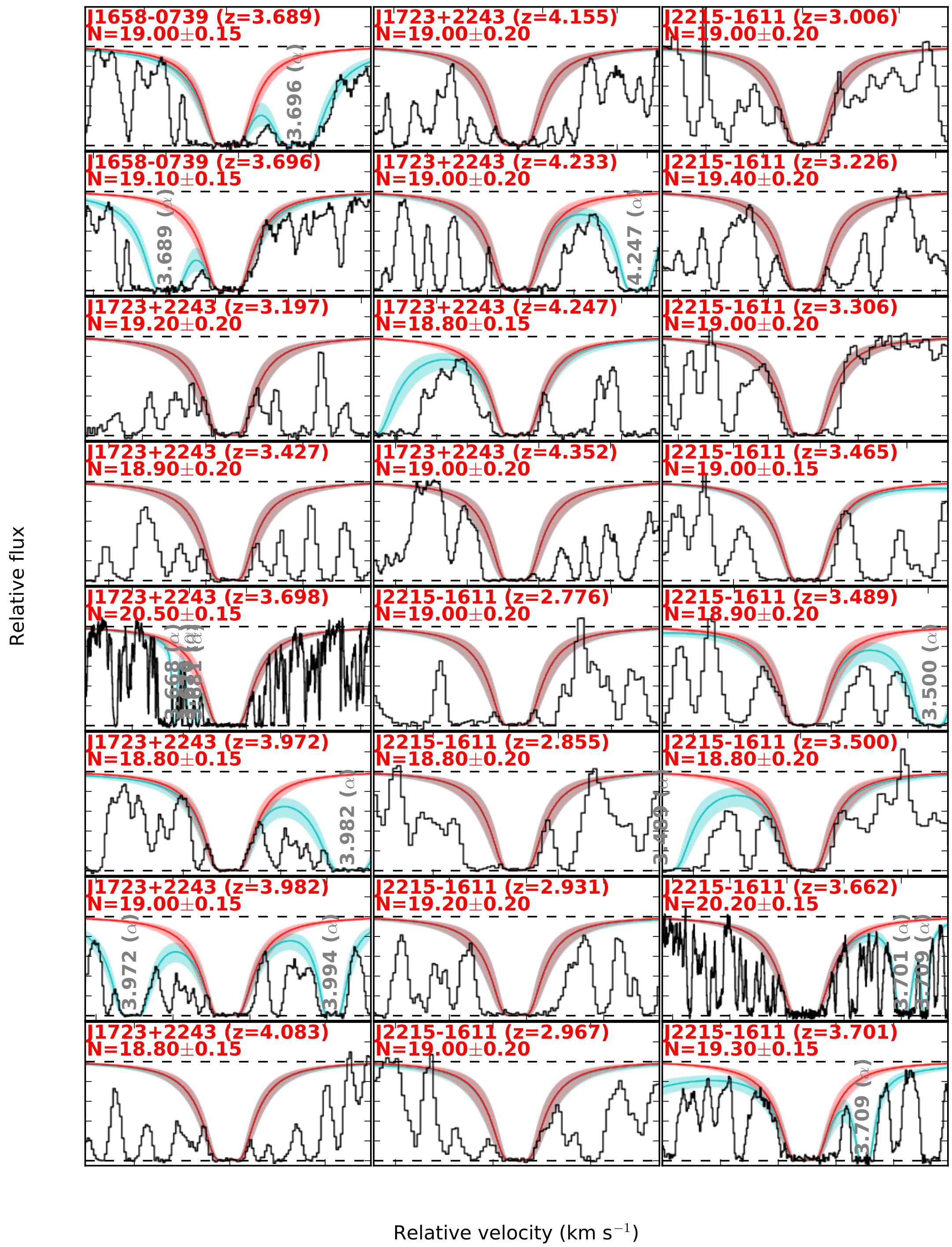

Figure A.14 The velocity profiles for the Lyα absorption lines of subDLAs and DLAs identified in the XQ-100 spectra. The notation is the same as Figure A.1.

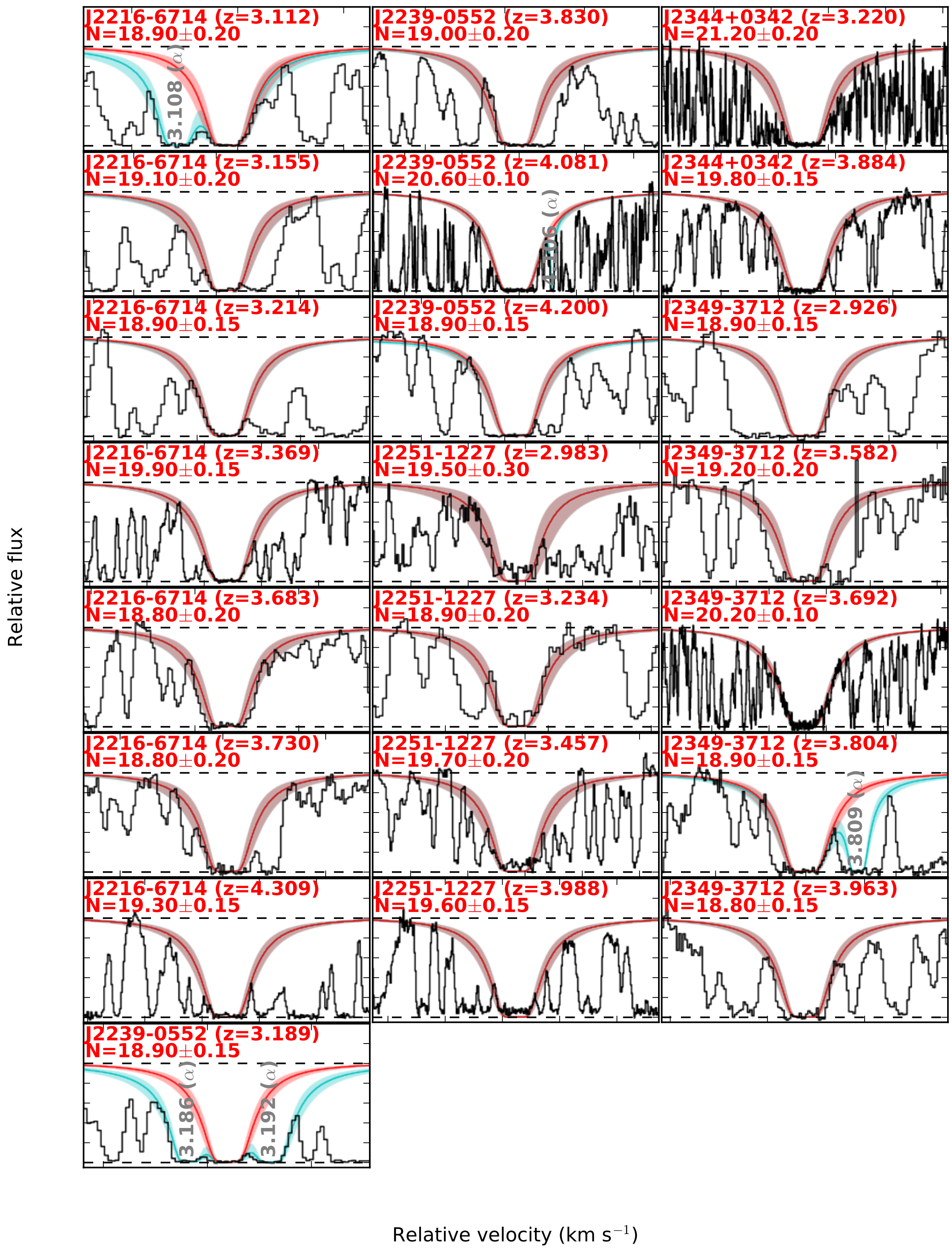

Figure A.15 The velocity profiles for the Lyα absorption lines of subDLAs and DLAs identified in the XQ-100 spectra. The notation is the same as Figure A.1.

Appendix B

Metal line velocity profiles and column density tables of the XQ-100 DLA sample

This appendix contains the measured column densities of metal species for the XQ-100 DLA sample (see Chapter 3). Section B.1 presents the data derived using the X-Shooter spectra, while Section B.2 presents the UVES spectra from the single sightline J0034-1639. Lastly, Section B.3 discusses the discrepancies between the metal column densities from XQ-100 and those previously measured in the literature.

B.1 XQ-100 sample

Table B.1 X-Shooter metal column densities for J0006−6208 (z_{abs}=3.203)

Ion	Line	λ Å	f	v_{min} km s^{-1}	v_{max} km s^{-1}	logN(X)	Included	$logN_{adopt}$
MgI	2852	2852.964	1.81E+00	-60	60	< 12.39	Y	–
MgI								< 12.39
MgII	2796	2796.352	6.12E-01	-90	70	13.33 ± 0.00	Y	–
MgII	2803	2803.531	3.05E-01	-90	70	< 13.63	N	–
MgII								13.33 ± 0.05
CaII	3934	3934.777	6.50E-01	-40	40	< 12.38	Y	–
CaII	3969	3969.591	3.22E-01	-60	60	< 12.14	N	–
CaII								< 12.38
TiII	1910	1910.750	2.02E-01	-40	40	< 13.02	Y	–
TiII								< 13.02
CrII	2056	2056.254	1.05E-01	-50	50	< 13.08	Y	–
CrII	2062	2062.234	7.80E-02	-50	50	< 13.45	N	–
CrII	2066	2066.161	5.15E-02	-50	50	< 13.61	N	–
CrII								< 13.08
FeII	1608	1608.451	5.80E-02	-60	60	13.85 ± 0.03	Y	–
FeII	1611	1611.200	1.36E-03	-60	60	< 14.99	N	–
FeII	2586	2586.650	6.91E-02	-70	80	13.74 ± 0.00	Y	–
FeII	2600	2600.173	2.39E-01	-70	80	> 13.67	Y	–
FeII								13.74 ± 0.05
NiII	1709	1709.604	3.24E-02	-20	80	< 13.86	Y	–
NiII	1741	1741.553	4.27E-02	-60	60	< 13.61	Y	–
NiII	1751	1751.916	2.77E-02	-60	60	< 13.77	Y	–
NiII								< 13.61
ZnII	2026	2026.136	4.89E-01	-50	50	< 12.40	Y	–
ZnII								< 12.40

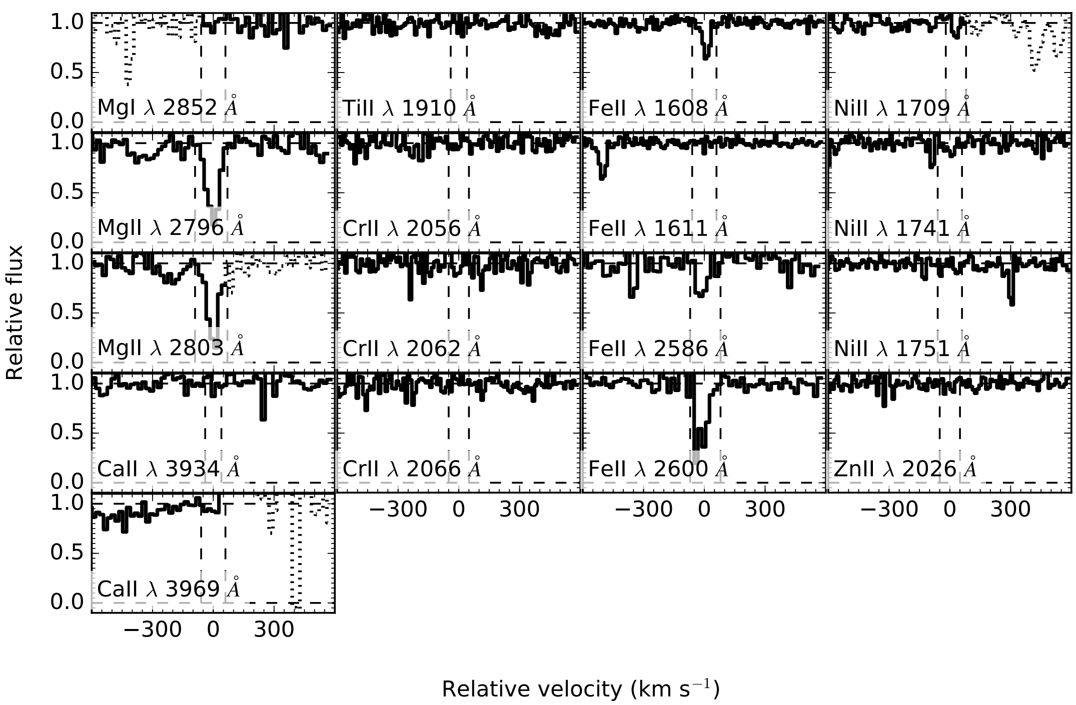

Figure B.1 Velocity profile of the XQ100 spectrum towards J0006-6208 (z_{abs}=3.203).

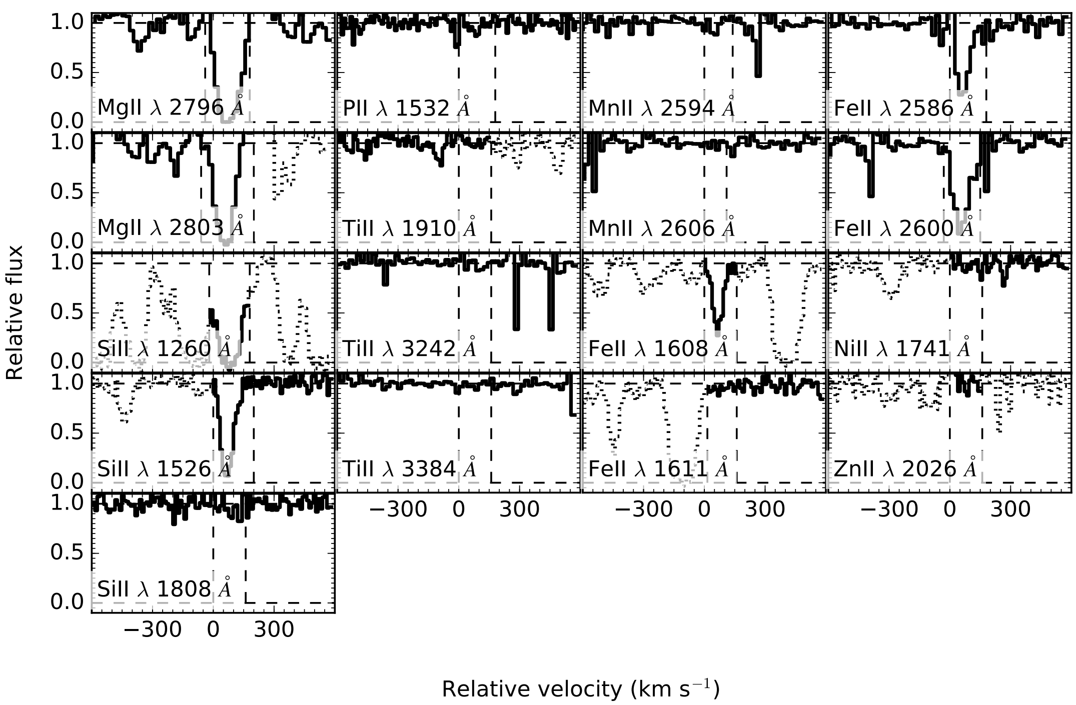

Figure B.2 Velocity profile of the XQ100 spectrum towards J0006-6208 (z_{abs}=3.775).

Table B.2 X-Shooter metal column densities for J0006−6208 (z_{abs}=3.775)

Ion	Line	λ Å	f	v_{min} km s^{-1}	v_{max} km s^{-1}	logN(X)	Included	$\log N_{adopt}$
MgII	2796	2796.352	6.12E-01	-40	180	$>$ 14.01	N	–
MgII	2803	2803.531	3.05E-01	-60	200	$>$ 14.01	Y	–
MgII								$>$ 14.01
SiII	1260	1260.422	1.01E+00	-20	180	$>$ 13.95	N	–
SiII	1526	1526.707	1.27E-01	0	200	$>$ 14.47	Y	–
SiII	1808	1808.013	2.19E-03	0	160	$<$ 15.16	Y	–
SiII								14.46–15.16
PII	1532	1532.533	7.61E-03	0	180	$<$ 14.49	Y	–
PII								$<$ 14.49
TiII	1910	1910.750	2.02E-01	0	160	$<$ 12.75	N	–
TiII	3242	3242.929	2.32E-01	0	160	$<$ 12.75	N	–
TiII	3384	3384.740	3.58E-01	0	160	$<$ 12.30	Y	–
TiII								$<$ 12.30
CrII	2056	2056.254	1.05E-01	-20	180	$<$ 15.31	Y	–
CrII								$<$ 15.31
MnII	2594	2594.499	2.71E-01	0	140	12.51 ± 0.00	Y	–
MnII	2606	2606.462	1.93E-01	0	110	$>$ 12.25	N	–
MnII								12.51 ± 0.05
FeII	1608	1608.451	5.80E-02	0	160	$>$ 14.39	Y	–
FeII	1611	1611.200	1.36E-03	15	160	$<$ 15.12	Y	–
FeII	2586	2586.650	6.91E-02	0	180	$>$ 14.26	Y	–
FeII	2600	2600.173	2.39E-01	-30	150	$>$ 13.96	N	–
FeII								14.40–15.12
NiII	1741	1741.553	4.27E-02	0	160	$<$ 13.54	Y	–
NiII								$<$ 13.54
ZnII	2026	2026.136	4.89E-01	0	160	$<$ 12.69	Y	–
ZnII								$<$ 12.69

Table B.3 X-Shooter metal column densities for J0034+1639 (z_{abs}=3.755)

Ion	Line	λ Å	f	v_{min} km s^{-1}	v_{max} km s^{-1}	logN(X)	Included	$\log N_{adopt}$
MgII	2796	2796.352	6.12E-01	-180	0	> 13.36	N	–
MgII	2803	2803.531	3.05E-01	-140	0	> 13.63	Y	–
MgII								> 13.63
SiII	1526	1526.707	1.27E-01	-140	0	> 14.05	Y	–
SiII	1808	1808.013	2.19E-03	-140	0	< 14.55	Y	–
SiII								14.05–14.55
TiII	1910	1910.750	2.02E-01	-140	0	< 12.83	N	–
TiII	3242	3242.929	2.32E-01	-140	0	< 12.31	Y	–
TiII	3384	3384.740	3.58E-01	-140	0	< 12.50	N	–
TiII								< 12.31
CrII	2062	2062.234	7.80E-02	-140	0	< 13.70	Y	–
CrII	2066	2066.161	5.15E-02	-140	0	< 15.03	N	–
CrII								< 13.70
MnII	2576	2576.877	3.51E-01	-140	0	< 12.49	Y	–
MnII	2594	2594.499	2.71E-01	-140	0	< 12.48	Y	–
MnII								< 12.48
FeII	2249	2249.877	1.82E-03	-140	0	< 14.96	N	–
FeII	2344	2344.214	1.14E-01	-140	0	13.66 ± 0.03	Y	–
FeII	2586	2586.650	6.91E-02	-140	-20	13.69 ± 0.04	Y	–
FeII	2600	2600.173	2.39E-01	-140	5	> 13.57	Y	–
FeII								13.67 ± 0.05
NiII	1709	1709.604	3.24E-02	-140	0	< 13.38	N	–
NiII	1741	1741.553	4.27E-02	-140	0	< 13.38	Y	–
NiII	1751	1751.916	2.77E-02	-140	0	< 13.44	N	–
NiII								< 13.38
ZnII	2026	2026.136	4.89E-01	-140	0	< 12.39	Y	–
ZnII	2062	2062.664	2.56E-01	-140	0	< 12.69	N	–
ZnII								< 12.39

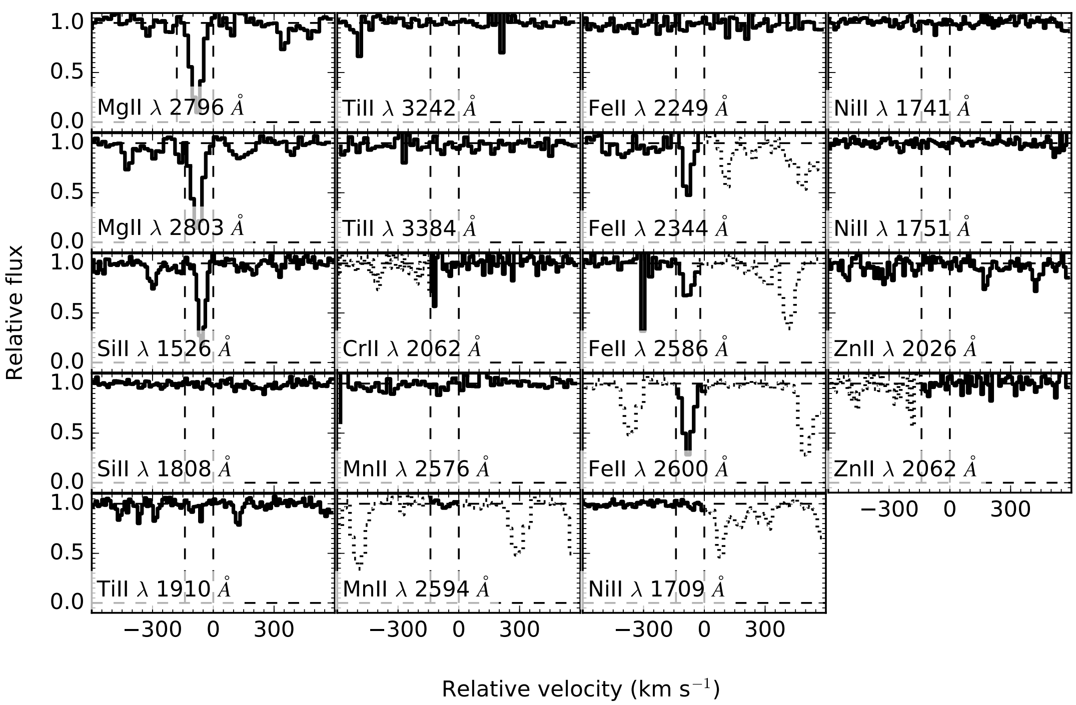

Figure B.3 Velocity profile of the XQ100 spectrum towards J0034+1639 (z_{abs}=3.755).

Table B.4 X-Shooter metal column densities for J0034+1639 (z_{abs}=4.284)

Ion	Line	λ Å	f	v_{min} km s^{-1}	v_{max} km s^{-1}	logN(X)	Included	$\log N_{adopt}$
CII	1334	1334.532	1.28E-01	-60	110	> 14.87	Y	–
CII								> 14.87
OI	1302	1302.168	4.89E-02	-60	110	> 15.17	N	–
OI								0.00 ± 0.05
MgI	2852	2852.964	1.81E+00	-70	90	12.13 ± 0.05	Y	–
MgI								12.13 ± 0.05
MgII	2803	2803.531	3.05E-01	-60	90	< 14.03	N	–
MgII								0.00 ± 0.05
SiII	1260	1260.422	1.01E+00	-50	150	> 13.99	N	–
SiII	1304	1304.370	9.40E-02	-50	110	> 14.72	N	–
SiII	1526	1526.707	1.27E-01	-50	110	> 14.61	Y	–
SiII								> 14.61
SII	1250	1250.584	5.43E-03	-40	20	14.30 ± 0.07	Y	–
SII	1259	1259.519	1.66E-02	-50	30	14.31 ± 0.03	Y	–
SII								14.31 ± 0.08
TiII	1910	1910.750	2.02E-01	-30	110	< 13.20	N	–
TiII	3073	3073.877	1.09E-01	-30	110	< 12.81	N	–
TiII	3242	3242.929	2.32E-01	-30	110	< 12.27	Y	–
TiII	3384	3384.740	3.58E-01	-30	110	< 12.59	N	–
TiII								< 12.27
CrII	2056	2056.254	1.05E-01	-50	110	< 13.21	Y	–
CrII	2062	2062.234	7.80E-02	-50	110	< 13.99	N	–
CrII	2066	2066.161	5.15E-02	-50	110	< 13.45	N	–
CrII								< 13.21
FeII	1608	1608.451	5.80E-02	-70	110	14.45 ± 0.01	Y	–
FeII	1611	1611.200	1.36E-03	-40	20	< 14.80	N	–
FeII	2249	2249.877	1.82E-03	-50	110	< 14.84	N	–
FeII	2344	2344.214	1.14E-01	-70	110	> 14.17	N	–
FeII	2374	2374.461	3.13E-02	-70	110	14.41 ± 0.02	Y	–
FeII								14.44 ± 0.05
NiII	1741	1741.553	4.27E-02	-70	110	< 13.56	Y	–
NiII	1751	1751.916	2.77E-02	-70	110	< 13.61	N	–
NiII								< 13.56
ZnII	2026	2026.136	4.89E-01	-70	110	< 12.81	Y	–
ZnII								< 12.81

Table B.5 X-Shooter metal column densities for J0034+1639 (z_{abs}=4.252)

Ion	Line	λ Å	f	v_{min} km s^{-1}	v_{max} km s^{-1}	logN(X)	Included	$logN_{adopt}$
CII	1334	1334.532	1.28E-01	-60	70	> 14.29	Y	–
CII								> 14.29
OI	1302	1302.168	4.89E-02	-60	70	> 14.71	Y	–
OI								> 14.71
MgII	2796	2796.352	6.12E-01	-100	70	> 13.20	Y	–
MgII	2803	2803.531	3.05E-01	-130	60	> 13.82	N	–
MgII								> 13.20
SiII	1260	1260.422	1.01E+00	-60	70	> 13.51	N	–
SiII	1304	1304.370	9.40E-02	-60	70	13.76 ± 0.03	Y	–
SiII	1526	1526.707	1.27E-01	-60	70	13.67 ± 0.02	Y	–
SiII	1808	1808.013	2.19E-03	-60	40	< 15.42	Y	–
SiII								13.71 ± 0.05
PII	1532	1532.533	7.61E-03	-60	40	< 14.12	Y	–
PII								< 14.12
SII	1250	1250.584	5.43E-03	-60	40	< 14.07	N	–
SII	1253	1253.811	1.09E-02	-60	40	< 13.87	Y	–
SII	1259	1259.519	1.66E-02	-60	40	< 13.79	Y	–
SII								< 13.79
TiII	3073	3073.877	1.09E-01	-60	40	< 12.41	N	–
TiII	3242	3242.929	2.32E-01	-60	40	< 12.71	N	–
TiII	3384	3384.740	3.58E-01	-60	40	< 12.36	Y	–
TiII								< 12.36
CrII	2066	2066.161	5.15E-02	-60	40	< 13.38	Y	–
CrII								< 13.38
FeII	1608	1608.451	5.80E-02	-60	40	13.43 ± 0.11	Y	–
FeII	2344	2344.214	1.14E-01	-60	40	13.35 ± 0.05	Y	–
FeII	2374	2374.461	3.13E-02	-60	40	< 13.33	N	–
FeII								13.36 ± 0.12
NiII	1709	1709.604	3.24E-02	-60	40	< 13.42	Y	–
NiII	1741	1741.553	4.27E-02	-60	40	< 13.41	Y	–
NiII	1751	1751.916	2.77E-02	-60	40	< 13.83	N	–
NiII								< 13.41
ZnII	2026	2026.136	4.89E-01	-60	40	< 12.47	Y	–
ZnII								< 12.47

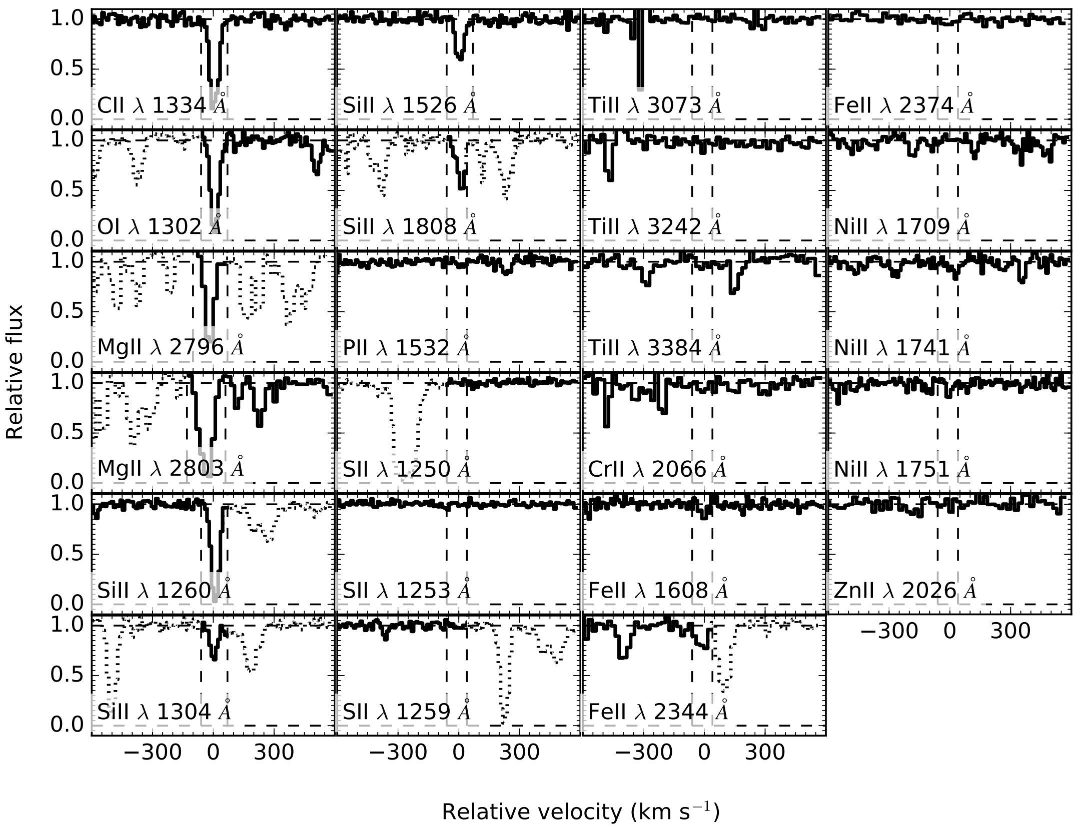

Figure B.4 Velocity profile of the XQ100 spectrum towards J0034+1639 (z_{abs}=4.251).

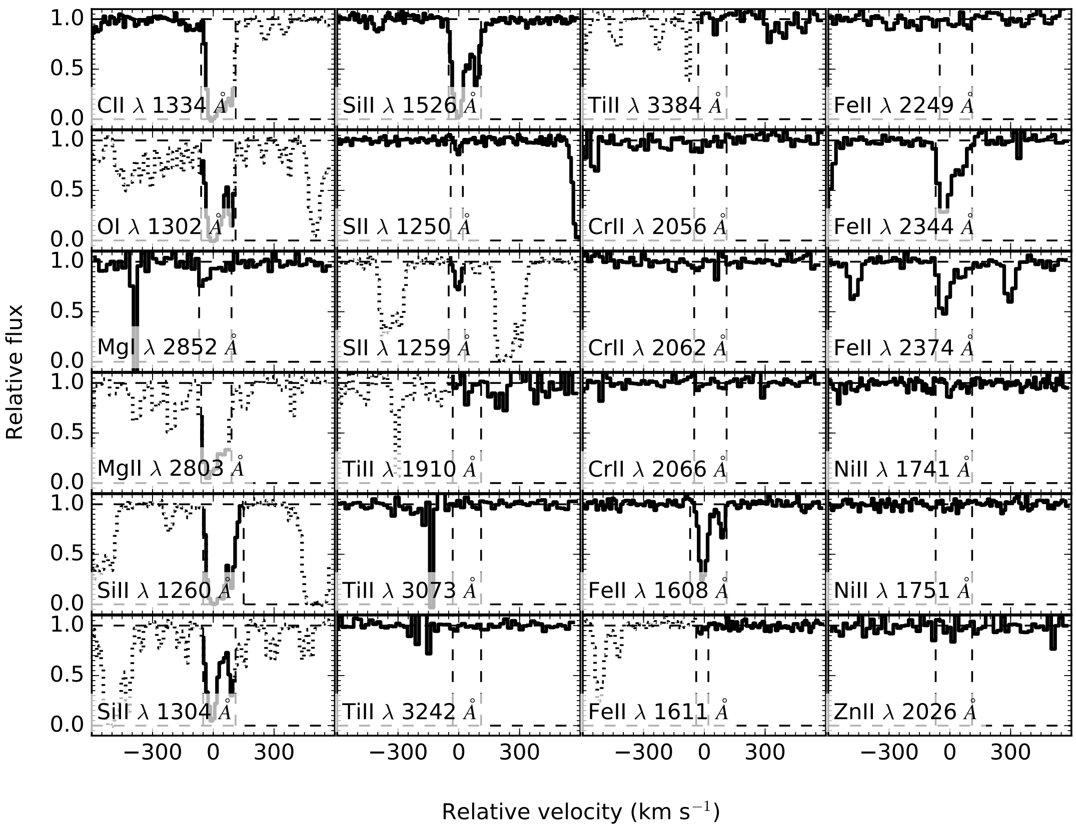

Figure B.5 Velocity profile of the XQ100 spectrum towards J0034+1639 (z_{abs}=4.283).

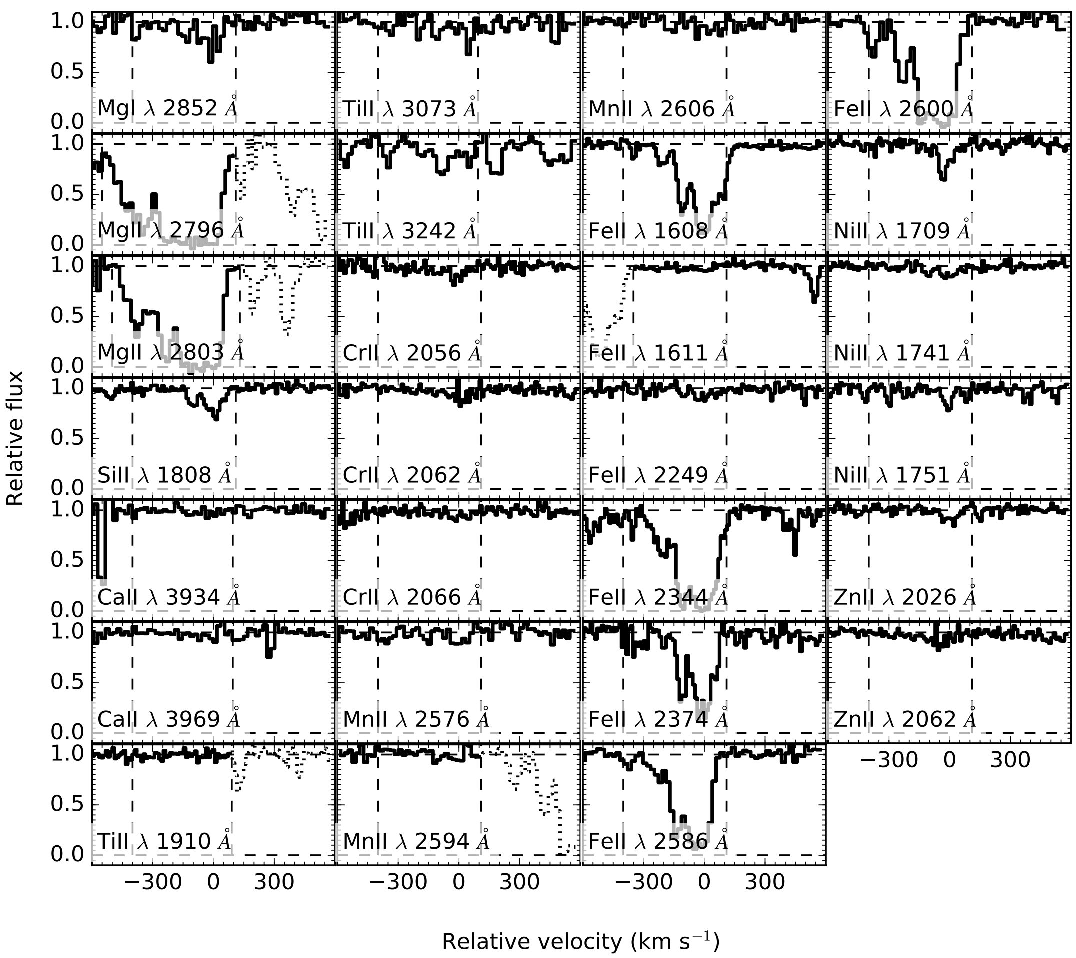

Figure B.6 Velocity profile of the XQ100 spectrum towards J0113-2803 (z_{abs}=3.106).

Table B.6 X-Shooter metal column densities for J0113−2803 (z_{abs}=3.106)

Ion	Line	λ Å	f	v_{min} km s^{-1}	v_{max} km s^{-1}	logN(X)	Included	logN_{adopt}
MgI	2852	2852.964	1.81E+00	-400	110	12.60 ± 0.06	Y	–
MgI								12.60 ± 0.06
MgII	2796	2796.352	6.12E-01	-550	110	> 14.42	Y	–
MgII	2803	2803.531	3.05E-01	-500	130	> 14.55	Y	–
MgII								> 14.55
SiII	1808	1808.013	2.19E-03	-400	110	15.60 ± 0.02	Y	–
SiII								15.60 ± 0.05
CaII	3934	3934.777	6.50E-01	-400	95	< 11.94	Y	–
CaII	3969	3969.591	3.22E-01	-400	95	< 12.35	N	–
CaII								< 11.94
TiII	1910	1910.750	2.02E-01	-400	90	< 12.61	Y	–
TiII	3073	3073.877	1.09E-01	-400	95	< 13.30	N	–
TiII	3242	3242.929	2.32E-01	-400	95	< 12.98	N	–
TiII								< 12.61
CrII	2056	2056.254	1.05E-01	-400	110	13.62 ± 0.04	Y	–
CrII	2062	2062.234	7.80E-02	-400	110	13.72 ± 0.06	Y	–
CrII	2066	2066.161	5.15E-02	-400	110	13.77 ± 0.06	Y	–
CrII								13.69 ± 0.09
MnII	2576	2576.877	3.51E-01	-400	110	13.00 ± 0.07	N	–
MnII	2594	2594.499	2.71E-01	-400	110	< 12.63	Y	–
MnII	2606	2606.462	1.93E-01	-400	110	13.21 ± 0.09	N	–
MnII								< 12.63
FeII	1608	1608.451	5.80E-02	-400	110	> 15.08	N	–
FeII	1611	1611.200	1.36E-03	-350	110	15.27 ± 0.06	N	–
FeII	2249	2249.877	1.82E-03	-400	110	15.29 ± 0.05	Y	–
FeII	2344	2344.214	1.14E-01	-400	110	> 14.91	N	–
FeII	2374	2374.461	3.13E-02	-400	110	> 15.06	N	–
FeII	2586	2586.650	6.91E-02	-400	110	> 14.92	N	–
FeII	2600	2600.173	2.39E-01	-400	110	> 14.42	N	–
FeII								15.29 ± 0.05
NiII	1709	1709.604	3.24E-02	-400	110	< 14.37	N	–
NiII	1741	1741.553	4.27E-02	-400	110	13.99 ± 0.04	Y	–
NiII	1751	1751.916	2.77E-02	-400	110	< 14.33	N	–
NiII								13.99 ± 0.05
ZnII	2026	2026.136	4.89E-01	-400	110	12.69 ± 0.05	Y	–
ZnII	2062	2062.664	2.56E-01	-400	110	13.21 ± 0.06	N	–
ZnII								12.69 ± 0.05

Table B.7 X-Shooter metal column densities for J0124+0044 (z_{abs}=2.261)

Ion	Line	λ Å	f	v_{min} km s^{-1}	v_{max} km s^{-1}	logN(X)	Included	$\log N_{adopt}$
MgI	2852	2852.964	1.81E+00	-80	190	12.50 ± 0.02	Y	–
MgI								12.50 ± 0.05
MgII	2796	2796.352	6.12E-01	-80	190	> 14.00	N	–
MgII	2803	2803.531	3.05E-01	-80	190	> 14.31	Y	–
MgII								> 14.31
SiII	1808	1808.013	2.19E-03	-80	190	15.36 ± 0.02	Y	–
SiII								15.36 ± 0.05
CaII	3934	3934.777	6.50E-01	-80	190	< 11.94	Y	–
CaII	3969	3969.591	3.22E-01	-80	190	< 12.29	N	–
CaII								< 11.94
TiII	1910	1910.750	2.02E-01	-80	190	< 12.74	N	–
TiII	3242	3242.929	2.32E-01	-80	190	< 12.58	N	–
TiII	3384	3384.740	3.58E-01	-80	100	12.35 ± 0.08	Y	–
TiII								12.35 ± 0.08
CrII	2056	2056.254	1.05E-01	-80	190	13.38 ± 0.04	Y	–
CrII	2062	2062.234	7.80E-02	-80	190	13.39 ± 0.05	Y	–
CrII	2066	2066.161	5.15E-02	-80	190	13.44 ± 0.07	Y	–
CrII								13.40 ± 0.09
MnII	2576	2576.877	3.51E-01	-80	190	12.70 ± 0.05	Y	–
MnII	2594	2594.499	2.71E-01	-80	190	12.80 ± 0.06	Y	–
MnII	2606	2606.462	1.93E-01	-80	190	12.83 ± 0.07	Y	–
MnII								12.77 ± 0.11
FeII	2249	2249.877	1.82E-03	-80	190	14.96 ± 0.05	Y	–
FeII	2374	2374.461	3.13E-02	-80	190	> 14.77	N	–
FeII	2586	2586.650	6.91E-02	-80	190	> 14.56	N	–
FeII	2600	2600.173	2.39E-01	-100	190	> 14.11	N	–
FeII								14.96 ± 0.05
ZnII	2026	2026.136	4.89E-01	-80	190	12.66 ± 0.05	Y	–
ZnII	2062	2062.664	2.56E-01	-80	190	< 12.91	N	–
ZnII								12.66 ± 0.05

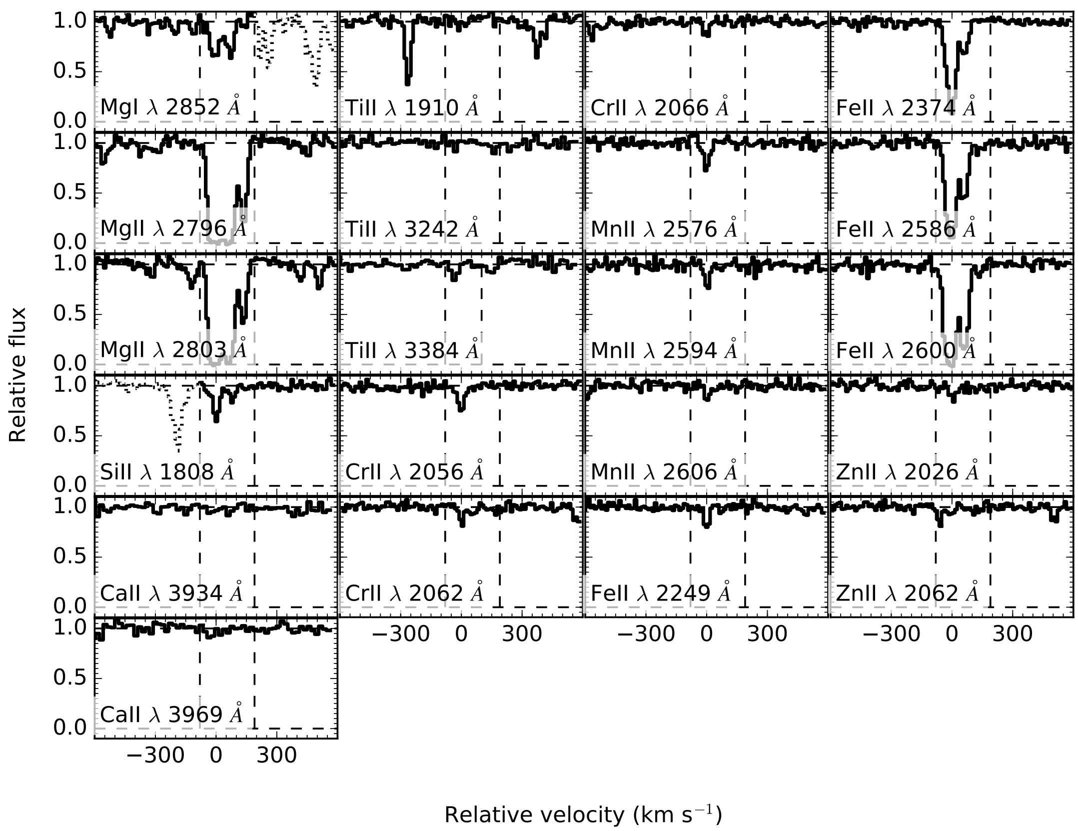

Figure B.7 Velocity profile of the XQ100 spectrum towards J0124+0044 (z_{abs}=2.261).

Table B.8 X-Shooter metal column densities for J0132+1341 (z_{abs}=3.936)

Ion	Line	λ Å	f	v_{min} km s^{-1}	v_{max} km s^{-1}	logN(X)	Included	$\log N_{adopt}$
CII	1334	1334.532	1.28E-01	-70	110	> 14.39	Y	–
CII								> 14.39
OI	1302	1302.168	4.89E-02	-50	65	> 14.77	Y	–
OI								> 14.77
SiII	1304	1304.370	9.40E-02	-50	60	13.87 ± 0.02	Y	–
SiII	1526	1526.707	1.27E-01	-40	70	13.87 ± 0.02	Y	–
SiII	1808	1808.013	2.19E-03	-40	70	< 14.72	N	–
SiII								13.87 ± 0.05
PII	1532	1532.533	7.61E-03	-15	70	< 13.98	Y	–
PII								< 13.98
TiII	3073	3073.877	1.09E-01	-40	70	< 12.74	N	–
TiII	3242	3242.929	2.32E-01	-40	70	< 12.36	Y	–
TiII								< 12.36
MnII	2576	2576.877	3.51E-01	-40	70	< 12.96	N	–
MnII	2606	2606.462	1.93E-01	-20	50	< 12.46	Y	–
MnII								< 12.46
FeII	1608	1608.451	5.80E-02	-40	50	13.71 ± 0.02	Y	–
FeII	1611	1611.200	1.36E-03	-20	30	< 14.56	N	–
FeII	2249	2249.877	1.82E-03	-45	50	< 14.92	N	–
FeII	2344	2344.214	1.14E-01	-50	60	13.64 ± 0.03	Y	–
FeII	2374	2374.461	3.13E-02	-40	20	13.63 ± 0.08	Y	–
FeII	2600	2600.173	2.39E-01	-50	60	> 13.34	N	–
FeII								13.68 ± 0.09
NiII	1709	1709.604	3.24E-02	-40	70	< 13.43	N	–
NiII	1741	1741.553	4.27E-02	-40	70	< 13.31	Y	–
NiII	1751	1751.916	2.77E-02	-40	70	< 13.43	N	–
NiII								< 13.31
ZnII	2062	2062.664	2.56E-01	-40	70	< 12.66	Y	–
ZnII								< 12.66

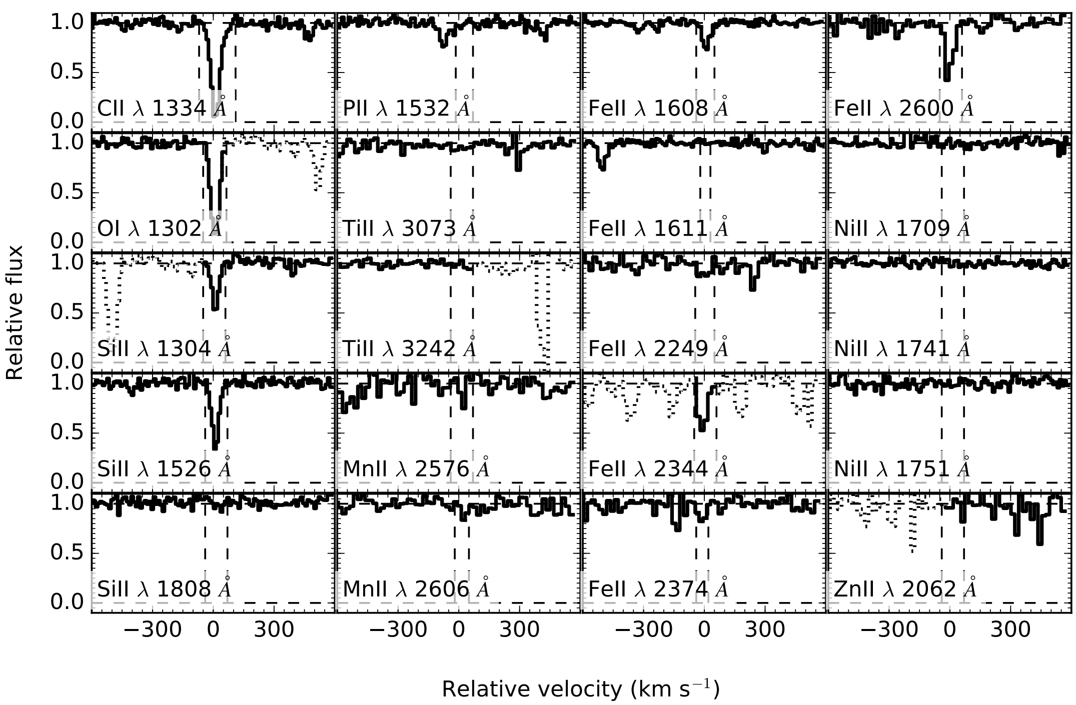

Figure B.8 Velocity profile of the XQ100 spectrum towards J0132+1341 (z_{abs}=3.936).

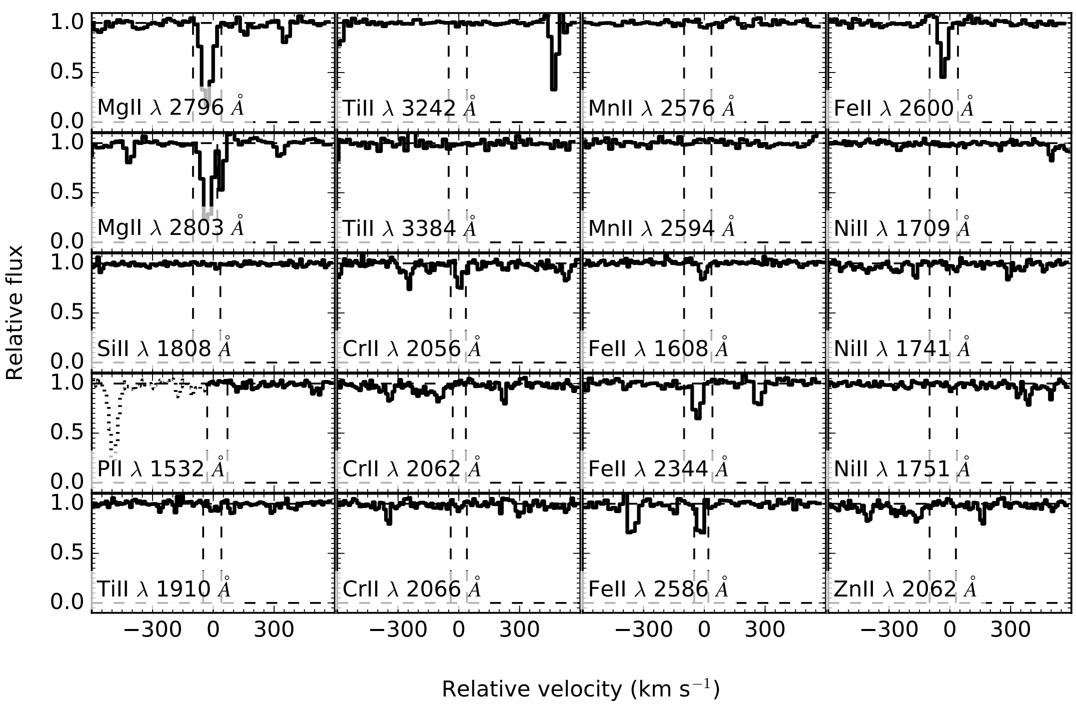

Figure B.9 Velocity profile of the XQ100 spectrum towards J0134+0400 (z_{abs}=3.692).

Table B.9 X-Shooter metal column densities for J0134+0400 (z_{abs}=3.692)

Ion	Line	λ Å	f	v_{min} km s^{-1}	v_{max} km s^{-1}	logN(X)	Included	$\log N_{adopt}$
MgII	2796	2796.352	6.12E-01	-100	40	> 13.26	N	–
MgII	2803	2803.531	3.05E-01	-100	20	> 13.49	Y	–
MgII								> 13.49
SiII	1808	1808.013	2.19E-03	-100	35	< 14.36	Y	–
SiII								< 14.36
PII	1532	1532.533	7.61E-03	-30	70	< 13.73	Y	–
PII								< 13.73
TiII	1910	1910.750	2.02E-01	-50	40	< 12.63	N	–
TiII	3242	3242.929	2.32E-01	-50	40	< 12.24	N	–
TiII	3384	3384.740	3.58E-01	-50	40	< 11.98	Y	–
TiII								< 11.98
CrII	2056	2056.254	1.05E-01	-40	35	< 13.19	Y	–
CrII	2062	2062.234	7.80E-02	-30	35	< 12.75	N	–
CrII	2066	2066.161	5.15E-02	-40	40	< 13.18	Y	–
CrII								< 13.18
MnII	2576	2576.877	3.51E-01	-100	35	< 12.37	N	–
MnII	2594	2594.499	2.71E-01	-100	35	< 12.30	Y	–
MnII								< 12.30
FeII	1608	1608.451	5.80E-02	-100	35	13.40 ± 0.04	Y	–
FeII	2344	2344.214	1.14E-01	-100	40	13.46 ± 0.03	Y	–
FeII	2586	2586.650	6.91E-02	-50	20	13.46 ± 0.11	Y	–
FeII	2600	2600.173	2.39E-01	-100	40	> 13.24	N	–
FeII								13.44 ± 0.12
NiII	1709	1709.604	3.24E-02	-100	35	< 13.08	N	–
NiII	1741	1741.553	4.27E-02	-100	0	< 13.01	Y	–
NiII	1751	1751.916	2.77E-02	-100	35	< 13.43	N	–
NiII								< 13.01
ZnII	2062	2062.664	2.56E-01	-100	30	< 12.35	Y	–
ZnII								< 12.35

Table B.10 X-Shooter metal column densities for J0134+0400 (z_{abs}=3.772)

Ion	Line	λ Å	f	v_{min} km s^{-1}	v_{max} km s^{-1}	logN(X)	Included	$logN_{adopt}$
CII	1334	1334.532	1.28E-01	-160	150	> 15.21	Y	–
CII								> 15.21
MgII	2796	2796.352	6.12E-01	-170	230	> 14.15	N	–
MgII	2803	2803.531	3.05E-01	-200	230	> 14.38	Y	–
MgII								> 14.38
SiII	1526	1526.707	1.27E-01	-170	230	> 14.95	N	–
SiII	1808	1808.013	2.19E-03	-90	230	15.30 ± 0.02	Y	–
SiII								15.30 ± 0.05
PII	1532	1532.533	7.61E-03	-90	230	< 13.94	Y	–
PII								< 13.94
TiII	3242	3242.929	2.32E-01	-100	230	< 12.33	N	–
TiII	3384	3384.740	3.58E-01	-100	230	< 12.21	Y	–
TiII								< 12.21
CrII	2056	2056.254	1.05E-01	-90	25	< 12.83	Y	–
CrII								< 12.83
MnII	2576	2576.877	3.51E-01	-100	230	< 12.39	Y	–
MnII	2594	2594.499	2.71E-01	-100	230	< 12.50	Y	–
MnII	2606	2606.462	1.93E-01	-100	230	< 12.59	Y	–
MnII								< 12.39
FeII	1608	1608.451	5.80E-02	-70	230	> 14.93	N	–
FeII	1611	1611.200	1.36E-03	-90	230	< 15.57	N	–
FeII	2249	2249.877	1.82E-03	-90	230	14.97 ± 0.07	Y	–
FeII	2374	2374.461	3.13E-02	-160	230	> 15.04	N	–
FeII	2586	2586.650	6.91E-02	-160	230	> 14.75	N	–
FeII	2600	2600.173	2.39E-01	-160	230	> 14.55	N	–
FeII								14.97 ± 0.07
NiII	1709	1709.604	3.24E-02	-100	230	13.99 ± 0.03	N	–
NiII	1741	1741.553	4.27E-02	-100	230	13.85 ± 0.03	Y	–
NiII	1751	1751.916	2.77E-02	-100	230	13.80 ± 0.05	Y	–
NiII								13.84 ± 0.06
ZnII	2026	2026.136	4.89E-01	-100	230	12.88 ± 0.04	Y	–
ZnII								12.88 ± 0.05

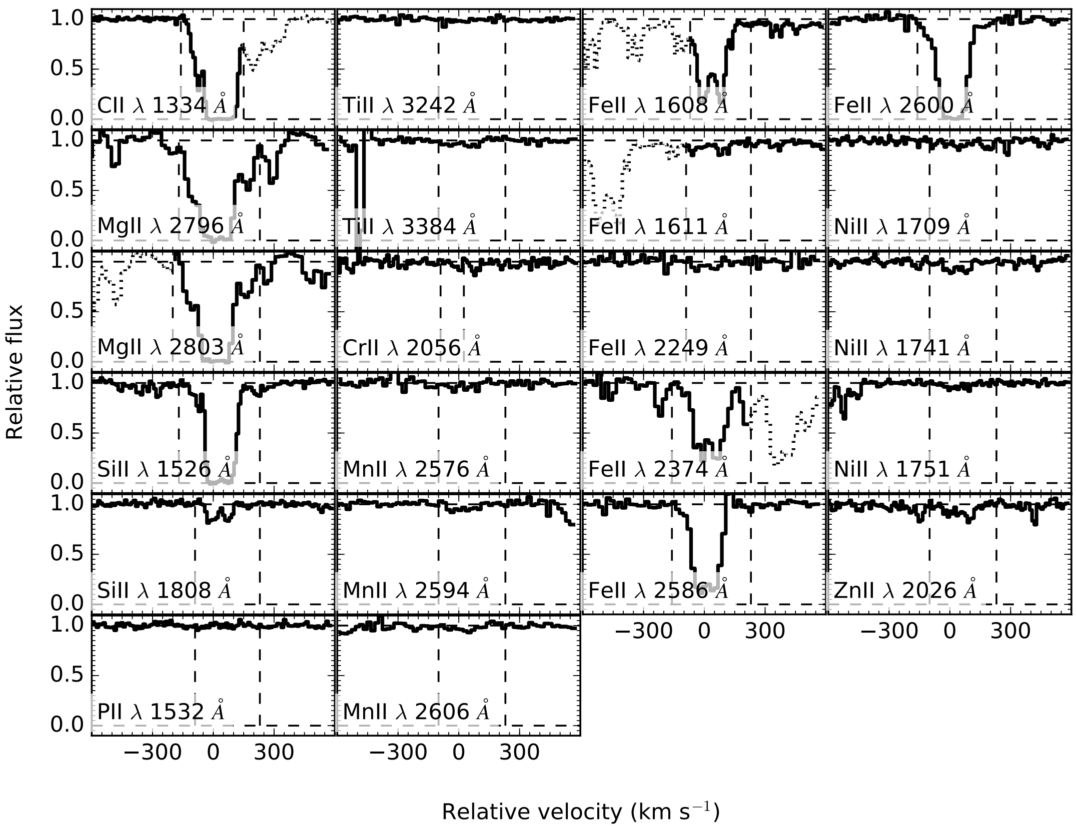

Figure B.10 Velocity profile of the XQ100 spectrum towards J0134+0400 (z_{abs}=3.772).

Table B.11 X-Shooter metal column densities for J0234−1806 (z_{abs}=3.693)

Ion	Line	λ Å	f	v_{min} km s^{-1}	v_{max} km s^{-1}	logN(X)	Included	logN_{adopt}
MgI	2852	2852.964	1.81E+00	-200	200	12.67 ± 0.02	Y	–
MgI								12.67 ± 0.05
MgII	2796	2796.352	6.12E-01	-200	330	> 14.04	N	–
MgII	2803	2803.531	3.05E-01	-175	330	> 14.30	Y	–
MgII								> 14.30
SiII	1526	1526.707	1.27E-01	-200	330	> 14.55	Y	–
SiII	1808	1808.013	2.19E-03	-200	330	< 14.62	Y	–
SiII								14.54–14.64
TiII	3242	3242.929	2.32E-01	-200	330	< 12.47	N	–
TiII	3384	3384.740	3.58E-01	-200	330	< 12.44	Y	–
TiII								< 12.44
CrII	2056	2056.254	1.05E-01	0	330	< 13.11	Y	–
CrII	2062	2062.234	7.80E-02	-150	90	< 13.20	N	–
CrII	2066	2066.161	5.15E-02	-200	330	< 14.35	N	–
CrII								< 13.11
MnII	2576	2576.877	3.51E-01	-200	330	< 12.62	Y	–
MnII	2594	2594.499	2.71E-01	-130	330	< 12.81	N	–
MnII								< 12.62
FeII	1608	1608.451	5.80E-02	-200	330	14.27 ± 0.02	Y	–
FeII	1611	1611.200	1.36E-03	-200	330	15.24 ± 0.09	N	–
FeII	2249	2249.877	1.82E-03	-200	330	14.97 ± 0.14	N	–
FeII	2344	2344.214	1.14E-01	-200	330	14.18 ± 0.03	Y	–
FeII	2600	2600.173	2.39E-01	-200	330	> 14.03	N	–
FeII								14.24 ± 0.05
NiII	1709	1709.604	3.24E-02	-200	330	< 13.59	Y	–
NiII	1751	1751.916	2.77E-02	-200	100	< 13.62	N	–
NiII								< 13.59

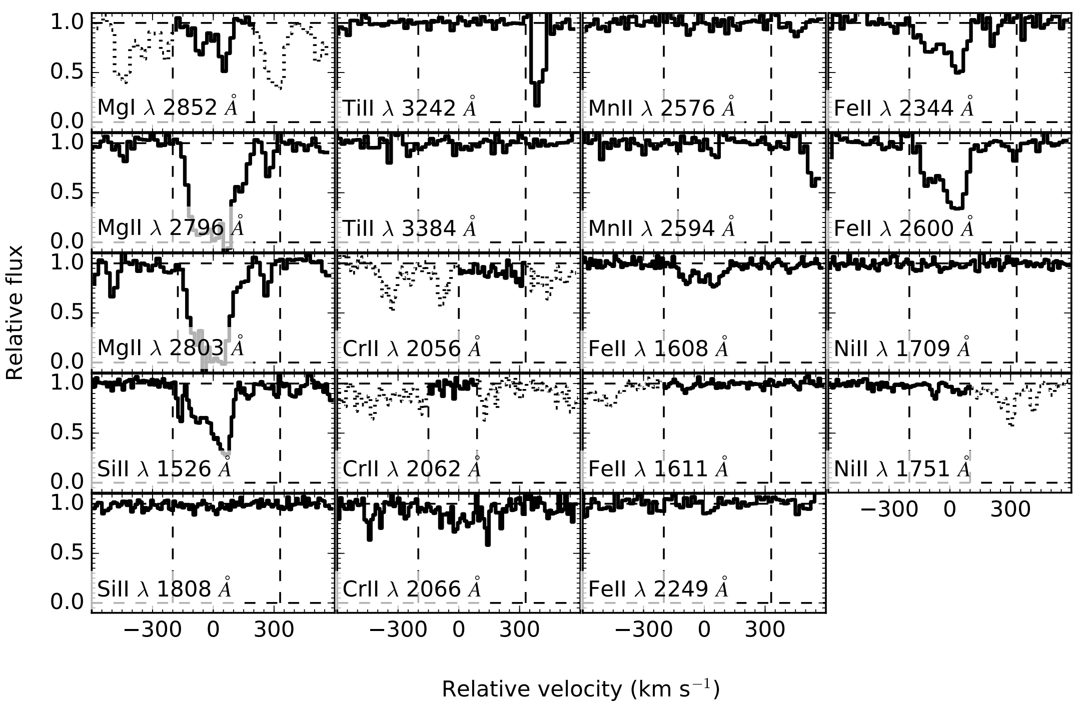

Figure B.11 Velocity profile of the XQ100 spectrum towards J0234-1806 (z_{abs}=3.693).

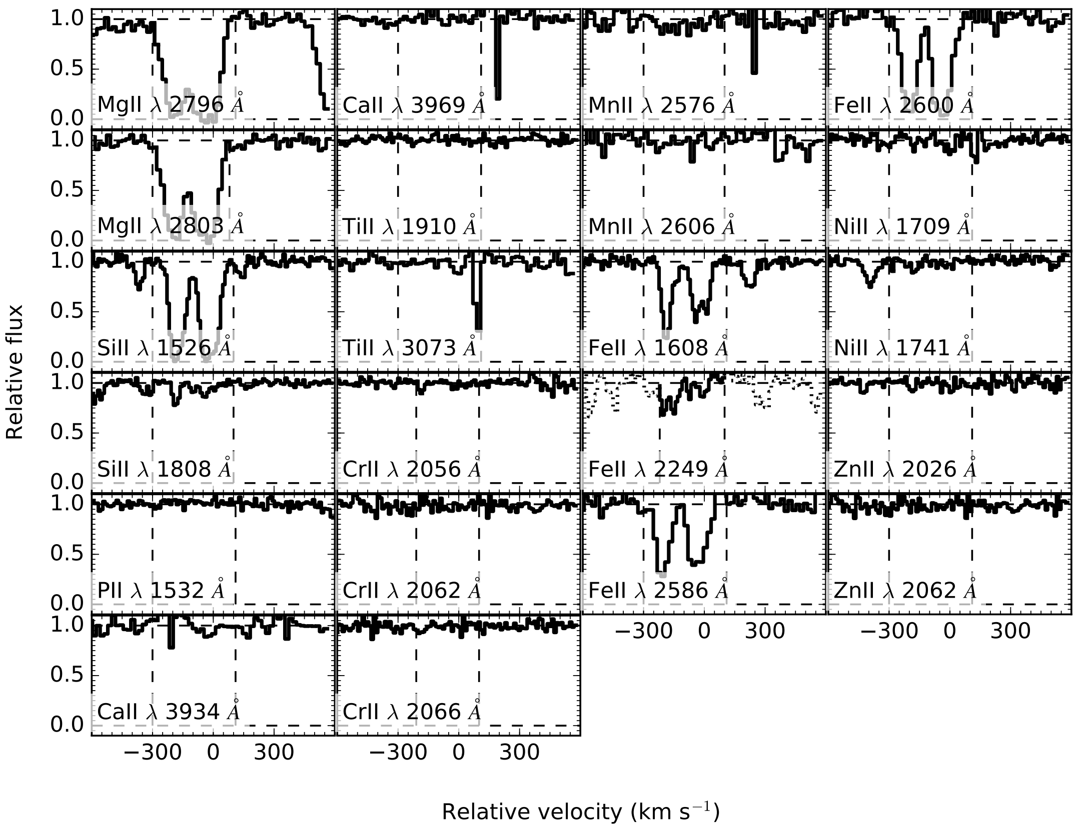

Figure B.12 Velocity profile of the XQ100 spectrum towards J0255+0048 (z_{abs}=3.256).

Table B.12 X-Shooter metal column densities for J0255+0048 (z_{abs}=3.256)

Ion	Line	λ Å	f	v_{min} km s^{-1}	v_{max} km s^{-1}	logN(X)	Included	$logN_{adopt}$
MgII	2796	2796.352	6.12E-01	-300	110	> 14.09	N	–
MgII	2803	2803.531	3.05E-01	-300	80	> 14.41	Y	–
MgII								> 14.41
SiII	1526	1526.707	1.27E-01	-300	100	> 15.01	N	–
SiII	1808	1808.013	2.19E-03	-300	100	15.33 ± 0.03	Y	–
SiII								15.33 ± 0.05
PII	1532	1532.533	7.61E-03	-300	110	< 14.05	Y	–
PII								< 14.05
CaII	3934	3934.777	6.50E-01	-300	110	< 12.45	N	–
CaII	3969	3969.591	3.22E-01	-300	110	< 12.37	Y	–
CaII								< 12.37
TiII	1910	1910.750	2.02E-01	-300	110	< 12.58	Y	–
TiII	3073	3073.877	1.09E-01	-300	110	< 13.32	N	–
TiII								< 12.58
CrII	2056	2056.254	1.05E-01	-210	100	< 12.86	Y	–
CrII	2062	2062.234	7.80E-02	-210	100	< 13.15	N	–
CrII	2066	2066.161	5.15E-02	-210	100	< 13.28	N	–
CrII								< 12.86
MnII	2576	2576.877	3.51E-01	-300	100	< 12.70	Y	–
MnII	2606	2606.462	1.93E-01	-300	100	< 12.95	N	–
MnII								< 12.70
FeII	1608	1608.451	5.80E-02	-300	110	> 14.75	Y	–
FeII	2249	2249.877	1.82E-03	-220	100	< 15.51	N	–
FeII	2586	2586.650	6.91E-02	-300	110	> 14.57	N	–
FeII	2600	2600.173	2.39E-01	-300	110	> 14.41	N	–
FeII								> 14.75
NiII	1709	1709.604	3.24E-02	-300	110	< 13.70	N	–
NiII	1741	1741.553	4.27E-02	-300	110	< 13.44	Y	–
NiII								< 13.44
ZnII	2026	2026.136	4.89E-01	-300	110	< 12.30	Y	–
ZnII	2062	2062.664	2.56E-01	-300	110	< 12.71	N	–
ZnII								< 12.30

Table B.13 X-Shooter metal column densities for J0255+0048 (z_{abs}=3.914)

Ion	Line	λ Å	f	v_{min} km s^{-1}	v_{max} km s^{-1}	logN(X)	Included	$\log N_{adopt}$
C II	1334	1334.532	1.28E-01	-70	70	> 14.55	Y	–
C II								> 14.55
O I	1302	1302.168	4.89E-02	-70	70	> 14.95	Y	–
O I								> 14.95
Si II	1260	1260.422	1.01E+00	-70	90	> 13.61	N	–
Si II	1304	1304.370	9.40E-02	-70	90	> 14.58	N	–
Si II	1526	1526.707	1.27E-01	-70	90	> 14.51	N	–
Si II	1808	1808.013	2.19E-03	-70	45	15.02 ± 0.05	Y	–
Si II								15.02 ± 0.05
P II	1532	1532.533	7.61E-03	-70	90	< 14.20	Y	–
P II								< 14.20
S II	1250	1250.584	5.43E-03	-70	70	14.87 ± 0.03	Y	–
S II	1253	1253.811	1.09E-02	-70	90	14.66 ± 0.03	Y	–
S II	1259	1259.519	1.66E-02	-70	90	14.70 ± 0.02	Y	–
S II								14.73 ± 0.05
Ti II	1910	1910.750	2.02E-01	-70	90	< 13.51	N	–
Ti II	3073	3073.877	1.09E-01	-70	90	< 12.91	N	–
Ti II	3242	3242.929	2.32E-01	-70	90	< 12.33	Y	–
Ti II	3384	3384.740	3.58E-01	-70	90	< 12.40	N	–
Ti II								< 12.33
Mn II	2576	2576.877	3.51E-01	-70	90	< 12.80	Y	–
Mn II	2594	2594.499	2.71E-01	-70	90	< 13.13	N	–
Mn II								< 12.80
Fe II	1144	1144.938	1.06E-01	-70	90	> 14.49	N	–
Fe II	1608	1608.451	5.80E-02	-70	90	> 14.51	Y	–
Fe II	1611	1611.200	1.36E-03	-70	90	< 14.83	Y	–
Fe II	2249	2249.877	1.82E-03	-70	90	< 16.19	N	–
Fe II	2344	2344.214	1.14E-01	-70	90	> 14.15	N	–
Fe II	2374	2374.461	3.13E-02	-70	90	> 14.50	Y	–
Fe II	2586	2586.650	6.91E-02	-70	90	> 14.30	N	–
Fe II	2600	2600.173	2.39E-01	-70	90	> 13.65	N	–
Fe II								14.51–14.83
Ni II	1709	1709.604	3.24E-02	-70	90	< 13.89	N	–
Ni II	1741	1741.553	4.27E-02	-70	90	13.52 ± 0.08	Y	–
Ni II	1751	1751.916	2.77E-02	-70	90	13.46 ± 0.12	Y	–
Ni II								13.50 ± 0.14

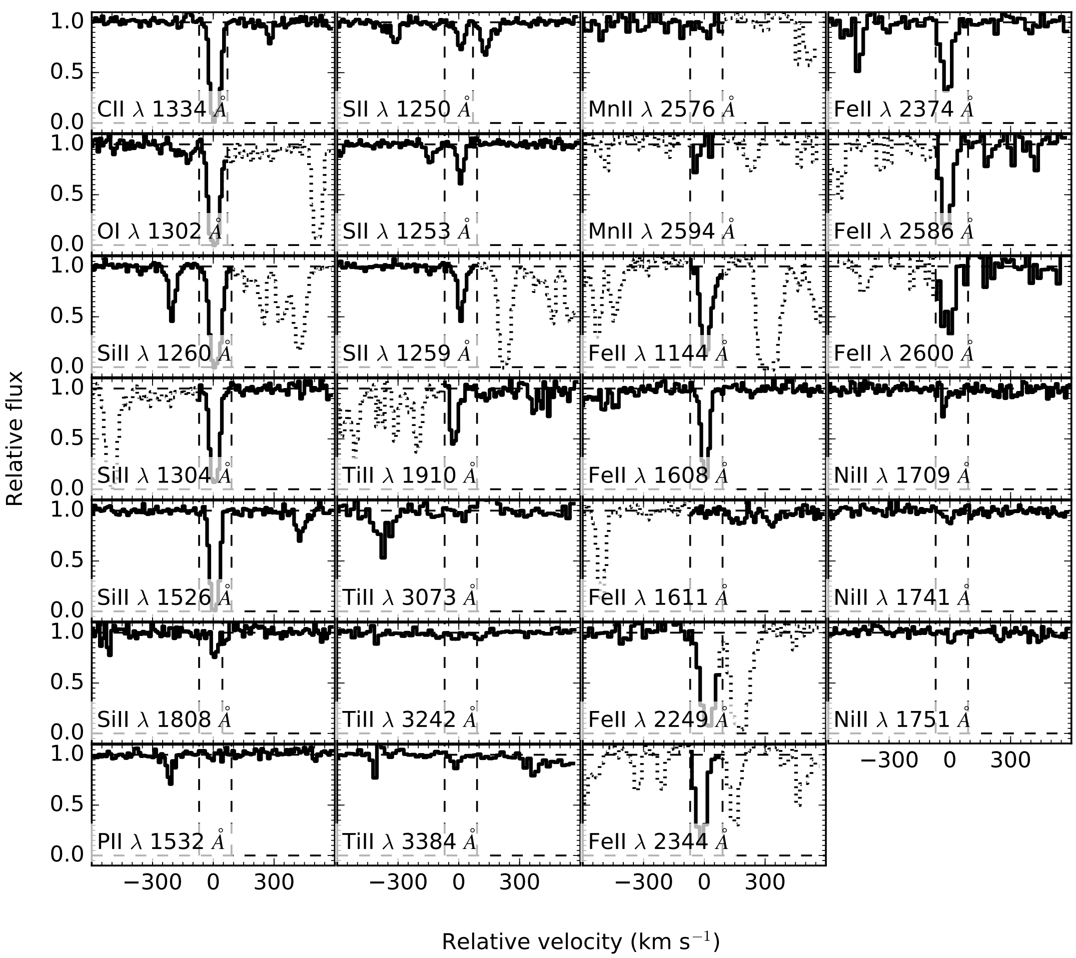

Figure B.13 Velocity profile of the XQ100 spectrum towards J0255+0048 (z_{abs}=3.914).

Table B.14 X-Shooter metal column densities for J0307−4945 (z_{abs}=3.591)

Ion	Line	λ Å	f	v_{min} km s^{-1}	v_{max} km s^{-1}	logN(X)	Included	$logN_{adopt}$
OI	1302	1302.168	4.89E-02	-170	100	> 15.17	Y	–
OI								> 15.17
MgI	2852	2852.964	1.81E+00	-170	100	12.21 ± 0.02	Y	–
MgI								12.21 ± 0.05
MgII	2796	2796.352	6.12E-01	-170	210	> 13.98	N	–
MgII	2803	2803.531	3.05E-01	-170	200	> 14.26	Y	–
MgII								> 14.26
SiII	1808	1808.013	2.19E-03	-60	25	< 14.26	Y	–
SiII								< 14.26
TiII	1910	1910.750	2.02E-01	-90	60	< 12.41	N	–
TiII	3384	3384.740	3.58E-01	-90	60	< 12.18	Y	–
TiII								< 12.18
MnII	2576	2576.877	3.51E-01	-40	50	< 12.05	N	–
MnII	2594	2594.499	2.71E-01	-40	50	< 11.93	Y	–
MnII	2606	2606.462	1.93E-01	-40	50	< 11.87	Y	–
MnII								< 11.87
FeII	1608	1608.451	5.80E-02	-30	100	14.16 ± 0.01	Y	–
FeII	1611	1611.200	1.36E-03	-40	50	< 14.74	N	–
FeII	2249	2249.877	1.82E-03	-70	100	< 14.68	N	–
FeII	2344	2344.214	1.14E-01	-170	100	14.12 ± 0.01	Y	–
FeII	2374	2374.461	3.13E-02	-90	100	14.19 ± 0.02	Y	–
FeII	2586	2586.650	6.91E-02	-120	100	14.20 ± 0.01	Y	–
FeII	2600	2600.173	2.39E-01	-180	110	> 14.02	N	–
FeII								14.17 ± 0.05
NiII	1709	1709.604	3.24E-02	-90	80	< 13.21	Y	–
NiII	1741	1741.553	4.27E-02	-90	80	< 13.23	N	–
NiII	1751	1751.916	2.77E-02	-90	80	< 13.88	N	–
NiII								< 13.21

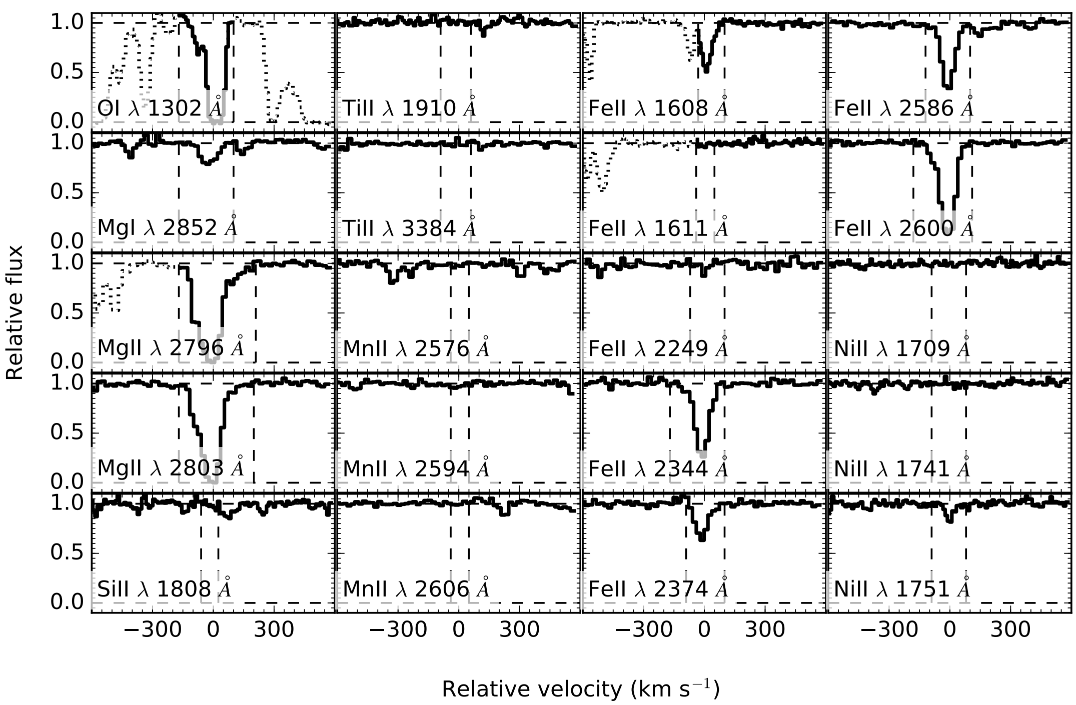

Figure B.14 Velocity profile of the XQ100 spectrum towards J0307-4945 (z_{abs}=3.591).

Table B.15 X-Shooter metal column densities for J0307−4945 (z_{abs}=4.466)

Ion	Line	λ Å	f	v_{min} km s^{-1}	v_{max} km s^{-1}	logN(X)	Included	logN_{adopt}
CII	1334	1334.532	1.28E-01	-200	140	> 15.01	Y	–
CII								> 15.01
OI	1302	1302.168	4.89E-02	-200	140	> 15.13	Y	–
OI								> 15.13
MgI	2852	2852.964	1.81E+00	-160	60	11.81 ± 0.10	Y	–
MgI								11.81 ± 0.10
MgII	2796	2796.352	6.12E-01	-200	140	> 14.00	N	–
MgII	2803	2803.531	3.05E-01	-200	140	> 14.18	Y	–
MgII								> 14.18
SiII	1304	1304.370	9.40E-02	-200	140	14.59 ± 0.00	Y	–
SiII	1526	1526.707	1.27E-01	-200	140	> 14.46	N	–
SiII								14.59 ± 0.05
PII	1532	1532.533	7.61E-03	-160	60	< 14.03	Y	–
PII								< 14.03
TiII	1910	1910.750	2.02E-01	-160	60	< 12.32	N	–
TiII	3073	3073.877	1.09E-01	-160	60	< 12.50	N	–
TiII	3242	3242.929	2.32E-01	-160	60	< 11.97	Y	–
TiII								< 11.97
FeII	1608	1608.451	5.80E-02	-200	140	14.12 ± 0.01	Y	–
FeII	1611	1611.200	1.36E-03	-160	60	< 14.53	N	–
FeII	2249	2249.877	1.82E-03	-160	60	< 14.59	N	–
FeII	2344	2344.214	1.14E-01	-200	140	14.10 ± 0.01	Y	–
FeII	2374	2374.461	3.13E-02	-210	140	14.17 ± 0.03	Y	–
FeII								14.11 ± 0.05
NiII	1751	1751.916	2.77E-02	-30	60	< 13.43	Y	–
NiII								< 13.43
ZnII	2026	2026.136	4.89E-01	-160	60	< 12.31	Y	–
ZnII								< 12.31

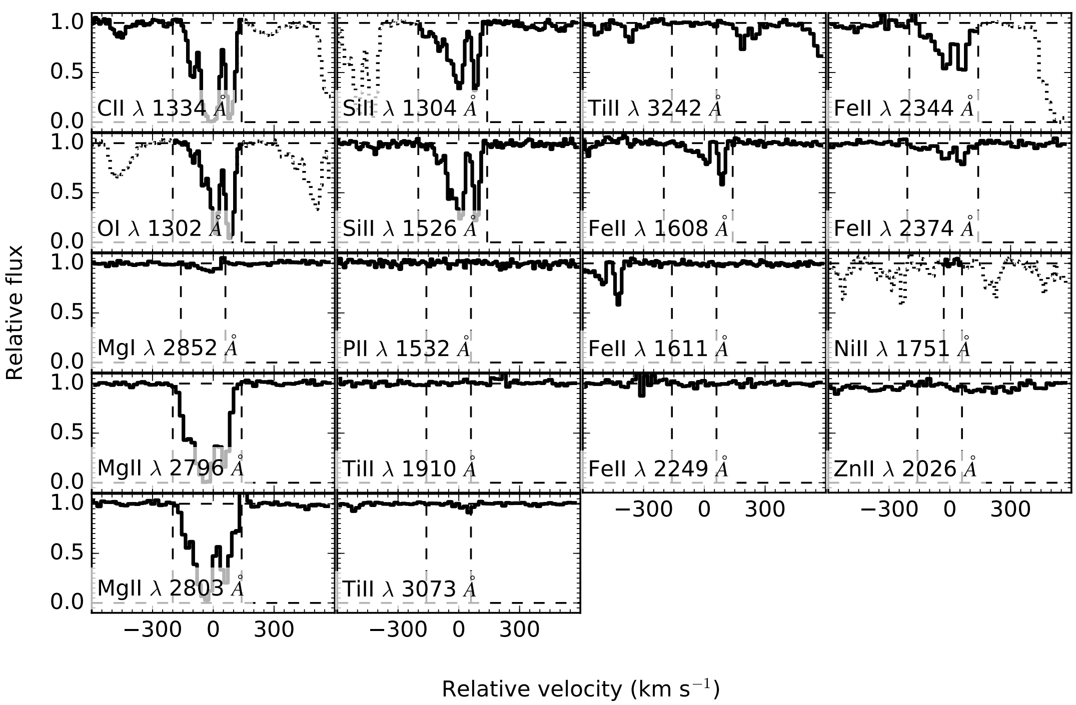

Figure B.15 Velocity profile of the XQ100 spectrum towards J0307-4945 (z_{abs}=4.466).

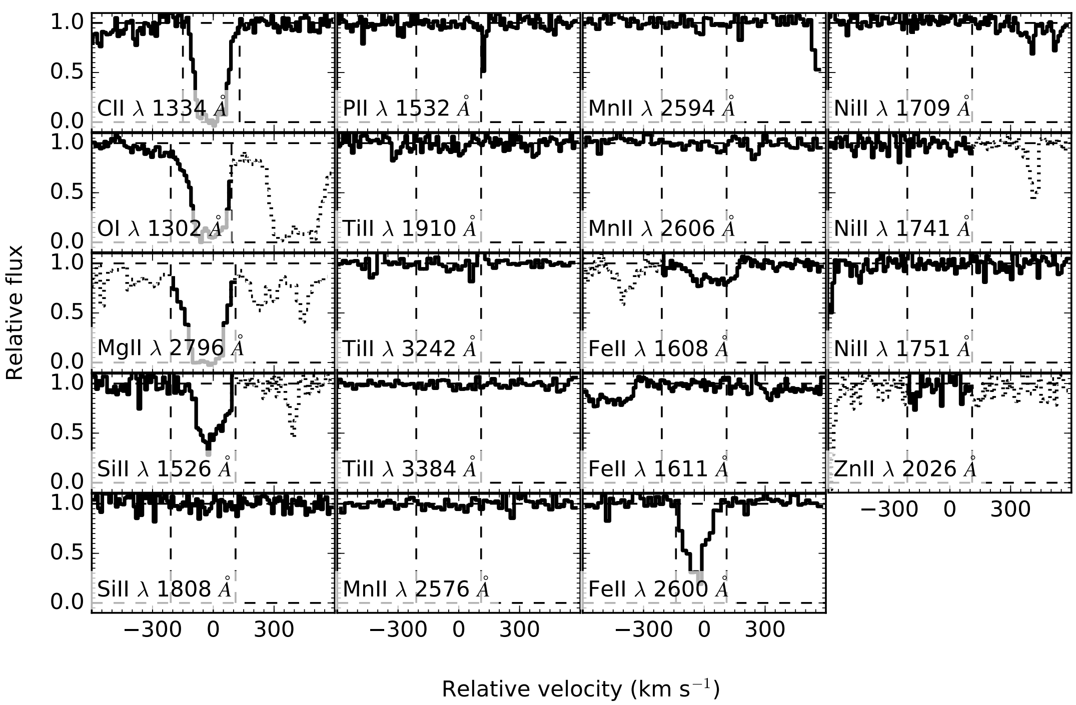

Figure B.16 Velocity profile of the XQ100 spectrum towards J0415-4357 (z_{abs}=3.808).

Table B.16 X-Shooter metal column densities for J0415−4357 (z_{abs}=3.808)

Ion	Line	λ Å	f	v_{min} km s^{-1}	v_{max} km s^{-1}	logN(X)	Included	logN$_{adopt}$
CII	1334	1334.532	1.28E-01	-150	130	$>$ 14.98	Y	–
CII								$>$ 14.98
OI	1302	1302.168	4.89E-02	-210	90	$>$ 15.50	Y	–
OI								$>$ 15.50
MgII	2796	2796.352	6.12E-01	-210	110	$>$ 13.95	Y	–
MgII								$>$ 13.95
SiII	1526	1526.707	1.27E-01	-210	110	$>$ 14.39	Y	–
SiII	1808	1808.013	2.19E-03	-210	110	$<$ 14.86	Y	–
SiII								14.39–14.85
PII	1532	1532.533	7.61E-03	-210	110	$<$ 14.20	Y	–
PII								$<$ 14.20
TiII	1910	1910.750	2.02E-01	-210	110	$<$ 12.88	N	–
TiII	3242	3242.929	2.32E-01	-210	110	$<$ 12.70	N	–
TiII	3384	3384.740	3.58E-01	-210	110	$<$ 12.28	Y	–
TiII								$<$ 12.28
MnII	2576	2576.877	3.51E-01	-210	110	$<$ 12.44	Y	–
MnII	2594	2594.499	2.71E-01	-210	110	$<$ 12.68	N	–
MnII	2606	2606.462	1.93E-01	-210	110	$<$ 12.66	N	–
MnII								$<$ 12.44
FeII	1608	1608.451	5.80E-02	-210	110	$<$ 14.21	Y	–
FeII	1611	1611.200	1.36E-03	-210	110	15.03 ± 0.11	N	–
FeII	2600	2600.173	2.39E-01	-140	110	$>$ 13.92	Y	–
FeII								13.91–14.19
NiII	1709	1709.604	3.24E-02	-210	110	$<$ 13.55	Y	–
NiII	1741	1741.553	4.27E-02	-210	110	$<$ 13.56	N	–
NiII	1751	1751.916	2.77E-02	-210	110	$<$ 13.96	N	–
NiII								$<$ 13.55
ZnII	2026	2026.136	4.89E-01	-210	110	$<$ 12.85	Y	–
ZnII								$<$ 12.85

Table B.17 X-Shooter metal column densities for J0424−2209 (z_{abs}=2.982)

Ion	Line	λ Å	f	v_{min} km s^{-1}	v_{max} km s^{-1}	logN(X)	Included	logN$_{adopt}$
MgII	2796	2796.352	6.12E-01	-80	100	> 13.62	Y	–
MgII								> 13.62
SiII	1808	1808.013	2.19E-03	-80	100	< 15.08	Y	–
SiII								14.44–15.08
CaII	3934	3934.777	6.50E-01	-80	60	< 12.07	Y	–
CaII	3969	3969.591	3.22E-01	-80	60	< 12.51	N	–
CaII								< 12.07
TiII	3073	3073.877	1.09E-01	-80	60	< 12.73	Y	–
TiII	3242	3242.929	2.32E-01	-80	60	< 12.82	N	–
TiII								< 12.73
CrII	2056	2056.254	1.05E-01	-80	60	< 13.01	Y	–
CrII	2062	2062.234	7.80E-02	-80	60	12.96 ± 0.09	N	–
CrII								< 13.01
MnII	2576	2576.877	3.51E-01	-80	60	< 12.65	Y	–
MnII	2606	2606.462	1.93E-01	-80	60	< 12.83	N	–
MnII								< 12.65
FeII	2249	2249.877	1.82E-03	-80	100	< 15.20	Y	–
FeII	2344	2344.214	1.14E-01	-80	100	> 14.25	N	–
FeII	2374	2374.461	3.13E-02	-80	60	> 14.46	Y	–
FeII	2586	2586.650	6.91E-02	-80	100	> 14.20	N	–
FeII	2600	2600.173	2.39E-01	-80	30	> 13.60	N	–
FeII								14.46–15.20
NiII	1709	1709.604	3.24E-02	-80	60	< 13.47	Y	–
NiII	1741	1741.553	4.27E-02	-80	60	< 13.48	Y	–
NiII	1751	1751.916	2.77E-02	-80	60	< 13.47	Y	–
NiII								< 13.47
ZnII	2026	2026.136	4.89E-01	-80	60	< 12.28	Y	–
ZnII	2062	2062.664	2.56E-01	-80	60	< 12.46	N	–
ZnII								< 12.28

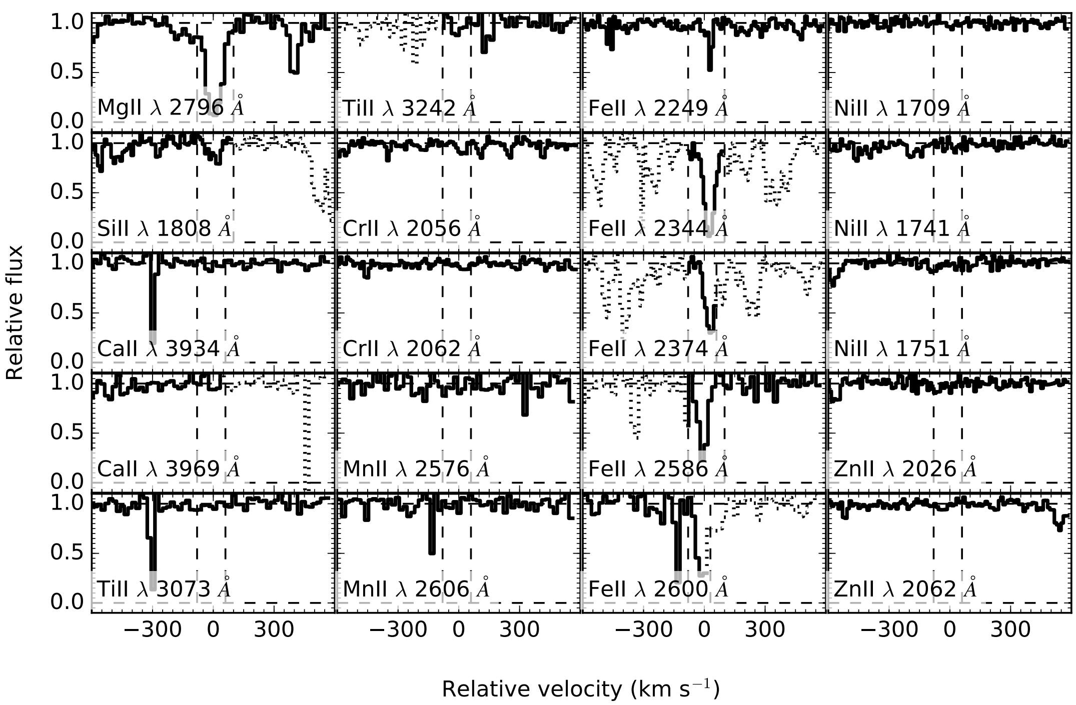

Figure B.17 Velocity profile of the XQ100 spectrum towards J0424-2209 (z_{abs}=2.982).

Table B.18 X-Shooter metal column densities for J0529−3552 (z_{abs}=3.684)

Ion	Line	λ Å	f	v_{min} km s^{-1}	v_{max} km s^{-1}	logN(X)	Included	$\log N_{adopt}$
MgII	2796	2796.352	6.12E-01	-80	50	13.09 ± 0.03	Y	–
MgII	2803	2803.531	3.05E-01	-80	50	13.08 ± 0.07	Y	–
MgII								13.08 ± 0.08
SiII	1526	1526.707	1.27E-01	-80	50	13.53 ± 0.05	Y	–
SiII								13.53 ± 0.05
FeII	1608	1608.451	5.80E-02	-80	50	< 13.80	Y	–
FeII								< 13.80

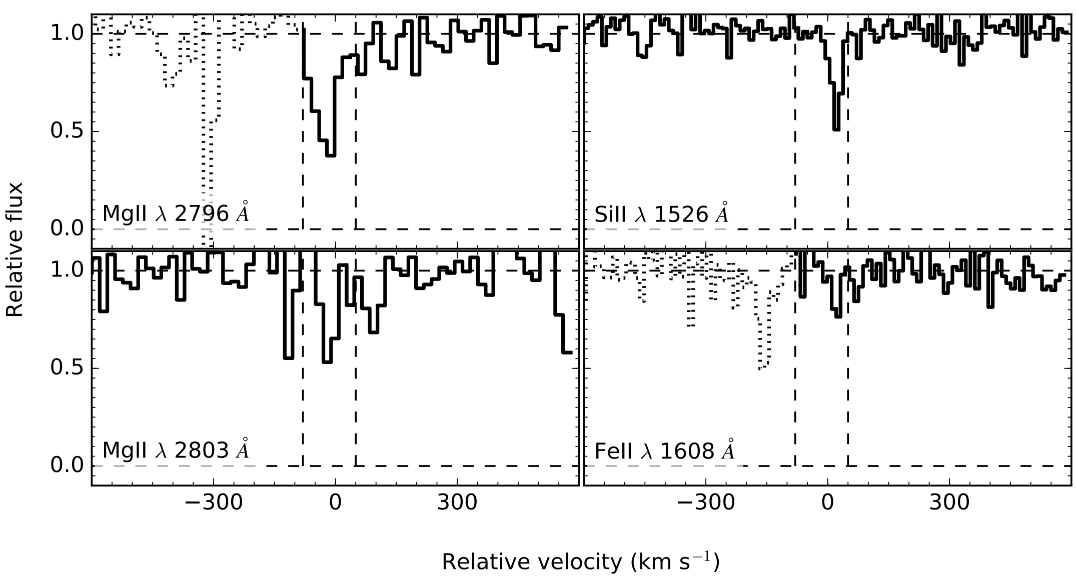

Figure B.18 Velocity profile of the XQ100 spectrum towards J0529-3552 (z_{abs}=3.684).

Table B.19 X-Shooter metal column densities for J0747+2739 (z_{abs}=3.424)

Ion	Line	λ Å	f	v_{min} km s^{-1}	v_{max} km s^{-1}	logN(X)	Included	$\log N_{adopt}$
MgI	2852	2852.964	1.81E+00	-200	100	< 11.85	Y	–
MgI								< 11.85
MgII	2796	2796.352	6.12E-01	-200	100	> 13.99	N	–
MgII	2803	2803.531	3.05E-01	-200	100	> 14.13	Y	–
MgII								> 14.13
SiII	1526	1526.707	1.27E-01	-200	100	> 14.58	Y	–
SiII	1808	1808.013	2.19E-03	-200	100	< 14.88	Y	–
SiII								14.58–14.88
PII	1532	1532.533	7.61E-03	-180	90	< 14.23	Y	–
PII								< 14.23
TiII	1910	1910.750	2.02E-01	-180	90	< 12.74	Y	–
TiII								< 12.74
FeII	1608	1608.451	5.80E-02	-200	100	14.43 ± 0.01	Y	–
FeII	1611	1611.200	1.36E-03	-200	100	14.87 ± 0.15	N	–
FeII	2344	2344.214	1.14E-01	-200	100	> 14.29	N	–
FeII	2374	2374.461	3.13E-02	-200	100	14.47 ± 0.00	Y	–
FeII	2586	2586.650	6.91E-02	-200	100	> 14.82	N	–
FeII	2600	2600.173	2.39E-01	-200	100	> 14.49	N	–
FeII								14.47 ± 0.05
NiII	1709	1709.604	3.24E-02	-180	90	< 13.49	N	–
NiII	1741	1741.553	4.27E-02	-180	90	< 13.46	Y	–
NiII	1751	1751.916	2.77E-02	-180	90	< 13.55	N	–
NiII								< 13.46

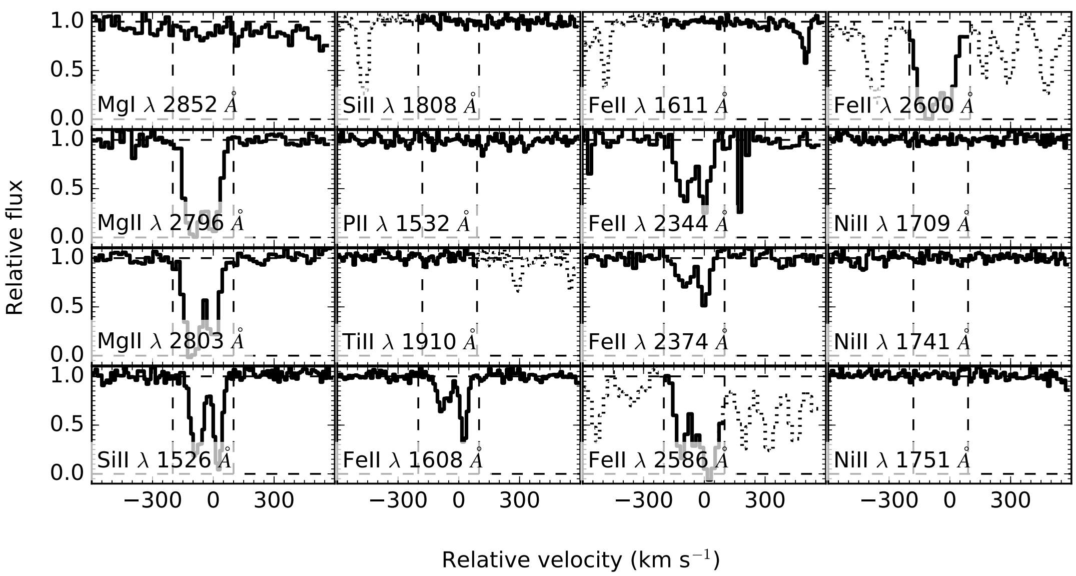

Figure B.19 Velocity profile of the XQ100 spectrum towards J0747+2739 (z_{abs}=3.424).

Table B.20 X-Shooter metal column densities for J0747+2739 (z_{abs}=3.901)

Ion	Line	λ Å	f	v_{min} km s^{-1}	v_{max} km s^{-1}	logN(X)	Included	$\log N_{adopt}$
CII	1036	1036.337	1.23E-01	-220	50	14.31 ± 0.02	Y	–
CII	1334	1334.532	1.28E-01	-220	50	> 14.54	N	–
CII								14.31 ± 0.05
OI	1302	1302.168	4.89E-02	-220	50	> 14.90	Y	–
OI								> 14.90
SiII	1304	1304.370	9.40E-02	-220	50	14.07 ± 0.02	Y	–
SiII	1526	1526.707	1.27E-01	-220	50	14.08 ± 0.02	Y	–
SiII	1808	1808.013	2.19E-03	-220	50	14.98 ± 0.08	N	–
SiII								14.08 ± 0.05
TiII	3073	3073.877	1.09E-01	-100	25	< 12.89	N	–
TiII	3242	3242.929	2.32E-01	-220	50	< 12.43	N	–
TiII	3384	3384.740	3.58E-01	-220	50	< 12.35	Y	–
TiII								< 12.35
MnII	2576	2576.877	3.51E-01	-220	50	< 12.74	Y	–
MnII	2594	2594.499	2.71E-01	-220	-30	< 12.62	N	–
MnII	2606	2606.462	1.93E-01	-220	50	< 13.12	N	–
MnII								< 12.74
FeII	1608	1608.451	5.80E-02	-220	50	14.01 ± 0.03	Y	–
FeII	1611	1611.200	1.36E-03	-220	50	< 14.98	N	–
FeII	2249	2249.877	1.82E-03	-100	50	< 15.00	N	–
FeII	2344	2344.214	1.14E-01	-220	50	< 14.27	N	–
FeII	2374	2374.461	3.13E-02	-220	50	14.03 ± 0.00	Y	–
FeII	2586	2586.650	6.91E-02	-220	50	14.07 ± 0.00	Y	–
FeII	2600	2600.173	2.39E-01	-220	50	> 13.73	N	–
FeII								14.06 ± 0.05
NiII	1709	1709.604	3.24E-02	-220	50	< 13.60	N	–
NiII	1741	1741.553	4.27E-02	-220	50	< 13.45	Y	–
NiII								< 13.45

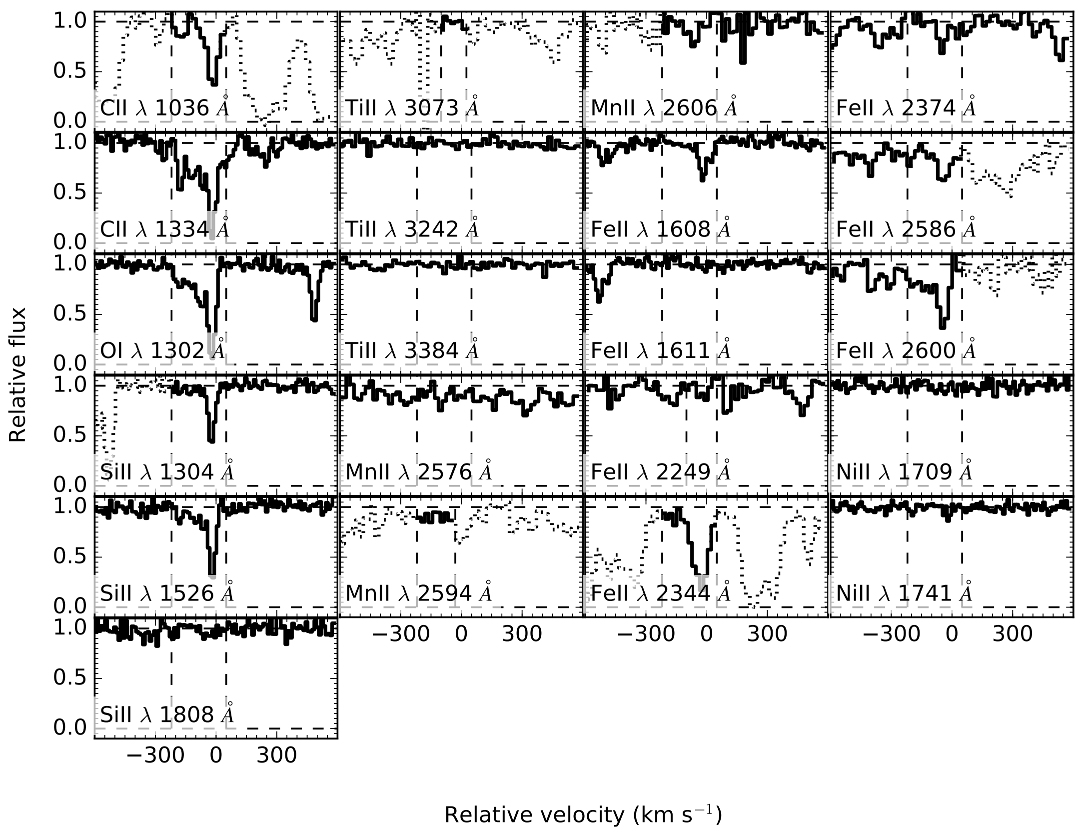

Figure B.20 Velocity profile of the XQ100 spectrum towards J0747+2739 (z_{abs}=3.901).

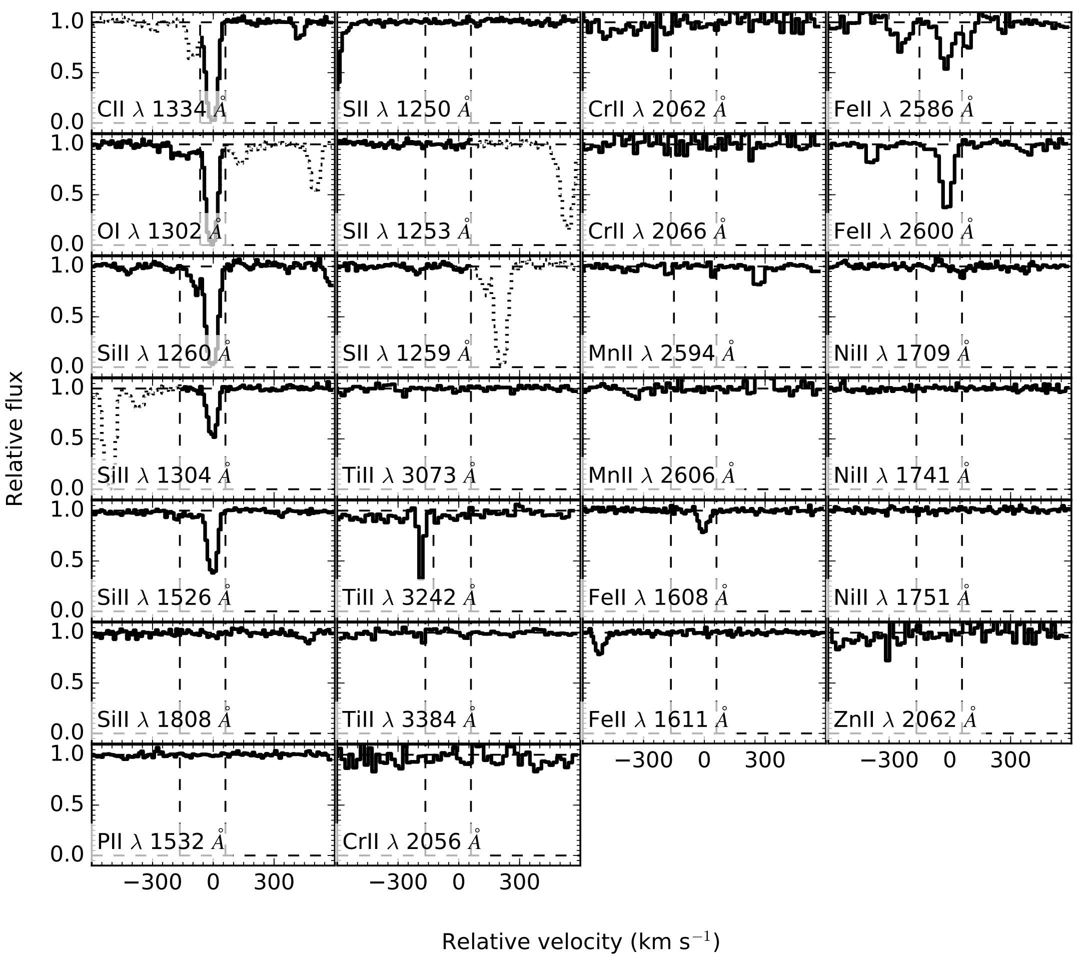

Figure B.21 Velocity profile of the XQ100 spectrum towards J0800+1920 (z_{abs}=3.946).

Table B.21 X-Shooter metal column densities for J0800+1920 (z_{abs}=3.946)

Ion	Line	λ Å	f	v_{min} km s^{-1}	v_{max} km s^{-1}	logN(X)	Included	$logN_{adopt}$
CII	1334	1334.532	1.28E-01	-65	60	> 14.58	Y	–
CII								> 14.58
OI	1302	1302.168	4.89E-02	-65	60	> 15.06	Y	–
OI								> 15.06
SiII	1260	1260.422	1.01E+00	-165	60	> 13.74	N	–
SiII	1304	1304.370	9.40E-02	-165	60	14.04 ± 0.01	Y	–
SiII	1526	1526.707	1.27E-01	-165	60	14.05 ± 0.01	Y	–
SiII	1808	1808.013	2.19E-03	-165	60	< 14.43	Y	–
SiII								14.05 ± 0.05
PII	1532	1532.533	7.61E-03	-165	60	< 13.59	Y	–
PII								< 13.59
SII	1250	1250.584	5.43E-03	-165	60	< 14.03	N	–
SII	1253	1253.811	1.09E-02	-165	60	< 13.88	N	–
SII	1259	1259.519	1.66E-02	-165	60	< 13.77	Y	–
SII								< 13.77
TiII	3073	3073.877	1.09E-01	-165	60	< 12.55	N	–
TiII	3242	3242.929	2.32E-01	-125	60	< 12.49	N	–
TiII	3384	3384.740	3.58E-01	-165	60	< 12.04	Y	–
TiII								< 12.04
CrII	2056	2056.254	1.05E-01	-165	60	< 13.13	Y	–
CrII	2062	2062.234	7.80E-02	-165	60	< 13.43	N	–
CrII	2066	2066.161	5.15E-02	-165	60	< 13.73	N	–
CrII								< 13.13
MnII	2594	2594.499	2.71E-01	-150	60	< 12.22	Y	–
MnII	2606	2606.462	1.93E-01	-165	60	< 12.70	N	–
MnII								< 12.22
FeII	1608	1608.451	5.80E-02	-165	60	13.73 ± 0.02	Y	–
FeII	1611	1611.200	1.36E-03	-165	60	< 14.67	N	–
FeII	2586	2586.650	6.91E-02	-150	60	< 13.93	N	–
FeII	2600	2600.173	2.39E-01	-165	60	> 13.58	N	–
FeII								13.73 ± 0.05
NiII	1709	1709.604	3.24E-02	-165	60	< 13.48	N	–
NiII	1741	1741.553	4.27E-02	-165	60	< 13.05	Y	–
NiII	1751	1751.916	2.77E-02	-165	60	< 13.32	N	–
NiII								< 13.05
ZnII	2062	2062.664	2.56E-01	-165	60	< 12.71	Y	–
ZnII								< 12.71

Table B.22 X-Shooter metal column densities for J0818+0958 (z_{abs}=3.306)

Ion	Line	λ Å	f	v_{min} km s^{-1}	v_{max} km s^{-1}	logN(X)	Included	$logN_{adopt}$
CII	1334	1334.532	1.28E-01	-100	300	> 14.88	Y	–
CII								> 14.88
MgII	2796	2796.352	6.12E-01	-200	300	> 13.97	N	–
MgII	2803	2803.531	3.05E-01	-200	300	> 14.12	Y	–
MgII								> 14.12
SiII	1526	1526.707	1.27E-01	-100	135	> 14.59	N	–
SiII	1808	1808.013	2.19E-03	-60	95	15.00 ± 0.00	Y	–
SiII								15.00 ± 0.05
PII	1532	1532.533	7.61E-03	-70	135	< 14.05	Y	–
PII								< 14.05
CaII	3934	3934.777	6.50E-01	-100	135	< 12.08	Y	–
CaII	3969	3969.591	3.22E-01	-40	135	< 12.20	N	–
CaII								< 12.08
CrII	2056	2056.254	1.05E-01	-50	110	13.26 ± 0.00	Y	–
CrII	2062	2062.234	7.80E-02	-70	40	13.13 ± 0.00	Y	–
CrII	2066	2066.161	5.15E-02	-70	50	13.21 ± 0.00	Y	–
CrII								13.22 ± 0.05
FeII	1608	1608.451	5.80E-02	-100	135	> 14.61	Y	–
FeII	1611	1611.200	1.36E-03	-40	40	< 14.70	Y	–
FeII	2249	2249.877	1.82E-03	-40	40	< 14.89	N	–
FeII	2344	2344.214	1.14E-01	-100	135	> 14.31	N	–
FeII	2374	2374.461	3.13E-02	-200	135	> 14.49	N	–
FeII								14.60–14.70
NiII	1709	1709.604	3.24E-02	-100	135	< 13.54	Y	–
NiII	1741	1741.553	4.27E-02	-100	135	13.52 ± 0.00	Y	–
NiII	1751	1751.916	2.77E-02	-100	135	13.54 ± 0.00	Y	–
NiII								13.53 ± 0.05
ZnII	2026	2026.136	4.89E-01	-100	135	12.12 ± 0.00	Y	–
ZnII	2062	2062.664	2.56E-01	-30	135	12.55 ± 0.00	Y	–
ZnII								12.41 ± 0.05

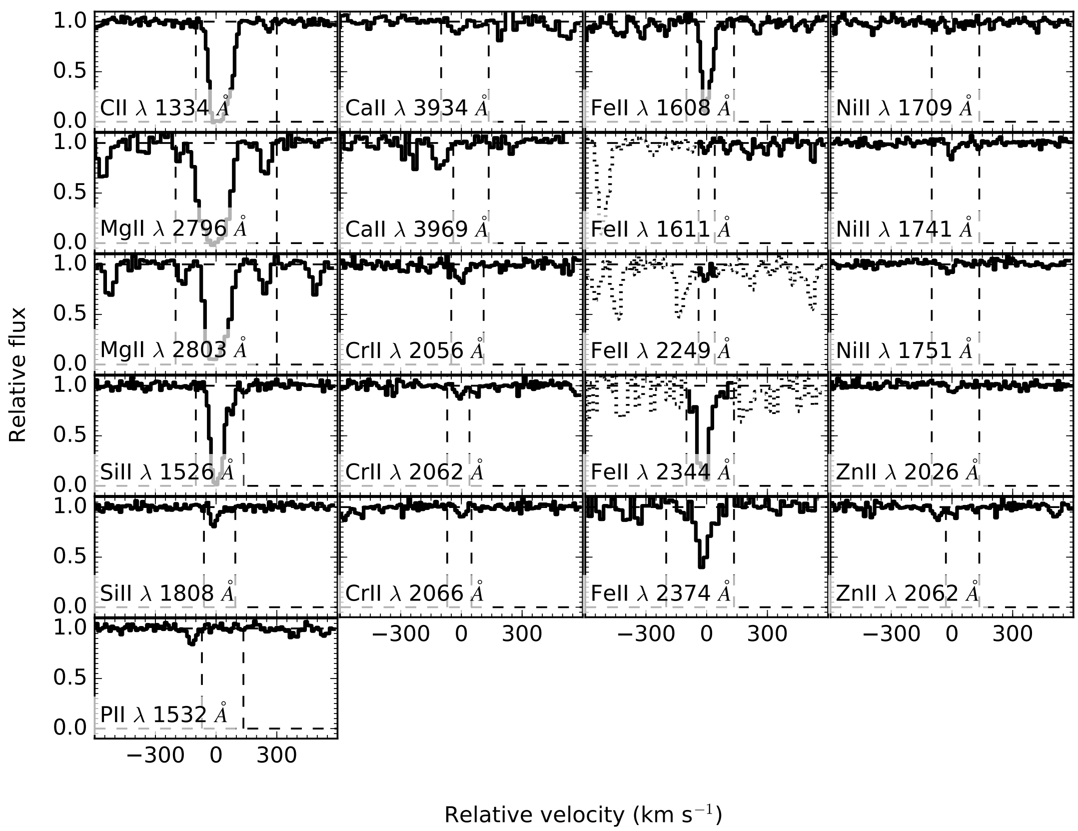

Figure B.22 Velocity profile of the XQ100 spectrum towards J0818+0958 (z_{abs}=3.306).

Table B.23 X-Shooter metal column densities for J0835+0650 (z_{abs}=3.955)

Ion	Line	λ Å	f	v_{min} km s^{-1}	v_{max} km s^{-1}	logN(X)	Included	$logN_{adopt}$
CII	1334	1334.532	1.28E-01	-75	75	> 14.62	N	–
CII								> 14.68
OI	1302	1302.168	4.89E-02	-75	90	> 15.02	Y	–
OI								> 15.02
SiII	1260	1260.422	1.01E+00	-75	90	> 13.72	N	–
SiII	1304	1304.370	9.40E-02	-75	90	14.10 ± 0.02	Y	–
SiII	1526	1526.707	1.27E-01	-75	40	> 14.04	N	–
SiII	1808	1808.013	2.19E-03	-30	90	< 14.58	N	–
SiII								14.10 ± 0.05
SII	1250	1250.584	5.43E-03	-75	40	< 14.28	N	–
SII	1253	1253.811	1.09E-02	-75	40	< 13.98	Y	–
SII	1259	1259.519	1.66E-02	-75	40	13.95 ± 0.10	Y	–
SII								13.95 ± 0.10
TiII	3073	3073.877	1.09E-01	-75	90	< 12.80	N	–
TiII	3242	3242.929	2.32E-01	-75	90	< 12.49	N	–
TiII	3384	3384.740	3.58E-01	-75	90	< 12.18	Y	–
TiII								< 12.18
CrII	2056	2056.254	1.05E-01	-75	40	< 13.26	Y	–
CrII	2062	2062.234	7.80E-02	-75	40	< 13.31	N	–
CrII	2066	2066.161	5.15E-02	-75	40	< 13.39	N	–
CrII								< 13.26
MnII	2576	2576.877	3.51E-01	-75	40	< 12.43	N	–
MnII	2594	2594.499	2.71E-01	-75	40	< 12.32	Y	–
MnII	2606	2606.462	1.93E-01	-75	40	< 12.62	Y	–
MnII								< 12.32
FeII	1608	1608.451	5.80E-02	-75	90	13.93 ± 0.02	Y	–
FeII	1611	1611.200	1.36E-03	-75	40	< 14.90	N	–
FeII	2344	2344.214	1.14E-01	-75	90	13.85 ± 0.02	Y	–
FeII	2374	2374.461	3.13E-02	-75	90	13.66 ± 0.08	Y	–
FeII	2586	2586.650	6.91E-02	-75	90	13.70 ± 0.03	Y	–
FeII	2600	2600.173	2.39E-01	-75	90	> 13.55	Y	–
FeII								13.84 ± 0.09
NiII	1709	1709.604	3.24E-02	-75	90	< 13.41	N	–
NiII	1741	1741.553	4.27E-02	-75	90	< 13.42	N	–
NiII	1751	1751.916	2.77E-02	-75	90	< 13.30	Y	–
NiII								< 13.30
ZnII	2062	2062.664	2.56E-01	-75	90	< 12.79	Y	–
ZnII								< 12.79

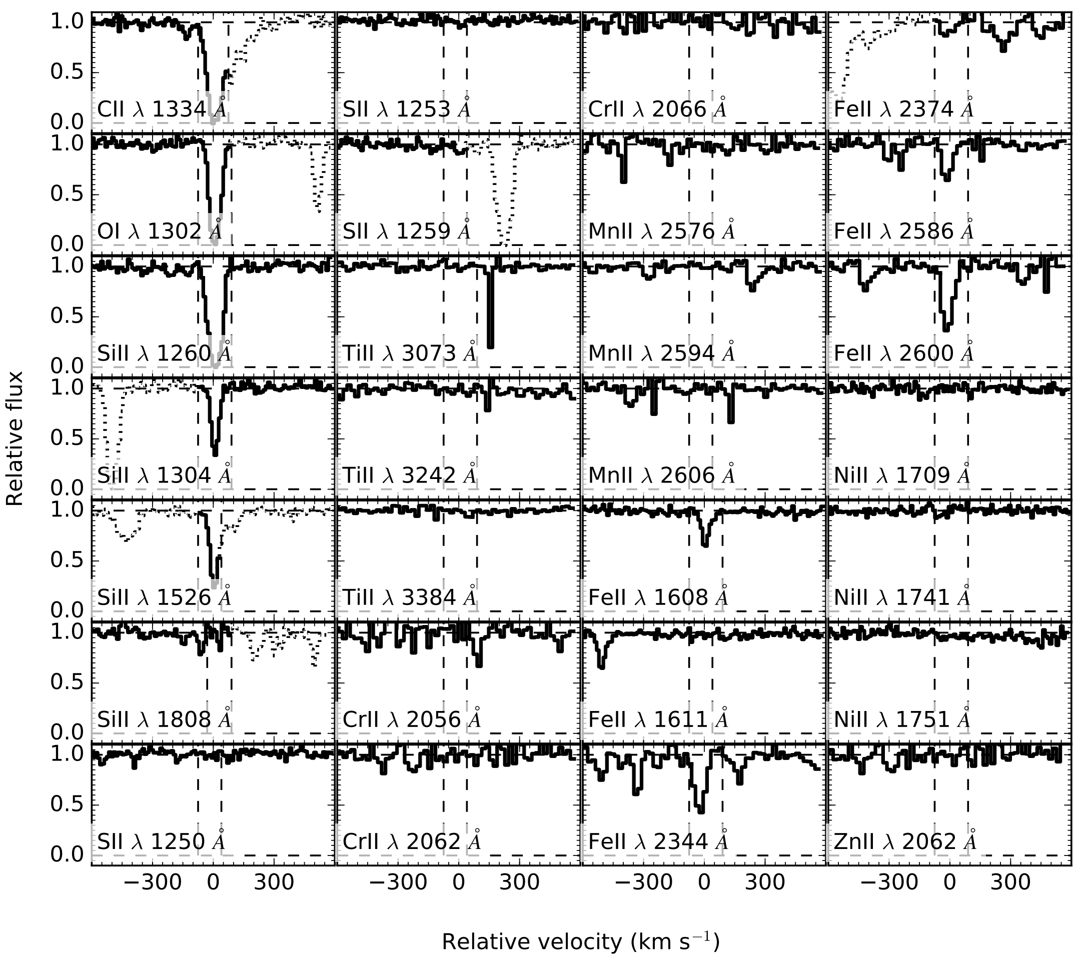

Figure B.23 Velocity profile of the XQ100 spectrum towards J0835+0650 (z_{abs}=3.955).

Table B.24 X-Shooter metal column densities for J0920+0725 (z_{abs}=2.238)

Ion	Line	λ Å	f	v_{min} km s^{-1}	v_{max} km s^{-1}	logN(X)	Included	$logN_{adopt}$
MgII	2796	2796.352	6.12E-01	-270	0	> 13.93	Y	–
MgII	2803	2803.531	3.05E-01	-270	20	> 14.27	N	–
MgII								> 13.93
SiII	1526	1526.707	1.27E-01	-200	20	> 14.60	Y	–
SiII	1808	1808.013	2.19E-03	-200	0	< 15.08	N	–
SiII								> 14.60
CaII	3934	3934.777	6.50E-01	-200	0	< 12.08	Y	–
CaII	3969	3969.591	3.22E-01	-200	0	< 12.21	N	–
CaII								< 12.08
TiII	1910	1910.750	2.02E-01	-200	0	< 12.51	Y	–
TiII	3242	3242.929	2.32E-01	-200	0	< 12.66	Y	–
TiII	3384	3384.740	3.58E-01	-200	0	< 12.81	N	–
TiII								< 12.51
CrII	2056	2056.254	1.05E-01	-200	0	< 12.93	Y	–
CrII	2066	2066.161	5.15E-02	-200	0	< 13.02	Y	–
CrII								< 12.93
MnII	2594	2594.499	2.71E-01	-200	0	< 12.40	N	–
MnII	2606	2606.462	1.93E-01	-200	0	< 12.39	Y	–
MnII								< 12.39
FeII	2249	2249.877	1.82E-03	-170	20	< 14.71	N	–
FeII	2344	2344.214	1.14E-01	-200	0	> 14.29	N	–
FeII	2374	2374.461	3.13E-02	-200	0	14.50 ± 0.01	Y	–
FeII	2586	2586.650	6.91E-02	-200	0	> 14.34	N	–
FeII	2600	2600.173	2.39E-01	-200	0	> 14.09	N	–
FeII								14.50 ± 0.05
NiII	1741	1741.553	4.27E-02	-200	0	< 13.31	Y	–
NiII	1751	1751.916	2.77E-02	-200	0	< 13.54	N	–
NiII								< 13.31
ZnII	2026	2026.136	4.89E-01	-200	0	< 12.13	Y	–
ZnII								< 12.13

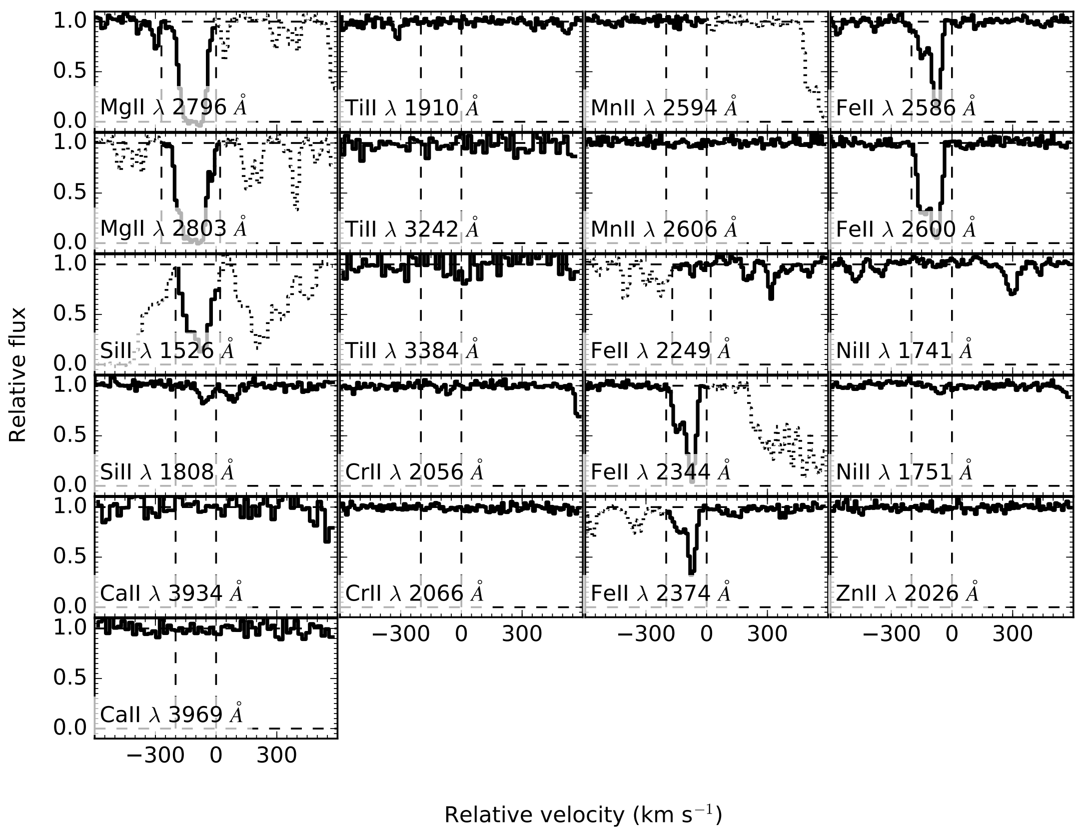

Figure B.24 Velocity profile of the XQ100 spectrum towards J0920+0725 (z_{abs}=2.238).

Table B.25 X-Shooter metal column densities for J0955−0130 (z_{abs}=4.024)

Ion	Line	λ Å	f	v_{min} km s^{-1}	v_{max} km s^{-1}	logN(X)	Included	logN$_{adopt}$
CII	1334	1334.532	1.28E-01	-270	190	> 15.18	Y	–
CII								> 15.18
SiII	1526	1526.707	1.27E-01	-270	200	> 14.68	Y	–
SiII								> 14.68
PII	1532	1532.533	7.61E-03	-270	200	< 14.16	Y	–
PII								< 14.16
TiII	3073	3073.877	1.09E-01	-150	200	< 12.73	N	–
TiII	3242	3242.929	2.32E-01	-270	200	< 12.55	N	–
TiII	3384	3384.740	3.58E-01	-270	-5	< 12.24	Y	–
TiII								< 12.24
CrII	2066	2066.161	5.15E-02	-170	200	< 13.87	Y	–
CrII								< 13.87
MnII	2576	2576.877	3.51E-01	-270	200	< 12.66	Y	–
MnII								< 12.66
FeII	1608	1608.451	5.80E-02	-260	200	< 14.61	N	–
FeII	2374	2374.461	3.13E-02	-270	200	14.31 ± 0.03	Y	–
FeII	2600	2600.173	2.39E-01	-285	200	> 14.05	N	–
FeII								14.31 ± 0.05
NiII	1709	1709.604	3.24E-02	-270	200	< 13.41	Y	–
NiII	1741	1741.553	4.27E-02	-270	200	< 13.44	N	–
NiII	1751	1751.916	2.77E-02	-270	200	< 13.47	N	–
NiII								< 13.41
ZnII	2026	2026.136	4.89E-01	-270	200	< 12.96	Y	–
ZnII								< 12.96

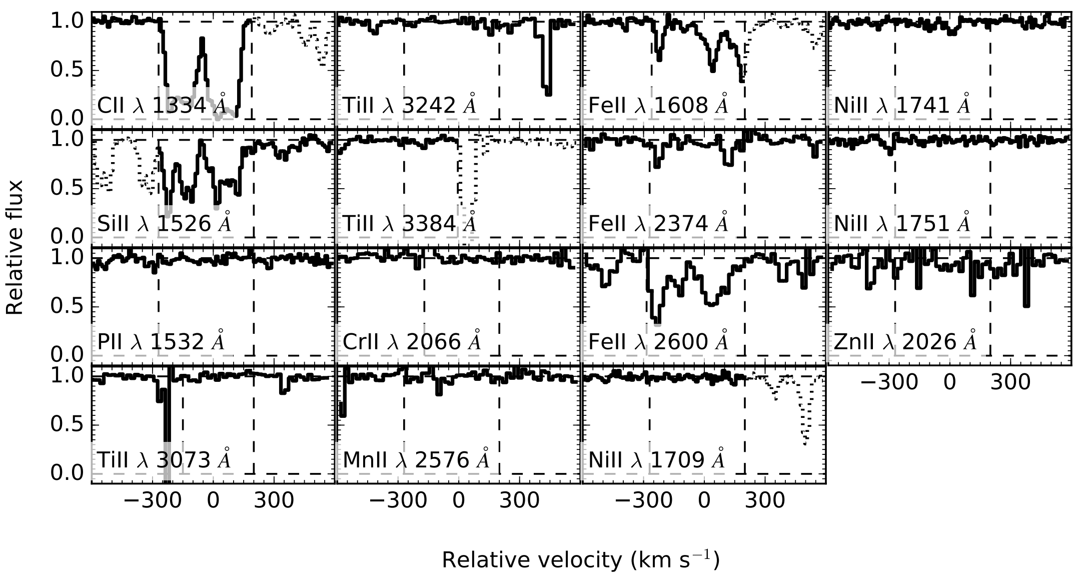

Figure B.25 Velocity profile of the XQ100 spectrum towards J0955-0130 (z_{abs}=4.024).

Table B.26 X-Shooter metal column densities for J1020+0922 (z_{abs}=2.592)

Ion	Line	λ Å	f	v_{min} km s^{-1}	v_{max} km s^{-1}	logN(X)	Included	$\log N_{adopt}$
OI	1302	1302.168	4.89E-02	0	200	> 14.98	Y	–
OI								> 14.98
SiII	1808	1808.013	2.19E-03	0	200	15.26 ± 0.04	Y	–
SiII								15.26 ± 0.05
TiII	1910	1910.750	2.02E-01	0	200	< 12.97	Y	–
TiII	3073	3073.877	1.09E-01	0	200	13.28 ± 0.08	N	–
TiII	3242	3242.929	2.32E-01	50	200	< 13.09	N	–
TiII	3384	3384.740	3.58E-01	0	200	12.73 ± 0.07	N	–
TiII								< 12.97
CrII	2056	2056.254	1.05E-01	0	130	13.33 ± 0.05	Y	–
CrII	2062	2062.234	7.80E-02	0	130	13.33 ± 0.06	Y	–
CrII	2066	2066.161	5.15E-02	0	130	13.44 ± 0.06	Y	–
CrII								13.36 ± 0.10
MnII	2576	2576.877	3.51E-01	25	130	12.55 ± 0.06	Y	–
MnII								12.55 ± 0.06
FeII	1608	1608.451	5.80E-02	0	200	> 14.32	N	–
FeII	1611	1611.200	1.36E-03	0	200	< 15.19	Y	–
FeII	2249	2249.877	1.82E-03	0	200	14.97 ± 0.06	Y	–
FeII	2344	2344.214	1.14E-01	0	200	> 13.97	N	–
FeII	2374	2374.461	3.13E-02	0	200	> 14.39	N	–
FeII	2586	2586.650	6.91E-02	0	120	> 14.00	N	–
FeII								14.97 ± 0.06
NiII	1709	1709.604	3.24E-02	0	200	13.85 ± 0.09	Y	–
NiII	1741	1741.553	4.27E-02	0	200	13.83 ± 0.06	Y	–
NiII	1751	1751.916	2.77E-02	0	200	< 14.06	N	–
NiII								13.84 ± 0.11
ZnII	2026	2026.136	4.89E-01	75	200	< 12.44	Y	–
ZnII	2062	2062.664	2.56E-01	75	200	< 12.52	N	–
ZnII								< 12.44

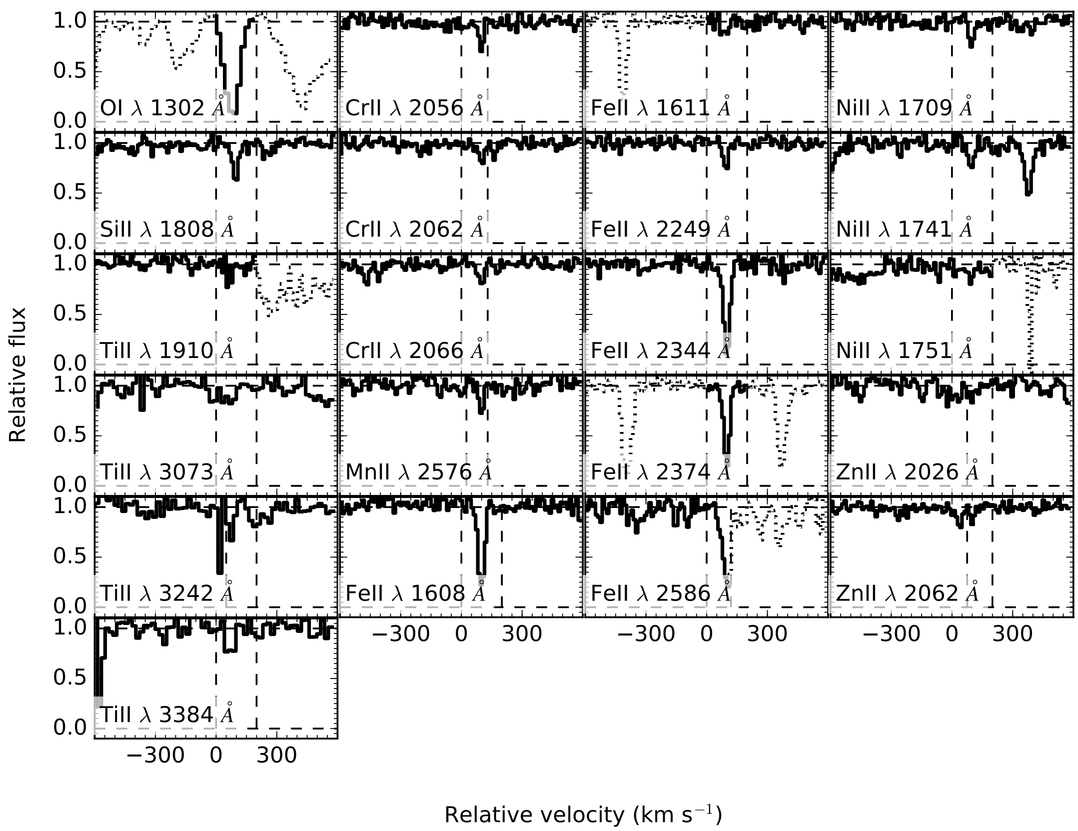

Figure B.26 Velocity profile of the XQ100 spectrum towards J1020+0922 (z_{abs}=2.592).

Table B.27 X-Shooter metal column densities for J1024+1819 (z_{abs}=2.298)

Ion	Line	λ Å	f	v_{min} km s^{-1}	v_{max} km s^{-1}	logN(X)	Included	$logN_{adopt}$
MgII	2796	2796.352	6.12E-01	-80	90	> 13.71	N	–
MgII	2803	2803.531	3.05E-01	-80	130	> 13.88	Y	–
MgII								> 13.88
SiII	1260	1260.422	1.01E+00	-80	130	> 13.93	N	–
SiII	1526	1526.707	1.27E-01	-80	130	> 14.51	N	–
SiII	1808	1808.013	2.19E-03	-80	100	15.36 ± 0.03	Y	–
SiII								15.36 ± 0.05
CaII	3934	3934.777	6.50E-01	-80	100	< 11.94	Y	–
CaII								< 11.94
TiII	3073	3073.877	1.09E-01	-80	100	< 13.46	N	–
TiII	3242	3242.929	2.32E-01	-80	100	< 12.69	Y	–
TiII								< 12.69
CrII	2056	2056.254	1.05E-01	-80	100	13.37 ± 0.04	Y	–
CrII	2062	2062.234	7.80E-02	-80	100	13.52 ± 0.04	Y	–
CrII								13.46 ± 0.06
MnII	2576	2576.877	3.51E-01	-80	100	12.73 ± 0.04	Y	–
MnII	2594	2594.499	2.71E-01	-80	100	12.70 ± 0.06	Y	–
MnII	2606	2606.462	1.93E-01	-80	100	12.78 ± 0.05	Y	–
MnII								12.74 ± 0.09
FeII	1608	1608.451	5.80E-02	-80	100	> 14.63	N	–
FeII	1611	1611.200	1.36E-03	-80	100	< 16.07	N	–
FeII	2249	2249.877	1.82E-03	-80	100	15.08 ± 0.04	Y	–
FeII	2344	2344.214	1.14E-01	-80	100	> 14.22	N	–
FeII	2374	2374.461	3.13E-02	-80	100	> 14.81	N	–
FeII	2586	2586.650	6.91E-02	-80	100	> 14.66	N	–
FeII	2600	2600.173	2.39E-01	-80	100	> 14.18	N	–
FeII								15.08 ± 0.05
NiII	1709	1709.604	3.24E-02	-80	100	13.73 ± 0.07	Y	–
NiII	1741	1741.553	4.27E-02	-80	100	13.83 ± 0.06	Y	–
NiII	1751	1751.916	2.77E-02	-80	100	13.76 ± 0.12	Y	–
NiII								13.78 ± 0.15
ZnII	2026	2026.136	4.89E-01	-80	100	< 12.07	Y	–
ZnII								< 12.07

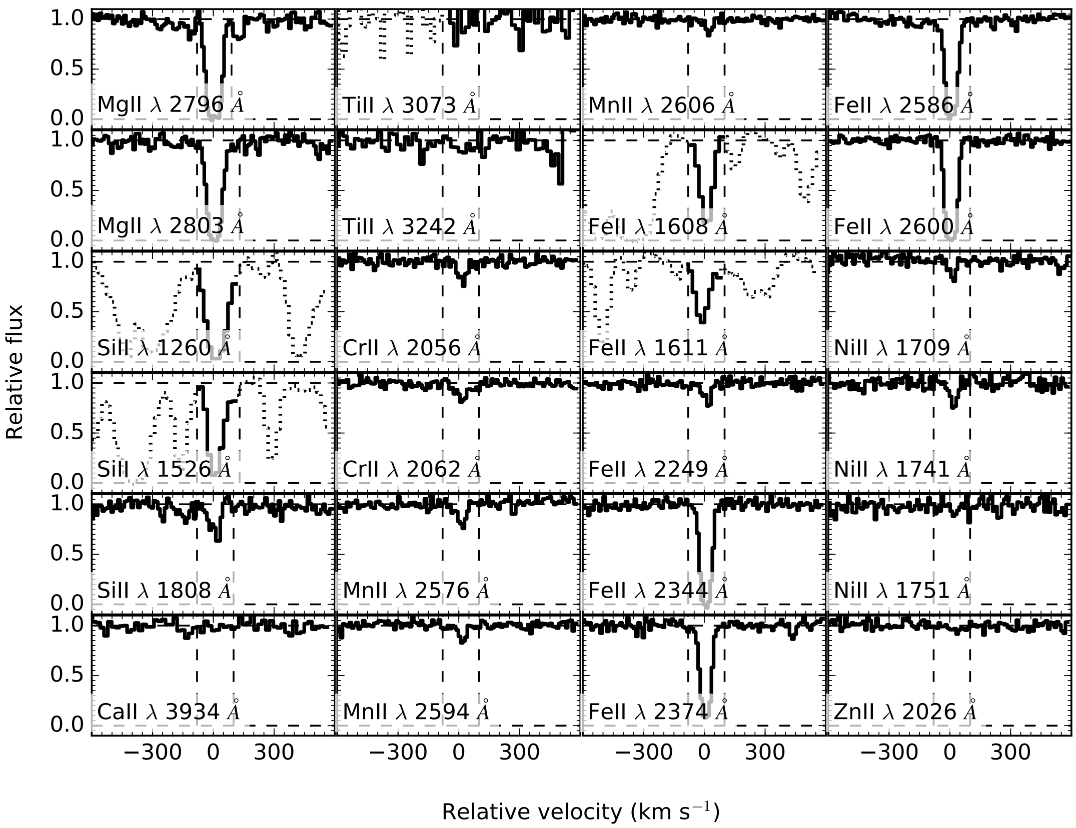

Figure B.27 Velocity profile of the XQ100 spectrum towards J1024+1819 (z_{abs}=2.298).

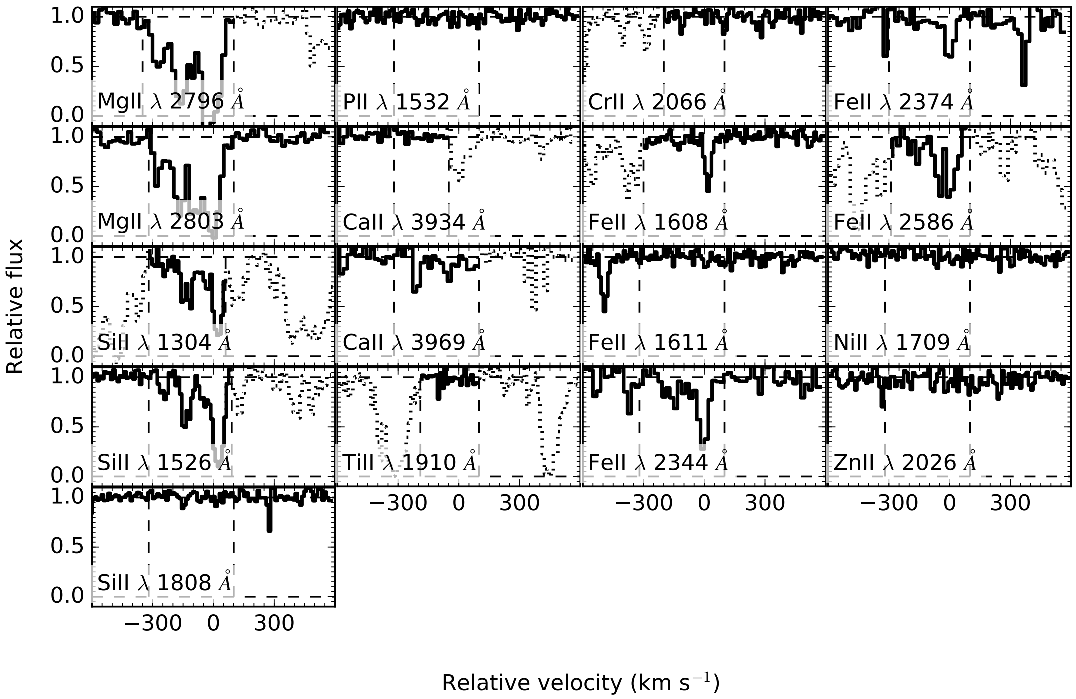

Figure B.28 Velocity profile of the XQ100 spectrum towards J1057+1910 (z_{abs}=3.373).

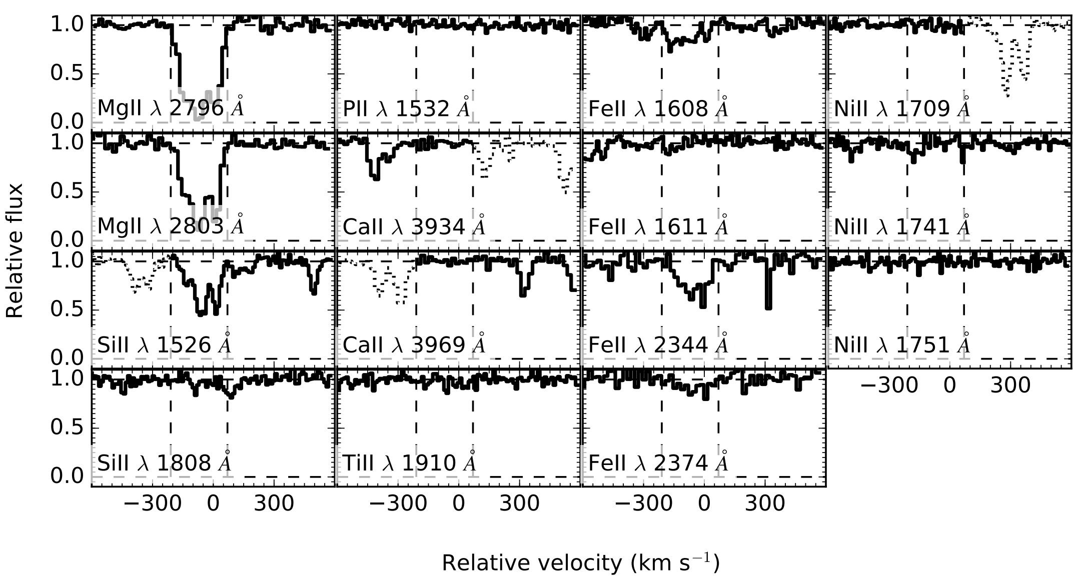

Figure B.29 Velocity profile of the XQ100 spectrum towards J1058+1245 (z_{abs}=3.432).

Table B.28 X-Shooter metal column densities for J1057+1910 (z_{abs}=3.373)

Ion	Line	λ Å	f	v_{min} km s^{-1}	v_{max} km s^{-1}	logN(X)	Included	logN_{adopt}
MgII	2796	2796.352	6.12E-01	-350	100	> 13.86	N	–
MgII	2803	2803.531	3.05E-01	-320	100	> 14.17	Y	–
MgII								> 14.17
SiII	1304	1304.370	9.40E-02	-320	60	> 14.63	N	–
SiII	1526	1526.707	1.27E-01	-320	90	> 14.51	Y	–
SiII	1808	1808.013	2.19E-03	-320	100	< 14.71	Y	–
SiII								14.51–14.71
PII	1532	1532.533	7.61E-03	-320	100	< 14.32	Y	–
PII								< 14.32
CaII	3934	3934.777	6.50E-01	-320	-50	< 11.99	N	–
CaII	3969	3969.591	3.22E-01	-320	100	< 13.06	Y	–
CaII								< 13.06
TiII	1910	1910.750	2.02E-01	-190	100	< 12.90	Y	–
TiII								< 12.90
CrII	2066	2066.161	5.15E-02	-200	100	< 13.43	Y	–
CrII								< 13.43
FeII	1608	1608.451	5.80E-02	-300	100	14.20 ± 0.04	Y	–
FeII	1611	1611.200	1.36E-03	-320	100	15.20 ± 0.11	N	–
FeII	2344	2344.214	1.14E-01	-320	100	> 14.12	Y	–
FeII	2374	2374.461	3.13E-02	-300	100	14.30 ± 0.07	Y	–
FeII	2586	2586.650	6.91E-02	-290	100	14.31 ± 0.06	Y	–
FeII								14.24 ± 0.10
NiII	1709	1709.604	3.24E-02	-320	100	< 13.73	Y	–
NiII								< 13.73
ZnII	2026	2026.136	4.89E-01	-320	100	< 12.56	Y	–
ZnII								< 12.56

Table B.29 X-Shooter metal column densities for J1058+1245 (z_{abs}=3.432)

Ion	Line	λ Å	f	v_{min} km s^{-1}	v_{max} km s^{-1}	logN(X)	Included	logN$_{adopt}$
MgII	2796	2796.352	6.12E-01	-210	70	> 13.93	N	–
MgII	2803	2803.531	3.05E-01	-210	70	> 14.04	Y	–
MgII								> 14.04
SiII	1526	1526.707	1.27E-01	-210	70	14.26 ± 0.01	Y	–
SiII	1808	1808.013	2.19E-03	-210	70	< 15.02	N	–
SiII								14.26 ± 0.05
PII	1532	1532.533	7.61E-03	-210	70	< 14.06	Y	–
PII								< 14.06
CaII	3934	3934.777	6.50E-01	-210	70	< 11.98	Y	–
CaII	3969	3969.591	3.22E-01	-210	70	< 12.15	Y	–
CaII								< 11.98
TiII	1910	1910.750	2.02E-01	-210	70	< 12.80	Y	–
TiII								< 12.80
FeII	1608	1608.451	5.80E-02	-210	70	14.16 ± 0.02	Y	–
FeII	1611	1611.200	1.36E-03	-210	70	15.12 ± 0.08	N	–
FeII	2344	2344.214	1.14E-01	-210	70	13.97 ± 0.03	Y	–
FeII	2374	2374.461	3.13E-02	-210	70	< 13.75	Y	–
FeII								14.10 ± 0.05
NiII	1709	1709.604	3.24E-02	-210	70	< 13.58	Y	–
NiII	1741	1741.553	4.27E-02	-210	70	< 13.80	Y	–
NiII	1751	1751.916	2.77E-02	-210	70	< 13.79	Y	–
NiII								< 13.58

Table B.30 X-Shooter metal column densities for J1108+1209 (z_{abs}=3.397)

Ion	Line	λ Å	f	v_{min} km s^{-1}	v_{max} km s^{-1}	logN(X)	Included	logN$_{adopt}$
CII	1334	1334.532	1.28E-01	-100	70	> 13.98	Y	–
CII								> 13.98
OI	1302	1302.168	4.89E-02	-100	70	14.64 ± 0.01	Y	–
OI								14.64 ± 0.05
MgI	2852	2852.964	1.81E+00	-50	70	11.94 ± 0.05	Y	–
MgI								11.94 ± 0.05
MgII	2796	2796.352	6.12E-01	-100	50	> 13.02	N	–
MgII	2803	2803.531	3.05E-01	-100	50	13.22 ± 0.05	Y	–
MgII								13.22 ± 0.05
SiII	1304	1304.370	9.40E-02	-50	15	< 13.77	Y	–
SiII	1526	1526.707	1.27E-01	-50	15	< 13.59	Y	–
SiII	1808	1808.013	2.19E-03	-100	50	< 14.34	N	–
SiII								< 13.59
PII	1532	1532.533	7.61E-03	-100	50	< 14.25	Y	–
PII								< 14.25
CaII	3934	3934.777	6.50E-01	-100	50	< 11.67	Y	–
CaII	3969	3969.591	3.22E-01	-80	50	< 12.63	N	–
CaII								< 11.67
TiII	1910	1910.750	2.02E-01	-100	50	< 12.92	Y	–
TiII								< 12.92
CrII	2056	2056.254	1.05E-01	-50	15	< 12.73	Y	–
CrII								< 12.73
FeII	1608	1608.451	5.80E-02	-70	50	13.54 ± 0.04	Y	–
FeII	1611	1611.200	1.36E-03	-70	50	< 14.67	N	–
FeII	2344	2344.214	1.14E-01	-50	50	13.17 ± 0.08	Y	–
FeII	2374	2374.461	3.13E-02	-70	50	13.48 ± 0.10	Y	–
FeII	2586	2586.650	6.91E-02	-50	50	13.45 ± 0.04	Y	–
FeII	2600	2600.173	2.39E-01	-100	50	13.28 ± 0.02	Y	–
FeII								13.36 ± 0.14
NiII	1709	1709.604	3.24E-02	-100	50	< 13.17	Y	–
NiII	1751	1751.916	2.77E-02	-100	50	< 13.43	N	–
NiII								< 13.17
ZnII	2026	2026.136	4.89E-01	-100	50	< 12.10	Y	–
ZnII								< 12.10

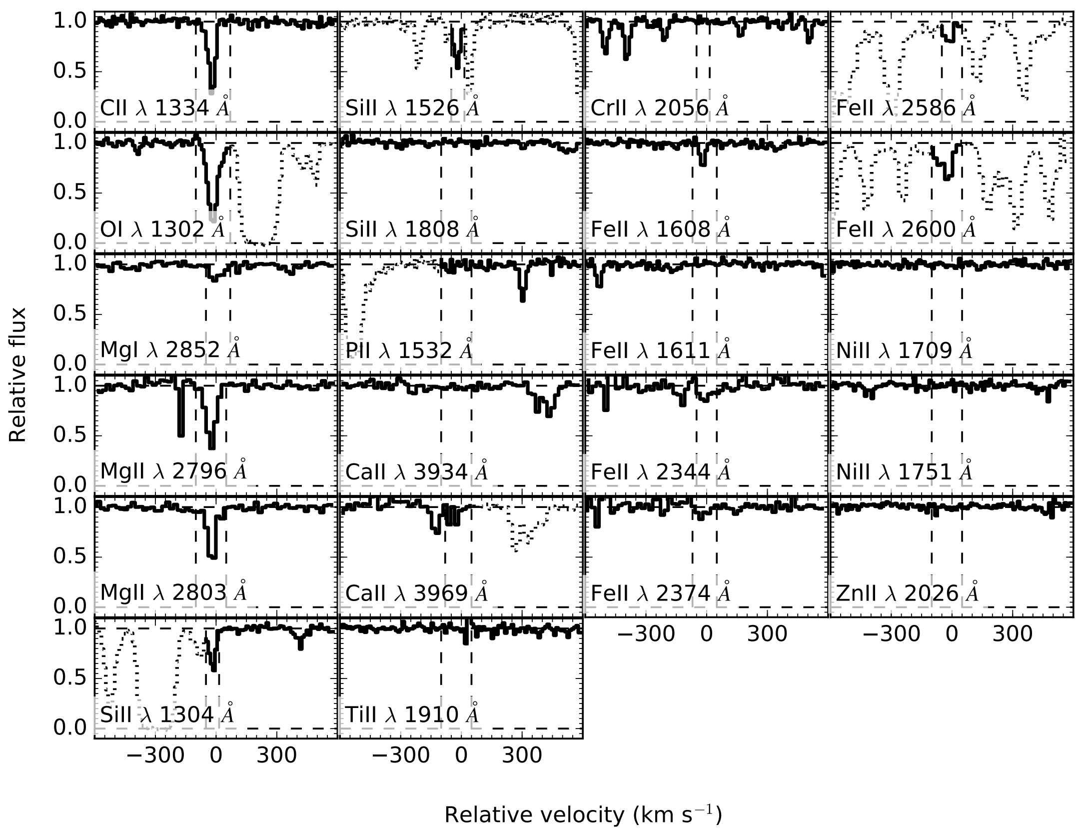

Figure B.30 Velocity profile of the XQ100 spectrum towards J1108+1209 (z_{abs}=3.397).

Table B.31 X-Shooter metal column densities for J1108+1209 (z_{abs}=3.546)

Ion	Line	λ Å	f	v_{min} km s^{-1}	v_{max} km s^{-1}	logN(X)	Included	logN$_{adopt}$
CII	1334	1334.532	1.28E-01	-200	110	> 15.06	Y	–
CII								> 15.06
OI	1302	1302.168	4.89E-02	-200	110	> 15.46	Y	–
OI								> 15.46
MgI	2852	2852.964	1.81E+00	-200	80	12.28 ± 0.02	Y	–
MgI								12.28 ± 0.05
MgII	2796	2796.352	6.12E-01	-200	110	> 13.75	N	–
MgII	2803	2803.531	3.05E-01	-200	110	> 14.13	Y	–
MgII								> 14.13
SiII	1260	1260.422	1.01E+00	-200	110	> 14.14	N	–
SiII	1304	1304.370	9.40E-02	-170	110	> 15.09	N	–
SiII	1808	1808.013	2.19E-03	-140	20	15.12 ± 0.03	Y	–
SiII								15.12 ± 0.05
PII	1532	1532.533	7.61E-03	-200	110	< 14.14	Y	–
PII								< 14.14
SII	1250	1250.584	5.43E-03	-140	70	14.81 ± 0.03	Y	–
SII	1253	1253.811	1.09E-02	-140	90	14.80 ± 0.01	Y	–
SII	1259	1259.519	1.66E-02	-140	40	< 15.13	N	–
SII								14.80 ± 0.05
TiII	1910	1910.750	2.02E-01	-200	110	12.56 ± 0.12	N	–
TiII	3384	3384.740	3.58E-01	-200	110	12.35 ± 0.08	Y	–
TiII								12.35 ± 0.08
MnII	2576	2576.877	3.51E-01	-200	90	< 12.79	Y	–
MnII	2594	2594.499	2.71E-01	-200	90	< 12.85	N	–
MnII	2606	2606.462	1.93E-01	-200	90	< 12.91	N	–
MnII								< 12.79
FeII	1608	1608.451	5.80E-02	-200	110	> 14.74	Y	–
FeII	1611	1611.200	1.36E-03	-200	110	< 14.97	Y	–
FeII	2249	2249.877	1.82E-03	-200	110	< 15.00	N	–
FeII	2344	2344.214	1.14E-01	-200	110	> 14.60	N	–
FeII	2374	2374.461	3.13E-02	-200	110	> 14.70	N	–
FeII	2586	2586.650	6.91E-02	-200	110	> 14.66	N	–
FeII								14.74–14.98
NiII	1709	1709.604	3.24E-02	-200	110	< 13.50	Y	–
NiII	1741	1741.553	4.27E-02	-200	110	< 13.46	Y	–
NiII	1751	1751.916	2.77E-02	-200	110	< 13.55	Y	–
NiII								< 13.46
ZnII	2026	2026.136	4.89E-01	-200	110	< 12.17	Y	–
ZnII								< 12.17

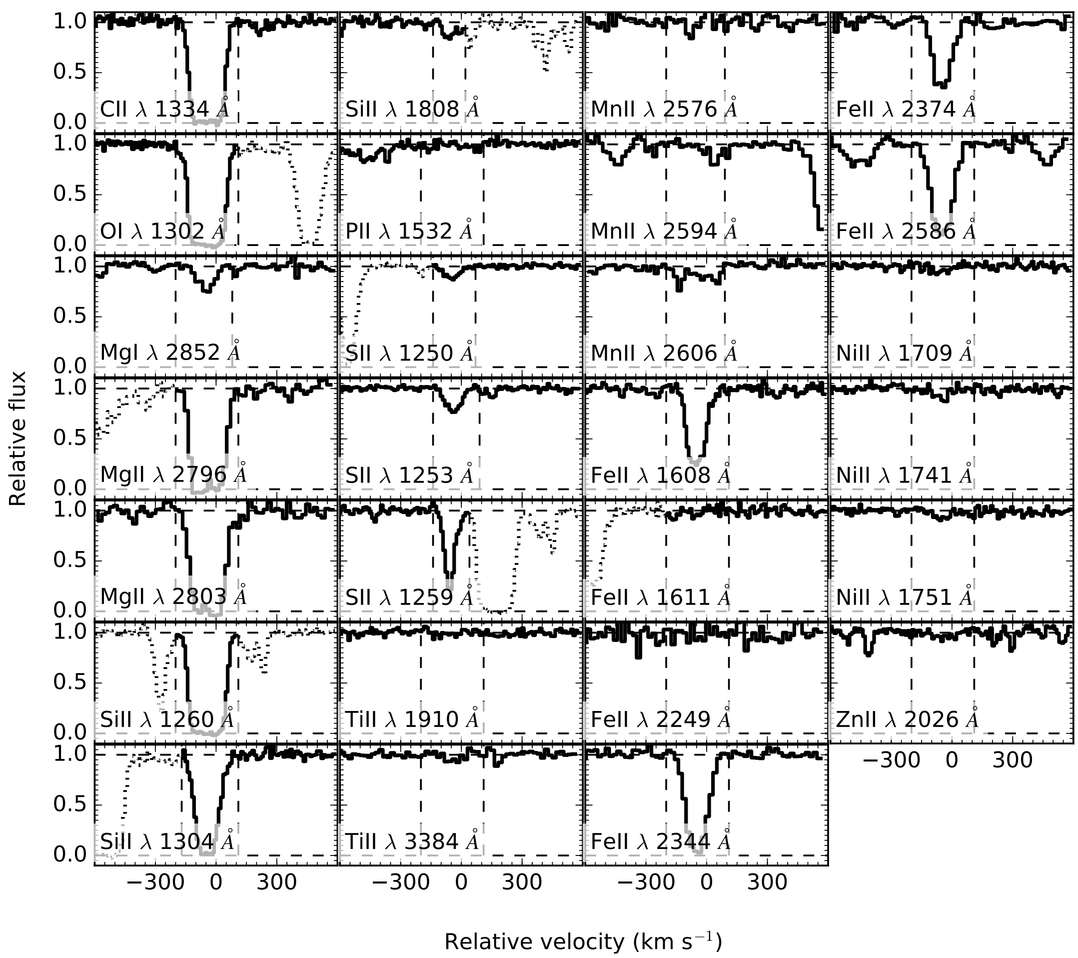

Figure B.31 Velocity profile of the XQ100 spectrum towards J1108+1209 (z_{abs}=3.546).

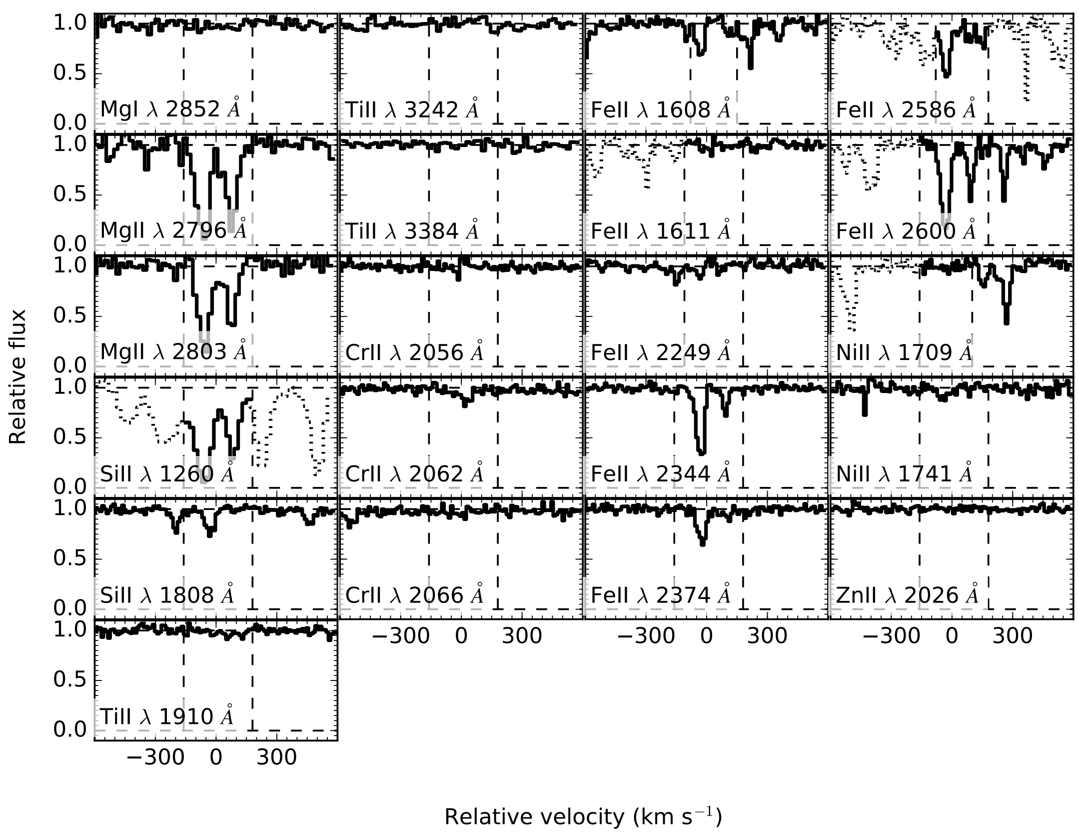

Figure B.32 Velocity profile of the XQ100 spectrum towards J1312+0841 (z_{abs}=2.660).

Table B.32 X-Shooter metal column densities for J1312+0841 (z_{abs}=2.660)

Ion	Line	λ Å	f	v_{min} km s^{-1}	v_{max} km s^{-1}	logN(X)	Included	$\log N_{adopt}$
MgI	2852	2852.964	1.81E+00	-160	180	< 11.67	Y	–
MgI								< 11.67
MgII	2796	2796.352	6.12E-01	-160	180	> 13.74	N	–
MgII	2803	2803.531	3.05E-01	-160	180	> 13.82	Y	–
MgII								> 13.82
SiII	1260	1260.422	1.01E+00	-160	180	> 13.94	Y	–
SiII	1808	1808.013	2.19E-03	-160	180	< 15.24	Y	–
SiII								13.94–15.24
TiII	1910	1910.750	2.02E-01	-160	180	< 12.60	N	–
TiII	3242	3242.929	2.32E-01	-160	180	< 12.51	N	–
TiII	3384	3384.740	3.58E-01	-160	180	< 12.26	Y	–
TiII								< 12.26
CrII	2056	2056.254	1.05E-01	-160	180	< 13.00	Y	–
CrII	2062	2062.234	7.80E-02	-160	180	< 13.19	N	–
CrII	2066	2066.161	5.15E-02	-160	180	< 13.18	N	–
CrII								< 13.00
FeII	1608	1608.451	5.80E-02	-80	150	< 13.96	N	–
FeII	1611	1611.200	1.36E-03	-110	180	14.98 ± 0.13	N	–
FeII	2249	2249.877	1.82E-03	-110	180	14.82 ± 0.07	N	–
FeII	2344	2344.214	1.14E-01	-160	180	> 13.95	N	–
FeII	2374	2374.461	3.13E-02	-160	180	14.15 ± 0.03	Y	–
FeII	2586	2586.650	6.91E-02	-80	180	< 14.07	N	–
FeII	2600	2600.173	2.39E-01	-160	180	> 13.80	N	–
FeII								14.15 ± 0.05
NiII	1709	1709.604	3.24E-02	-160	100	< 13.52	N	–
NiII	1741	1741.553	4.27E-02	-160	180	< 13.49	Y	–
NiII								< 13.49
ZnII	2026	2026.136	4.89E-01	-160	180	< 11.99	Y	–
ZnII								< 11.99

Table B.33 X-Shooter metal column densities for J1421−0643 (z_{abs}=3.449)

Ion	Line	λ Å	f	v_{min} km s^{-1}	v_{max} km s^{-1}	logN(X)	Included	$logN_{adopt}$
CII	1334	1334.532	1.28E-01	-160	200	> 14.68	Y	–
CII								> 14.68
OI	1302	1302.168	4.89E-02	-150	200	> 14.97	Y	–
OI								> 14.97
MgII	2796	2796.352	6.12E-01	-180	200	> 13.58	N	–
MgII	2803	2803.531	3.05E-01	-180	200	> 13.77	Y	–
MgII								> 13.77
SiII	1304	1304.370	9.40E-02	-110	160	> 14.29	Y	–
SiII	1526	1526.707	1.27E-01	-110	180	> 14.26	N	–
SiII	1808	1808.013	2.19E-03	-200	200	< 14.61	Y	–
SiII								14.29–14.61
PII	1532	1532.533	7.61E-03	-200	200	< 14.01	Y	–
PII								< 14.01
CaII	3934	3934.777	6.50E-01	-250	0	< 11.93	N	–
CaII								0.00 ± 0.05
TiII	1910	1910.750	2.02E-01	-200	200	< 12.56	Y	–
TiII	3384	3384.740	3.58E-01	-200	200	< 12.78	N	–
TiII								< 12.56
CrII	2056	2056.254	1.05E-01	-200	200	< 12.84	Y	–
CrII	2062	2062.234	7.80E-02	-200	40	< 13.05	N	–
CrII	2066	2066.161	5.15E-02	-200	200	< 13.37	N	–
CrII								< 12.84
FeII	1144	1144.938	1.06E-01	-200	40	13.95 ± 0.02	Y	–
FeII	1608	1608.451	5.80E-02	-200	40	14.10 ± 0.02	Y	–
FeII	1611	1611.200	1.36E-03	-200	200	15.09 ± 0.07	N	–
FeII	2344	2344.214	1.14E-01	-200	40	> 13.84	N	–
FeII	2374	2374.461	3.13E-02	-200	40	14.04 ± 0.03	Y	–
FeII	2600	2600.173	2.39E-01	-200	40	> 13.61	N	–
FeII								14.05 ± 0.05
NiII	1741	1741.553	4.27E-02	-200	200	< 13.36	Y	–
NiII	1751	1751.916	2.77E-02	-200	200	< 13.53	N	–
NiII								< 13.36
ZnII	2062	2062.664	2.56E-01	-200	200	< 13.25	Y	–
ZnII								< 13.25

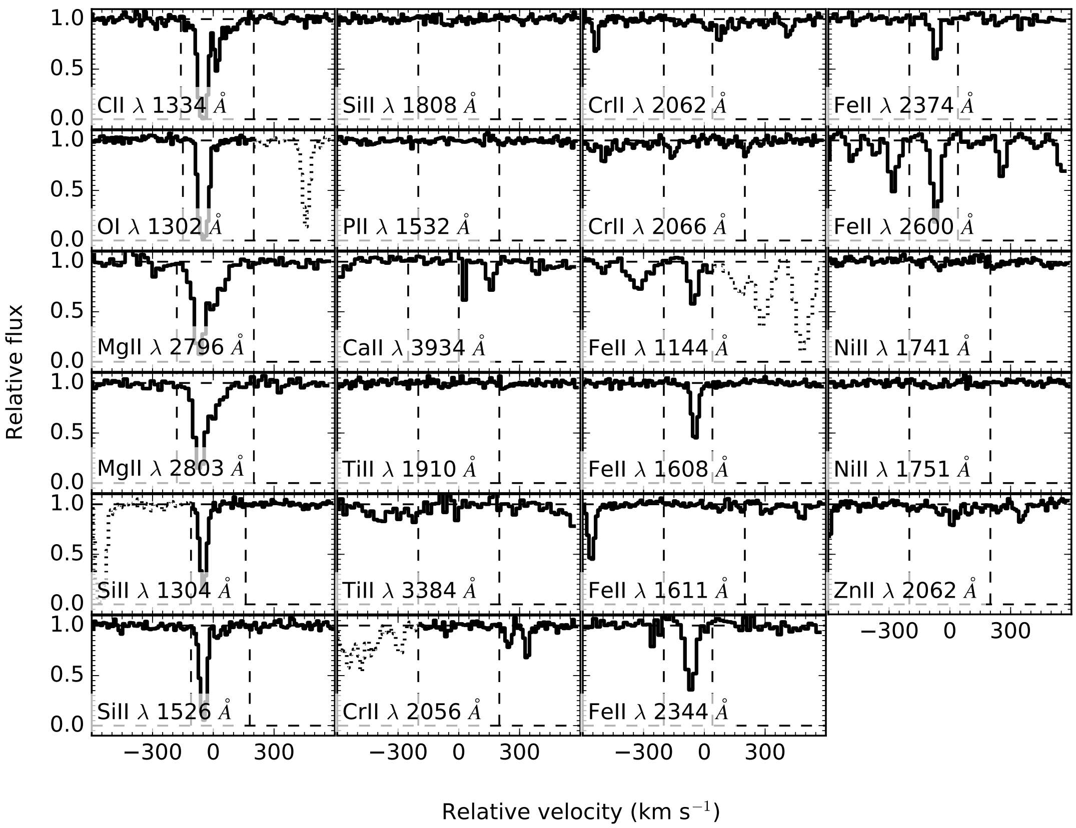

Figure B.33 Velocity profile of the XQ100 spectrum towards J1421-0643 (z_{abs}=3.449).

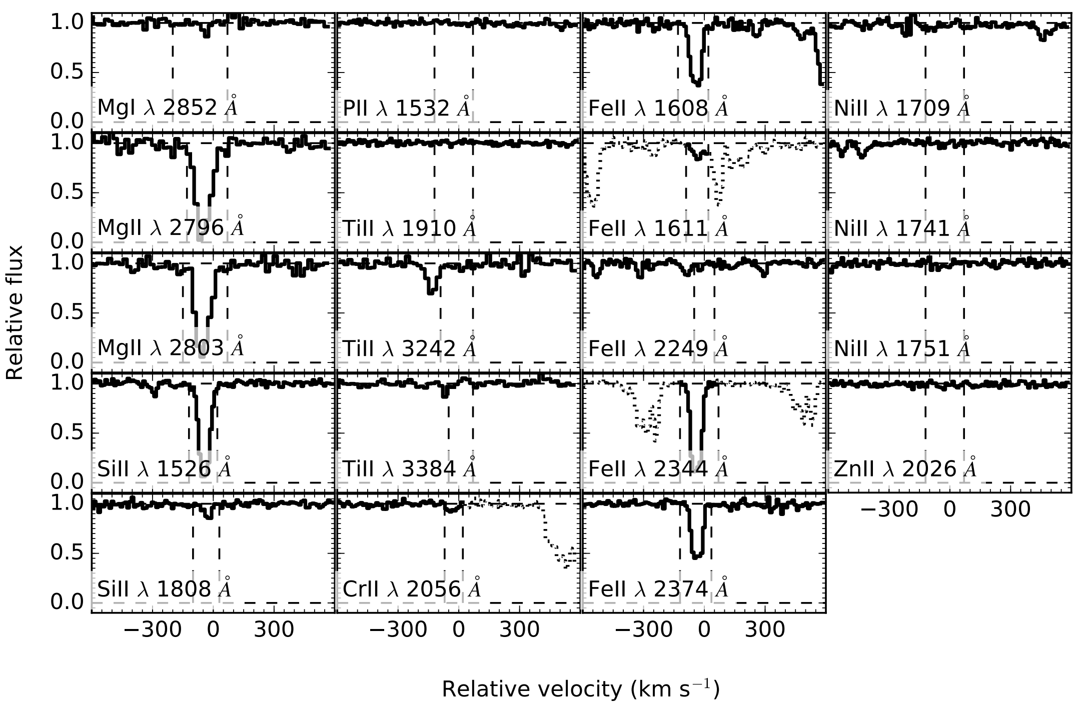

Figure B.34 Velocity profile of the XQ100 spectrum towards J1517+0511 (z_{abs}=2.688).

Table B.34 X-Shooter metal column densities for J1517+0511 (z_{abs}=2.688)

Ion	Line	λ Å	f	v_{min} km s^{-1}	v_{max} km s^{-1}	logN(X)	Included	logN_{adopt}
MgI	2852	2852.964	1.81E+00	-200	70	< 11.72	Y	–
MgI								< 11.72
MgII	2796	2796.352	6.12E-01	-130	70	> 13.63	N	–
MgII	2803	2803.531	3.05E-01	-150	70	> 13.85	Y	–
MgII								> 13.85
SiII	1526	1526.707	1.27E-01	-120	20	> 14.43	N	–
SiII	1808	1808.013	2.19E-03	-100	30	14.85 ± 0.05	Y	–
SiII								14.85 ± 0.05
PII	1532	1532.533	7.61E-03	-120	70	< 13.86	Y	–
PII								< 13.86
TiII	1910	1910.750	2.02E-01	-120	70	< 12.33	Y	–
TiII	3242	3242.929	2.32E-01	-90	70	< 12.27	Y	–
TiII	3384	3384.740	3.58E-01	-50	70	< 12.26	Y	–
TiII								< 12.26
CrII	2056	2056.254	1.05E-01	-70	20	12.91 ± 0.05	Y	–
CrII								12.91 ± 0.05
FeII	1608	1608.451	5.80E-02	-130	20	14.38 ± 0.01	Y	–
FeII	1611	1611.200	1.36E-03	-90	20	< 15.26	N	–
FeII	2249	2249.877	1.82E-03	-50	50	< 14.33	N	–
FeII	2344	2344.214	1.14E-01	-120	70	> 14.21	N	–
FeII	2374	2374.461	3.13E-02	-120	35	14.39 ± 0.01	Y	–
FeII								14.39 ± 0.05
NiII	1709	1709.604	3.24E-02	-120	70	< 13.44	N	–
NiII	1741	1741.553	4.27E-02	-120	70	< 13.21	Y	–
NiII	1751	1751.916	2.77E-02	-120	70	< 13.51	N	–
NiII								< 13.21
ZnII	2026	2026.136	4.89E-01	-120	70	< 12.06	Y	–
ZnII								< 12.06

Table B.35 X-Shooter metal column densities for J1552+1005 (z_{abs}=3.601)

Ion	Line	λ Å	f	v_{min} km s^{-1}	v_{max} km s^{-1}	logN(X)	Included	logN$_{adopt}$
CII	1334	1334.532	1.28E-01	-120	80	> 14.77	Y	–
CII								> 14.77
OI	1302	1302.168	4.89E-02	-120	80	> 15.12	Y	–
OI								> 15.12
MgII	2796	2796.352	6.12E-01	-120	80	> 13.66	N	–
MgII	2803	2803.531	3.05E-01	-150	80	> 14.04	Y	–
MgII								> 14.04
SiII	1260	1260.422	1.01E+00	-120	80	> 13.97	N	–
SiII	1304	1304.370	9.40E-02	-120	80	> 14.62	N	–
SiII	1526	1526.707	1.27E-01	-90	80	> 14.53	N	–
SiII	1808	1808.013	2.19E-03	-120	35	15.04 ± 0.04	Y	–
SiII								15.04 ± 0.05
PII	1532	1532.533	7.61E-03	-70	80	< 14.12	Y	–
PII								< 14.12
SII	1253	1253.811	1.09E-02	-60	40	14.50 ± 0.03	Y	–
SII	1259	1259.519	1.66E-02	-80	80	< 15.29	Y	–
SII								14.50 ± 0.05
TiII	1910	1910.750	2.02E-01	-70	80	< 12.75	N	–
TiII	3384	3384.740	3.58E-01	-70	80	< 12.67	Y	–
TiII								< 12.67
MnII	2576	2576.877	3.51E-01	-80	40	< 12.09	Y	–
MnII								< 12.09
FeII	1608	1608.451	5.80E-02	-120	80	> 14.41	Y	–
FeII	1611	1611.200	1.36E-03	-120	80	< 14.80	Y	–
FeII	2249	2249.877	1.82E-03	-120	80	< 15.20	N	–
FeII	2344	2344.214	1.14E-01	-120	80	> 14.16	N	–
FeII	2374	2374.461	3.13E-02	-120	0	> 14.31	N	–
FeII	2586	2586.650	6.91E-02	-120	80	> 14.26	N	–
FeII	2600	2600.173	2.39E-01	-80	80	> 13.97	N	–
FeII								14.40–14.80
NiII	1709	1709.604	3.24E-02	-70	80	< 13.42	Y	–
NiII	1741	1741.553	4.27E-02	-70	80	< 13.52	N	–
NiII	1751	1751.916	2.77E-02	-70	80	< 13.53	N	–
NiII								< 13.42

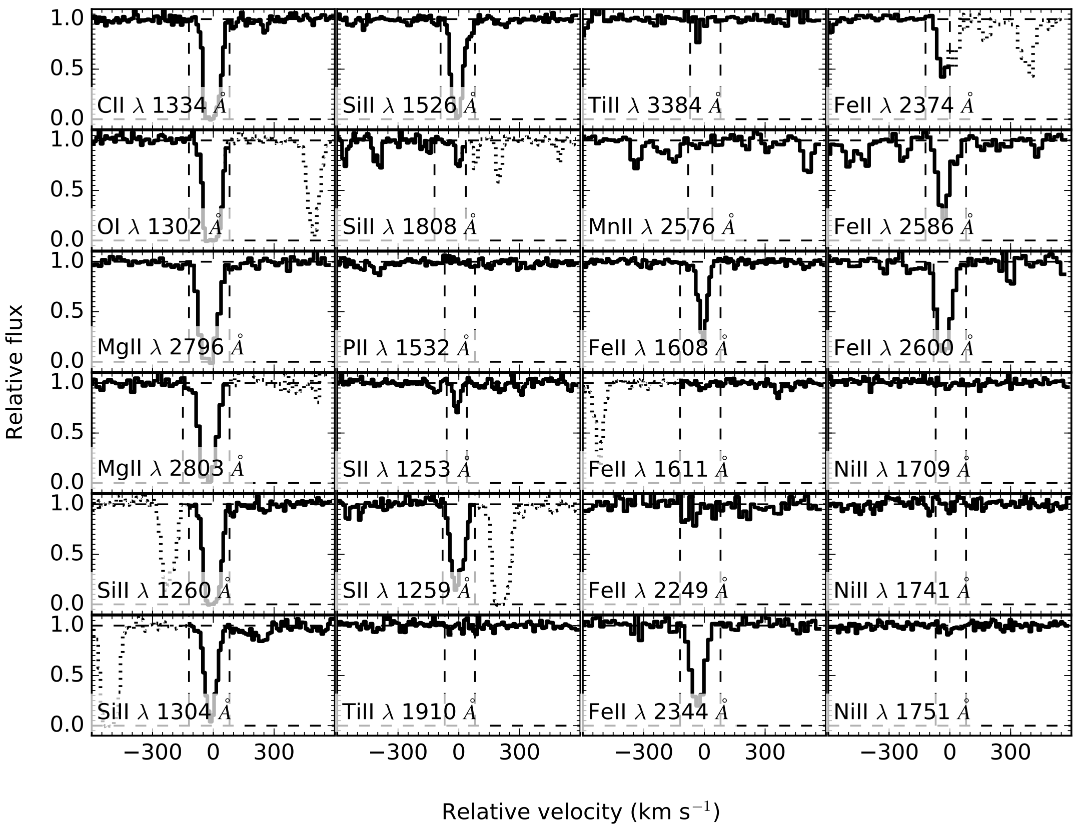

Figure B.35 Velocity profile of the XQ100 spectrum towards J1552+1005 (z_{abs}=3.601).

Table B.36 X-Shooter metal column densities for J1552+1005 (z_{abs}=3.667)

Ion	Line	λ Å	f	v_{min} km s^{-1}	v_{max} km s^{-1}	logN(X)	Included	logN$_{adopt}$
CII	1334	1334.532	1.28E-01	-260	200	>14.87	Y	–
CII								>14.87
OI	1302	1302.168	4.89E-02	-260	200	>15.18	Y	–
OI								>15.18
MgII	2796	2796.352	6.12E-01	-270	200	>13.86	N	–
MgII	2803	2803.531	3.05E-01	-270	200	>13.96	Y	–
MgII								>13.96
SiII	1260	1260.422	1.01E+00	-260	180	>14.05	N	–
SiII	1304	1304.370	9.40E-02	-230	170	>14.43	N	–
SiII	1526	1526.707	1.27E-01	-270	200	>14.46	Y	–
SiII	1808	1808.013	2.19E-03	-260	200	<14.79	Y	–
SiII								14.46–14.78
PII	1532	1532.533	7.61E-03	-260	130	<13.99	Y	–
PII								<13.99
SII	1250	1250.584	5.43E-03	-60	60	<14.40	Y	–
SII	1253	1253.811	1.09E-02	-60	60	<14.27	Y	–
SII								<14.27
TiII	1910	1910.750	2.02E-01	-260	160	<12.63	N	–
TiII	3242	3242.929	2.32E-01	-260	160	<12.53	Y	–
TiII	3384	3384.740	3.58E-01	-260	160	<12.63	N	–
TiII								<12.53
MnII	2594	2594.499	2.71E-01	-150	50	<12.31	Y	–
MnII	2606	2606.462	1.93E-01	-150	50	<12.75	N	–
MnII								<12.31
FeII	1608	1608.451	5.80E-02	-260	200	14.21 ± 0.01	Y	–
FeII	1611	1611.200	1.36E-03	-260	200	14.79 ± 0.14	N	–
FeII	2249	2249.877	1.82E-03	-90	60	14.78 ± 0.08	N	–
FeII	2344	2344.214	1.14E-01	-260	200	>13.99	N	–
FeII	2374	2374.461	3.13E-02	-240	220	14.66 ± 0.02	N	–
FeII	2586	2586.650	6.91E-02	-260	180	14.26 ± 0.01	Y	–
FeII	2600	2600.173	2.39E-01	-240	200	>13.86	N	–
FeII								14.24 ± 0.05
NiII	1709	1709.604	3.24E-02	-260	200	<13.49	N	–
NiII	1741	1741.553	4.27E-02	-260	200	<13.40	Y	–
NiII								<13.40

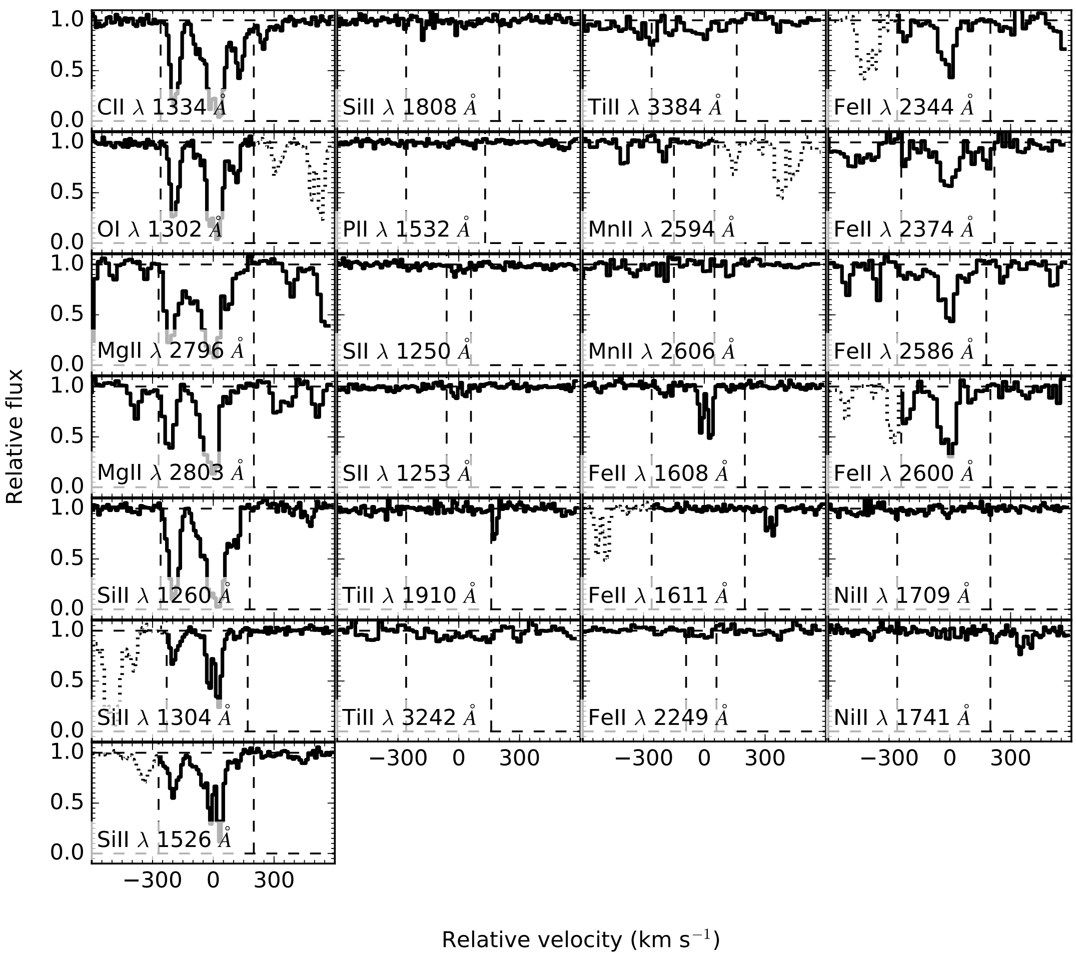

Figure B.36 Velocity profile of the XQ100 spectrum towards J1552+1005 (z_{abs}=3.667).

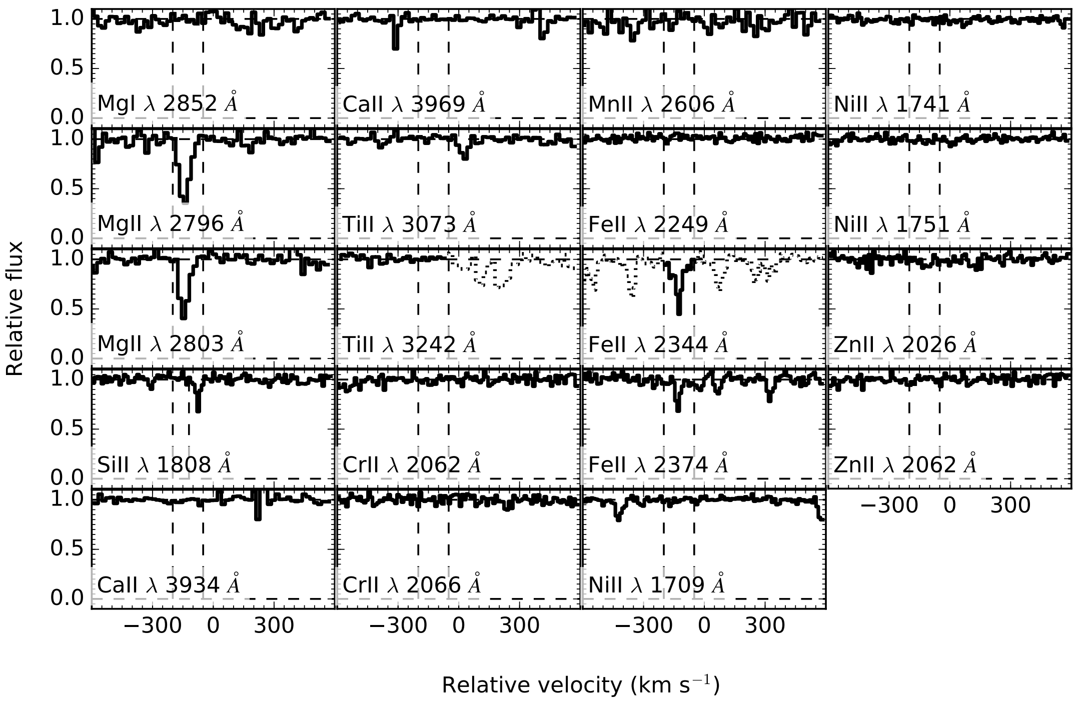

Figure B.37 Velocity profile of the XQ100 spectrum towards J1633+1411 (z_{abs}=2.882).

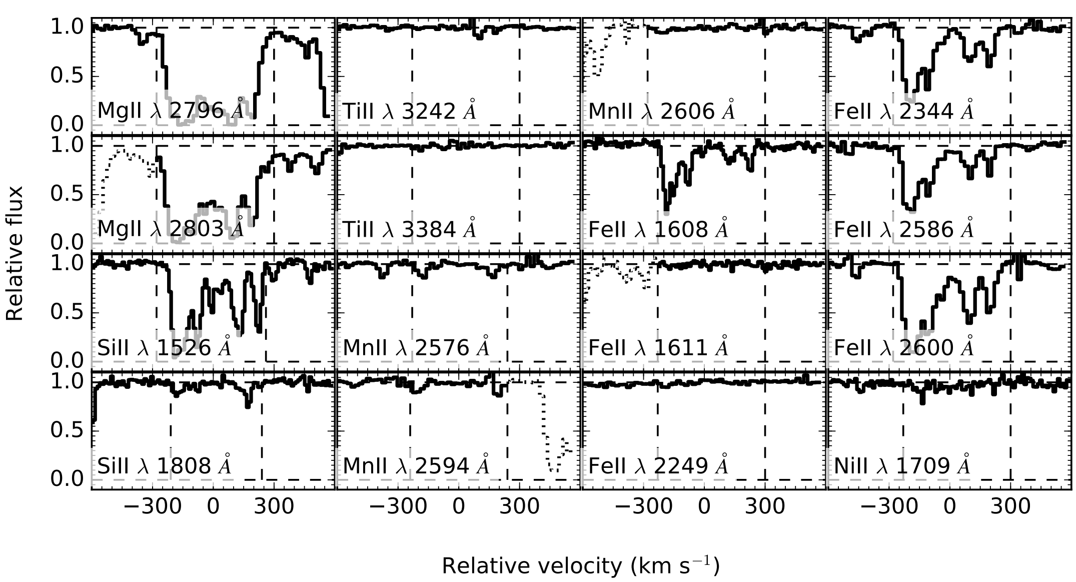

Figure B.38 Velocity profile of the XQ100 spectrum towards J1723+2243 (z_{abs}=3.698).

Table B.37 X-Shooter metal column densities for J1633+1411 (z_{abs}=2.882)

Ion	Line	λ Å	f	v_{min} km s^{-1}	v_{max} km s^{-1}	logN(X)	Included	$\log N_{adopt}$
MgI	2852	2852.964	1.81E+00	-200	-50	$<$ 11.60	Y	–
MgI								$<$ 11.60
MgII	2796	2796.352	6.12E-01	-200	-50	$>$ 13.09	N	–
MgII	2803	2803.531	3.05E-01	-200	-50	$>$ 13.27	Y	–
MgII								$>$ 13.27
SiII	1808	1808.013	2.19E-03	-200	-120	$<$ 14.45	Y	–
SiII								$<$ 14.45
CaII	3934	3934.777	6.50E-01	-200	-50	$<$ 11.51	Y	–
CaII	3969	3969.591	3.22E-01	-200	-50	$<$ 11.97	N	–
CaII								$<$ 11.51
TiII	3073	3073.877	1.09E-01	-200	-50	$<$ 12.67	N	–
TiII	3242	3242.929	2.32E-01	-200	-50	$<$ 12.08	Y	–
TiII								$<$ 12.08
CrII	2062	2062.234	7.80E-02	-200	-50	$<$ 12.90	Y	–
CrII	2066	2066.161	5.15E-02	-200	-50	$<$ 13.24	N	–
CrII								$<$ 12.90
MnII	2606	2606.462	1.93E-01	-200	-50	$<$ 12.90	Y	–
MnII								$<$ 12.90
FeII	2249	2249.877	1.82E-03	-200	-50	$<$ 14.52	N	–
FeII	2344	2344.214	1.14E-01	-200	-50	13.63 $\pm$ 0.02	Y	–
FeII	2374	2374.461	3.13E-02	-200	-50	13.79 $\pm$ 0.05	Y	–
FeII								13.67 $\pm$ 0.05
NiII	1709	1709.604	3.24E-02	-200	-50	$<$ 13.31	Y	–
NiII	1741	1741.553	4.27E-02	-200	-50	$<$ 13.23	Y	–
NiII	1751	1751.916	2.77E-02	-200	-50	$<$ 13.41	Y	–
NiII								$<$ 13.23
ZnII	2026	2026.136	4.89E-01	-200	-50	$<$ 12.28	Y	–
ZnII	2062	2062.664	2.56E-01	-200	-50	$<$ 12.40	N	–
ZnII								$<$ 12.28

Table B.38 X-Shooter metal column densities for J1723+2243 (z_{abs}=3.698)

Ion	Line	λ Å	f	v_{min} km s^{-1}	v_{max} km s^{-1}	logN(X)	Included	$logN_{adopt}$
MgII	2796	2796.352	6.12E-01	-280	300	> 14.41	N	–
MgII	2803	2803.531	3.05E-01	-280	300	> 14.57	Y	–
MgII								> 14.57
SiII	1526	1526.707	1.27E-01	-280	260	> 14.89	Y	–
SiII	1808	1808.013	2.19E-03	-210	240	< 15.37	Y	–
SiII								14.89–15.37
TiII	3242	3242.929	2.32E-01	-230	300	< 12.51	N	–
TiII	3384	3384.740	3.58E-01	-230	300	< 12.10	Y	–
TiII								< 12.10
MnII	2576	2576.877	3.51E-01	-230	240	< 12.55	N	–
MnII	2594	2594.499	2.71E-01	-240	240	< 12.71	N	–
MnII	2606	2606.462	1.93E-01	-280	300	< 12.46	Y	–
MnII								< 12.46
FeII	1608	1608.451	5.80E-02	-230	300	14.62 ± 0.01	Y	–
FeII	1611	1611.200	1.36E-03	-230	300	15.09 ± 0.09	N	–
FeII	2249	2249.877	1.82E-03	-230	300	14.72 ± 0.00	N	–
FeII	2344	2344.214	1.14E-01	-280	300	> 14.47	N	–
FeII	2586	2586.650	6.91E-02	-280	300	> 14.55	N	–
FeII	2600	2600.173	2.39E-01	-280	300	> 14.35	N	–
FeII								14.62 ± 0.05
NiII	1709	1709.604	3.24E-02	-230	300	< 13.63	Y	–
NiII								< 13.63

Table B.39 X-Shooter metal column densities for J2239−0552 (z_{abs}=4.080)

Ion	Line	λ Å	f	v_{min} km s^{-1}	v_{max} km s^{-1}	logN(X)	Included	$\log N_{adopt}$
CII	1334	1334.532	1.28E-01	-160	70	> 14.80	Y	–
CII								> 14.80
SiII	1526	1526.707	1.27E-01	-160	70	14.16 ± 0.00	Y	–
SiII	1808	1808.013	2.19E-03	-130	20	< 14.42	Y	–
SiII								14.16 ± 0.05
TiII	3073	3073.877	1.09E-01	-130	20	< 12.23	N	–
TiII	3242	3242.929	2.32E-01	-130	20	< 11.71	N	–
TiII	3384	3384.740	3.58E-01	-130	20	< 11.69	Y	–
TiII								< 11.69
CrII	2056	2056.254	1.05E-01	-130	20	< 12.63	Y	–
CrII	2066	2066.161	5.15E-02	-130	20	< 12.62	Y	–
CrII								< 12.62
MnII	2576	2576.877	3.51E-01	-130	20	< 12.44	N	–
MnII	2594	2594.499	2.71E-01	-130	20	< 12.05	Y	–
MnII								< 12.05
FeII	1608	1608.451	5.80E-02	-150	70	< 14.19	N	–
FeII	2249	2249.877	1.82E-03	-160	70	< 15.06	N	–
FeII	2344	2344.214	1.14E-01	-160	70	13.86 ± 0.01	Y	–
FeII	2374	2374.461	3.13E-02	-160	70	13.85 ± 0.04	Y	–
FeII	2586	2586.650	6.91E-02	-160	70	14.07 ± 0.01	Y	–
FeII	2600	2600.173	2.39E-01	-160	50	13.76 ± 0.01	N	–
FeII								14.00 ± 0.05
NiII	1709	1709.604	3.24E-02	-130	20	< 13.02	Y	–
NiII	1741	1741.553	4.27E-02	-130	20	< 13.17	Y	–
NiII	1751	1751.916	2.77E-02	-130	20	< 13.27	N	–
NiII								< 13.02
ZnII	2026	2026.136	4.89E-01	-130	20	< 12.51	Y	–
ZnII								< 12.51

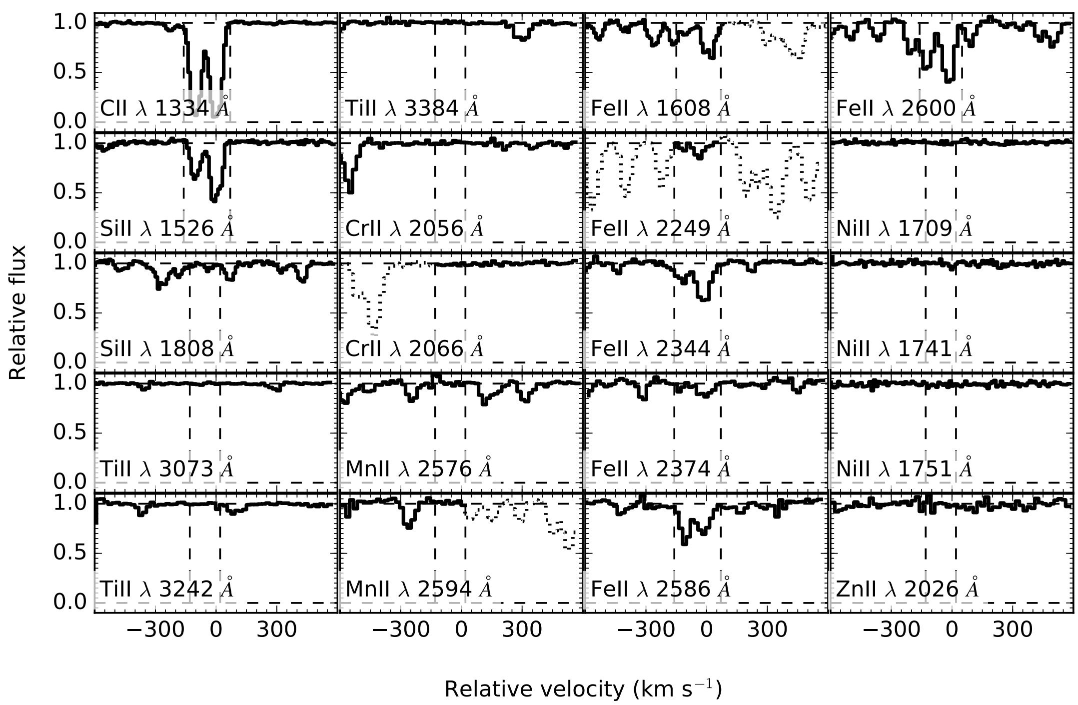

Figure B.39 Velocity profile of the XQ100 spectrum towards J2239-0552 (z_{abs}=4.080).

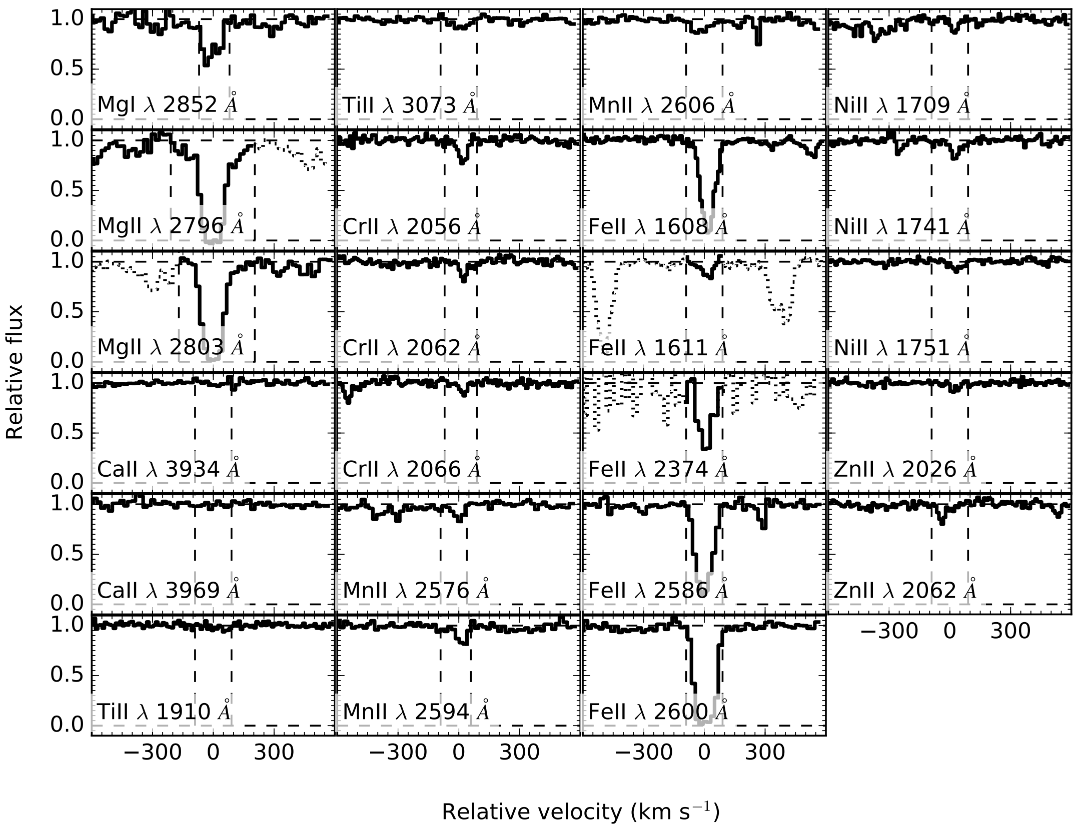

Figure B.40 Velocity profile of the XQ100 spectrum towards J2344+0342 (z_{abs}=3.220).

Table B.40 X-Shooter metal column densities for J2344+0342 (z_{abs}=3.220)

Ion	Line	λ Å	f	v_{min} km s^{-1}	v_{max} km s^{-1}	logN(X)	Included	logN$_{adopt}$
MgI	2852	2852.964	1.81E+00	-70	80	12.56 ± 0.01	Y	–
MgI								12.56 ± 0.05
MgII	2796	2796.352	6.12E-01	-210	205	> 13.74	N	–
MgII	2803	2803.531	3.05E-01	-170	205	> 14.18	Y	–
MgII								> 14.18
CaII	3934	3934.777	6.50E-01	-90	90	< 11.78	Y	–
CaII	3969	3969.591	3.22E-01	-90	90	< 12.07	N	–
CaII								< 11.78
TiII	1910	1910.750	2.02E-01	-90	90	< 12.53	Y	–
TiII	3073	3073.877	1.09E-01	-90	90	< 12.97	Y	–
TiII								< 12.53
CrII	2056	2056.254	1.05E-01	-70	90	13.38 ± 0.03	Y	–
CrII	2062	2062.234	7.80E-02	-70	90	< 13.28	Y	–
CrII	2066	2066.161	5.15E-02	-70	90	< 13.29	Y	–
CrII								13.38 ± 0.05
MnII	2576	2576.877	3.51E-01	-90	40	12.69 ± 0.05	Y	–
MnII	2594	2594.499	2.71E-01	-90	60	12.88 ± 0.05	Y	–
MnII	2606	2606.462	1.93E-01	-90	90	13.05 ± 0.04	N	–
MnII								12.79 ± 0.07
FeII	1608	1608.451	5.80E-02	-90	90	> 14.76	Y	–
FeII	1611	1611.200	1.36E-03	-90	90	< 15.29	Y	–
FeII	2374	2374.461	3.13E-02	-90	90	> 14.62	N	–
FeII	2586	2586.650	6.91E-02	-90	90	> 14.55	N	–
FeII	2600	2600.173	2.39E-01	-90	90	> 14.33	N	–
FeII								14.75–15.29
NiII	1709	1709.604	3.24E-02	-90	90	13.70 ± 0.05	Y	–
NiII	1741	1741.553	4.27E-02	-90	90	13.81 ± 0.03	Y	–
NiII	1751	1751.916	2.77E-02	-90	90	13.65 ± 0.06	Y	–
NiII								13.76 ± 0.08
ZnII	2026	2026.136	4.89E-01	-90	90	12.27 ± 0.08	N	–
ZnII	2062	2062.664	2.56E-01	-90	90	< 12.85	Y	–
ZnII								< 12.85

Table B.41 UVES metal column densities for J0034+1639 (z_{abs}=3.752)

Ion	Line	λ Å	f	v_{min} km s^{-1}	v_{max} km s^{-1}	logN(X)	Included	logN$_{adopt}$
CII	1036	1036.337	1.23E-01	-50	60	> 14.64	N	–
CII	1334	1334.532	1.28E-01	-60	40	> 14.72	Y	–
CII								> 14.72
OI	1302	1302.168	4.89E-02	-40	60	> 15.02	Y	–
OI								> 15.02
SiII	1260	1260.422	1.01E+00	-50	60	> 13.69	N	–
SiII	1304	1304.370	9.40E-02	-30	40	14.16 ± 0.01	Y	–
SiII	1526	1526.707	1.27E-01	-30	40	14.17 ± 0.04	Y	–
SiII	1808	1808.013	2.19E-03	-30	40	14.52 ± 0.05	N	–
SiII								14.16 ± 0.05
SII	1259	1259.519	1.66E-02	-30	40	< 14.70	Y	–
SII								< 14.70
FeII	1611	1611.200	1.36E-03	-50	40	< 14.01	Y	–
FeII								< 14.01
NiII	1709	1709.604	3.24E-02	-50	60	< 13.24	N	–
NiII	1741	1741.553	4.27E-02	-50	60	< 13.24	N	–
NiII	1751	1751.916	2.77E-02	-50	60	< 12.55	Y	–
NiII								< 12.55

B.2 UVES data J0034+1639

B.3 Abundance discrepancies of the XQ-100 DLA sample from literature values

J0003−2603 (z_{abs}= 3.39)

The Fe II literature column density was taken from Molaro et al. (2000). The discrepancy with the XQ-100 derived column density of 0.12 dex is the result of a difference in the adopted oscillator strengths. Molaro et al. (2000) uses an Fe II 1611 Å oscillator strength 33% higher than the value adopted from Morton (2003); matching the size of the discrepancy in column densities. I continue using the XQ-100 column density as the adopted value.

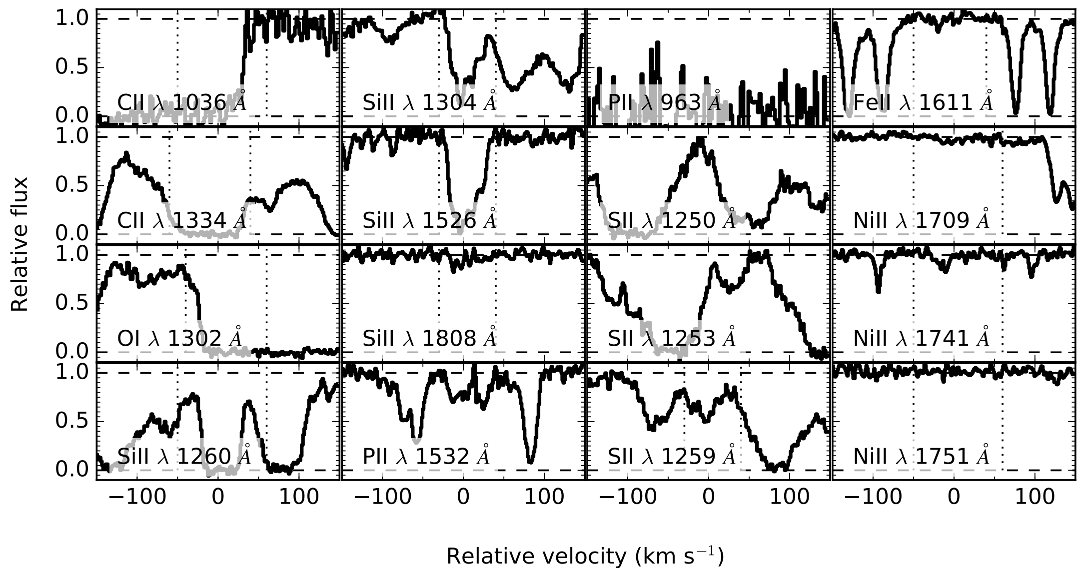

Figure B.41 Velocity profile of the UVES spectrum towards J0034+1639 (z_{abs}=3.752).

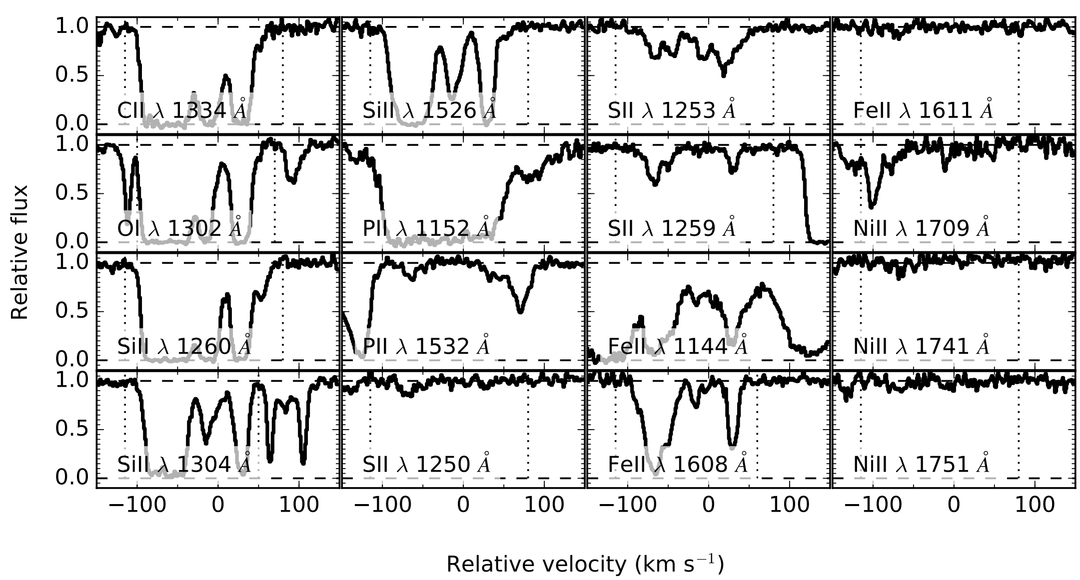

Figure B.42 Velocity profile of the UVES spectrum towards J0034+1639 (z_{abs}=4.282).

Table B.42 UVES metal column densities for J0034+1639 (z_{abs}=4.283)

Ion	Line	λ Å	f	v_{min} km s^{-1}	v_{max} km s^{-1}	logN(X)	Included	logN$_{adopt}$
CII	1334	1334.532	1.28E-01	-115	80	> 14.83	Y	–
CII								> 14.83
OI	1302	1302.168	4.89E-02	-100	70	> 15.29	Y	–
OI								> 15.29
SiII	1260	1260.422	1.01E+00	-115	80	> 14.04	N	–
SiII	1304	1304.370	9.40E-02	-115	50	> 14.83	Y	–
SiII	1526	1526.707	1.27E-01	-115	80	> 14.63	N	–
SiII								> 14.83
SII	1250	1250.584	5.43E-03	-115	80	14.53 ± 0.04	Y	–
SII	1253	1253.811	1.09E-02	-115	80	< 15.02	N	–
SII	1259	1259.519	1.66E-02	-115	80	14.59 ± 0.02	Y	–
SII								14.56 ± 0.05
FeII	1608	1608.451	5.80E-02	-115	60	14.54 ± 0.01	Y	–
FeII	1611	1611.200	1.36E-03	-115	80	14.83 ± 0.07	N	–
FeII								14.54 ± 0.05
NiII	1709	1709.604	3.24E-02	-115	80	< 14.27	N	–
NiII	1741	1741.553	4.27E-02	-115	80	< 13.05	Y	–
NiII	1751	1751.916	2.77E-02	-115	80	< 13.20	N	–
NiII								< 13.05

J0134+0400 (z_{abs}= 3.77)

The literature data is primarily taken from Prochaska et al. (2003b), and was obtained with ESI. Both the literature and XQ-100 spectra show Si II 1808 lines free from contamination, and provide abundances that are consistent with a saturated Si II 1526 lines. I suspect that my Si II 1808 measurement is more reliable as it reproduces the same velocity profile of other metal lines, whereas there appears to be an additional blue component (~ -75km s^{-1}) in the Prochaska et al. (2003b) profile.

The 0.14 dex discrepancy in the logN(Ni II) is likely due to inaccurate oscillator strengths of many Ni II lines (e.g. Jenkins & Tripp, 2006). Prochaska et al. (2003b) use the Ni II 1370Å line, whereas my value uses a combination of Ni II 1741 and 1751 Å lines. Given that adopted Ni II 1370Å line from Prochaska et al. (2003b) is also similarly higher ($\sim$ 0.12 dex) than from Morton (2003, my source of oscillator strengths), I believe accounting for this discrepancy in oscillator strengths would place the two column densities in agreement. I continue to adopt the XQ-100 derived column density.

J0255+0048 (z_{abs}= 3.25 and 3.91)

For both DLAs towards J0255+0048, I found discrepant Ni II from the values derived in Prochaska et al. (2001). For the DLA at z_{abs}= 3.25, Prochaska et al. (2001) claim a detection of the Ni II 1709 line, whereas I do not see any significant absorption in the XQ-100 spectra for the Ni II 1709 line. As my 3σ limit in column density is consistent with the detection by Prochaska et al. (2001), it is unclear whether the Ni II 1709 line is actually detected. I therefore conservatively adopt my logN(N II) limit.

The large discrepancy in the logN(Ni II) in the DLA at z_{abs}= 3.91 is likely due to inaccurate oscillator strengths of many Ni II lines. For the Ni II 1709, 1741, and 1751 lines; the oscillator strengths adopted in both works agree. However for Ni II 1317 and 1370, the oscillator strengths adopted in Prochaska et al. (2001) are $\sim$ 0.15 dex higher than ours. Accounting for this discrepancy in oscillator strength, my derived column density would be consistent with that measured by Prochaska et al. (2001). Jenkins & Tripp (2006) focused on independently measuring the oscillator strengths of Ni. The oscillator strengths from Morton (2003) (which I adopted) are consistent with those measured by Jenkins & Tripp (2006). I therefore adopt the XQ-100 column densities.

J1421−0643 (z_{abs}= 3.45)

The Fe II abundance was taken from Akerman et al. (2005), and is 0.09 dex higher than what I measured. The discrepancy in column density is driven by the inclusion of the Fe II 1144Å and 2374Å lines in the XQ-100 value, as the lower Fe II 1608Å column density agrees with the measured value of the 1608Å line from the literature (Akerman, 2005; Akerman et al., 2005). As multiple Fe II lines should provide a better estimate of the true column density, I continue to use the XQ-100 adopted column density.

Appendix C

Velocity profiles and equivalent widths

In this appendix, I present the velocity profiles and measured EWs for the COS-AGN sample on a sightline by sightline basis (see Chapter 4). For the five sightlines with absorption lines that appear marginally contaminated but could very well be real, I have justified why I did not adopt the measured EWs below.

J0042−1037 (z_{gal}=0.036)

The region of the Lyα absorption towards J0042−1037 at the redshift of the AGN host (z_{gal}=0.036) is heavily contaminated by Milky Way S II 1259 Å and Si II 1260 Å absorption lines (see Figure C.1). As a result, I could not constrain the amount of Lyα absorption in the CGM around this galaxy. The presence of a strong Si III 1206 Å line with minimal Lyα absorption is extremely unlikely, thus I did not trust the absorption present at the location of Si III 1206 Å (Figure C.1) to be associated with the CGM of the AGN host.

J1117+2634 (z_{gal}=0.029)

The CGM around the AGN host towards the QSO J1117+2634 (z_{gal}=0.029) is the only absorber whose Lyα feature is kinematically offset by a large amount (+350km s^{-1}; Figure C.8) relative to the host galaxy. This feature at +350km s^{-1} was selected as the associated CGM material as it is the only absorption not associated with the Galaxy (the component at ≈ -100km s^{-1} is Galactic S II 1250 Å) or another system at a different redshift. However, I am cautious in adopting the measured EW as this gas is highly offset, with no other absorption line to confirm this offset.

J1155+2922 (z_{gal}=0.046)

I flagged the absorption towards J1155+2922 at the expected location of Fe II 1144 Å of the AGN host (z_{gal}=0.046) as tenuous. The strongest component of the Fe II 1144 Å absorption is on the edge of the entire Lyα absorption feature. Given that the neutral CGM gas should be coincidental, and that the feature in question is uniquely very strong compared to other systems; I suspect this absorption is not from the CGM of the AGN host.

J1214+0825 (z_{gal}=0.074)

I note that for the AGN host towards J1214+0825 (z_{gal}=0.074) that the Lyα EW is heavily blended with the O I 1302 Å emission line from the Galaxy, making it impossible to determine a robust measurement of the EW. As a result, I did not adopt this EW into my final catalogue, even though the absorption feature is present.

J2133−0712 (z_{gal}=0.064)

The apparent Si III 1206 Å absorption for the AGN host towards J2133−0712 (z_{gal}=0.064) is offset $\approx +200$km s^{-1} from the Lyα absorption feature. Such strong velocity offsests are rarely seen for Si III from neutral H I in the CGM. I note the possibility that this absorption feature is coincident with an O VI 1037 Å absorber at higher redshift (z= 0.238), which is confirmed by a tenuously detected O VI 1031 Å feature at the same redshift. As a result, I did not associate this absorption with the AGN host.

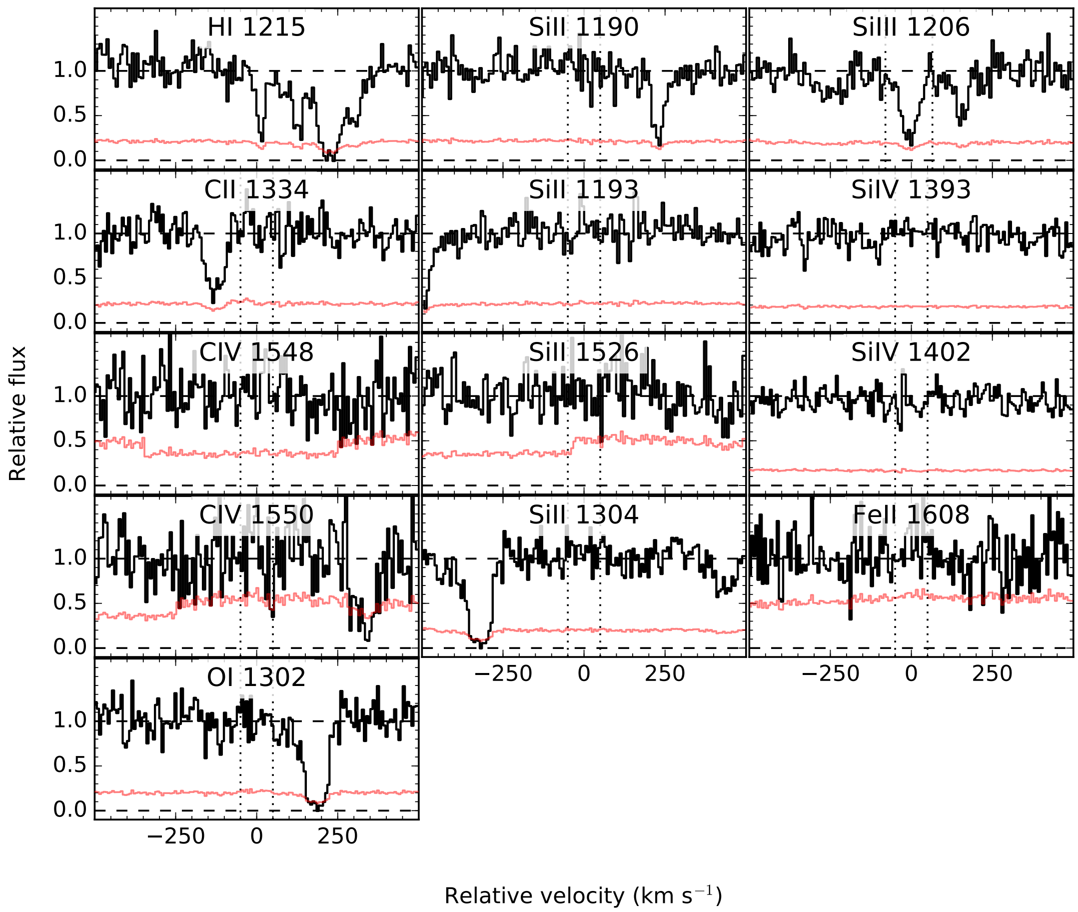

Figure C.1 Velocity profiles for the sightline towards J0042−1037 (z_{gal}=0.036).

Table C.1 Measured EWs for J0042-1037 195_406 (z=0.036)

Ion	λ Å	f	$v_{\rm min}$ km s^{-1}	$v_{\rm max}$ km s^{-1}	EW mÅ	flag*
HI	1215.670	4.164E-01	85	160	. . .	2
CII	1334.532	1.278E-01	-50	50	< 78	**5**
CIV	1548.195	1.908E-01	-50	50	< 148	**5**
CIV	1550.770	9.522E-02	-50	50	< 230	**5**
OI	1302.168	4.887E-02	-50	50	< 74	**5**
SiII	1190.416	2.502E-01	-50	50	< 71	**5**
SiII	1193.290	4.991E-01	-50	50	< 69	**5**
SiII	1526.707	1.270E-01	-50	50	< 192	**5**
SiII	1304.370	9.400E-02	-50	50	< 71	**5**
SiIII	1206.500	1.660E+00	-80	65	206 ± 22	**1**
SiIV	1393.755	5.280E-01	-50	50	< 64	**5**
SiIV	1402.770	2.620E-01	-50	50	< 57	**5**
FeII	1608.451	5.800E-02	-50	50	< 244	**5**

*The data quality flags represent a sum of whether or not the line is: adopted (+1), blended (+2), undetected (+4), or saturated (+8).

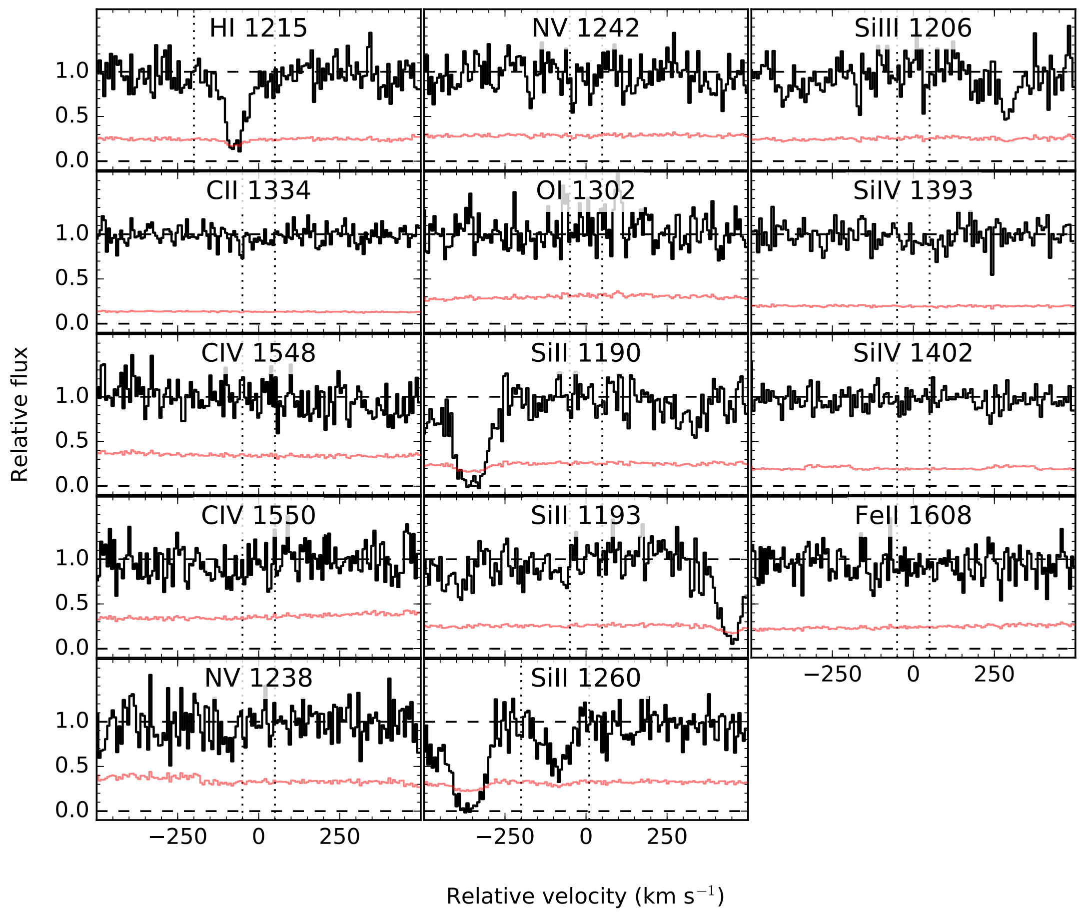

Figure C.2 Velocity profiles for the sightline towards J0116+1429 (z_{gal}=0.060).

Table C.2 Measured EWs for J0116+1429 (z=0.060)

Ion	λ [Å]	f	$v_{\min}$ [km s^{-1}]	$v_{\max}$ [km s^{-1}]	EW [mÅ]	flag*
H I	1215.670	4.164E-01	-200	50	306 ± 38	**9**
C II	1334.532	1.278E-01	-50	50	< 45	**5**
C IV	1548.195	1.908E-01	-50	50	< 138	**5**
C IV	1550.770	9.522E-02	-50	50	< 141	**5**
N V	1238.821	1.570E-01	-50	50	< 103	**5**
N V	1242.804	7.823E-02	-50	50	< 89	**5**
O I	1302.168	4.887E-02	-50	50	< 106	**5**
Si II	1190.416	2.502E-01	-50	50	< 84	**5**
Si II	1193.290	4.991E-01	-50	50	< 83	**5**
Si II	1260.422	1.007E+00	-200	10	< 190	**3**
Si III	1206.500	1.660E+00	-50	50	< 85	**5**
Si IV	1393.755	5.280E-01	-50	50	< 72	**5**
Si IV	1402.770	2.620E-01	-50	50	< 75	**5**
Fe II	1608.451	5.800E-02	-50	50	< 100	**5**

*The data quality flags represent a sum of whether or not the line is: adopted (+1), blended (+2), undetected (+4), or saturated (+8).

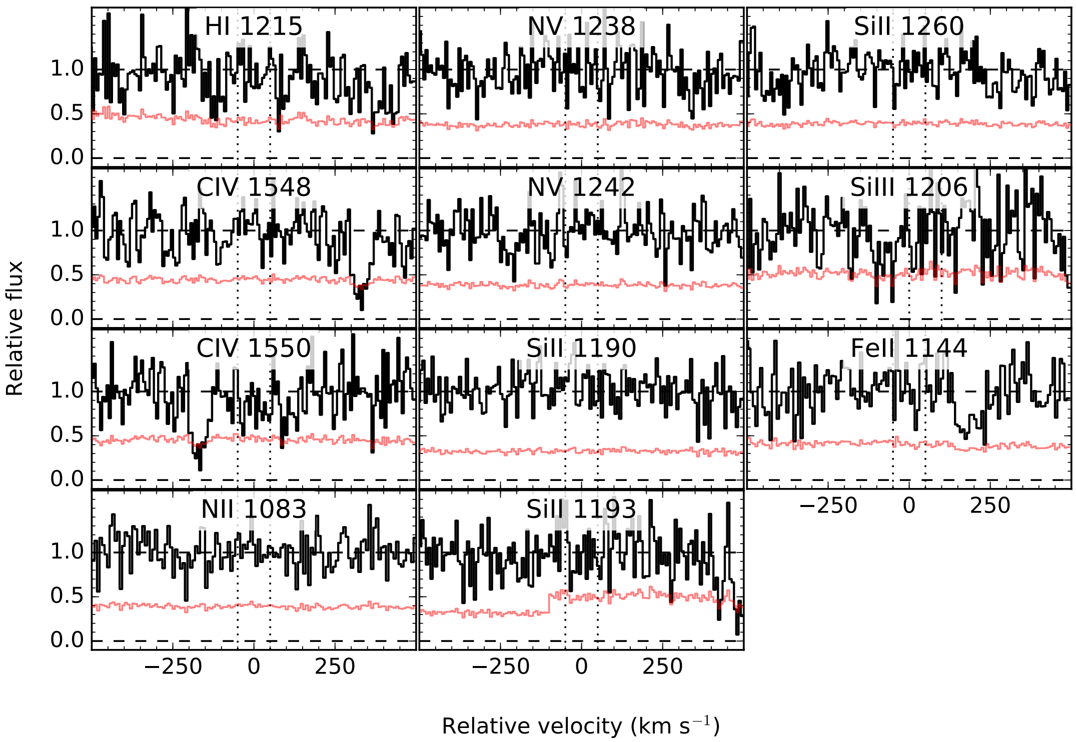

Figure C.3 Velocity profiles for the sightline towards J0843+4117 (z_{gal}=0.068).

Table C.3 Measured EWs for J0843+4117 (z=0.068)

Ion	λ [Å]	f	v_{min} [km s^{-1}]	v_{max} [km s^{-1}]	EW [mÅ]	flag*
H I	1215.670	4.164E-01	-50	50	< 131	**5**
C IV	1548.195	1.908E-01	-50	50	< 188	**5**
C IV	1550.770	9.522E-02	-50	50	< 188	**5**
N II	1083.990	1.031E-01	-50	50	< 123	**5**
N V	1238.821	1.570E-01	-50	50	< 124	**5**
N V	1242.804	7.823E-02	-50	50	< 127	**5**
Si II	1190.416	2.502E-01	-50	50	< 104	**5**
Si II	1193.290	4.991E-01	-50	50	< 156	**5**
Si II	1260.422	1.007E+00	-50	50	< 128	**5**
Si III	1206.500	1.660E+00	0	100	< 172	**5**
Fe II	1144.938	1.060E-01	-50	50	< 129	**5**

*The data quality flags represent a sum of whether or not the line is: adopted (+1), blended (+2), undetected (+4), or saturated (+8).

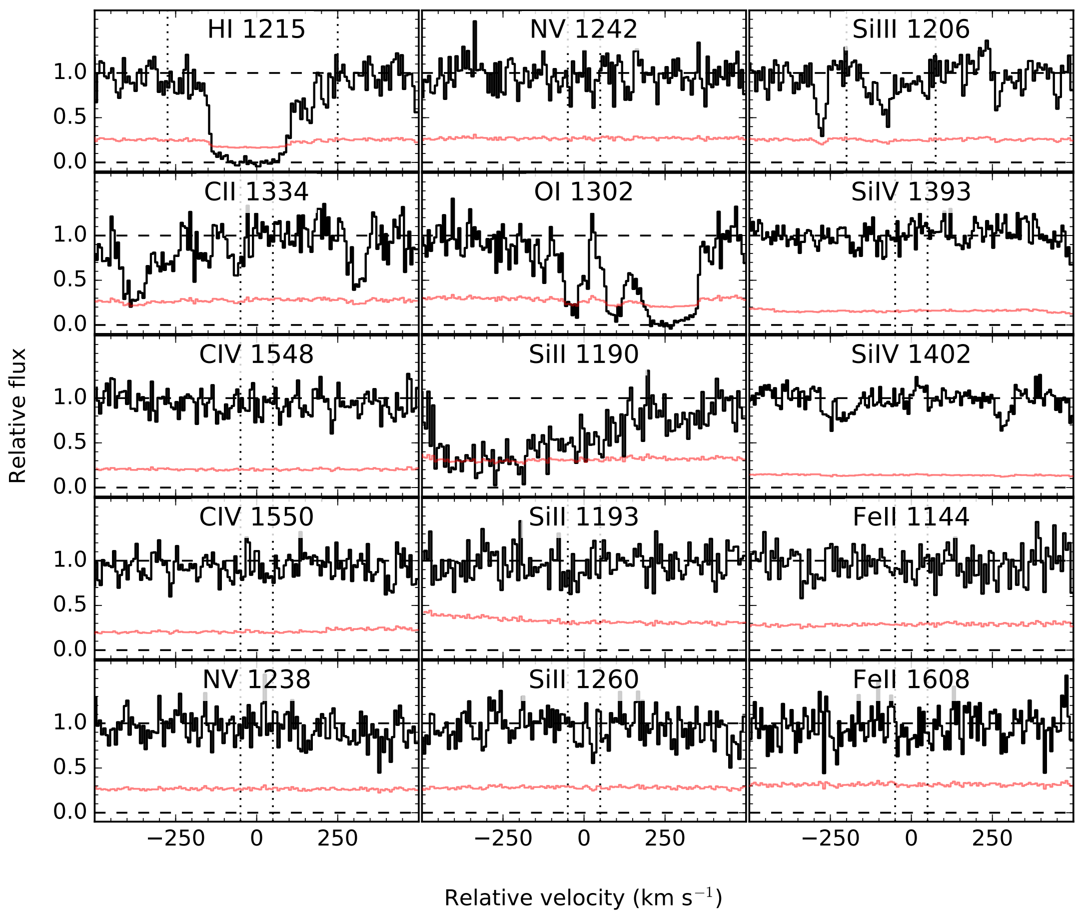

Figure C.4 Velocity profiles for the sightline towards J0851+4243 (z_{gal}=0.024).

Table C.4 Measured EWs for J0851+4243 (z=0.024)

Ion	λ [Å]	f	$v_{\rm min}$ [km s^{-1}]	$v_{\rm max}$ [km s^{-1}]	EW [mÅ]	flag*
H I	1215.670	4.164E-01	-275	250	1066 ± 53	**9**
C II	1334.532	1.278E-01	-50	50	< 64	**7**
C IV	1548.195	1.908E-01	-50	50	< 84	**5**
C IV	1550.770	9.522E-02	-50	50	< 85	**5**
N V	1238.821	1.570E-01	-50	50	< 92	**5**
N V	1242.804	7.823E-02	-50	50	< 87	**5**
O I	1302.168	4.887E-02	-275	250	. . .	2
Si II	1190.416	2.502E-01	-275	250	. . .	2
Si II	1193.290	4.991E-01	-50	50	< 98	**5**
Si II	1260.422	1.007E+00	-50	50	< 92	**5**
Si III	1206.500	1.660E+00	-200	75	165 ± 44	**1**
Si IV	1393.755	5.280E-01	-50	50	< 56	**5**
Si IV	1402.770	2.620E-01	-50	50	. . .	6
Fe II	1144.938	1.060E-01	-50	50	< 91	**5**
Fe II	1608.451	5.800E-02	-50	50	< 128	**5**

*The data quality flags represent a sum of whether or not the line is: adopted (+1), blended (+2), undetected (+4), or saturated (+8).

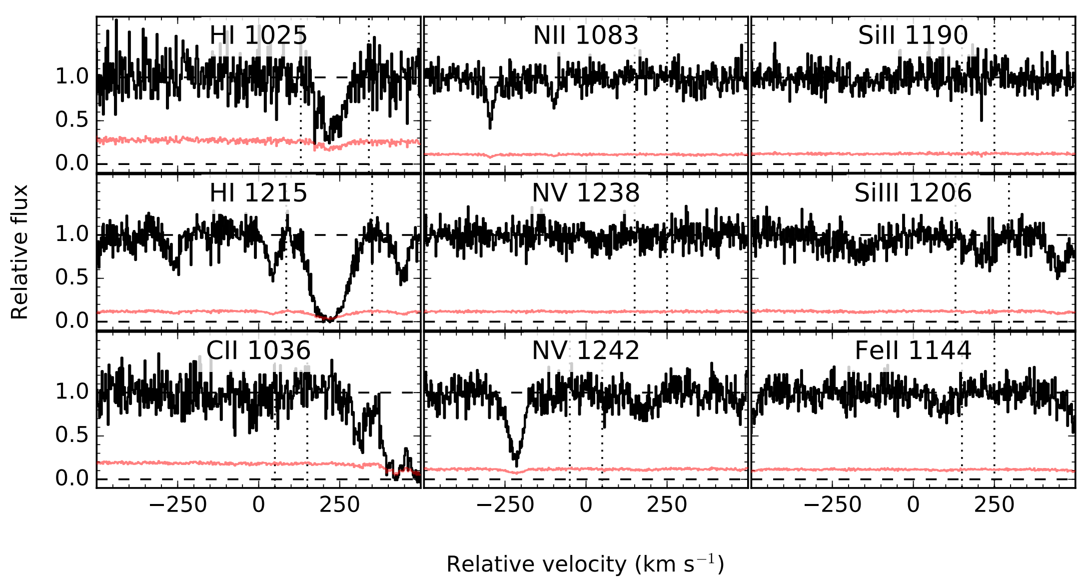

Figure C.5 Velocity profiles for the sightline towards J0853+4349 ($z_{\rm gal}$=0.090).

Table C.5 Measured EWs for J0853+4349 (z=0.090)

Ion	λ [Å]	f	v_{min} [km s^{-1}]	v_{max} [km s^{-1}]	EW [mÅ]	flag*
H I	1025.722	7.912E-02	130	340	185 ± 19	**9**
H I	1215.670	4.164E-01	85	350	512 ± 9	**9**
C II	1036.337	1.231E-01	50	150	< 30	**5**
N II	1083.990	1.031E-01	150	250	< 20	**5**
N V	1238.821	1.570E-01	150	250	< 21	**5**
N V	1242.804	7.823E-02	-50	50	< 22	**5**
Si II	1190.416	2.502E-01	150	250	< 22	**5**
Si III	1206.500	1.660E+00	130	295	71 ± 9	**1**
Fe II	1144.938	1.060E-01	150	250	< 20	**5**

*The data quality flags represent a sum of whether or not the line is: adopted (+1), blended (+2), undetected (+4), or saturated (+8).

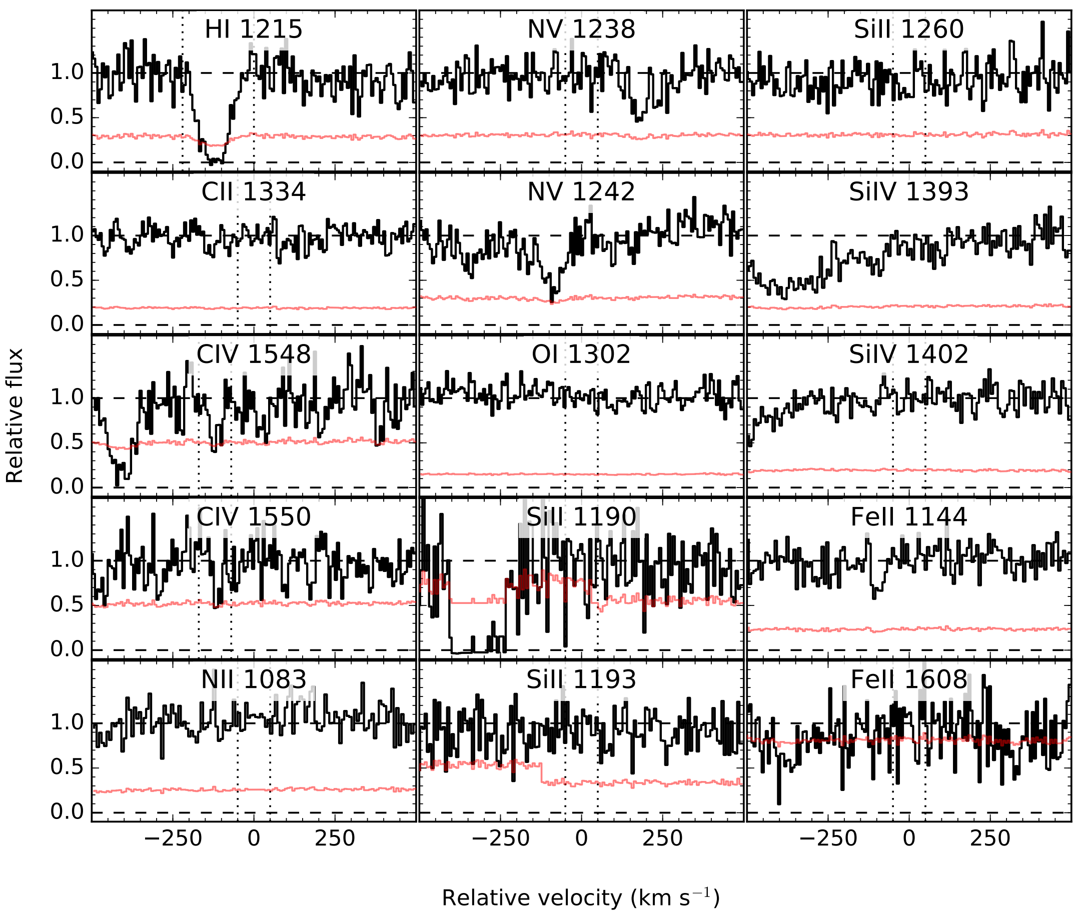

Figure C.6 Velocity profiles for the sightline towards J0948+5800 (z_{gal}=0.084).

Table C.6 Measured EWs for J0948+5800 (z=0.084)

Ion	λ [Å]	f	$v_{\rm min}$ [km s^{-1}]	$v_{\rm max}$ [km s^{-1}]	EW [mÅ]	flag*
H I	1215.670	4.164E-01	-220	0	398 ± 39	**9**
C II	1334.532	1.278E-01	-50	50	< 64	**5**
C IV	1548.195	1.908E-01	-170	-70	107 ± 67	**1**
C IV	1550.770	9.522E-02	-170	-70	29 ± 70	**1**
N II	1083.990	1.031E-01	-50	50	< 77	**5**
N V	1238.821	1.570E-01	-50	50	< 100	**5**
N V	1242.804	7.823E-02	-220	0	. . .	2
O I	1302.168	4.887E-02	-50	50	< 49	**5**
Si II	1190.416	2.502E-01	-50	50	< 221	**5**
Si II	1193.290	4.991E-01	-50	50	< 106	**5**
Si II	1260.422	1.007E+00	-50	50	< 98	**5**
Si IV	1393.755	5.280E-01	-220	0	. . .	6
Si IV	1402.770	2.620E-01	-50	50	< 74	**5**
Fe II	1144.938	1.060E-01	-200	-25	. . .	2
Fe II	1608.451	5.800E-02	-50	50	< 335	**5**

*The data quality flags represent a sum of whether or not the line is: adopted (+1), blended (+2), undetected (+4), or saturated (+8).

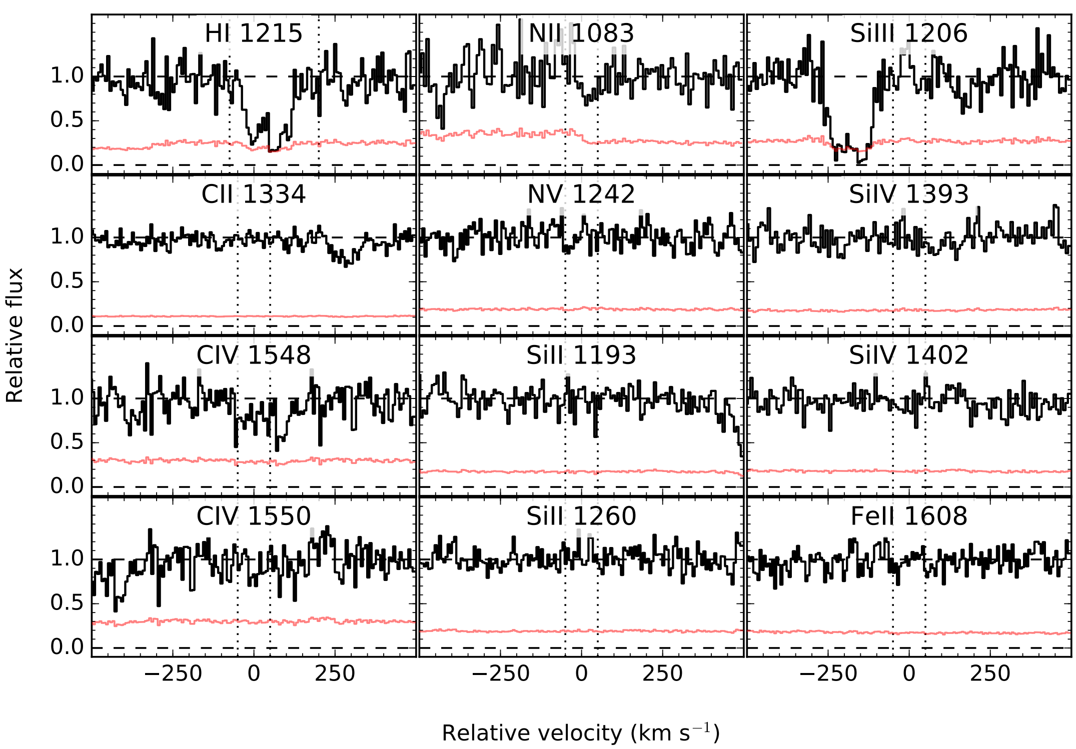

Figure C.7 Velocity profiles for the sightline towards J1117+2634 ($z_{\rm gal}$=0.065).

Table C.7 Measured EWs for J1117+2634 (z=0.065)

Ion	λ [Å]	f	$v_{\rm min}$ [km s^{-1}]	$v_{\rm max}$ [km s^{-1}]	EW [mÅ]	flag*
H I	1215.670	4.164E-01	-75	200	453 ± 38	**9**
C II	1334.532	1.278E-01	-50	50	< 38	**5**
C IV	1548.195	1.908E-01	-50	50	< 113	**5**
C IV	1550.770	9.522E-02	-50	50	< 118	**5**
N II	1083.990	1.031E-01	-50	50	< 96	**5**
N V	1242.804	7.823E-02	-50	50	< 61	**5**
Si II	1193.290	4.991E-01	-50	50	< 54	**5**
Si II	1260.422	1.007E+00	-50	50	< 63	**5**
Si III	1206.500	1.660E+00	-50	50	< 87	**5**
Si IV	1393.755	5.280E-01	-50	50	< 68	**5**
Si IV	1402.770	2.620E-01	-50	50	< 68	**5**
Fe II	1608.451	5.800E-02	-50	50	< 68	**5**

*The data quality flags represent a sum of whether or not the line is: adopted (+1), blended (+2), undetected (+4), or saturated (+8).

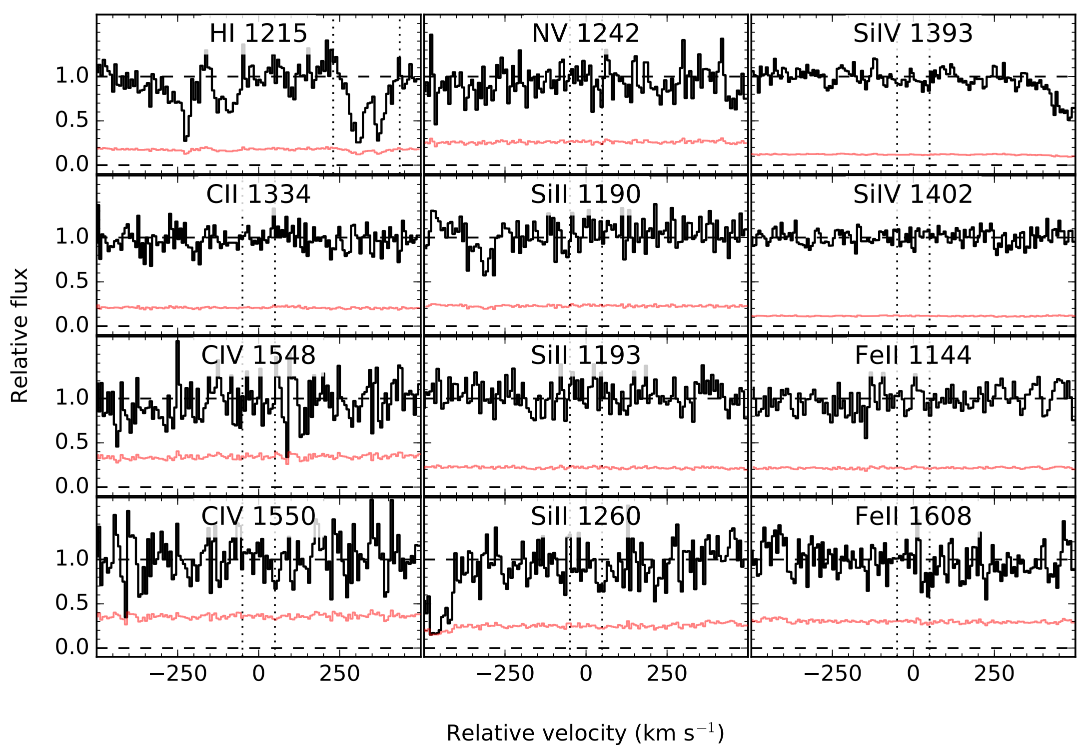

Figure C.8 Velocity profiles for the sightline towards J1117+2634 ($z_{\rm gal}$=0.029).

Table C.8 Measured EWs for J1117+2634 (z=0.029)

Ion	λ [Å]	f	$v_{\rm min}$ [km s^{-1}]	$v_{\rm max}$ [km s^{-1}]	EW [mÅ]	flag*
H I	1215.670	4.164E-01	230	435	256 ± 25	**9**
C II	1334.532	1.278E-01	-50	50	< 73	**5**
C IV	1548.195	1.908E-01	-50	50	< 138	**5**
C IV	1550.770	9.522E-02	-50	50	< 148	**5**
N V	1242.804	7.823E-02	-50	50	< 86	**5**
Si II	1190.416	2.502E-01	-50	50	< 77	**5**
Si II	1193.290	4.991E-01	-50	50	< 74	**5**
Si II	1260.422	1.007E+00	-50	50	< 82	**5**
Si IV	1393.755	5.280E-01	-50	50	< 41	**5**
Si IV	1402.770	2.620E-01	-50	50	< 42	**5**
Fe II	1144.938	1.060E-01	-50	50	< 68	**5**
Fe II	1608.451	5.800E-02	-50	50	< 124	**5**

*The data quality flags represent a sum of whether or not the line is: adopted (+1), blended (+2), undetected (+4), or saturated (+8).

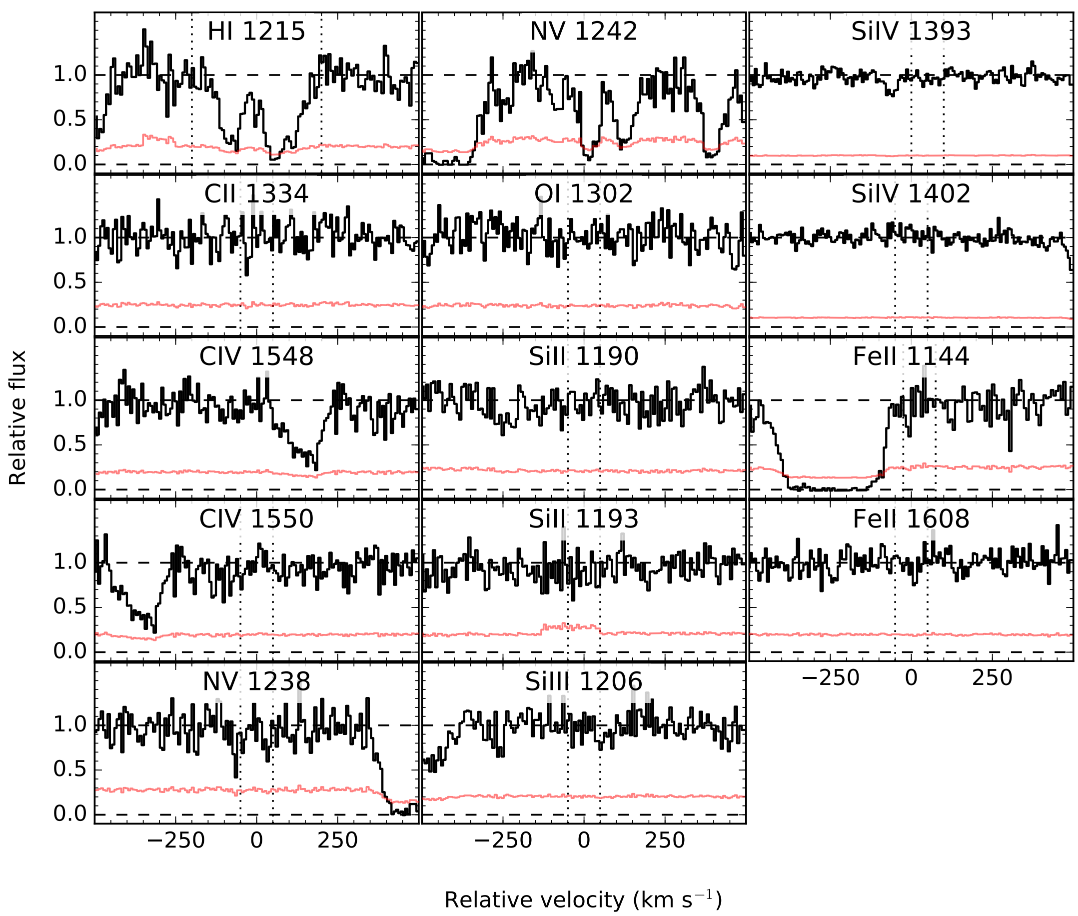

Figure C.9 Velocity profiles for the sightline towards J1127+2654 ($z_{\rm gal}$=0.033).

Table C.9 Measured EWs for J1127+2654 (z=0.033)

Ion	λ [Å]	f	$v_{\rm min}$ [km s^{-1}]	$v_{\rm max}$ [km s^{-1}]	EW [mÅ]	flag*
H I	1215.670	4.164E-01	-200	200	723 ± 36	**9**
C II	1334.532	1.278E-01	-50	50	< 83	**5**
C IV	1548.195	1.908E-01	-200	200	. . .	2
C IV	1550.770	9.522E-02	-50	50	< 79	**5**
N V	1238.821	1.570E-01	-50	50	< 88	**5**
N V	1242.804	7.823E-02	-200	200	. . .	2
O I	1302.168	4.887E-02	-50	50	< 80	**5**
Si II	1190.416	2.502E-01	-50	50	< 66	**5**
Si II	1193.290	4.991E-01	-50	50	< 90	**5**
Si III	1206.500	1.660E+00	-50	50	< 66	**5**
Si IV	1393.755	5.280E-01	0	100	< 34	**5**
Si IV	1402.770	2.620E-01	-50	50	< 39	**5**
Fe II	1144.938	1.060E-01	-25	75	< 83	**5**
Fe II	1608.451	5.800E-02	-50	50	< 80	**5**

*The data quality flags represent a sum of whether or not the line is: adopted (+1), blended (+2), undetected (+4), or saturated (+8).

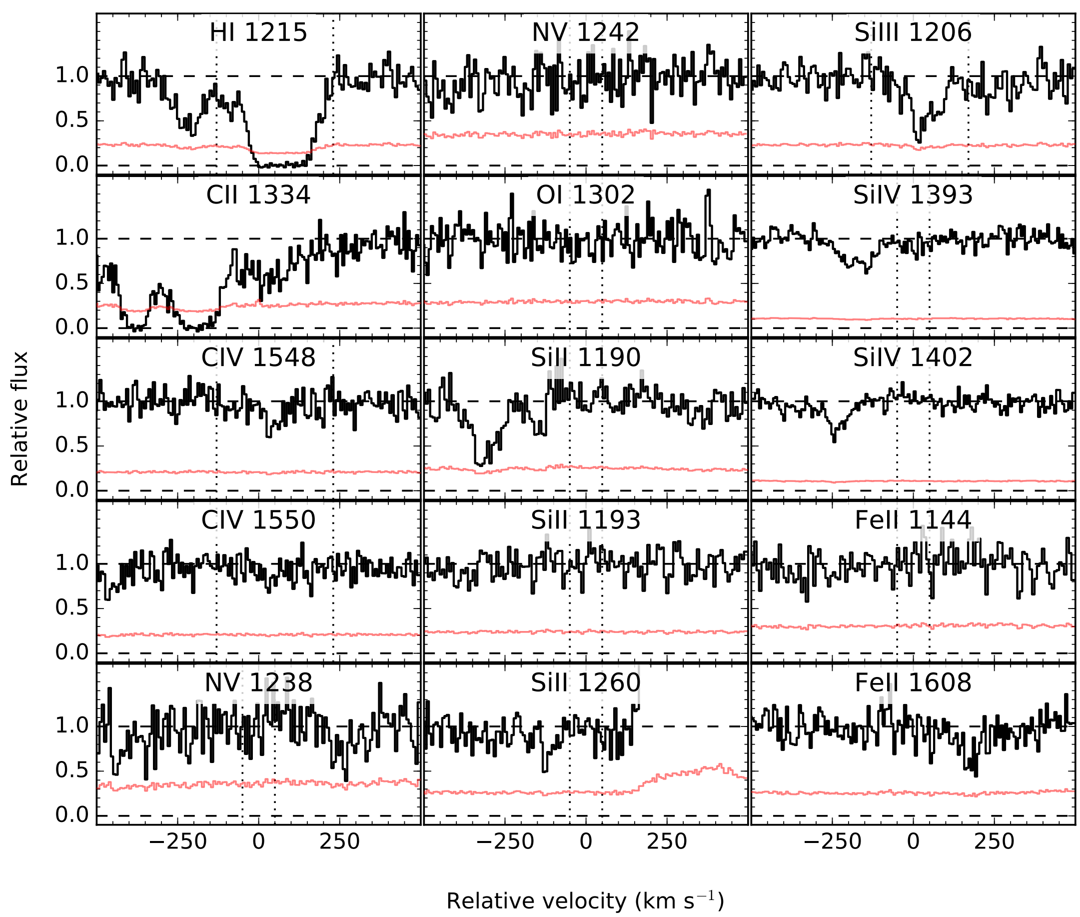

Figure C.10 Velocity profiles for the sightline towards J1142+3016 ($z_{\rm gal}$=0.032).

Table C.10 Measured EWs for J1142+3016 (z=0.032)

Ion	λ [Å]	f	$v_{\rm min}$ [km s^{-1}]	$v_{\rm max}$ [km s^{-1}]	EW [mÅ]	flag*
H I	1215.670	4.164E-01	-130	230	927 ± 36	**9**
C II	1334.532	1.278E-01	-230	130	. . .	2
C IV	1548.195	1.908E-01	-130	230	167 ± 53	**1**
C IV	1550.770	9.522E-02	-130	230	129 ± 54	**1**
N V	1238.821	1.570E-01	-50	50	< 123	**5**
N V	1242.804	7.823E-02	-50	50	< 114	**5**
O I	1302.168	4.887E-02	-50	50	< 100	**5**
Si II	1190.416	2.502E-01	-50	50	< 82	**5**
Si II	1193.290	4.991E-01	-50	50	< 76	**5**
Si II	1260.422	1.007E+00	-50	50	< 86	**5**
Si III	1206.500	1.660E+00	-130	170	268 ± 41	**1**
Si IV	1393.755	5.280E-01	-50	50	< 36	**5**
Si IV	1402.770	2.620E-01	-50	50	< 38	**5**
Fe II	1144.938	1.060E-01	-50	50	< 98	**5**
Fe II	1608.451	5.800E-02	-50	50	. . .	4

*The data quality flags represent a sum of whether or not the line is: adopted (+1), blended (+2), undetected (+4), or saturated (+8).

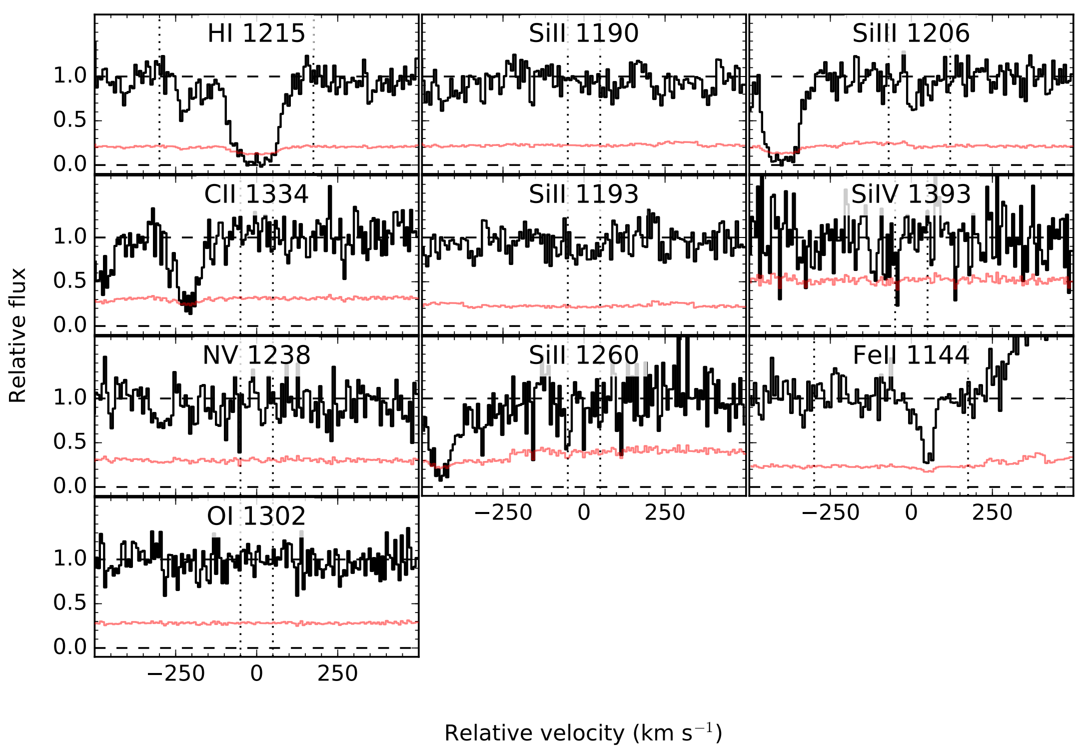

Figure C.11 Velocity profiles for the sightline towards J1155+2922 ($z_{\rm gal}$=0.046).

Table C.11 Measured EWs for J1155+2922 (z=0.046)

Ion	λ [Å]	f	$v_{\rm min}$ [km s^{-1}]	$v_{\rm max}$ [km s^{-1}]	EW [mÅ]	flag*
H I	1215.670	4.164E-01	-300	175	721 ± 43	**9**
C II	1334.532	1.278E-01	-50	50	< 109	**5**
N V	1238.821	1.570E-01	-50	50	< 100	**5**
O I	1302.168	4.887E-02	-50	50	< 97	**5**
Si II	1190.416	2.502E-01	-50	50	< 71	**5**
Si II	1193.290	4.991E-01	-50	50	< 69	**5**
Si II	1260.422	1.007E+00	-50	50	< 124	**5**
Si III	1206.500	1.660E+00	-70	120	73 ± 33	**1**
Si IV	1393.755	5.280E-01	-50	50	< 177	**5**
Fe II	1144.938	1.060E-01	-300	175	85 ± 52	**1**

*The data quality flags represent a sum of whether or not the line is: adopted (+1), blended (+2), undetected (+4), or saturated (+8).

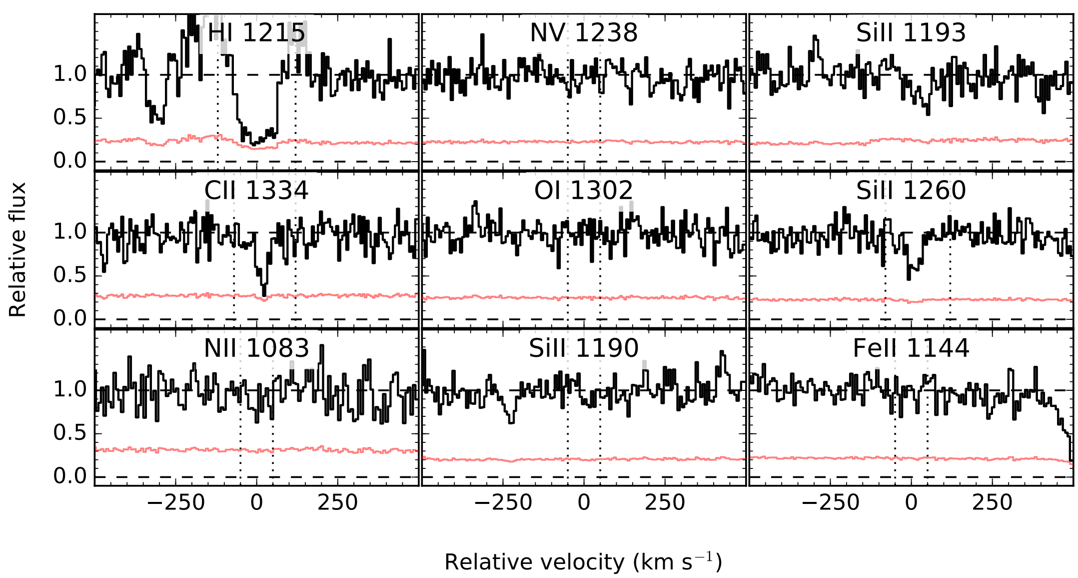

Figure C.12 Velocity profiles for the sightline towards J1214+0825 ($z_{\rm gal}$=0.074).

Table C.12 Measured EWs for J1214+0825 (z=0.074)

Ion	λ [Å]	f	$v_{\rm min}$ [km s^{-1}]	$v_{\rm max}$ [km s^{-1}]	EW [mÅ]	flag*
H I	1215.670	4.164E-01	-120	120	229 ± 34	**9**
C II	1334.532	1.278E-01	-70	120	154 ± 41	**1**
N II	1083.990	1.031E-01	-50	50	< 92	**5**
N V	1238.821	1.570E-01	-50	50	< 74	**5**
O I	1302.168	4.887E-02	-50	50	< 83	**5**
Si II	1190.416	2.502E-01	-50	50	< 66	**5**
Si II	1193.290	4.991E-01	-50	120	. . .	2
Si II	1260.422	1.007E+00	-80	120	107 ± 34	**1**
Fe II	1144.938	1.060E-01	-50	50	< 65	**5**

*The data quality flags represent a sum of whether or not the line is: adopted (+1), blended (+2), undetected (+4), or saturated (+8).

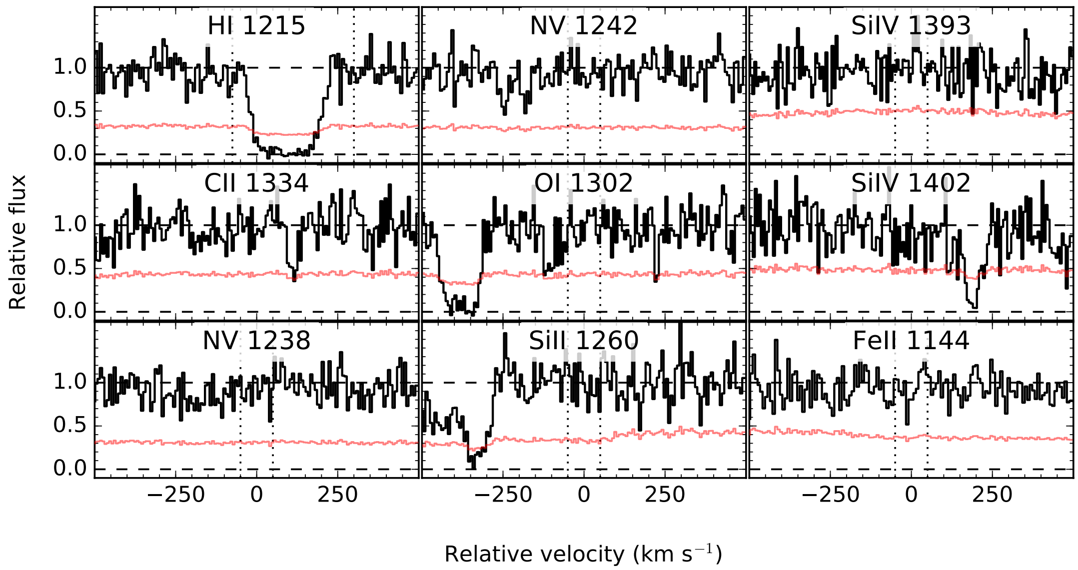

Figure C.13 Velocity profiles for the sightline towards J1404+3353 (z_{gal}=0.026).

Table C.13 Measured EWs for J1404+3353 (z=0.026)

Ion	λ [Å]	f	v_{min} [km s^{-1}]	v_{max} [km s^{-1}]	EW [mÅ]	flag*
H I	1215.670	4.164E-01	-75	300	736 ± 58	**9**
C II	1334.532	1.278E-01	0	200	. . .	2
N V	1238.821	1.570E-01	-50	50	< 101	**5**
N V	1242.804	7.823E-02	-50	50	< 103	**5**
O I	1302.168	4.887E-02	-50	50	< 147	**5**
Si II	1260.422	1.007E+00	-50	50	< 108	**5**
Si IV	1393.755	5.280E-01	-50	50	< 179	**5**
Si IV	1402.770	2.620E-01	70	300	. . .	10
Fe II	1144.938	1.060E-01	-50	50	< 117	**5**

*The data quality flags represent a sum of whether or not the line is: adopted (+1), blended (+2), undetected (+4), or saturated (+8).

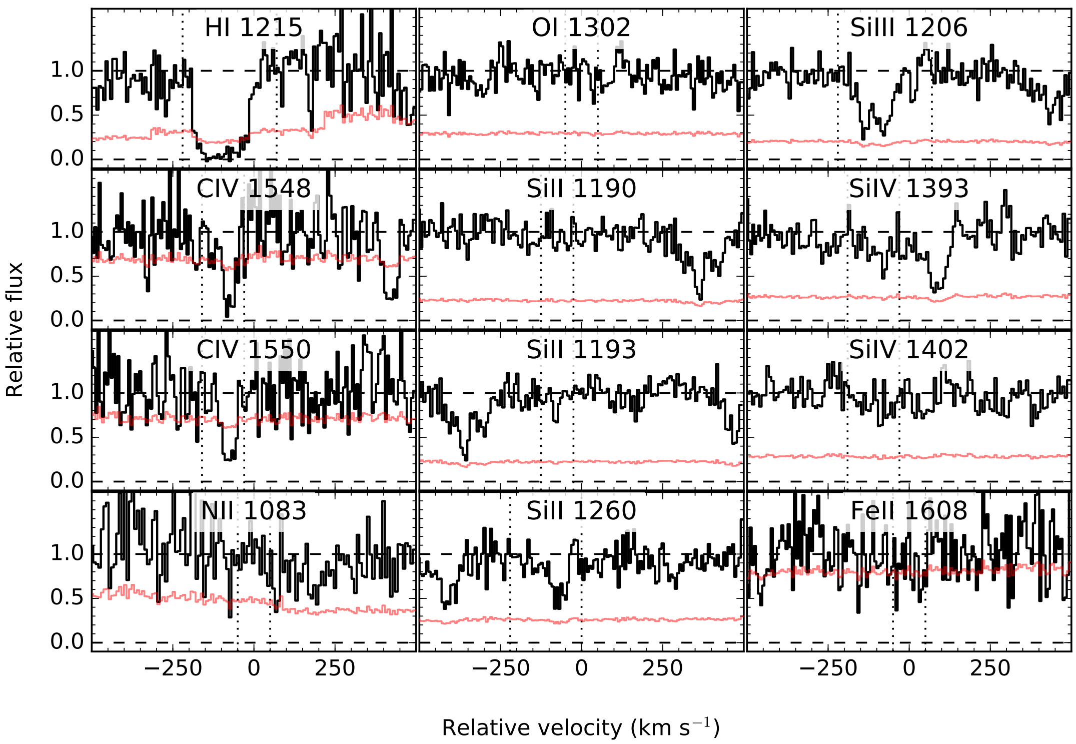

Figure C.14 Velocity profiles for the sightline towards J1419+0606 (z_{gal}=0.049).

Table C.14 Measured EWs for J1419+0606 (z=0.049)

Ion	λ [Å]	f	$v_{\rm min}$ [km s^{-1}]	$v_{\rm max}$ [km s^{-1}]	EW [mÅ]	flag*
H I	1215.670	4.164E-01	-220	70	575 ± 48	**9**
C IV	1548.195	1.908E-01	-160	-30	135 ± 100	**9**
C IV	1550.770	9.522E-02	-160	-30	107 ± 103	**9**
N II	1083.990	1.031E-01	-50	50	< 146	**5**
O I	1302.168	4.887E-02	-50	50	< 97	**5**
Si II	1190.416	2.502E-01	-125	-25	< 71	**5**
Si II	1193.290	4.991E-01	-125	-25	< 70	**5**
Si II	1260.422	1.007E+00	-220	0	158 ± 41	**1**
Si III	1206.500	1.660E+00	-220	70	294 ± 34	**1**
Si IV	1393.755	5.280E-01	-190	-30	119 ± 43	**1**
Si IV	1402.770	2.620E-01	-190	-30	93 ± 44	**1**
Fe II	1608.451	5.800E-02	-50	50	< 331	**5**

*The data quality flags represent a sum of whether or not the line is: adopted (+1), blended (+2), undetected (+4), or saturated (+8).

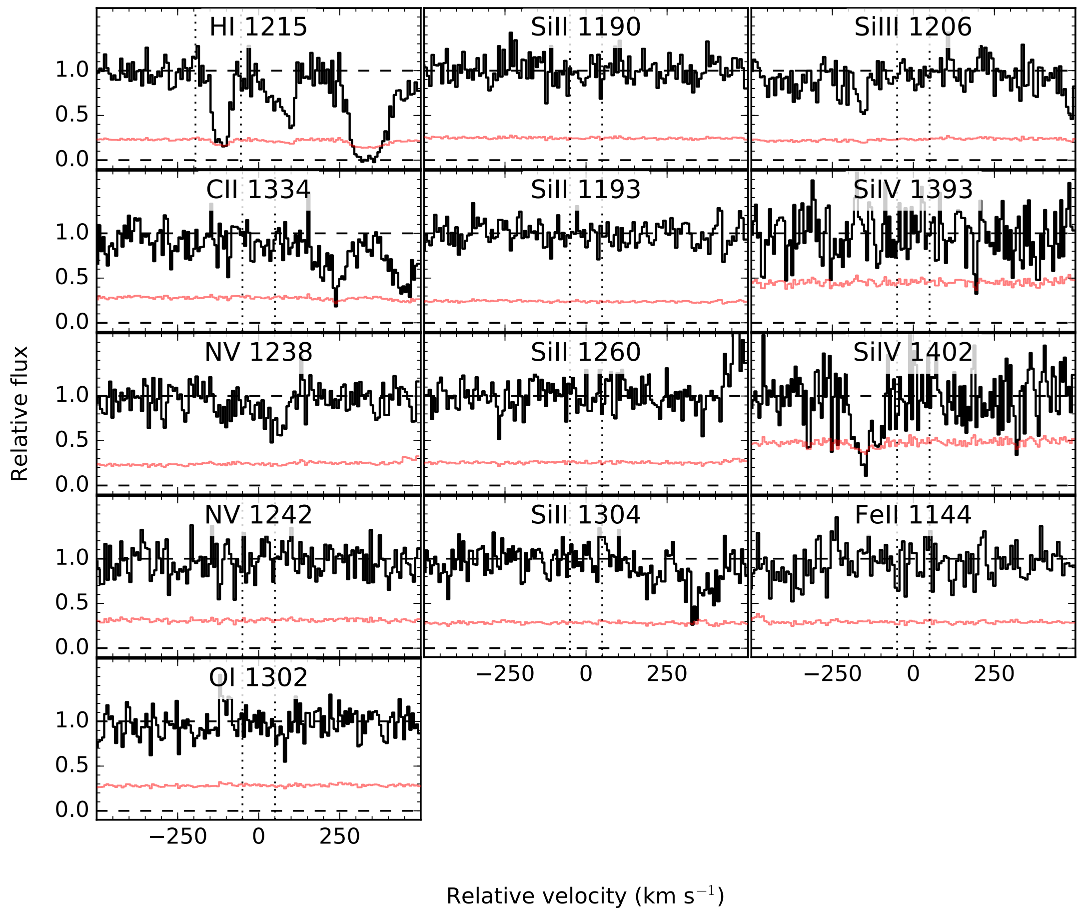

Figure C.15 Velocity profiles for the sightline towards J1454+3046 (z_{gal}=0.031).

Table C.15 Measured EWs for J1454+3046 (z=0.031)

Ion	λ [Å]	f	v_{min} [km s^{-1}]	v_{max} [km s^{-1}]	EW [mÅ]	flag*
H I	1215.670	4.164E-01	-195	-55	194 ± 27	**9**
C II	1334.532	1.278E-01	-50	50	< 95	**5**
N V	1238.821	1.570E-01	-50	50	. . .	2
N V	1242.804	7.823E-02	-50	50	< 105	**5**
O I	1302.168	4.887E-02	-50	50	< 97	**5**
Si II	1190.416	2.502E-01	-50	50	< 80	**5**
Si II	1193.290	4.991E-01	-50	50	< 78	**5**
Si II	1260.422	1.007E+00	-50	50	< 84	**5**
Si II	1304.370	9.400E-02	-50	50	< 97	**5**
Si III	1206.500	1.660E+00	-50	50	< 76	**5**
Si IV	1393.755	5.280E-01	-50	50	< 160	**5**
Si IV	1402.770	2.620E-01	-50	50	< 170	**5**
Fe II	1144.938	1.060E-01	-50	50	< 92	**5**

*The data quality flags represent a sum of whether or not the line is: adopted (+1), blended (+2), undetected (+4), or saturated (+8).

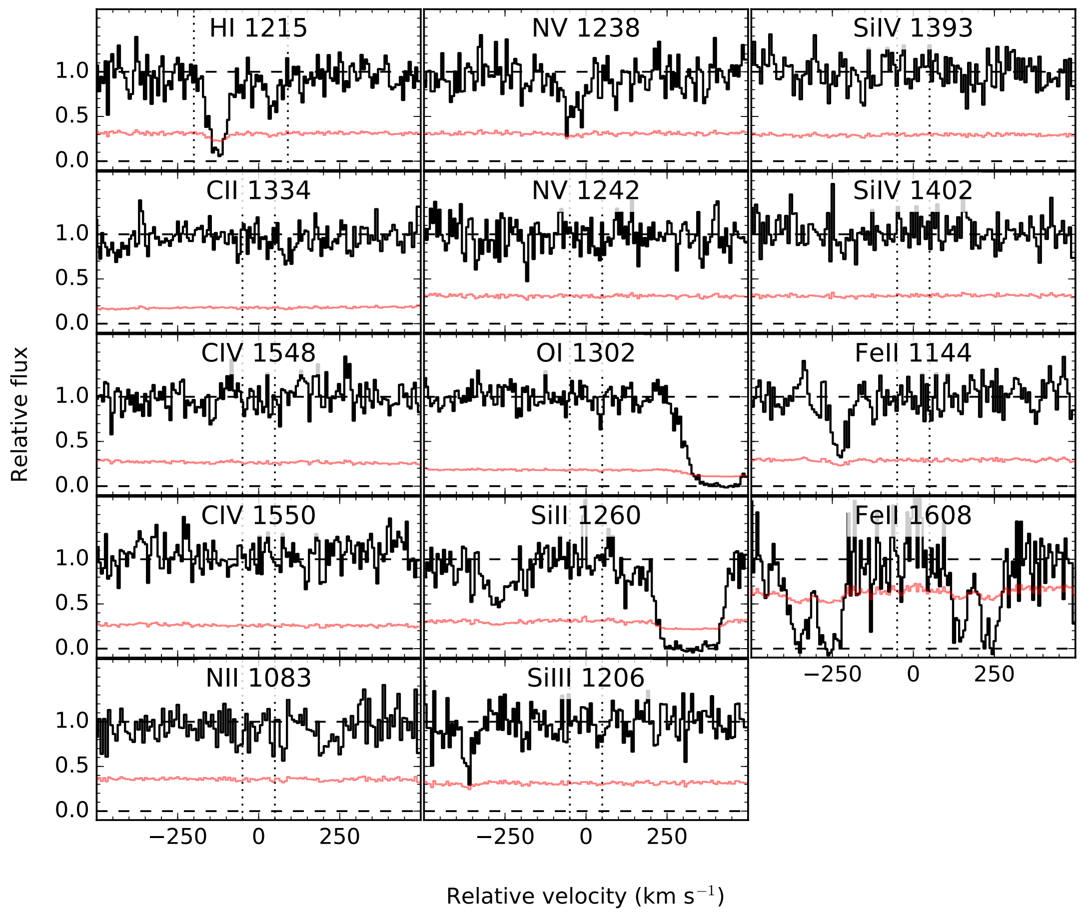

Figure C.16 Velocity profiles for the sightline towards J1536+1412 (z_{gal}=0.093).

Table C.16 Measured EWs for J1536+1412 (z=0.093)

Ion	λ [Å]	f	v_{min} [km s^{-1}]	v_{max} [km s^{-1}]	EW [mÅ]	flag*
H I	1215.670	4.164E-01	-200	90	367 ± 52	**9**
C II	1334.532	1.278E-01	-50	50	< 61	**5**
C IV	1548.195	1.908E-01	-50	50	< 105	**5**
C IV	1550.770	9.522E-02	-50	50	< 101	**5**
N II	1083.990	1.031E-01	-50	50	< 108	**5**
N V	1238.821	1.570E-01	-175	-75	. . .	6
N V	1242.804	7.823E-02	-50	50	< 97	**5**
O I	1302.168	4.887E-02	-50	50	< 59	**5**
Si II	1260.422	1.007E+00	-50	50	< 100	**5**
Si III	1206.500	1.660E+00	-50	50	< 96	**5**
Si IV	1393.755	5.280E-01	-50	50	< 111	**5**
Si IV	1402.770	2.620E-01	-50	50	< 119	**5**
Fe II	1144.938	1.060E-01	-50	50	< 89	**5**
Fe II	1608.451	5.800E-02	-50	50	< 267	**5**

*The data quality flags represent a sum of whether or not the line is: adopted (+1), blended (+2), undetected (+4), or saturated (+8).

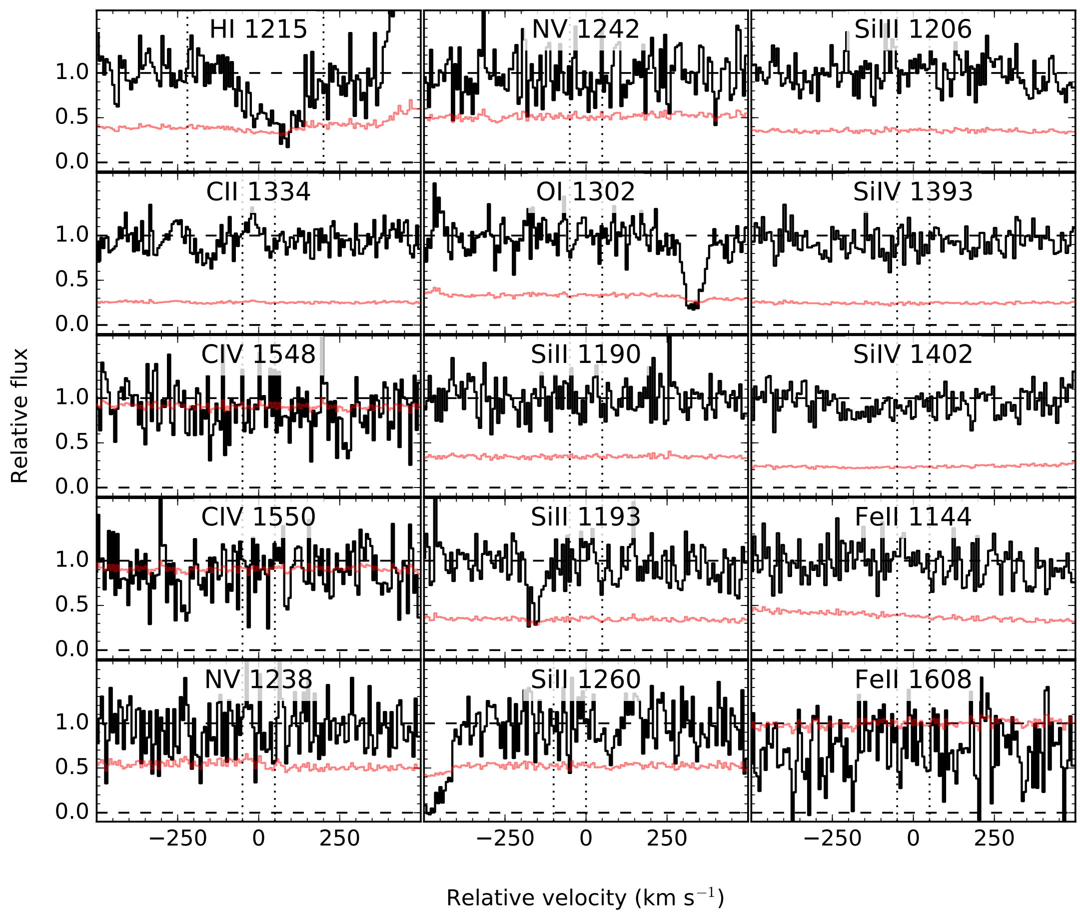

Figure C.17 Velocity profiles for the sightline towards J1607+1334 (z_{gal}=0.069).

Table C.17 Measured EWs for J1607+1334 (z=0.069)

Ion	λ [Å]	f	$v_{\rm min}$ [km s^{-1}]	$v_{\rm max}$ [km s^{-1}]	EW [mÅ]	flag*
H I	1215.670	4.164E-01	-220	200	400 ± 82	**9**
C II	1334.532	1.278E-01	-50	50	< 87	**5**
C IV	1548.195	1.908E-01	-50	50	< 363	**5**
C IV	1550.770	9.522E-02	-50	50	< 361	**5**
N V	1238.821	1.570E-01	-50	50	< 182	**5**
N V	1242.804	7.823E-02	-50	50	< 165	**5**
O I	1302.168	4.887E-02	-50	50	< 108	**5**
Si II	1190.416	2.502E-01	-50	50	< 112	**5**
Si II	1193.290	4.991E-01	-50	50	< 111	**5**
Si II	1260.422	1.007E+00	-100	0	< 172	**5**
Si III	1206.500	1.660E+00	-50	50	< 113	**5**
Si IV	1393.755	5.280E-01	-50	50	< 93	**5**
Si IV	1402.770	2.620E-01	-50	50	< 85	**5**
Fe II	1144.938	1.060E-01	-50	50	< 121	**5**
Fe II	1608.451	5.800E-02	-50	50	< 412	**5**

*The data quality flags represent a sum of whether or not the line is: adopted (+1), blended (+2), undetected (+4), or saturated (+8).

Table C.18 Measured EWs for J2133-0712 (z=0.064)

Ion	λ [Å]	f	$v_{\rm min}$ [km s^{-1}]	$v_{\rm max}$ [km s^{-1}]	EW [mÅ]	flag*
H I	1215.670	4.164E-01	-200	120	501 ± 37	**9**
C II	1334.532	1.278E-01	-140	-50	53 ± 18	**1**
C IV	1548.195	1.908E-01	-50	50	< 205	**5**
C IV	1550.770	9.522E-02	-50	50	< 212	**5**
N V	1238.821	1.570E-01	-50	50	< 74	**5**
N V	1242.804	7.823E-02	-50	50	< 83	**5**
O I	1302.168	4.887E-02	-50	50	< 73	**5**
Si II	1190.416	2.502E-01	-50	50	< 46	**5**
Si II	1193.290	4.991E-01	-50	50	< 47	**5**
Si II	1260.422	1.007E+00	-50	50	< 84	**5**
Si III	1206.500	1.660E+00	75	370	243 ± 18	**1**
Si IV	1393.755	5.280E-01	-50	50	< 75	**5**
Si IV	1402.770	2.620E-01	-50	50	< 59	**5**
Fe II	1608.451	5.800E-02	-50	50	< 252	**5**

*The data quality flags represent a sum of whether or not the line is: adopted (+1), blended (+2), undetected (+4), or saturated (+8).

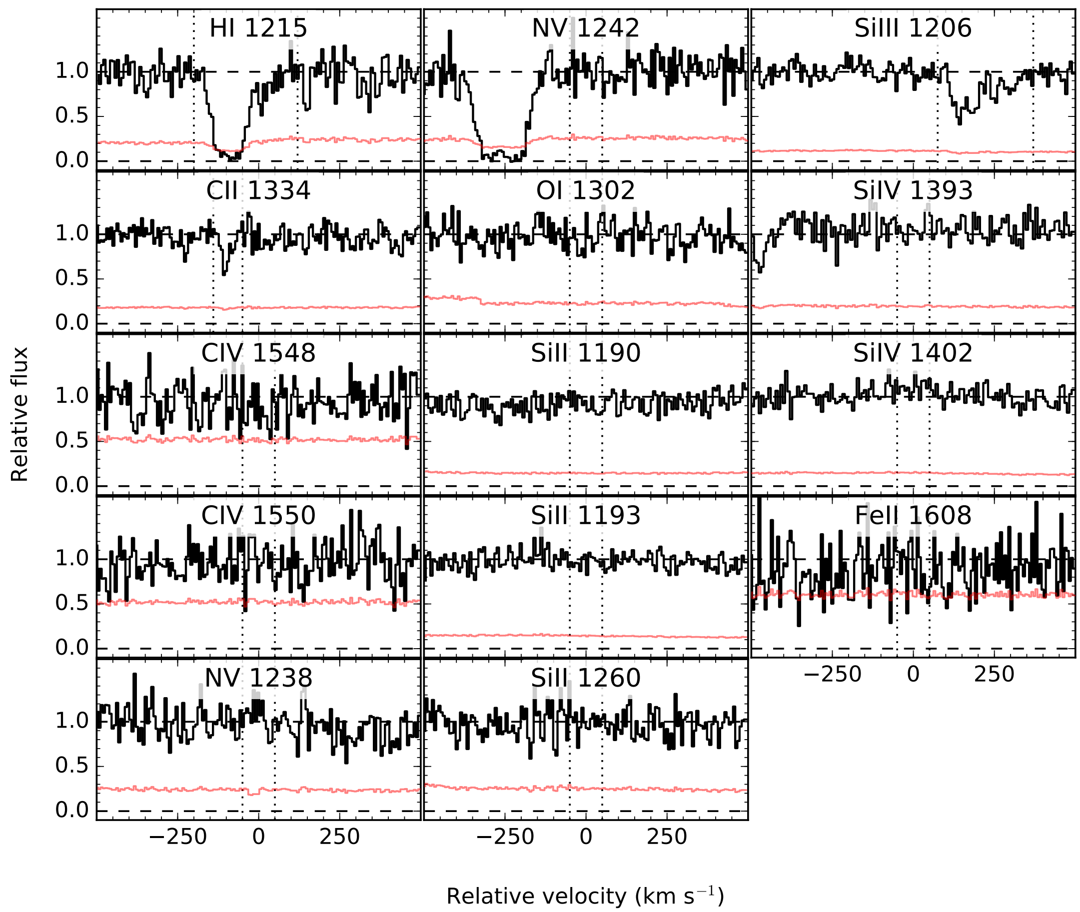

Figure C.18 Velocity profiles for the sightline towards J2133−0712 (z_{gal}=0.064).

Table C.19 Measured EWs for J2322-0053 (z=0.081)

Ion	λ [Å]	f	$v_{\rm min}$ [km s^{-1}]	$v_{\rm max}$ [km s^{-1}]	EW [mÅ]	flag⋆
H I	1215.670	4.164E-01	-250	220	785 ± 48	**9**
C II	1334.532	1.278E-01	-250	120	63 ± 29	**1**
C IV	1548.195	1.908E-01	-235	50	350 ± 90	**1**
C IV	1550.770	9.522E-02	-200	50	244 ± 85	**1**
N II	1083.990	1.031E-01	-50	50	< 63	**5**
N V	1238.821	1.570E-01	-60	40	< 78	**5**
N V	1242.804	7.823E-02	-50	50	< 77	**5**
O I	1302.168	4.887E-02	-50	50	< 39	**5**
Si II	1193.290	4.991E-01	-50	50	< 119	**5**
Si II	1260.422	1.007E+00	-100	0	< 78	**5**
Si IV	1393.755	5.280E-01	-200	0	79 ± 33	**1**
Si IV	1402.770	2.620E-01	-200	0	137 ± 34	**1**
Fe II	1144.938	1.060E-01	-50	50	< 56	**5**
Fe II	1608.451	5.800E-02	-50	50	< 202	**5**

⋆The data quality flags represent a sum of whether or not the line is: adopted (+1), blended (+2), undetected (+4), or saturated (+8).

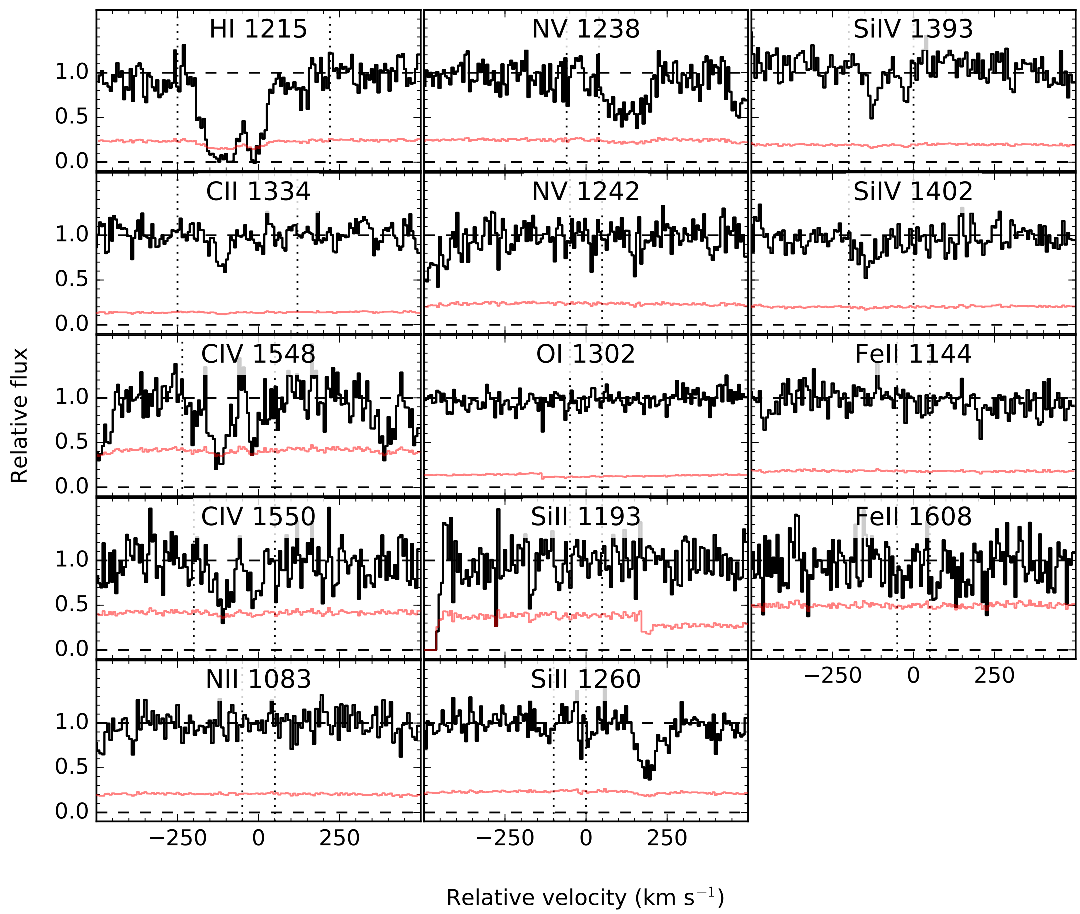

Figure C.19 Velocity profiles for the sightline towards J2322−0053 (z_{gal}=0.081).